The interannual variability of the South Vietnam Upwelling : contributions of atmospheric, oceanic, hydrologic forcing and the ocean intrinsic variability

Da Nguyen Dac

THÈSE

En vue de l'obtention du

DOCTORAT DE L'UNIVERSITÉ DE TOULOUSE

Délivré par : *L'Université Toulouse 3 Paul Sabatier*

Présentée et soutenue par : NGUYEN DAC DA

Le 18/05/2018

Titre :

VARIABILITÉ INTERANNUELLE DE L'UPWELLING DU SUD VIETNAM

Contributions du forçage atmosphérique,océanique, hydrologique et de la variabilité intrinsèque océanique

JURY

ISABELLE DADOU	Présidente	Professeur Université Paul Sabatier, France
JOHN WILKIN	Rapporteur	Professeur Rutgers University, USA
VINCENT ECHEVIN	Rapporteur	Chargé de Recherche Univ Paris 6, France
ANNE PETRENKO	Rapporteur	Maître de Conférences Aix-Marseille Université, France
ROSEMARY MORROW	Directrice de thèse	Physicienne Université Paul Sabatier, France
MARINE HERRMANN	Co-directrice de thèse	Chargé de Recherche IRD, France
FERNANDO NIÑO	Co-supervisor	Ingénieur de Recherche IRD, France
NGUYEN MINH HUAN	Co-supervisor	Associate Professor VNU University of Science, Vietnam

École doctorale et discipline ou spécialité:

SDU2E : Océan, Atmosphère, Climate

Unité de recherche :

Laboratoire d'Etudes en Géophysique et Océanographie Spatiales (UMR5566)

PhD Manuscript

Title: The interannual variability of the South Vietnam Upwelling : contributions of atmospheric, oceanic, hydrologic forcing and the ocean intrinsic variability

Nguyen Dac Da

Defended on: 18/05/2018

Thesis Directors: Marine Herrmann, Rosemary Morrow

Co-supervisors: Fernando Niño, Nguyen Minh Huan

Doctoral School: Sciences of the Universe, Environment and Space (SDU2E)

Discipline: Ocean, Atmosphere, Climate

Research Institution: Laboratory of Spatial Research in Geophysics and Oceanography (LEGOS), Toulouse, France

Acknowledgements

This PhD manuscript is the result of my work from March 2014 to June 2018. I would like to take this moment to thank to the people who have been beside me during this journey.

First of all, I owe my deepest gratitude to my principal advisor Dr. Marine Herrmann for her continuous support in every aspect of research conditions from finding financial resources, providing working facilities, giving intellectual advice and emotional encourage. She directed my research from the very beginning, closely followed my progression, and brought me back on track whenever I felt lost. I really appreciate her enthusiasm, patience and countless time that she devoted to help me overcome difficult time. Whenever I needed her help, she was there to help me no matter if it's the weekend or during her vacation.

I'm deeply grateful for the enthusiastic support of my thesis Co-Director Dr. Rosemary Morrow. She has spent countless time in her already busy schedule to help me cope with my research problems and to edit my PhD manuscript. Her advice really helped lighten my work; and her encouragement helped me keep an optimistic view of my research outcome. Her usual friendly smile and humor always helped chilling me out even in my most stressful time.

I'm indebted to my co-supervisor, Dr. Fernando Niño who lead me to the world of satellite altimetry in particular and satellite oceanography in general which played a crucial part in my PhD thesis. I always get almost instant supports from him on my technical problems with computing systems, programming skills, data analysis and everything. Above all, I was touched by his thoughtful supports for a much easier life in Toulouse which helped me spare time and focus on my research.

The last co-supervisor of my PhD thesis is Dr. Nguyen Minh Huan from Hanoi University of Science. I would like to give my special thanks to his support on giving me a background knowledge of the upwelling area, the South China Sea dynamics and available in situ data. He is also the one who enlightened me on how to become a researcher in oceanography in my fresh year of Bachelor. He has been beside me in every turn of my career path.

Besides my PhD advisors, I've also had precious supports from other colleagues who significantly contributed to the progression of my research. I'm thankful to all of the useful discussions with Dr. Yves Morel from Laboratory d'Etudes

en Géophysique et Océanographie Spatiales (LEGOS) and Dr. Vincent Comb from CEOAS, Oregon State University. I also would like to express my gratitude to Dr. Kipp Shearman and Prof. Ted Strub at CEOAS for a very meaningful internship which helped broadening my knowledge in observational oceanography. My special thanks to Prof. Sylvain Ouillon, former head of Water - Environment - Oceanography department at the University of Science and Technology of Hanoi (WEO-USTH) for his meaningful supports since 2011, to Dr. Le Toan Thuy (CESBIO) who continuously encouraged me and closely followed up on my progression, to Mr. Kiên who manages HILO cluster at USTH for being supportive to my computing problems.

I am grateful to my thesis reviewers: Prof. John Wilkin, Dr. Vincent Echevin, Dr. Anne Petrenko for their hard work, careful review, useful comments and interesting questions which helped me improve my thesis. I'm also thankful to other jury members: Prof. Isabelle Dadou, Dr. Thomas Pohlmann for their kind comments and challenging and interesting questions during my defense which gave me different views of my thesis.

I was lucky to get funded by ARTS fellowship from the Institute of Research for the Development (IRD) and to be warmly hosted by three different institutions: LEGOS, WEO-USTH, the Department of Oceanography, Hanoi University of Science (HUS). I would like to thank the secretaries of LEGOS Martine Mena, Brigitte Counou, Nadine Lacroux, the head of LEGOS Yves Morel and Alexander Ganachaud and the Doctoral School secretary Madame Marie-Claude Cathala for their supports for my paper works.

My thanks to all of my colleagues and friends at LEGOS (Nadia Ayoub, Gildas Cambon, Patrick Machesiello, Sylvain Biancamara, Sara Fleury, Lionel,), at WEO Department (Thái, Ngọc, Dr. Tú, Dr. Thu, Dr. Hiền, Dr. Hợi, Dr. Dương, Dr. Huệ), at HUS (Prof. Bộ, Prof. Ưu, Prof. Vy, Prof. Phạm Huấn, Dr. Đạt, anh Hữu, Dr. Cương, Dr. Hương, Cô Hà, Trung, Trang, Vui, Mai), at CESBIO (Hoa, Ludovic Villard, Stephan), at Aerology (Dr. Thomas Duhaut), and all of the other colleagues who I cannot name here for their relaxing and meaningful discussions.

It would be a miserable PhD life without the companionship of my Vietnamese friends (Kiên-Hoa, Việt gà, Tùng, Bích, mama Chi, Khánh-Mai, Hạnh, Luyến, Thu, Cường-Lan, anh Sơn, Nhất, Thành …) and international friends (Vandhna, Ilya, Ali, Sheng, Ruka, Xu Yang, Xiaoyue, Xiaomin, Maria ...). My special thanks for the relaxing lunches with my dear friends Cori Pegliasco, Marine Roge, Kevin Guerro, Alice Carret, Gael, Violaine .... Thanks to the ping-poong team: Xu Yang, Malek, Horlando, Zaiz (Lebanon), Sheng; and to the football team: Fifi Adodo, Michel

Tchibou, Money Guillaume, Kevin …. Those relaxing and fun moments with you guys really helped recharging my energy. You are an important part of my Toulouse life that I will never forget.

My deepest gratitudes to all of my family members: my parents (bố Nhật, mẹ Thư), my brothers (anh Mỹ, anh Đức, anh Thuấn), my sisters (chị Anh, chị Hồng), my nephews (cu Bát, cu Hiệp), my niece (con Lợn) and my close friends Dũng-Hà for always being supportive in my difficult time. A special kiss to my beautiful girlfriend who is now my beloved wife Trang for all she has done for me.

This thesis is dedicated to my beloved father who passed away when I began this thesis and to my beloved brother Đức who was unlucky to have mental illnesses. I love you!

This is just the beginning of another journey! I wish to always have you guys beside me.

Thank you all again!!!

Hà Nội, 08/06/2018

Résumé

L'upwelling du Sud Vietnam (SVU) joue un rôle clef dans la dynamique océanique et la productivité biologique en Mer de Chine du Sud. Cette thèse vise à quantifier la variabilité interannuelle du SVU et identifier les facteurs et mécanismes en jeu. Pour cela, un jeu de simulations numériques pluri-annuelles à haute résolution a été utilisé. Le réalisme du modèle a été évalué et optimisé par comparaison aux observations in-situ et satellites. Les résultats montrent que la grande variabilité du SVU est fortement pilotée par le rotationnel du vent estival, et liée à l'oscillation ENSO via son impact sur le vent. Cependant, cette influence du vent est significativement modulée par la variabilité intrinsèque océanique liée aux interactions entre la vorticité associée aux tourbillons océaniques et le vent, et dans une moindre mesure par la circulation océanique de grande échelle et les fleuves. Ces conclusions sont robustes aux choix effectués pour corriger la dérive de surface du modèle.

Mots Clefs:
upwelling, variabilité interannuelle, ENSO, interactions vent-tourbillons, Mer de Chine du Sud, modélisation régionale océanique, OIV

Abstract

The summer South Vietnam Upwelling (SVU) is a major component of the South China Sea circulation that also influences the ecosystems. The objectives of this thesis are first to quantitatively assess the interannual variability of the SVU in terms of intensity and spatial extent, second to quantify the respective contributions from different factors (atmospheric, river and oceanic forcings; ocean intrinsic variability OIV; El-Niño Southern Oscillation ENSO) to the SVU interannual variability, and third to identify and examine the underlying physical mechanisms. To fulfill these goals we use a set of sensitivity eddy-resolving simulations of the SCS circulation performed with the ROMS_AGRIF ocean regional model at 1/12° resolution for the period 1991-2004. The ability of the model to realistically represent the water masses and dynamics of the circulation in the SCS and SVU regions was first evaluated by comparison with available satellite and in-situ observations. We then defined a group of sea-surface-temperature upwelling indices to quantify in detail the interannual variability of the SVU in terms of intensity, spatial distribution and duration. Our results reveal that strong SVU years are offshore-dominant with upwelling centers located in the area within 11-12ºN and 110-112ºE, whereas weak SVU years are coastal-dominant with upwelling centers located near the coast and over a larger latitude range (10-14ºN). The first factor that triggers the strength and extent of the SVU is the summer wind curl associated with the summer monsoon. However, its effect is modulated by several factors including first the OIV, whose contribution reaches 50% of the total SVU variability, but also the river discharge and the remote ocean circulation. The coastal upwelling variability is strongly related to the variability of the eastward jet that develops from the coast. The offshore upwelling variability is impacted by the spatio-temporal interactions of the ocean cyclonic eddies with the wind stress curl, which are responsible for the impact of the OIV. The ocean and river forcing also modulate the SVU variability due to their contribution to the eddy field variability. ENSO has a strong influence on the SVU, mainly due to its direct influence on the summer wind. Those results regarding the interannual variability of the SVU are robust to the choice of the surface bias correction method used in the model. We finally present in Appendix-A2 preliminary results about the impacts of tides.

KEYWORDS : upwelling, interannual variability, ENSO, wind-eddy interactions, South China Sea, regional ocean modeling, OIV

Table of contents

Acknowledgements 5

Résumé 8

Abstract 9

List of Figures 13

List of Tables 15

Introduction (français) 16

Context 19

Chapter 1: Introduction 22

1.1 The SCS 22

1.1.1 Geomorphology - complex topography 22

1.1.2 Forcing systems 25

a) Atmospheric forcing 25

b) Oceanic transport through Luzon Strait 31

c) River forcing 32

d) Tidal forcing 33

1.1.3 The SCS Dynamics 35

a) Large scale ocean Circulation 35

b) Meso-scale structures 37

c) Thermohaline structure 40

d) Upwelling systems 43

1.2 The South Vietnam Upwelling (SVU) 44

1.2.1 Dynamical and biogeochemical role 44

1.2.2 Mechanisms 47

1.2.3 Seasonal variations 51

1.2.4 Interannual Variability 52

1.3 Objectives 53

Chapter 2. Methods and tools 55

2.1 The numerical hydrodynamical model ROMS (Regional Ocean Modeling System) 56

2.1.1 Governing equations 56

2.1.2 Terrain-following coordinate system 59

2.1.3 Reasons for the choice of tool 60

2.2 Grid and forcings 63

2.3 Reference and Sensitivity Simulations 66

2.4 In-situ and satellite observation datasets 67

Chapter 3. Evaluation of model results 69

3.1 Seasonal spatial patterns of surface circulation and water

masses properties 69
3.1.1 Sea Level Anomaly (SLA), surface geostrophic circulation and eddy kinetic energy (EKE). 69
3.1.2 Sea Surface Temperature (SST) 72
3.1.3 Sea Surface Salinity (SSS) 73
3.2 Seasonal and interannual variations of surface circulation and water masses properties 76
3.3 Temperature and salinity vertical structure 79
3.4 Model SLA versus tide gauges SLA 82

Chapter 4. Interannual variability of SVU and contribution of different factors 85
4.1. Upwelling index definition 85
4.2 Interannual variability of the SVU 89
4.3 Contribution of different forcings to the interannual variability of SVU 92
4.3.1 Atmospheric forcing 93
4.3.2 Oceanic forcing 95
4.3.3 River forcing 96
4.3.4 Ocean intrinsic variability (OIV) 97
4.4 Interactions between atmospheric and oceanic forcing 99
4.5 Discussion : Mechanisms contributing to the SVU variability 101
4.5.1 Impact of atmospheric variability: the confirmed key role of wind 101
4.5.2 Impact of background ocean circulation 102
4.5.3 Variability of the SVU via vertical velocity (w) and limitations of w-based upwelling index 111
4.5.3 The role of El Niño-Southern Oscillation (ENSO) 113
4.6 Summary of main results 121

Chapter 5. Sensitivity of results to the model configuration choices : surface bias correction and river freshwater fluxes 122
5.1 Configuration of the reference simulation : impact of the surface bias correction method and the river mouth locations. 122
5.1.1 Test on the Pearl River plume representation. 123
5.1.2. Tests on the surface biases correction method. 126
5.2 Adjustment of T0, and Tref 129
5.3 Variability of the SVU associated with the relocation of the Pearl river, heat and water flux filters and SST-SSS relaxation. 131
5.4 Impacts of relaxation on the relation between SVU, wind, vorticity and ENSO 135
5.4.1 SVU Uly vs wind 135
5.4.2 Uly vs surface vorticity 135
5.4.3 Uly vs ENSO 136

Chapter 6. Conclusion and future work 137
6.1. Objectives and methodology 137

6.2 Interannual variability of the SVU : estimation, driving factors and mechanisms 138
6.3 Robustness of previous results to the configuration of the model: impacts surface bias correction method 142
6.4 Limitations and perspectives 143

Conclusion finale (français) 146
Objectifs et méthodologie 146
Variabilité interannuelle du SVU 147
Perspectives 148

APPENDIX 151

A1. Impacts of the relocation of the Pearl River on the SSS distribution 151

A2. Influence of Tides 151
A2.1. Representation of tides 152
A2.2 Impacts of tidal forcings on the SCS dynamics 155

BIBLIOGRAPHY 158

List of Figures

Context **19**
Figure 0 : Socio-economic importance of the South China Sea region 19

Chapter 1 - Introduction **22**
Figure 1.1 Geography and bathymetry of the South China Sea 23
Figure 1.2 Monsoon in the Southeast Asia 24
Figure 1.3 Seasonal wind distribution in the SCS 26
Figure 1.4: Annual mean of wind, heat flux and water flux in the SCS 27
Figure 1.5 Climatological seasonal net surface heat and water flux distribution in the SCS 28
Figure 1.6 Madden Julian Oscillation 29
Figure 1.7 Indian Ocean Dipole 30
Figure 1.8 El Nino Southern Oscillation atmospheric-ocean system 31
Figure 1.9 Kuroshio intrusion observed by altimeter satellite. 32
Figure 1.10 : Climatological monthly freshwater discharges from the Mekong, Red and Pearl Rivers 33
Figure 1.11 Tidal amplitude of M2, K2, S2 and O1 components in the SCS 34
Figure 1.12 : SCS circulation at different depths in August and December 37
Figure 1.13 Seasonal permanent eddies in the SCS 38
Figure 1.14: Seasonal maps of SST, SSS and MLD in the SCS 41
Figure 1.15: Mean TS profiles from SCSPOD14 dataset at locations indicated in Figure 1.1 42
Figure 1.16 The SCS domain, locations of TS-profiles and tide gauges, and August climatological dynamical background 45
Figure 1.17 Impacts of the SVU to regional biomass and climate. 46
Figure 1.18 Schematic summary of the mechanisms of the SVU 47
Figure 1.19 Climatological summer wind and respective Ekman pumping over the SCS. 49
Figure 1.20 Evidence of the SVU via Meris Chlorophyll and AVHRR SST. 49
Figure 1.21. Wind independent mechanism of the SVU proposed by Chen et al. 2012. 50
Figure 1.22 Intraseasonal and interannual variability of the SVU via AVHRR SST 51

Chapter 2 - Methods and tool **55**
Figure 2.1: Data coverage of the AVHRR SST dataset 55
Figure 2.2 Characteristics of Z and sigma vertical coordinates 60
Figure 2.3 CFSR wind vs. QuikScat and NCAR wind in the SCS 64
Figure 2.4 Inter-comparison of original and corrected CFSR net heat flux with TropFlux and OAflux 65
Figure 2.5 SCSPOD14 data coverage 68

Chapter 3 - Evaluation of model results **69**
Figure 3.1. Comparison between CTRL and ALTI SLA 70

Figure 3.2. Eddy kinetic energy between CTRL and ALTI 71
Figure 3.3. Comparison between CTRL and AVHRR SST 72
Figure 3.4. Comparison between CTRL and SCSPOD14 SSS 74
Figure 3.5 A zoom in of Pearl river mouth (Source: Google Map) 75
Figure 3.6: Annual and interannual variation of SST, SSS and SLA between CTRL and observations 77
Figure 3.7: Comparison between CTRL and SCSPOD14 TS-profiles 80
Figure 3.8. Comparison of CTRL and tide gauges SLA 83

Chapter 4 - Interannual variability of the SVU and contribution of different factors 85
Figure 4.1. Upwelling frequency with respect to different temperature thresholds T0 86
Figure 4.2. Cumulative upwelling intensity in CTRL simulation (maps) 88
Figure 4.3: Upwelling indexes in the CTRL and sensitivity simulations (time series) 90
Figure 4.4: CTRL vs AVHRR SST: individual events 91
Figure 4.5: Geographical locations of upwelling centers in different simulations 93
Figure 4.6. Upwelling and wind relation 102
Figure 4.7. Upwelling and wind relation in different years of CTRL simulation 103
Figure 4.8. Difference of upwelling in CTRL, SimR and SimO under the same wind conditions 104
Figure 4.9 Offshore upwelling mechanism revealed by CTRL simulation 106
Figure 4.10 Confirmation of offshore upwelling mechanism in different sensitivity simulations 108
Figure 4.11. Impacts of OIV to the SVU revealed by SimI 109
Figure 4.12 Confirmation of offshore upwelling mechanism in SimI 110
Figure 4.13 Cumulative Vertical positive velocity at 50m over the SVU 112
Figure 4.14 Effectiveness of the SVU in terms of upward vertical water flux. 113
Figure 4.15. Upwelling and ENSO relations 114
Figure 4.16: ENSO vorticity preconditioning mechanisms (time evolution maps) 116
Figure 4.17: Significance of ENSO vorticity preconditioning in JET+ and OFF+ regions 120

Chapter 5 - Robustness of results in Chapter 4 122
Figure 5.1 : SST biases and trends and the calculation of T0 and Tref in CTRL, CTRL2 and NoRel 129
Figure 5.2 Cumulative upwelling intensity of CTRL (new method of computation and new domain) 131
Figure 5.3 Cumulative upwelling intensity of CTRL2 132
Figure 5.4 Cumulative Upwelling intensity of NoRel 132
Figure 5.5: The movement of a strong northern eddy in 1992 133
Figure 5.6 Upwelling vs. wind vs. ENSO: CTRL, CTRL2 and NoRel 135

Chapter 6. Conclusion and future work 137
Figure 6.1 Schematic summary of different mechanisms of the SVU 141

APPENDIX 151

A1. Impacts of the relocation of the Pearl River on the SSS distribution 151

Figure A1.1 - Summer SSS in CTRL, CTRL2 (with Pearl river bay closed) and SCSPOD14. 151

A2. Influence of Tides **151**

Figure A2.1 Comparison of amplitudes of major components (M2, S2, K1, O1) between Test-0t-a and TPXO7 154

Figure A2.2 Comparisons of phase of K1, O1, M2, S2 between Test-0t-a and TPXO7 155

List of Tables

Table 2.1 Simulation parameters 61

Table 4.1: Quantification of upwelling index: mean and variability 95

Table 5.1 Impacts of relaxation and heat and water flux correction on model performances 124

Introduction (français)

La Mer de Chine Méridionale (SCS), en Asie du Sud Est, est l'une des plus grandes mers marginales de l'océan mondial, et est le siège d'immenses enjeux économiques, géopolitiques, environnementaux et sociétaux. Selon les estimations de la Banque Mondiale, les régions côtières de la SCS réunissent 26% de la population mondiale et 18% du PIB, et on y observe les densités de population les plus élevées du monde, dépassant les 1000 habitants.km-2. Cette forte densité de population s'accompagne d'un développement économique frénétique, avec une augmentation annuelle du PIB d'environ 6.3% (contre 2.5% à l'échelle mondiale). En 2016, 3370 milliards de dollars de marchandises y ont transité. Cette population, qui dépend en grande partie des ressources maritimes (tourisme, pêche, aquaculture), vit le long des côtes dans des régions de faible élévation, et est donc très fortement soumise aux aléas climatiques : typhons, inondations, sécheresses, oscillation climatique ENSO (El Niño Southern Oscillation), érosion littorale... Une dizaine de typhons traversent la région chaque année (Goh and Chan, 2010). L'événement El Niño exceptionnel de 2015-16 a eu des conséquences dramatiques en Asie du Sud Est : le Sud du Vietnam a ainsi connu la sécheresse la plus intense des 90 dernières années (FAO, 2016), alors que les inondations de 2016 au Nord du Vietnam ont provoqué plus d'une centaine de morts. Le trait de côte dans le delta du Mékong (Sud Vietnam) a reculé de 90 km en 2016, le plus fort recul jamais observé (UNESCAP, 2016). Réciproquement, cette importante activité humaine à de multiples conséquences sur l'environnement littoral, côtier et marin. Ainsi en 2016, le largage accidentel de plus de 300 tonnes de produits toxiques par l'aciérie de Formosa au Nord du Vietnam a conduit à la destruction quasi-totale de la faune et de la flore marine sur plus de 200 km de côtes (Tri et al., 2017). Les conséquences du changement climatique s'y font aussi sentir : le niveau de la mer est monté dans la SCS de 20 cm au cours des 50 dernières années, et la hausse de 1 m prévue pour 2100 provoquerait une disparition de 30 à 50% des terres du Delta du Fleuve Rouge (Duc & Umeyama, 2012). La SCS est donc soumise à des forçages de différentes échelles (de l'événement extrême à la variabilité interannuelle et au changement climatique) et de différentes origines (atmosphérique, océanique, hydrologique et anthropique), et mieux comprendre l'influence de ces forçages est donc un enjeu majeur à l'échelle régionale. C'est également un enjeu à l'échelle globale : la SCS est en effet une région clef dans les échanges de masses d'eau de la circulation thermohaline globale entre l'océan Pacifique et l'Océan Indien (le "South China Sea Throughflow", SCSTF, Qu et al., 2009).

Ces facteurs de variabilité font intervenir et participent à des interactions complexes entre les différents compartiments du système couplé océan-atmosphère-continent dans cette région. Afin de mieux comprendre ces facteurs et de prévoir et mitiger leurs conséquences, il est essentiel d'améliorer notre connaissance de ce système. Ce travail de thèse s'inscrit dans cette problématique, en s'intéressant à l'une des composantes majeures de ce système, l'océan. L'objectif scientifique général de cette thèse est de mieux comprendre les processus qui gouvernent la dynamique océanique en SCS et leur réponse aux différents facteurs de variabilité. Pour cela, nous nous penchons en particulier sur l'upwelling du Sud Vietnam (SVU).

Le SVU se développe pendant la mousson d'été et joue un rôle majeur dans la dynamique océanique de la région. De plus il y conditionne la productivité biologique et donc les ressources halieutiques, et peut être à l'origine de « marées rouges » (Loick et al., 2007; Dippner et al., 2011). Il présente une forte variabilité quotidienne, saisonnière, et interannuelle. Les études existantes ont suggéré un rôle déterminant du vent dans le déclenchement du SVU et ont émis l'hypothèse de l'influence d'ENSO, et ont également soulevé la question de l'influence des panaches de fleuves et de la marée (Xie et al., 2003 ; Dippner et al., 2007 ; Loick-Wilde et al. 2017…). Par ailleurs, plusieurs études récentes ont mis en évidence dans d'autres régions de l'océan global, et suggéré en SCS, l'impact significatif de la variabilité intrinsèque océanique sur les processus impliqués dans la circulation océanique, liée à son comportement chaotique associé notamment aux structures de (sub)mésoéchelle (voir par exemple Penduff et al., 2011; Li et al., 2014 ; Waldman et al., 2018). Les études précédentes de la circulation en SCS et du SVU ont été effectuées sur de courtes périodes, ou avec des modèles numériques de basse résolution ne permettant pas de résoudre correctement ces structures. Si plusieurs études ont permis d'identifier certains des facteurs qui gouvernent la variabilité du SVU, l'estimation précise de cette variabilité et l'identification des mécanismes physiques associés restent encore à faire, en particulier en ce qui concerne la variabilité interannuelle. Ceci constitue l'objectif précis de cette thèse, qui vise à mettre en place des simulations pluriannuelles à haute résolution, permettant de résoudre la méso-échelle (eddy-resolving) afin d'estimer quantitativement la variabilité interannuelle du SVU ainsi que les contributions respectives des différents facteurs de variabilité (forçage atmosphérique, circulation océanique de grande échelle, panaches des fleuves, marée, variabilité intrinsèque océanique et ENSO), et d'identifier les mécanismes physiques associés.

La structure de ce manuscrit de thèse est la suivante. Dans un premier chapitre nous présentons une revue bibliographique de la connaissance actuelle de la zone

d’étude (forçages, circulation océanique, variabilité) en abordant d’abord la SCS puis en nous concentrant sur le SVU. Dans le deuxième chapitre nous détaillons les outils et la méthodologie adoptés : observations satellites et in-situ, modèle numérique et stratégie de modélisation. Le troisième chapitre est consacré à l’évaluation du réalisme de notre simulation de référence. Nous analysons les résultats obtenus dans cette simulation de référence ainsi que dans des simulations de sensibilité associées dans le quatrième chapitre, où sont présentés les principaux résultats concernant la variabilité interannuelle du SVU et les mécanismes associés. La robustesse de nos résultats aux choix de configuration du modèle est testée dans le chapitre 5. Nous rappelons les principaux résultats et dressons un inventaire des perspectives de ce travail dans le dernier chapitre de conclusion. L’annexe A2 présente des résultats préliminaires concernant la prise en compte et le rôle de la marée.

Ce document a été rédigé en anglais, mais un résumé, une introduction et une conclusion en français ont été inclus.

Context

The South China Sea (SCS) is a crucial economical-political location of the world. It is a vital route of worldwide goods exchange between large economies including China, Japan, Korea, ASEAN (Association of Southeast Asian Nations), European and American countries (Figure 0a). In 2016, $3.37 trillion worth of goods was transported through the SCS (China Power Team, 2017). It is surrounded by 9 East and South East Asian countries including Vietnam, Cambodia, Thailand, Malaysia, Singapore, Indonesia, Brunei, Philippines and China. According to the World Bank, in 2016, this region accounted for 26.3% of the 7.44 billion world population, and 18% of the $75.845 trillion world GDP (Gross Domestic Production). This is also a fast growing region with a weighted average GDP growth rate of 6.3% compared to 2.5% of the world average in 2016.

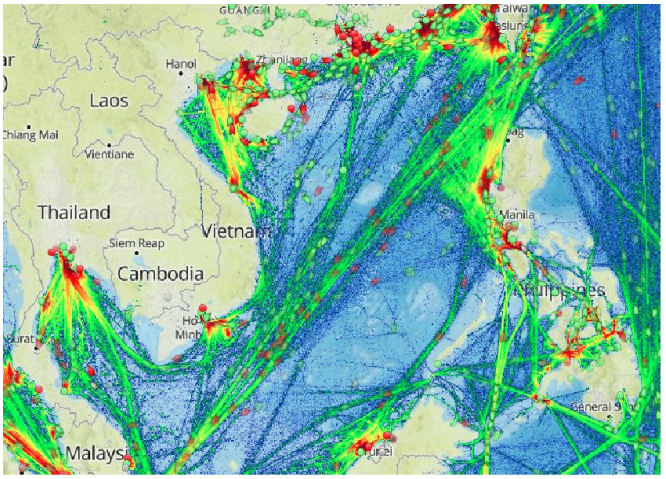

a) Ship routes in the South China Sea (source: MarineTraffic)

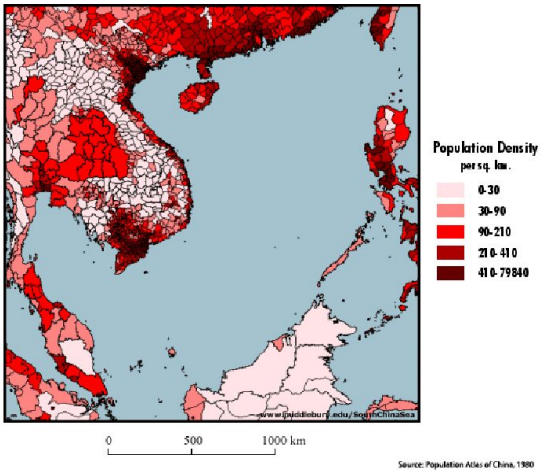

b) Population density around the South China Sea (source: Population Atlas of China, 1980)

Figure 0 : Socio-economic importance of the South China Sea region

SCS coastal areas are among the most densely populated in the world (>1000 hab/km^2 in some areas including Vietnam, Figure 0b) because these areas are particularly adapted to rice production, and due to the presence of marine resources including aquaculture, fisheries, transportation and tourism.These low elevated and densely populated areas are therefore most vulnerable to extreme weather events that hit the region, including typhoons, storm surges, floods and droughts. Human and economic loss due to frequent typhoons (~10/year in the SCS, Goh and Chan, 2010) can result directly from the ocean via storm surges or indirectly via excessive wind strength, rainfall as well as flooding and inland landslide . In addition, the climate system in the SCS is modulated by multiple ocean-atmosphere interactions processes at different time scales from

intra-seasonal (Madden Julian Oscillation, MJO), to inter-annual i.e. Indian Ocean Dipole (IOD) and El Niño Southern Oscillation (ENSO). According to Food and Agriculture Organization (FAO) of the United Nations, in 2016, Vietnam experienced for example its strongest drought in the last 90 years due to El Niño. At larger time scales, climate change has been a hot issue over the last decades. Global warming, earth poles' ice melting, sea level rise and increasing trend of heavy precipitation events in a number of region were reported by the Intergovernmental Panel on Climate Change (IPCC) in 2014. It is essentially important to estimate and forecast regional impacts of climate change, in particular for low elevated and densely populated regions like Vietnam coastal and deltaic regions, which could be hugely impacted by sea level rise.

The fast growing economy in the region also comes with environmental consequences. Under strong economic pressure, environmental damages occurs more often and at larger scales. Industrial pollution is released to the air, soil and water (either to rivers or the ocean) and the air-sea coupled system is an important means of transport of this pollution to larger scales. For example, in April 2016, a Formosa Steel plant located on the coast of Ha Tinh province in Vietnam released more than 300 tons of toxic substance to the ocean which caused massive fish mortality along a 200 km coastal area south of the steel plant (Tri et al., 2017). It impacted millions of people whose income is based on fishing, aquaculture and tourism. This shows that environmental damage can sometimes be more costly than the economic benefits. These damages can be irreversible or take decades to return to their initial state.

Understanding and forecasting the response of the SCS regional coupled atmosphere-ocean-continent coupled system to those sources of variability of different scales and origins is therefore a strong scientific and socio-economic challenge, that requires improvements in our knowledge of the dynamics of this system as well as its tele-connection with other regions in the world. The ocean is one of the key components of the coupled regional system. Better understanding the functioning and variability of the processes that participate to the ocean circulation is therefore essential for a better understanding of the whole system.

This wider scientific objective constitutes the fundamental motivation of this thesis : the objectives of this PhD are to study the governing processes of the SCS dynamics, and their responses to variations in the overlying atmosphere. We focus here on the study of the South Vietnam Upwelling (SVU) – one of the key features of the SCS dynamics in summer, which also impacts on the local marine ecosystems : it is associated with strong primary production which can provide fishing resources to

local people but also induce “red tides” (Loick et al., 2007; Dippner et al., 2011). Thus it represents a direct connection between the natural variability and that influenced by human society, between economic resources and cost. Its variations exhibit multiple time scales (Xie et al., 2003, 2007; Liu et al., 2012; Li et al., 2014), therefore understanding the factors involved in these variations has both a strong scientific and socio-economic stake.

The structure of the thesis is as follow: Chapter 1 gives an overview of the main forcing factors that affect the SCS dynamics including atmospheric forcing, remote oceanic circulation, tidal influence and river input. Then we present the current knowledge of the SCS dynamics, including large scale circulation, mesoscale eddies, thermohaline structure and upwelling systems. In Chapter 2, we describe our methodology as well as the observation data and numerical tools used for this study. Evaluations of the model outputs are shown in Chapter 3. Next, our findings on inter-annual variability of the South Vietnam Upwelling in relation with atmospheric forcing, lateral oceanic forcing, river forcing, ocean intrinsic variability and ENSO are explained in Chapter 4. The robustness of our conclusions to the choices of configuration of the numerical model is examined in Chapter 5. Finally, chapter 6 gives the conclusions and perspectives. Preliminary work concerning the influence of tides on SCS dynamics and SVU is presented in Appendix-A2

Chapter 1: Introduction: forcing factors, circulation and hydrodynamical processes in the South China Sea and South Vietnam Upwelling region.

In this chapter we first present a literature review of our current knowledge of the forcing factors and hydrodynamical processes involved in the functioning and variability of the SCS ocean circulation. We then focus on the SVU. We finally present the detailed objectives of this thesis.

1.1 The SCS

1.1.1 Geomorphology - complex topography

The South China Sea (SCS) located south of China and east of Vietnam within about (2.5°S - 25°N and 99°E - 121°E) is one of the largest marginal seas in the world, covering ~ 3.6 million km^2. Figure 1.1 shows the bathymetry of the SCS plotted using Gebco_08 dataset released by British Oceanographic Data Centre (BODC) in 2010 (www.gebco.net). Almost half of the area of the SCS (1.6 million km^2) is shallow shelf with depth < 100m. In the North, the shelf starts from Taiwan strait then extends southwestward to Hainan with a mean width of about 100km. Then the shelf covers the whole Gulf of Tonkin. In the South, all of the area west of 108°E including the Gulf of Thailand is shallow shelf. The continuity of the northern and southern shelves is disrupted by the steep continental slope near central Vietnam. The central part of the SCS is deep ocean (depth from 1000 m up to 5000 m), located east of the 110°E and covering about 1.3 million km^2. The SCS has an average depth of 1000 m.

There are two major groups of islands in the SCS: Hoang Sa (Paracel islands) located at in the northwest of the deep SCS basin and Truong Sa (Spratly Islands) located in the south and southwest of the deep SCS basin. The SCS has many connections with other seas and oceans: with East China Sea and the Pacific in the northeast via Taiwan Strait and Luzon Strait, with Soulu Sea via Mindoro and Balabac strait in the East, with Java Sea in the South via Kalimantan Strait and with Indian Ocean in the Southwest via Malacca Strait. Most of the straits are either shallow and/or narrow with depths < 100m (except Mindoro and Luzon) and widths ranging from 30 km in Malacca Strait to 350 km in Luzon Strait. Of all the straits,

Luzon Strait is by far the most important one with largest width and deepest sill depth (~2000 m).

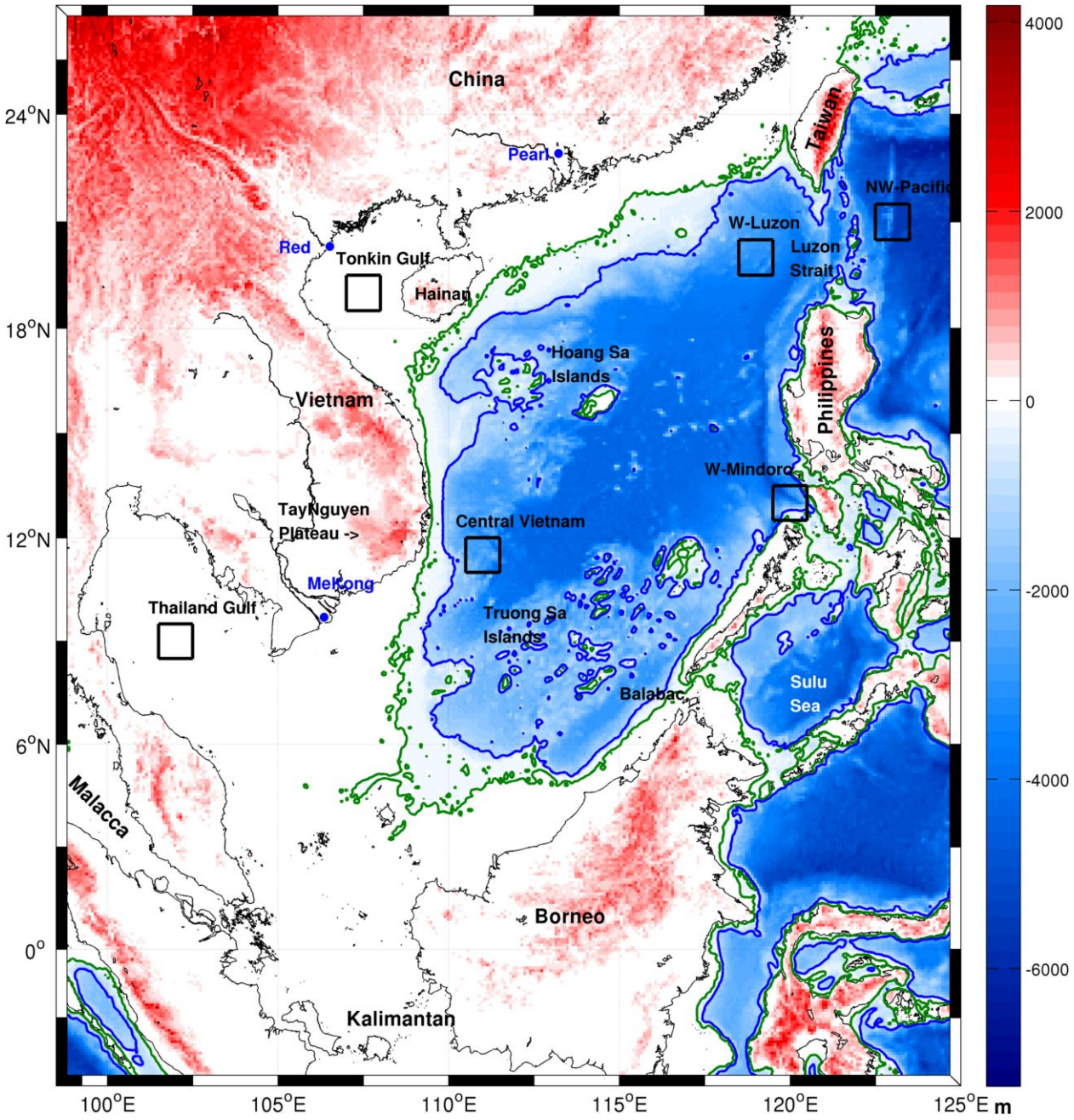

Figure 1.1 Geography and bathymetry of the South China Sea. The green and blue contours represent isobaths of 100 and 1000 m (data from GEBCO). The black rectangles represent locations and area (1°x1°) for calculation of mean temperature-salinity profiles in Figure 1.15.

Several mountain ranges with heights up to 2000 m surround the South China Sea and impact on the wind field. The ones along Vietnam, Taiwan and Philippines are perpendicular to the predominant monsoon direction over the SCS (see next section). They can cause a strong orographic effect and thus can induce distinct wind stress curl patterns over the SCS.

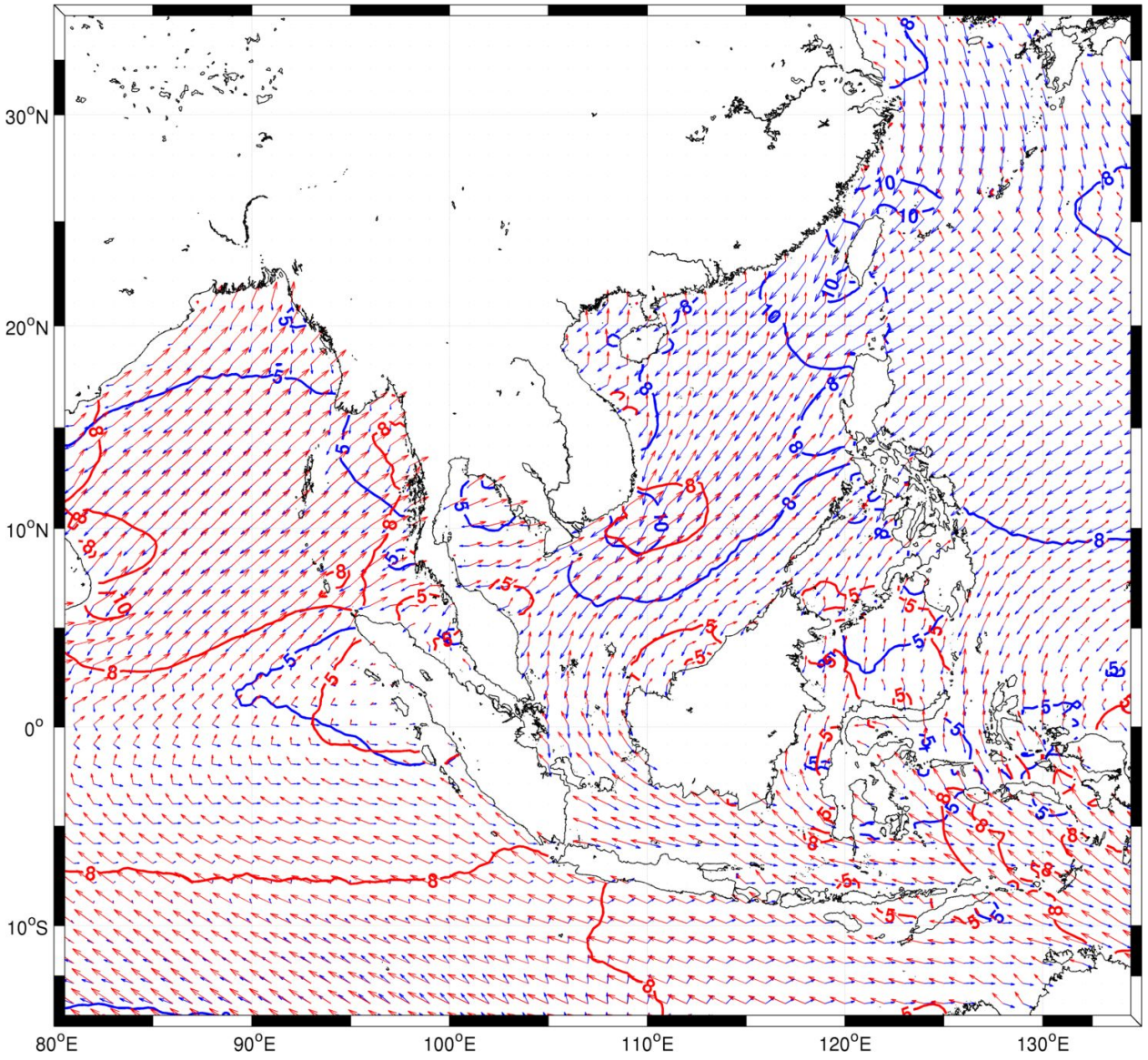

Figure 1.2 Monsoon in the Southeast Asia. Climatological seasonal wind at 10m above the sea surface over South East Asia from QuikScat satellite data (2000-2008). Dark red shaded inland area represent topography > 500m. Red/blue arrows represent summer (JJA) / winter (DJF) wind speed and direction, and contours show the associated values (m/s) of wind speed.

1.1.2 Forcing systems

a) Atmospheric forcing

The SCS is located inside the Northwestern Tropical Pacific monsoon system (Wang et al., 2009) and is connected to other monsoon systems including the East Asian Monsoon, the Indian Monsoon and the Australian Monsoon. Near the surface, the connections of the SCS monsoon with the other monsoon systems are constrained by land topography. Taiwan Strait, Thailand Peninsula and Kalimantan Strait are the main connections with East Asian, Indian and Australian monsoon systems respectively (Figure 1.2). The summer monsoon (with winds observed by QuikSCAT indicated by red arrows in Figure 1.2) dominates the Indian and Australian monsoons whereas the winter monsoon (winds indicated by blue arrows) dominates the East Asian Monsoon and the Northwestern Tropical Pacific Monsoon. Clearly, the monsoon over the SCS shows a strong and highly seasonal asymmetric reversal.

A more detailed view of this reversal of wind direction from winter to summer in the SCS is shown in Figures 1.3 and 1.4a. The winter monsoon lasts from November to March with almost homogeneous northeast (NE) direction over the whole SCS (Figure 1.3). Its mean speed peaks in December with about 7.8 m/s (Figure 1.4a). The NE wind maximizes at Taiwan, Luzon Strait and Southeast of Vietnam (10-13 m/s). The wind blows eastward over the Thailand Gulf with weakest speed (5-6 m/s), probably due to the shadowing effect of the southern Vietnam land mass in winter. The summer monsoon starts from June with a mean wind speed of 5.5 m/s and peaks in August with a mean wind speed of 6.3 m/s. It veers from southwest (south of 18^{o}N) to north (north of 18^{o}N). Wind speed peaks off southern Vietnam with about 9 m/s and is weakest off the Thailand Peninsula, Borneo and northern central Vietnam where the shadowing effects of land are active. Xie et al. (2003, 2007) proposed that the wind jet off southern Vietnam in summer is due to an orographic effect, passing around TayNguyen Plateau in Southern Vietnam (see Figure 1.1). Fall (Sep-Oct) and Spring (April-May) are two transitional periods for the monsoon. In September, the SW wind is still strong south of 15^{o}N, while a NE to E wind starts occurring in the northern part of the SCS. The conflict of wind directions leads to a quiet zone between 16-18^{o}N. In October, weaker SW to W wind blows over the southern SCS whereas a strong NE wind prevails in the northern SCS. April is the weakest month in terms of wind speed (4.4 m/s), the NE wind is active over most of the SCS whereas the SE wind dominates in the Gulfs of Tonkin and Thailand. In May in the southern SCS, the wind changes to the SW whereas the

northern part remains the same. Average wind speed is stronger in Fall with 5.8 m/s than in Spring with 4.7 m/s (Figure 1.4).

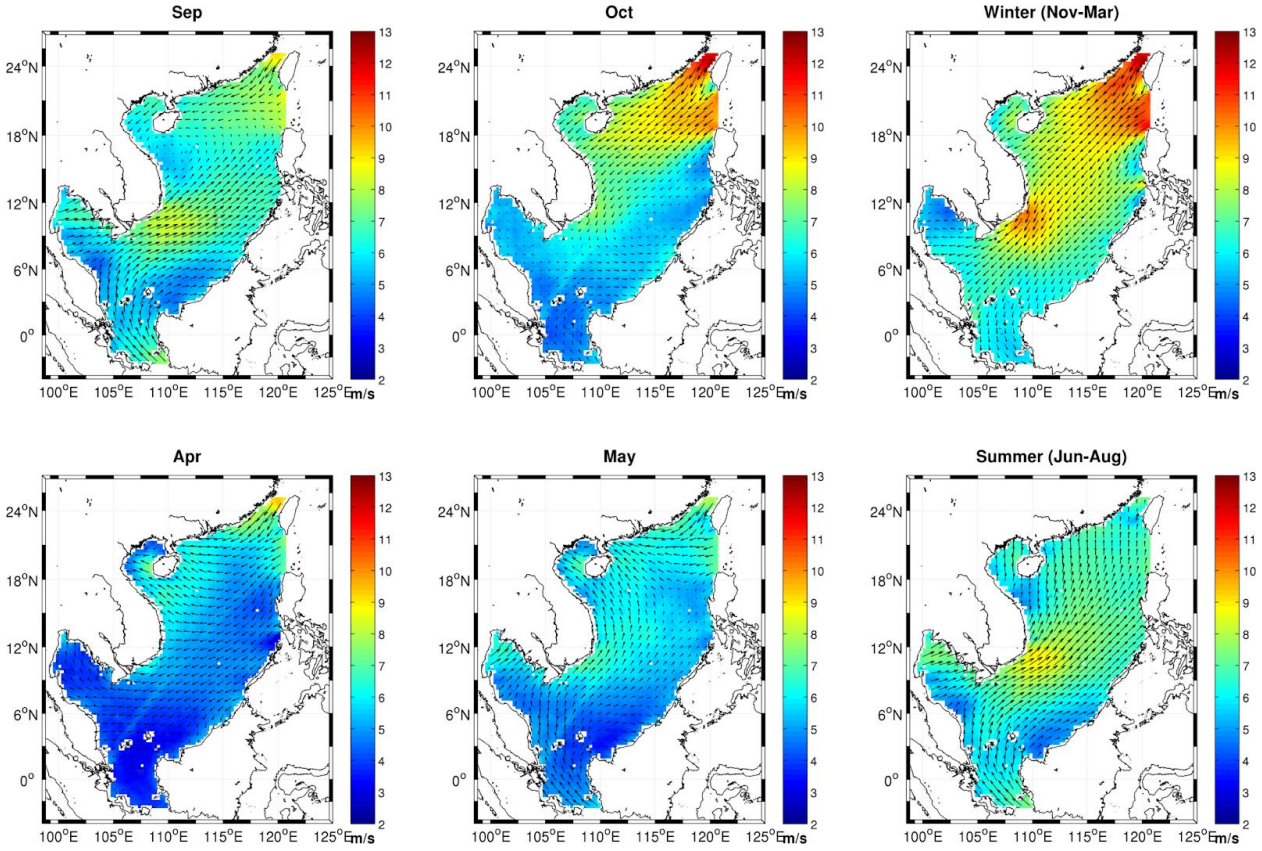

Figure 1.3 Seasonal wind distribution in the SCS. Climatological wind speed (color shades, m/s) and direction (arrows) over the SCS for winter and summer and transition periods Sep-Oct and Apr-May.

The winter monsoon originates from the Siberian High (Wang & He, 2012) and thus is cold and dry; whereas the summer monsoon originates from the Southern Pacific and Indian Ocean (Lau and Yang, 1997; Figure 1.2) and thus is warm and humid. Consequently, the SCS shows a strong seasonal rainfall variability : driest from January to April with net water flux of -1 mm/day i.e. evaporation stronger than precipitation (Figure 1.4b) and wettest in Summer and Fall (~10 mm/day). The transition from Spring to Summer monsoon in the latter half of May is marked by a sudden increase of precipitation over the whole SCS (Lau and Yang, 1997; Wang et al., 2009; Figure 1.4b).

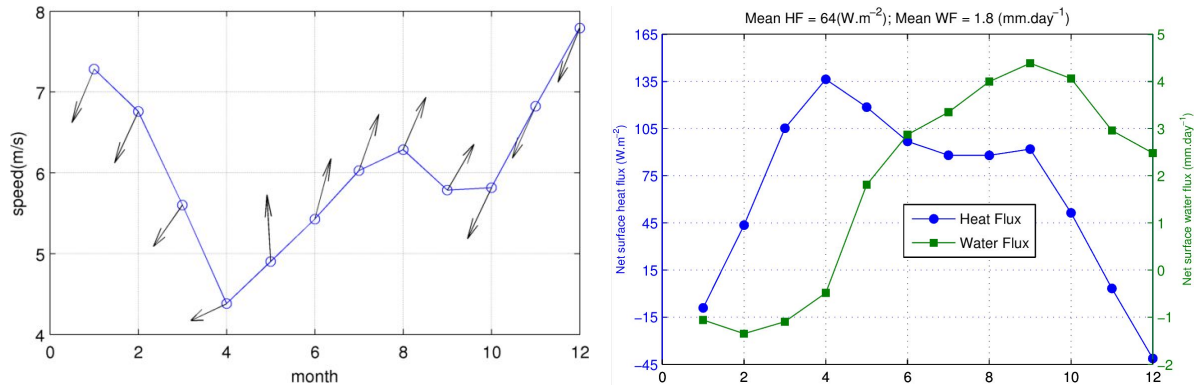

a) b)

Figure 1.4: Annual mean of wind, heat flux and water flux in the SCS. a) Evolution of the 10m above sea level wind speed (blue line) and direction (black arrows with oceanographic convention) averaged over SCS (from QuickScat data 2000-2008). b) Climatological mean surface net heat flux and water flux over the SCS computed based on NCEP CFSR reanalysis over the period 1991-2004 (Saha et al., 2010).

Similar to the wind forcing, the distributions of heat and water fluxes are not homogeneous over the SCS. In winter, the SCS loses heat in the northern part while it continues to gain heat in the south (Figure 1.5a). It gains heat over almost the whole domain in summer with stronger flux in the northern part (Figure 1.5b). There is more rain in the southern SCS from Fall till Spring yet more rain in central SCS in summer (Lau and Yang 1997; Figure 1.5 c,d). This meridional variation of rainfall is related to the movement of Inter-Tropical Convergence Zone (ITCZ) associated with strong convective activities. A seasonal east-west variation of rainfall also occurs due to orographic effects: there is more rain in the western SCS along the Vietnamese coast in winter and more rain in the eastern SCS along the Philippines coasts in summer (Wang et al. 2009; Figure 1.5 c,d). The annual mean values of net heat flux into the SCS varies from one dataset to another. Qu et al. (2009) found a mean value of 23 $W.m^{-2}$ from COADS dataset (Comprehensive Ocean-Atmosphere Dataset, Oberhuber 1988) and 49 $W.m^{-2}$ from OAFlux dataset (Yu and Weller, 2007). The value computed based on NCEP CFSR data for the period 1991-2004 is 64 $W.m^{-2}$ (Figure 1.4b). Net water flux computed based on this dataset has a mean value of 1.8 mm/day (Figure 1.4b). Whereas Qu et al. (2009) found that the SCS gains about 0.1 Sv (1 Sv = 10^6 $m^3.s^{-1}$) of fresh water from the atmosphere which is equivalent to about 2.5 mm/day over 3.5 million km^2 area of the SCS. This fresh water gain leads to a lower sea surface salinity (~1 psu) for the SCS than the surrounding oceans (Qu et al., 2009).

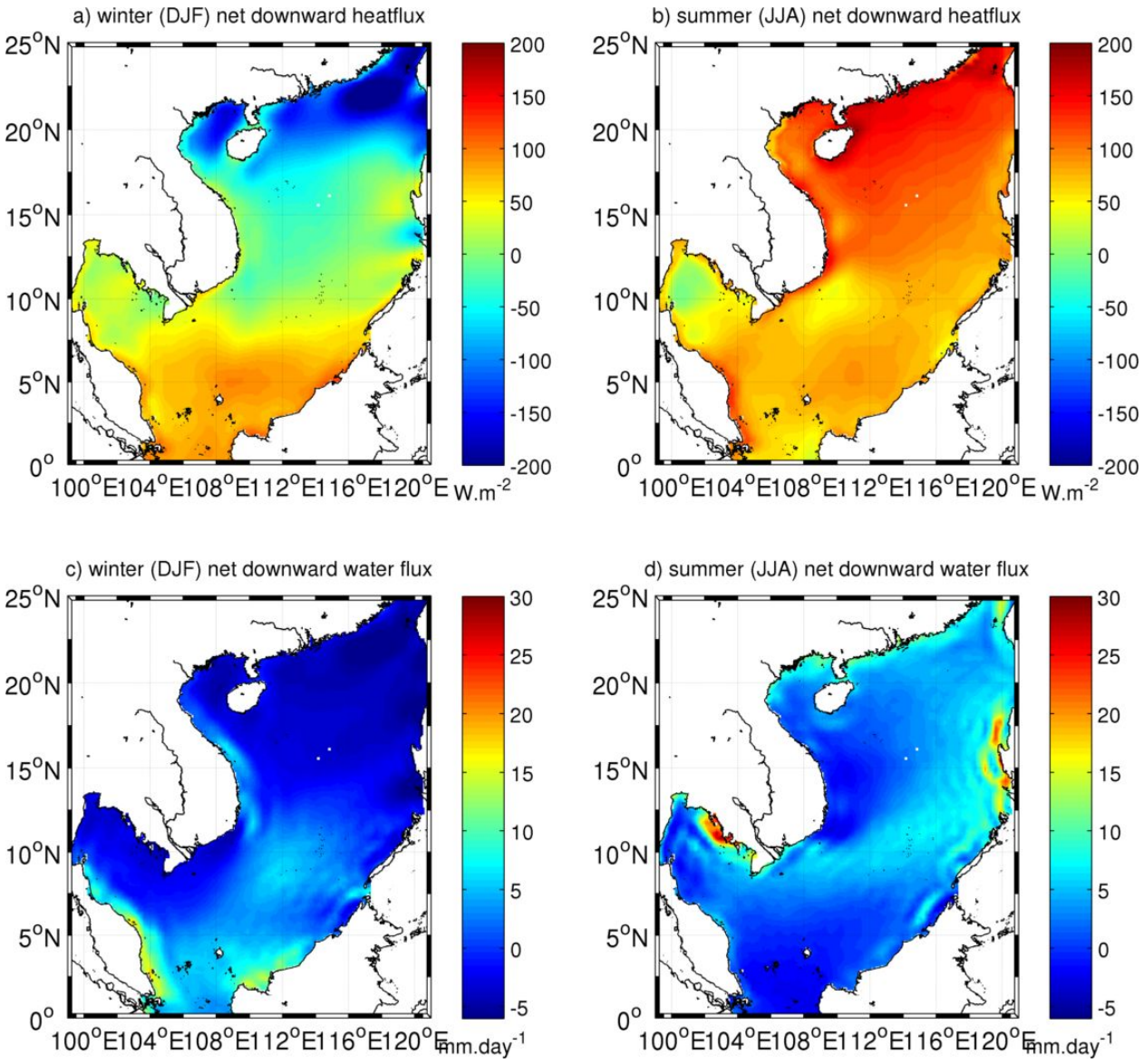

Figure 1.5 Climatological seasonal net surface heat and water flux distribution in the SCS (computed from NCEP CFSR dataset for the period 1991-2004).

The SCS is one of the densest areas for tropical cyclones. From 1965 to 2005, there were 9.8 tropical cyclones each year in the SCS : 60% originated from the neighbouring Pacific and 40% formed locally (Goh and Chan, 2010). Besides the severe impacts in terms of human and economic loss, tropical cyclones are associated with strong impulses of momentum, heat and water exchanges between the ocean and the atmosphere and thus can induce strong intraseasonal variations in the thermohaline structure of the upper layer in the SCS (Chu and Li, 2000; Lin et al. 2003; Tseng et al., 2010; Chang et al., 2010). They can also strongly impact the wind-driven circulation and could possibly impact the South Vietnam Upwelling in summer (Liu et al. 2012). Tropical cyclones occur mostly from June to November when the ITCZ is positioned in the SCS.

Finally, three main climatic phenomena strongly impact the South China Sea climate system : the Madden Julian Oscillation (MJO), the Indian Ocean Dipole (IOD) and the El Niño Southern Oscillation (ENSO). These phenomena influence the fluxes of momentum, heat and water fluxes to the SCS that are associated either with air-sea interactions, river discharge or Luzon Strait Transport at intraseasonal time scale (MJO) and inter-annual time scale (IOD and ENSO).

MJO is named after Madden and Julian who discovered the existence of a stationary oscillation of period from 40-50 days in atmospheric pressure, zonal wind, rainfall etc. in the troposphere (Madden and Julian, 1971, 1972, 1994). This oscillation is due to the eastward movement of a large circulation cell coupled with deep convection in the troposphere of the tropics, and starts in the Indian Ocean moving to the mid Pacific Ocean with a mean speed of 5 m/s (Zhang 2005; Figure 1.6). Zhang and Dong (2004) discovered that the MJO migrates meridionally from south of the equator during boreal winter to north of the equator during boreal summer. Thus over the SCS, the MJO has its most significant impact mainly in summer. Migration of the MJO leads to a northward moving trough (low pressure band) over the SCS. This trough is in phase with the mid-latitude trough in the large scale atmospheric Hadley cell, which can induce westerlies and thus control the onset and strength of summer SW monsoon in the SCS (Tong et al., 2009; Liu et al., 2012). The MJO contributes to about 10% of the intra-seasonal anomalous precipitations over the Southern China Continent in summer (Zhang et al., 2009).

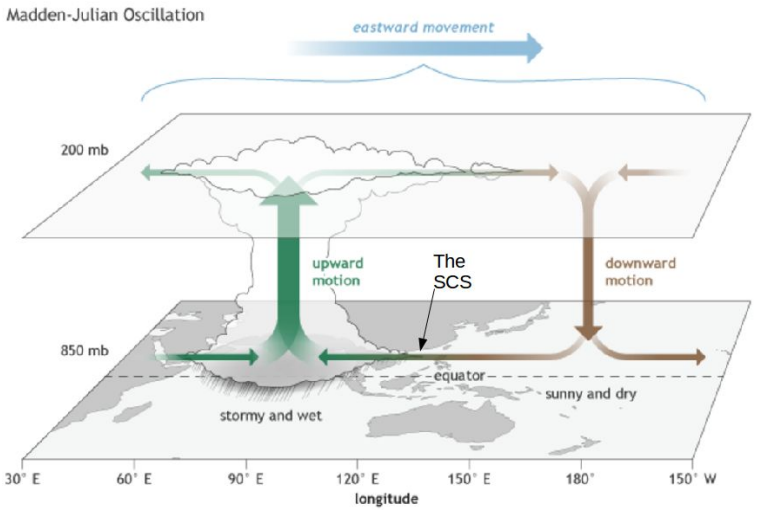

Figure 1.6 Madden Julian Oscillation (after WeatherNation, 2018)

The IOD is associated with a SST dipole that develops between two regions in the Indian Ocean: the western Indian Ocean and off Sumatra (Saji et al., 1999). Positive IOD is characterized by positive anomalous SST over the western Indian Ocean and negative anomalous SST off Sumatra and vice versa (Figure 1.7). IOD does not only impact on the Indian Ocean monsoon and rainfall over India, eastern

Africa and Indonesia (Saji et al., 1999; Ashok et al., 2001) but also impacts on the onset of the summer monsoon in the SCS and rainfall over China (Yuan et al., 2008; Qiu et al., 2014) : Yuan et al. (2008) suggested that early/late summer monsoon onset over the SCS is due to positive/negative IOD.

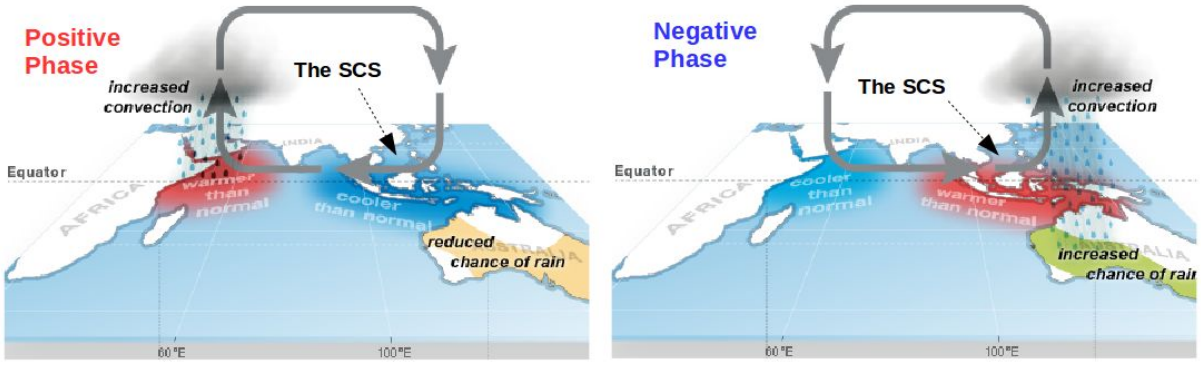

Source: Common Wealth of Australia, 2013 (modified)

Figure 1.7 Indian Ocean Dipole and respective atmospheric circulation and convection activities

ENSO is a coupled oscillation of SST in the Central Pacific and overlying atmosphere (Trenberth, 1997) at inter-annual time scales. It is the strongest natural mode of the ocean-atmosphere system (Philander, 1985). ENSO has warming/cooling phases called El Niño/La Niña which were originally named due to their positive/negative SST anomalies over the coast of Peru and Ecuador. During the El Niño warming phase, the positive SST anomaly induces cyclonic zonal circulation over the Pacific which weakens trade winds and the monsoon over East Asia (David Neelin and Latif, 1998; Wang et al., 1999; Figure 1.8). During the La Niña cooling phase, negative SST anomalies over the region induce an anti-cyclonic zonal circulation over the Pacific which strengthens trade winds and the monsoon (Philander, 1985; David Neelin and Latif, 1998; Figure 1.8). Over the SCS, many studies have suggested that the SCS summer monsoon is modulated by ENSO such that El Niño/La Niña phases weaken/strengthen the summer monsoon with a later/earlier onset (Lau and Yang, 1997; Chou et al., 2003; Liu et al., 2012; Dippner et al., 2013). Dippner (2013) proposed that the main mechanism whereby ENSO impacts on the summer monsoon in the SCS is via the position of atmospheric trough associated with strong convection in the Inter-Tropical Convergence Zone. Chou et al. (2003) showed that the overall correlation of the SCS summer monsoon and Niño 3.4 index is weak (about 0.5) for the period 1979-2000. This is because in non-ENSO years, other mechanisms modulate the summer monsoon such as the meridional gradient of upper troposphere temperature. In addition, the IOD may also modulate the summer monsoon strength in non-ENSO years (Liu et al.,2012; Dippner 2013). Less is known about the relation between the winter monsoon over the SCS and ENSO. Wang and He (2012) showed that during El Niño/La Niña years,

the East Asian winter monsoon is weakened/strengthened. The connection between the East Asian winter monsoon and the SCS monsoon (Figure 1.2) via Taiwan and Luzon Strait suggest that ENSO may also impacts the SCS winter monsoon.

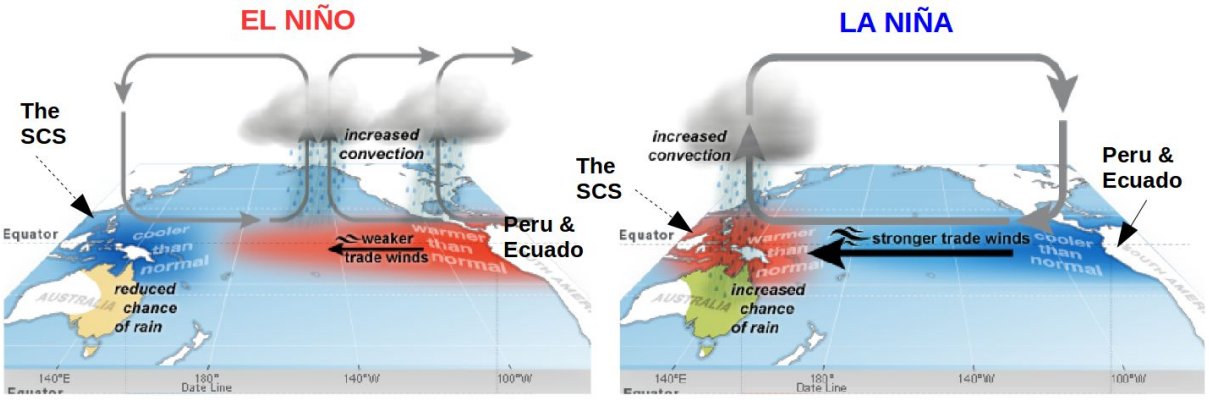

Source: Bureau of Meteorology, Australia, 2012 (modified)

Figure 1.8 El Nino Southern Oscillation atmospheric-ocean system

b) Oceanic transport through Luzon Strait

The net Luzon Strait Transport (LST) is the inflowing part of the more global South China Sea Through Flow which conveys water from the Pacific through the SCS to East China Sea, Sulu Sea and Java Sea (Qu et al., 2009). Thus it actively contributes to the heat, salt and water balance of the SCS as well as the thermohaline structure inside SCS which will be described in detail in section 1.1.3c. LST varies with time and depth due to different mechanisms. Metzger and Hubert (1996) discovered that the LST consists of barotropic and baroclinic fluxes which are driven by monsoon and gradients of temperature and salinity between Northwestern Pacific water and SCS water respectively. Their sensitivity simulations also showed that wind stress curl and model geometry strongly impact the modeled variability and mean value of LST. In agreement with Metzger and Hubert, a modeling study of Gan et al. (2006) showed that, on the surface, LST is controlled by seasonal monsoons which produce inward/outward flow to/from the SCS. Whereas at greater depth the LST is governed by ageostrophic inward flows due to a westward gradient pressure induced by the Kuroshio Current variations (Gan et al., 2006).

Due to its importance to the SCS dynamics, many studies have attempted to quantify LST using observations (Chu & Li 2000) or modeling (Xue et al., 2004; Qu et al. 2004; Wang et al., 2006c; Fang et al., 2009). These studies showed that the seasonal variability of the LST is controlled by the monsoon with much stronger net LST into the SCS in winter than in summer. However, their findings diverge on the annual mean value of LST ranging from 2 to 6.5 Sv. At interannual time scale, LST is

controlled by the strength of the Kuroshio and during El Niño years, the Kuroshio is weakened and LST is strengthened (Qu et al., 2004; Gan et al., 2006).

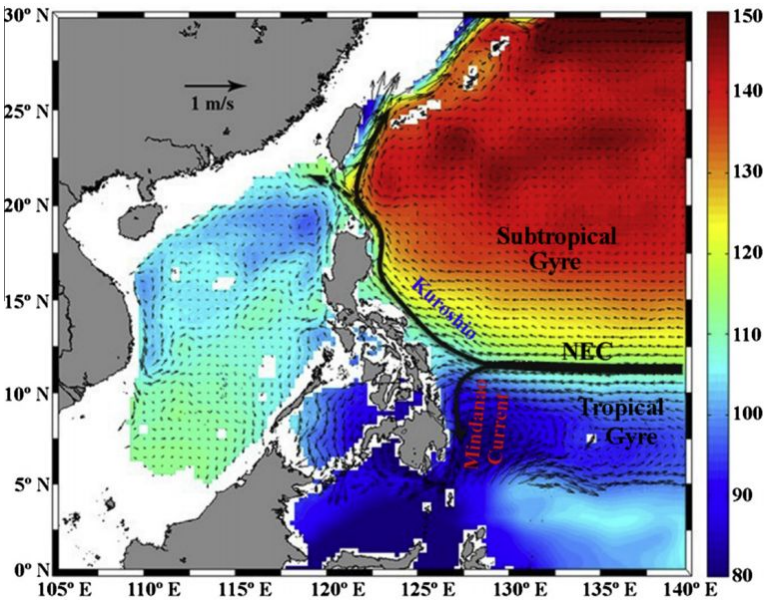

Figure 1.9 Mean Absolute Dynamic Topography (units: cm) and the corresponding surface geostrophic currents (units: m/s) derived from the 18-year (1993–2010) satellite altimeter data. Black solid lines represent a schematic of the North Equatorial Current (NEC), Mindanao current and Kuroshio current - the NMK current system (after Nan et al., 2015).

c) River forcing

River inputs into the SCS provide a major source of freshwater, sediments and nutrients into the coastal waters and thus are important to the coastal ecosystems and biomass. They also impact on the ocean water masses and dynamics by modifying the salinity. The three major river systems in the SCS are located in the western part where the southeast Asia continent allows the formation of large catchments for the Mekong, Red and Pearl rivers (Figure 1.1). Figure 1.10 shows the climatological discharge computed by compiling available data from Pardé (1938) for the Red River, from the Mekong River Commission (2010) for the Mekong river and from Fekete et al., (2002) for the Pearl river. The Mekong River is the largest one with mean discharge of 14200 m^3s^{-1}. The second is the Pearl River with a mean annual discharge of 9800 m^3s^{-1}. The Red River is the third with a mean annual discharge of 3500 m^3s^{-1}. Although the volume of discharge is small compared to the SCS volume, they can have large scale impacts due to the large scale circulation which can advect fresh water hundreds of kilometers from the river mouth (Gan et

al., 2009). High discharge periods of the three rivers coincide with the SCS summer monsoon (from Spring to Autumn). Variations in discharge are strongly impacted by monsoonal rain (Gao et al., 2015) as well as human impacts (Le et al., 2007; Zhang et al., 2008; Gao et al., 2015) : many dams have been built upstream of these river system for hydropower which leads to a more unnatural regulated flow regime and to a strong decrease of suspended particulate matter at the river mouth (Le et al., 2007).

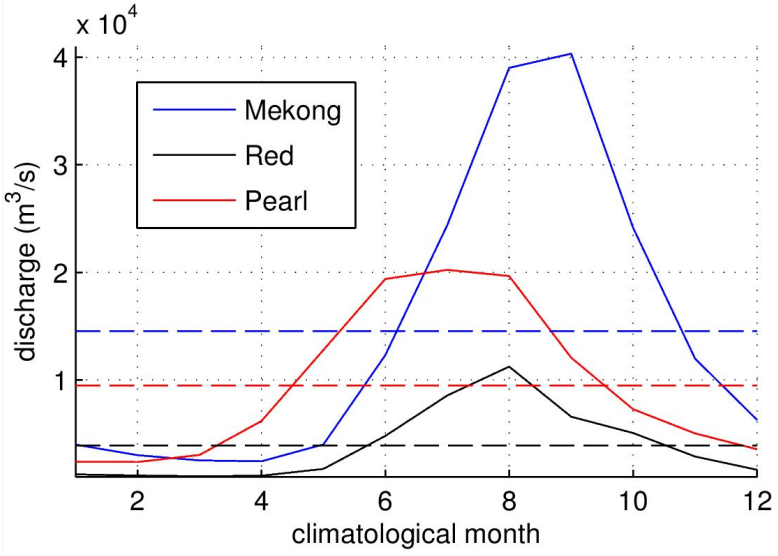

Figure 1.10 : Climatological monthly freshwater discharges from the Mekong, Red and Pearl Rivers (from respectively Mekong River Commission (2010), Pardé (1938), and Fekete et al., (2002)).

d) Tidal forcing

Tidal currents and breaking tide-induced internal waves play a crucial role in the ocean mixing at all depths and participate to drive the deep circulation (Stewart 2008). Tidal mixing is particularly strong in shallow areas and can strongly influence coastal sediment transport and mixing in the river mouths. Tidal forcing is thus particularly important in the SCS with 50% of the SCS area covered by shallow shelves and three large river systems including the Mekong, the Red and the Pearl rivers (see figure 1.1) whose maximum discharges exceed 10^4 m^3s^{-1} (Li et al., 2006; Wolanski et al., 1998; Mao et al., 2004). Over deep water, however, barotropic tides only have a minor impact on the upper layer thermal structure compared to other forcings (Chang et al., 2010), although there are strong seasonal variations in the internal tide amplitude in the north SCS (Ray and Zaron, 2011).

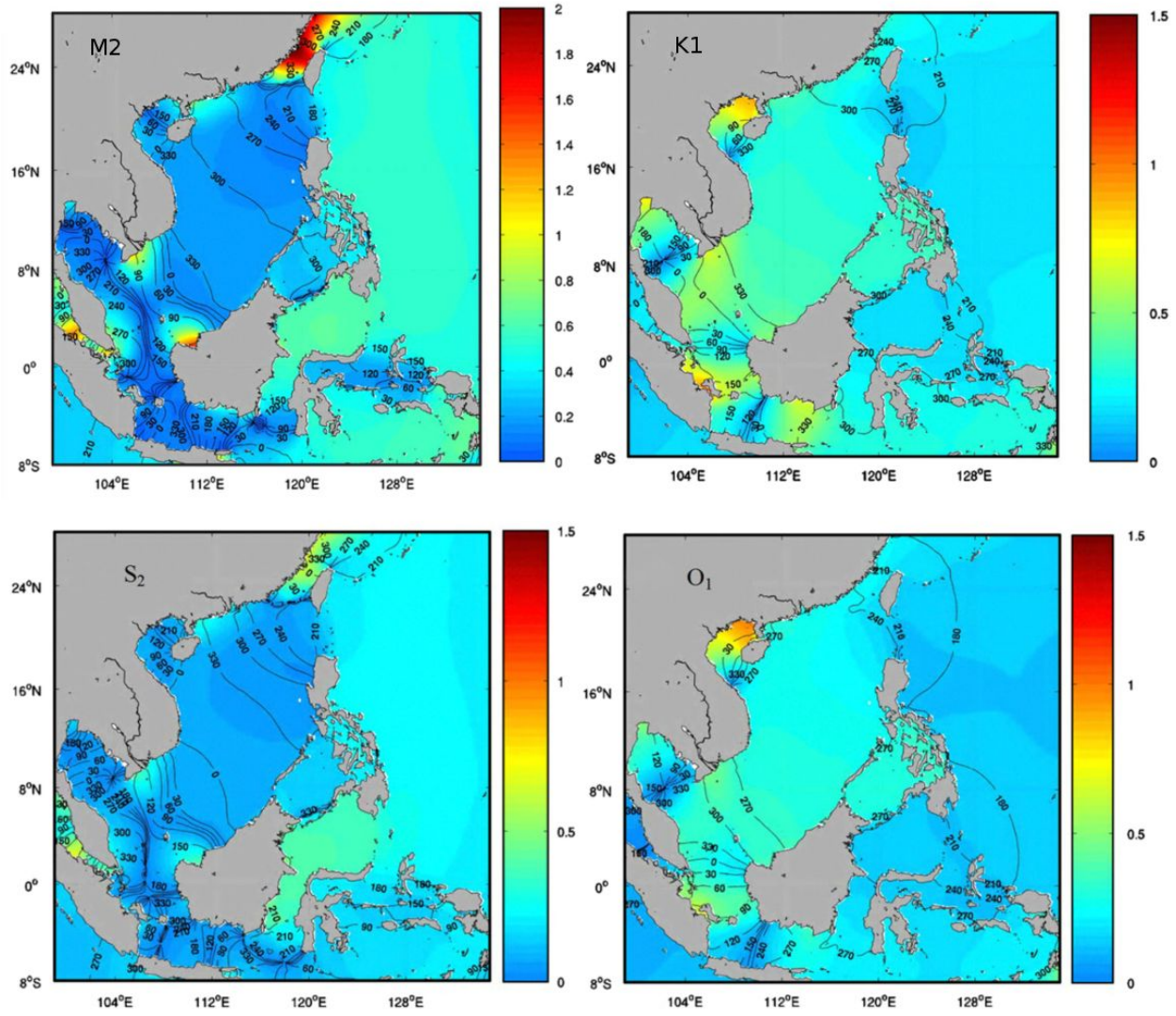

Figure 1.11 Tidal amplitude of M2, K2, S2 and O1 components in the SCS (Zu et al., 2008)

Due to the small deep basin size of the SCS, barotropic tides in the SCS are mainly transferred from the Pacific via Luzon Strait (Fang et al., 1999; Zu et al., 2008), which is the major connection of the SCS with the large Pacific water body. However, tidal frequency, wavelengths and amplitude are strongly modified by local SCS geometry and bottom topography (Jan et al., 2007; Zu et al., 2008). Zu et al. (2008) found that the amplitude of M2 decreases while the amplitude of K1 increases from the Pacific to the SCS via Luzon Strait. Based on altimetry data, Yanagi et al. (1997) consequently found that tides in the SCS are mostly diurnal, with the ratio (K1 + O1)/(M2+S2) > 1.25 over most SCS area. Shallow shelves and the Tonkin and Thailand gulfs shows stronger variation of tidal amplitude ranging from 0 to 2m compared to homogeneous tidal amplitude in the deep basin (Zu et al., 2008, Figure 1.11). There are several amphidromic points along the Vietnam continental shelf and the two gulfs (Yanagi et al., 1997; Zu et al., 2008; Figure 1.11).

Moreover the interaction of tides with bathymetry can cause partial transformation of the barotropic tide to baroclinic tides e.g. the formation of internal tides in the vicinity of Luzon Strait as observed by Liu et al. (1998), Lien et al. (2005), Zhao et al. (2004) using synthetic aperture radar (SAR) images. Jan et al. (2007) found that about ⅓ of K1 energy is transferred to baroclinic energy while propagating from the Pacific through Luzon Strait. Chang et al. (2010) discovered that internal tides are actually active basin wide. Ray and Zaron (2011) noted that the northern SCS is the only place in the world with a strong seasonal variation in the internal tide amplitudes. Cai et al. (2006), based on sensitivity modeling, suggested the need to include baroclinic tidal effects in modeling studies for a better accuracy of tidal simulations. Including tidal forcing in a ocean general circulation model also improves the ocean thermal structure, circulation and mixing due to the internal tide-current interactions.

1.1.3 The SCS Dynamics

a) Large scale ocean Circulation

The large scale circulation in the SCS is largely driven by the atmospheric monsoon winds system. Previous studies based on modeling (Shaw and Chao 1994) and observations (Wyrtki 1961; Xu et al., 1982; Morimoto et al., 2000; Chu and Li 2000; Fang et al., 2002) found a reversal of the SCS general surface circulation in response to the monsoon reversal. In winter, NE winds induce basin-wide cyclonic surface circulation with an intense southward jet along the western coast. In contrast, weaker summer SW monsoon induces an anti-cyclonic circulation over Southern SCS with a NE western boundary current which turns eastward/offshore between 11-13^{o}N Southern Vietnam, called the eastward jet hereafter. The strength of the jets can characterize the strength of the seasonal circulations. On average, the winter jet has a mean speed of 0.9 m/s whereas the summer jet has a mean speed of 0.5 m/s. Later studies based on modeling (Wang et al., 2006b; Gan et al., 2006) confirmed the key role of the monsoon but also revealed the important role of Kuroshio intrusions via the Luzon Strait Transport (LST) in the surface circulation, especially in the northern SCS. Intrusion of Pacific water via Luzon Strait maintains the weak cyclonic circulation in summer even though the southwest to south monsoon prevails in the northern SCS (Figure 1.3). Wang et al. (2006b) decomposed the SCS upper layer circulation over the period 1982-2004 using Empirical Orthogonal Function (EOF) and found two dominant modes. Mode-1 corresponds to 49% of the variability

and characterizes the winter cyclonic SCS circulation. Mode-2 accounts for 27% of the variability and characterizes the summer SCS anti-cyclonic circulation.

The impact of the surface monsoon forcing is strong down to 150m depth and the seasonal circulation patterns remain similar up to the surface, yet the current speed decreases rapidly with depth (Chao et al 1996; Figure 1.12a). The western boundary current at 150 m depth has a mean speed of about 0.1 - 0.2 m/s. At intermediate depth (900m), modeling outputs from Chao et al. (1996) show a basin-wide anti-cyclonic circulation in August and a northeastward jet of mean speed of 0.005 m/s flowing from the southwest end of the deep basin to Luzon Strait in December (Figure 1.12b). At deep layers (>2000m), the Luzon Strait transport shapes the circulation pattern inside the SCS (Chao et al., 1996; Lan et al., 2015; Figure 1.12c): there is a strong and narrow inward flow in the northern part of the Luzon Strait which leads to a basin-wide cyclonic circulation (Lan et al., 2015).

At interannual time scale, Wang et al. (2006b) suggested that ENSO impacts SCS upper layer circulation via modulation of wind stress curl due to strong correlations between them (they found a strong correlation of 0.92 between time coefficient of mode-1 of wind stress curl and the mode-1 of circulation). They found a 5-month lagged correlation of 0.7 between the time coefficient of the mode-1 and Nino3.4 index over the period 1982-2004, and showed that in El Niño years, upper layer cyclonic circulation is weakened.

There have been very few studies on the impacts of river and tidal forcing on the SCS large scale circulation. Using sensitivity simulations, Chen et al. (2012) suggested that freshwater discharge from the Red river could induce a buoyancy current in the northern SCS along the Vietnamese coast which could meet a tidal rectification current from the south in central Vietnam where the usual NE jet turns offshore, thus participating to the eastward jet formation.

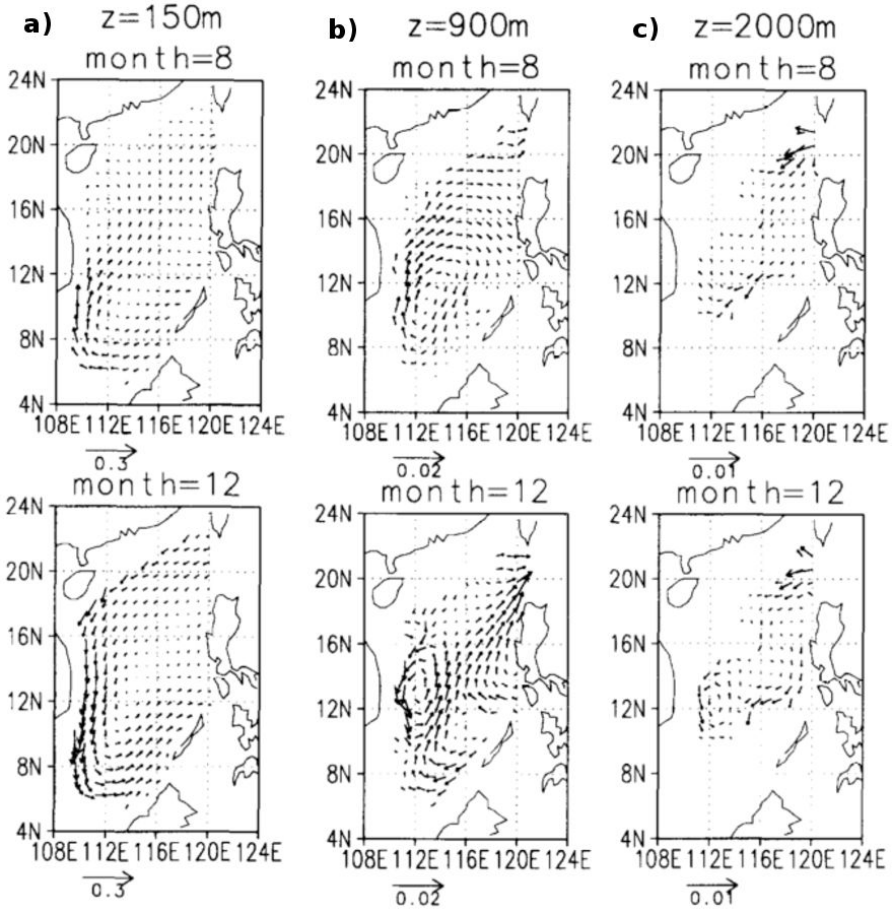

Figure 1.12 : SCS circulation at different depths in August and December (after Chao et al., 1996)

b) Meso-scale structures

Mesoscale eddies with spatial scale of tens to hundreds km and temporal scale of weeks to months are more energetic than the mean circulation (Richardson 1983; Chelton et al., 2007). They are often formed by barotropic/baroclinic instabilities in the mean circulation (Holland, 1978; Qiu and Chen, 2004) over deep water. The SCS has a strong monsoon-driven circulation with impacts of Kuroshio intrusion via the deep Luzon Strait and a deep basin west of Luzon. Mesoscale eddies occur ubiquitously over the SCS and participate to upper layer thermal variability as well as heat and salt flux with the Pacific via Luzon Strait (Wu and Chiang 2007; Chen et al. 2011).

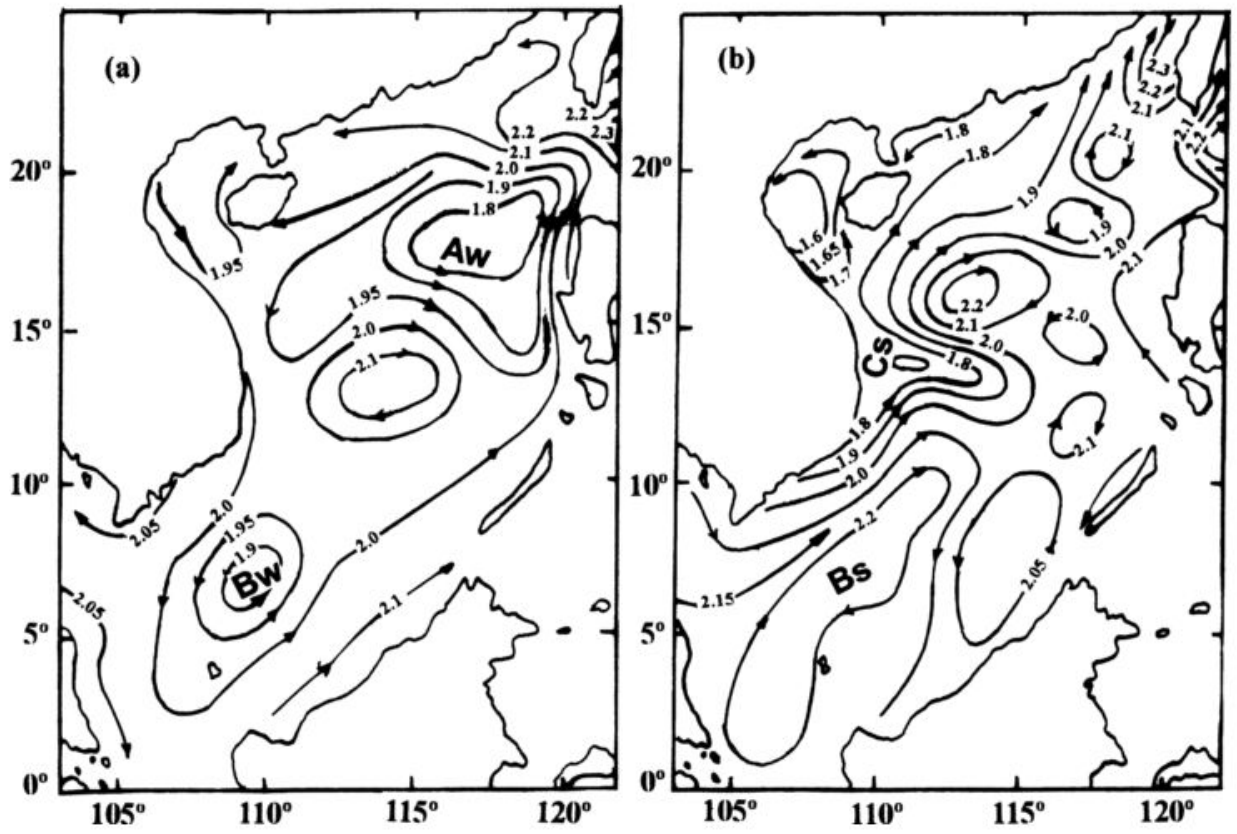

Figure 1.13 Seasonal permanent eddies in the SCS. Permanent eddies Aw, Bw in winter (a) and Bs, Cs in summer (b), after Xu et al., (1982)

In-situ observations in the SCS are generally too sparse to provide comprehensive information about mesoscale activities of the whole SCS basin yet they set our initial understanding of the role of mesoscale eddies in the SCS dynamics. Xu et al. (1982), based on synthesis of available observations, were among the first who discovered the existence of seasonal permanent cyclonic eddies west of Luzon and southeast of Vietnam in winter and of an anticyclonic eddy southeast of Vietnam in paired with a cyclonic eddy off central Vietnam in summer (Figure 1.13). These seasonal permanent eddies are formed in response to the reversal of monsoon in the SCS. Li et al. (1998) showed that eddies originating from the Kuroshio current could transport water of different properties from the Pacific into the SCS. Therefore, eddies play an important role in the exchange of water, heat and salt between the Pacific and the SCS via Luzon Strait. Based on buoy data collected from 1997 to 2000, Chang et al. (2010) concluded that intraseasonal variability of the upper layer thermal structure in central SCS is due to eddy activity.

The great advancements of satellite observations in particular sea surface height (SSH) as well as sea surface temperature (SST) and surface wind have brought new insights of mesoscale activities in the ocean (see Morrow et al., 2017 for a review) including those in the SCS. Using Topex/Poseidon (T/P) sea level anomaly (SLA) data from 1992 - 1997, Morimoto et al. (2000) discovered that both

cold and warm eddies develop in the vicinity of Luzon and propagate westward, meanwhile Wang et al. (2000) found two bands with high mesoscale SLA variability in deep water in the Northern SCS (north of 10°N): one is along the Vietnamese coast and the other has a Southwest-Northeast orientation starting from Southeast Hainan to Luzon Strait. Based on blended SLA from multi-mission altimeters and/or modeling, many studies have revealed important characteristics of mesoscale eddies in the SCS: their magnitude, polarity, lifetime, growing phase, breeding ground and traveling path. Wang et al. (2003) proposed that the SCS is anti-cyclonic dominant with eddies generated mainly during and after the cessation of the winter monsoon. Later studies (Xiu et al., 2010; Chen et al., 2011) based on SLA data over a longer period and modeling however showed that there is no significant difference between the number of anticyclonic and cyclonic eddies in the SCS. Xiu et al. (2010) based on modeling and gridded altimeter data from 1993 to 2007 found that 70% of eddies in the SCS have radius smaller than 100 km, and that on average there are about 30 eddies per year. They also found a linear relationship between eddy magnitude, vertical extent and lifetime i.e. stronger eddies have deeper extents and longer lifetimes and vice versa. In addition, Chen et al. (2011), based on 17 years of gridded altimeter data found that eddies generated in different areas have different sizes and lifetimes and that their growing and decaying phase are asymmetric. These studies highlight the ubiquitous presence of mesoscale eddies in the deeper regions of the SCS.

The mechanism for the formation of eddies in the SCS was first investigated by Chu et al. (1998) from sensitivity simulations. They concluded that both wind stress curl and LST can generate deep basin eddies of either polarity. Many other studies highlighted the dominant role of the winter monsoon in eddy genesis either via the wind jet and associated wind stress curl off Luzon or stronger intrusions of Kuroshio waters during winter, making the deep eastern SCS the breeding ground for eddies (Wang et al., 2003; Wu and Chiang 2007; Wang et al., 2008; Chen et al., 2011). The summer orographic induced wind jet and associated wind stress curl was found to be responsible for the generation of eddy dipole off Central Vietnam (Xie et al., 2003; Li et al., 2014). So far, eddy genesis was associated with either wind stress curl or Luzon Strait Transport. To our knowledge, no studies have been conducted to investigate the influence of tidal and river forcing on mesoscale structures generation.

The abundance of mesoscale activities is associated with highly non-linear dynamics and a strong ocean intrinsic variability (OIV, see for example Penduff et al., 2011; Grégorio et al., 2015; Serazin et al., 2016; Waldman et al., 2018). However, only very few studies have been conducted to study OIV in the SCS until

now. Gan and Qu (2008) used an eddy-resolving model and discovered that the summer eastward jet in the SCS has a strong flow variability due to the presence ocean eddies. Li et al. (2014) based on ocean general circulation model (of 1/4^{o} resolution) suggested that 20% of the variability of the summer eastward jet could result from nonlinear interactions between the eastward jet and ocean eddies.

c) Thermohaline structure

Under the impacts of the Southeast Asian monsoon and water exchange with the Northwestern Pacific, the thermohaline structure in the SCS shows a strong spatio-temporal variability. Figure 1.14 shows the climatological distribution of SST, sea surface salinity (SSS) and mixed layer depth (MLD) in summer and winter from satellite and in-situ observations. In winter, SST, SSS and MLD show a clear North-South gradient in response to the strong NE monsoon driven surface circulation. This dry and cold NE monsoon promotes evaporation, heat loss and increases the vertical mixing leading to colder SST, higher SSS and deeper MLD in the North than in the South. In addition, the large scale circulation driven by NE-monsoon also brings cold and salty water from the East China Sea and the Pacific via Taiwan and Luzon Straits (see section 1.1.3a). The strong winter jet along Vietnamese coast is visible as a strip of cold SST and high SSS.

In summer, due to higher radiation from the sun, and weaker, warmer and more humid SW summer monsoon coming from the Southern Pacific and the Indian Ocean, the SCS has higher SST associated with strong convection of the overlying atmosphere. The summer monsoon together with atmospheric convection thus bring a lot of precipitation to the SCS (Lau and Yang 1997; Wang et al., 2009). Warmer and fresher upper layers lead to a more stratified upper ocean and thus the MLD is much shallower in summer than in winter (<35m over most of the SCS vs. 35-70 m over deep water in winter). SST, SSS and MLD become spatially more homogeneous with a variation range of 3.5-4^{o}C, 1.5 - 2 psu and 10-50 m compared to 10^{o}C, 4 psu and 10 - 70m in winter respectively. SST is higher near continental shelves and in weak dynamics area. Lowest SST occur in upwelling areas that can be observed on SST maps off the central coast of Vietnam, Northeast of Hainan and in Taiwan Strait. SSS and MLD show higher values in the deep basin than over the shallow shelves.

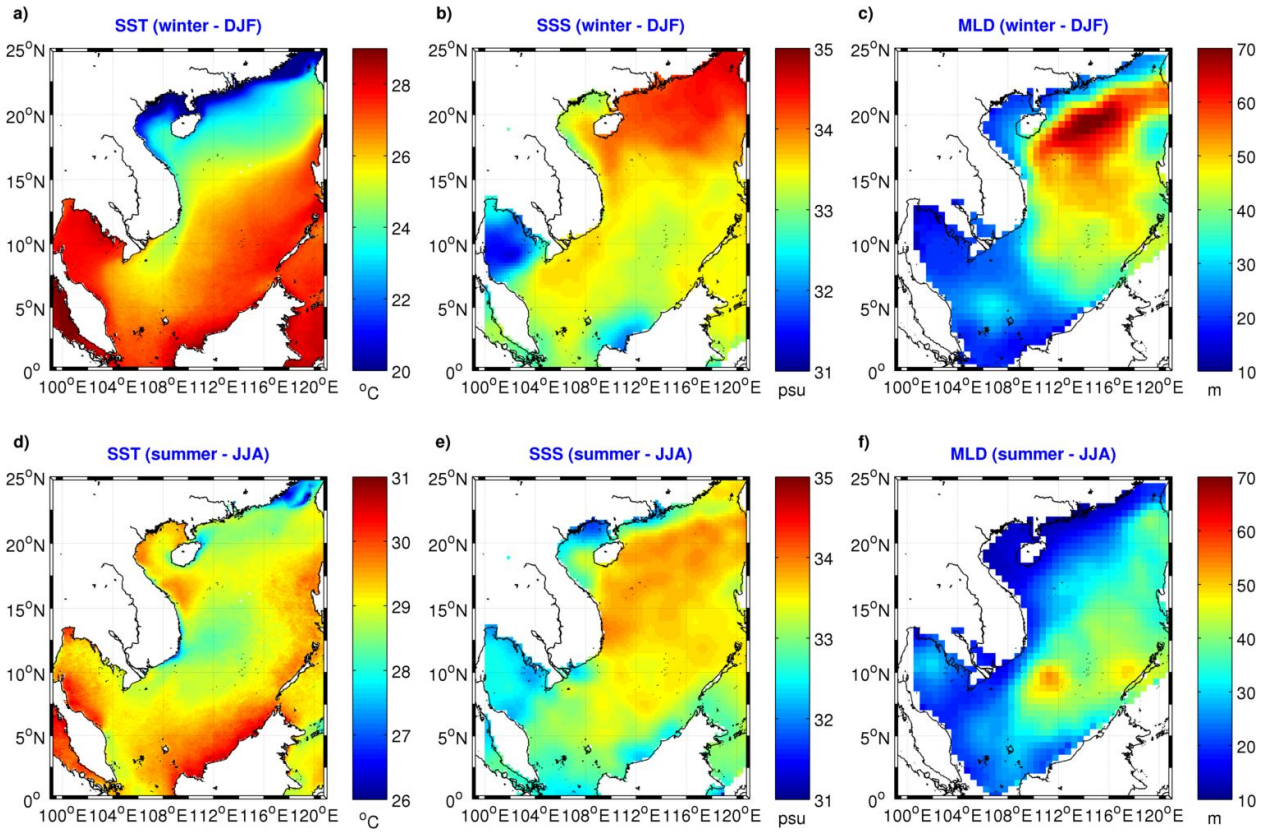

Figure 1.14: Seasonal maps of SST, SSS and MLD in the SCS. Winter (December-February) and summer (June-August) averaged SST derived from AVHRR satellite data, SSS and mixed layer depth derived from SCSPOD14 in-situ data set (Zen et al., 2016)

The origin of water masses inside the SCS can be traced back to the northwestern Pacific (Qu et al., 2000; Liu and Gan 2017). Qu et al. (2002) based on Godfrey's 'island rule' and historical observations estimated that, on average, Pacific water intrudes into the SCS via Luzon Strait at a rate of about 4 Sv. To better illustrate the vertical thermohaline structure and its spatio temporal variability inside the SCS, Figure 1.15 shows climatological Temperature - Salinity (TS) profiles at 6 locations: Northwestern Pacific, Western Luzon Strait, Central Vietnam, Tonkin Gulf, Thailand Gulf and Western Mindoro Strait (see Figure 1.1 for locations) computed based on SCSPOD14 dataset (Zeng et al., 2016). To a certain extent, the SCS deep waters replicate TS profiles of the northwestern (NW) Pacific water, yet with strong modifications. In winter, mixed layer depth in the NW Pacific is twice as deep as in the SCS with colder temperature and higher salinity. Western Luzon Strait water shows the closest TS properties to the NW Pacific water. In summer, only the upper layer salinity can distinguish NW Pacific water from the SCS ones. In deeper layers, larger differences of 5°C and a wider range of salinity exist year-round in NW Pacific water (0.8 compared to 0.2 psu in SCS waters) from 100 - 600m depth. These facts suggest that SCS waters originate from the NW Pacific via Kuroshio intrusion, yet the multi-scale driven dynamics inside SCS strongly modify these properties.

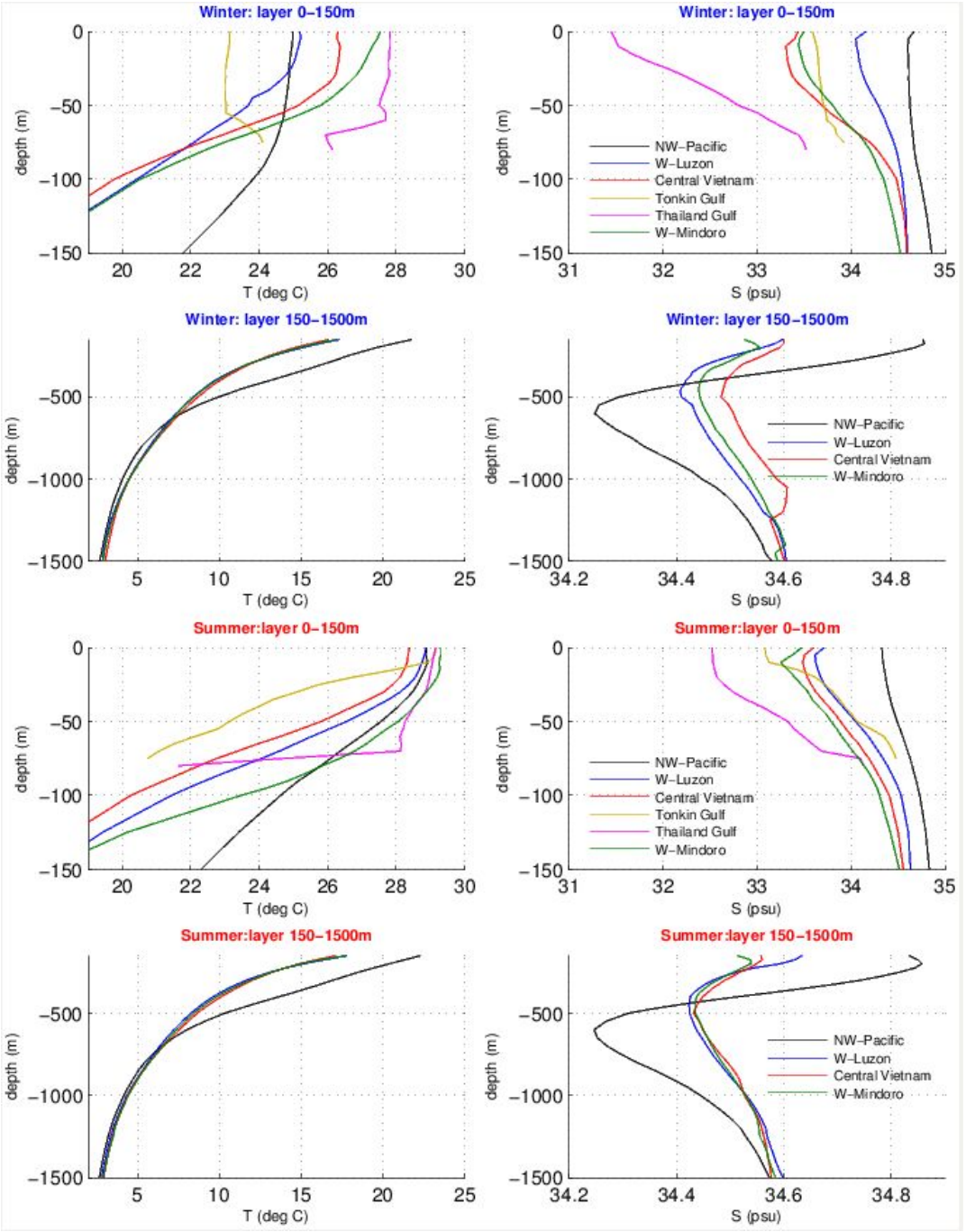

Figure 1.15: Mean TS profiles from SCSPOD14 dataset at locations indicated in Figure 1.1.

Inside the SCS, deep water mean profiles at the western Luzon Strait, Central Vietnam and western Mindoro Strait have a similar shape meaning that the deep SCS basin water is quite well mixed (Figure 1.15). The T/S properties in the shallow gulfs are well mixed over the upper 50 m with extreme T/S values due to their shallowness as well as impacts from nearby rivers (Mekong for Thailand Gulf and Red river for Tonkin Gulf). Tonkin Gulf and Thailand Gulf show the coldest and warmest waters for the upper layer respectively. The salinity in the Thailand Gulf stands out as the freshest water yearound.

At interannual time scales, the variation of SST anomaly is closely related to the variation of the Asian Monsoon and ENSO (Ose et al., 1997; Park and Choi 2016; Tan et al., 2016). El Niño events weaken monsoon in both winter and summer over the SCS which leads to weakened ocean heat loss to the atmosphere and weakened advection of cold water from the northeast of the SCS, hence higher SST in the SCS. In addition, the weakened monsoon leads to weaker upwelling in the Northeast of SCS in winter and off Vietnamese coast in summer which also induces positive SST anomaly in the SCS (Xie et al., 2003; Park and Choi, 2016). Based on SST data from Simple Ocean Data Assimilation V.2.2.4 (SODA, Carton and Giese, 2008) and Hadley Centre Sea Ice and Sea Surface Temperature (HadISST, Rayner et al., 2003), Park and Choi (2016) reported a surface warming trend up to 0.25 ^{o}C/decade of the SCS over the period 1950 - 2008. Until now, there is no study on long-term variation of SSS and mixed layer depth over the SCS.

d) Upwelling systems

Inside the SCS, there are several seasonal upwelling systems associated with the seasonal variability of the monsoon. These upwelling systems are important to primary production in the SCS because they bring nutrient rich deep waters to the surface, where photosynthesis can then occur. In winter, there is an upwelling centered at 100 km off Luzon, between 16-19^{o}N (Shaw et al., 1996). This upwelling system is driven mainly by large scale circulation in winter. Whereas, in summer, there are several monsoon driven upwelling systems, as seen on Figure. 1.16: the South Vietnam Upwelling (SVU) located off the Vietnamese coast at 12^{o}N (Wyrtki, 1961; Xie et al., 2003) and two smaller ones along the northern continental shelf of the SCS northeast of Hainan island and near Taiwan Strait (Jing et al., 2011; Song et al., 2012). Previous studies suggested that both along-shore wind and wind stress curl are important to the SVU (Xie et al., 2003) whereas wind stress curl is more important to upwelling NE of Hainan and along shore wind is more important to upwelling near Taiwan Strait (Jing et al., 2009). Characteristics of the largest upwelling in the SCS i.e. the SVU, which constitutes the scope of this PhD study, will be detailed in the following sections.

1.2 The South Vietnam Upwelling (SVU)

1.2.1 Dynamical and biogeochemical role

The SVU is one of the major features of the SCS summer thermodynamics. In section 1.1.3.a, we mentioned that the eastward jet off southern Vietnam can characterize the strength of the SCS surface circulation in summer. Figure 1.16 shows August climatological mean circulation (the month of strongest SVU according to Xie et al., 2007) derived from CMEMS (Copernicus Marine and Environment Monitoring Service) altimetry satellite data as well as Advanced Very High Resolution Radiometer (AVHRR) SST of the SCS. It reveals that along with this jet is a large cooled SST area over the central SCS which corresponds to the SVU and that the SVU and the jet may be related. Figure 1.16 shows two features of the SVU : a coastal cold tongue located near 11.5°N, 109°E upstream of the summer eastward jet and the offshore cold water area, respectively about 2°C and 1°C colder than the surrounding water.

The SVU is associated with a high bio-productivity (Tang et al., 2006; Loick et al., 2007; Bombar et al., 2010) and is a major area for the halieutic industry in Vietnam. Levadoux et al., (1935) mentioned that Binh Thuan province, whose waters include the upwelling area, has a large fish catch especially from April to October. Figure 1.17a reveals that the SVU is a unique deep water region in the SCS with very high Chlorophyll-a concentrations. However, the upwelling can also cause blooms of haptophyte algae which are harmful for local coastal ecosystems and aquaculture (Hai et al., 2010; Dippner et al., 2011).

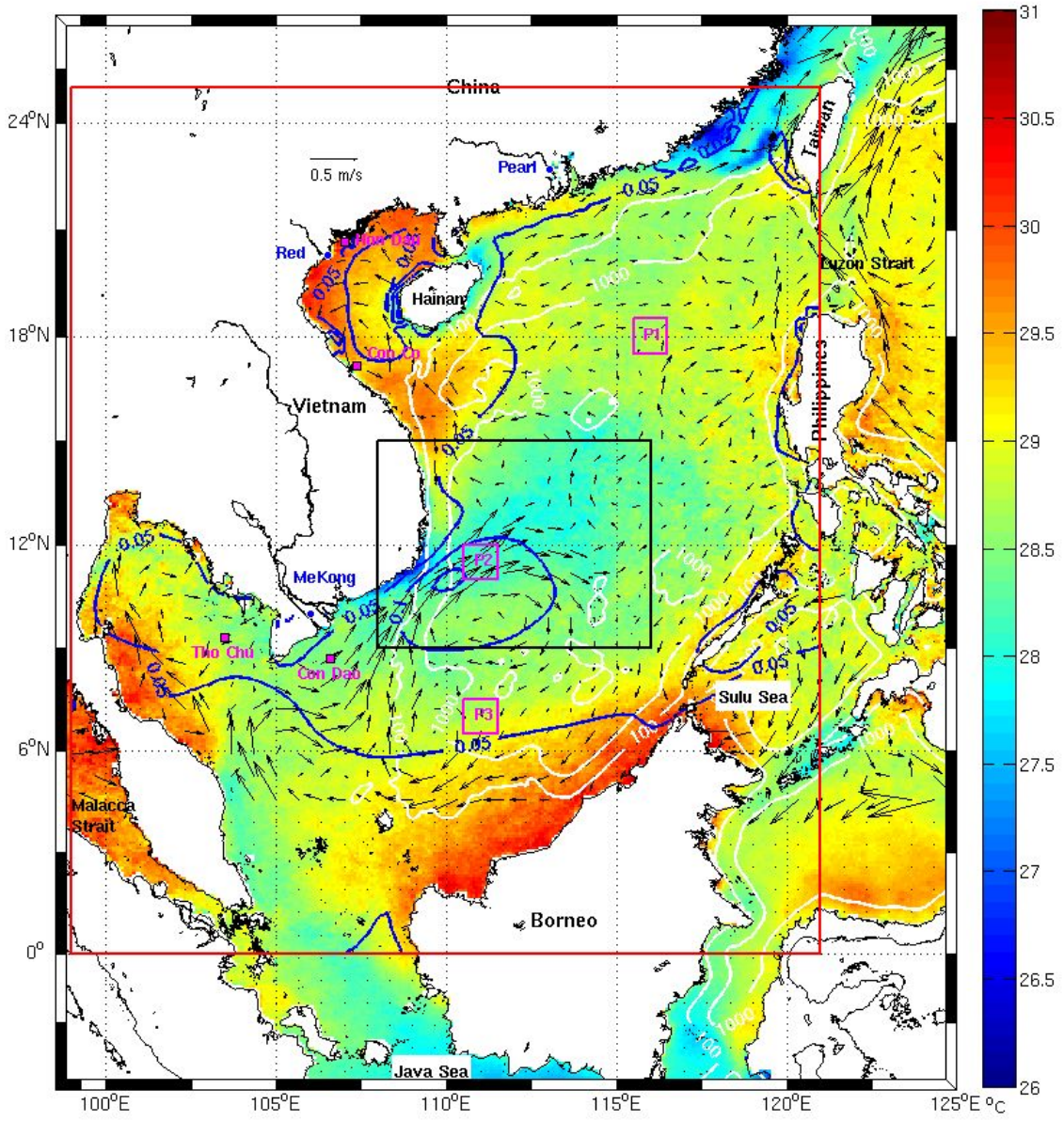

Figure 1.16 The SCS domain, locations of TS-profiles and tide gauges, and August climatological dynamical background. Bathymetry contours of 100m and 1000m are white solid lines. Also shown are the climatological August mean of SST (ºC, color shade, from AVHRR SST satellite data for 1991-2004), surface circulation ($m.s^{-1}$, vector, from CMEMS altimetry data for 1993-2004) and mean wind stress ($N.m^{-2}$, blue solid line, from NCEP CFSR reanalysis for 1991-2004, see section 2.3 for a description of the data). The magenta squares near the coast depict the locations of tide gauges. The magenta frames show the averaging areas around stations P1, P2, P3 used for evaluation of hydrological profiles in the CTRL simulation. The black and red rectangles show respectively the SVU and SCS subdomains.

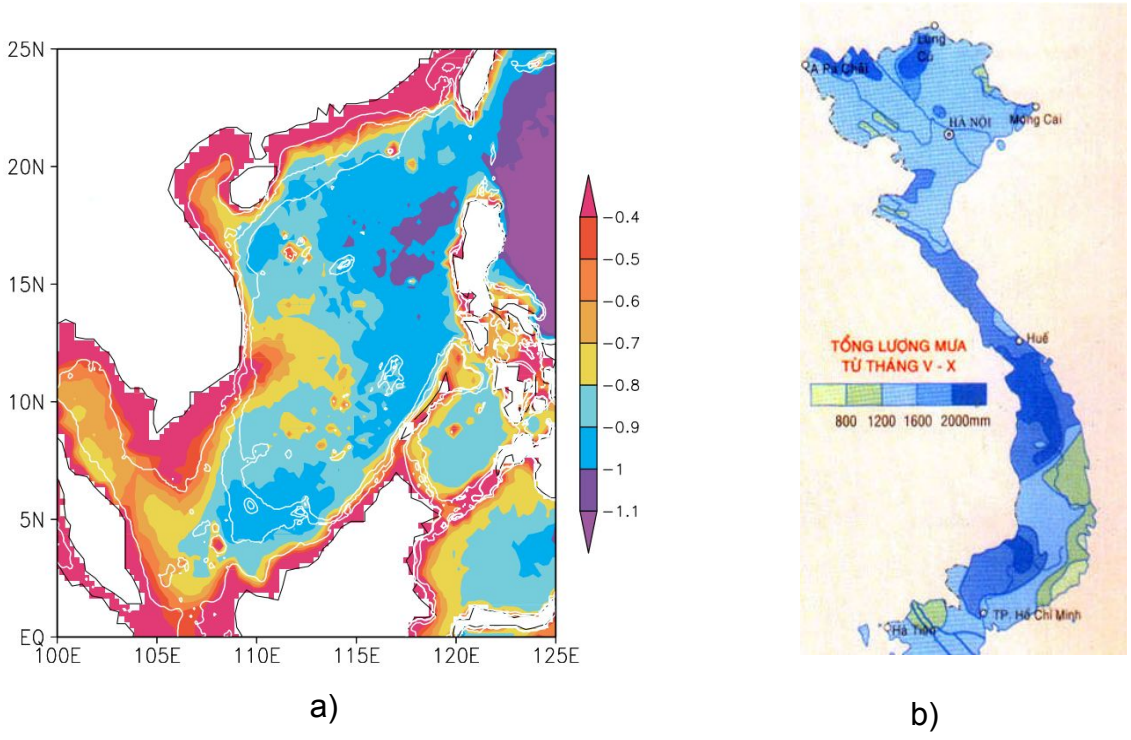

a) b)

Figure 1.17 (a) averaged concentration of SeaWiFS Chlorophyll (Log10, mg.m^{-3}) in July-August 1999-2002 over the SCS along with bottom topography contours for 50, 100, and 500 m (after Xie et al., 2003). (b) Climatological total rainfall of Vietnam from May to October (Geographical Atlas of Vietnam, 2004).

In addition to its important role in the functioning of local marine ecosystems, SVU impacts on the regional weather and climate. In years with strong upwelling, the SST in the SCS has a semi annual cycle with a local minimum in mid-summer caused by the upwelling cooling processes (Xie et al., 2003). Xie et al., (2007) found that this surface cooling in the SVU area can reduce precipitation and surface wind speed by up to 3m.s^{-1}, compared to areas outside of the SVU zone. They found a positive correlation of 0.6 between SST and 1-week-lagged precipitation in the central SCS, suggesting that the surface cooling can also reduce precipitation here. The SST cooling contributes to stabilizing the atmosphere above and suppressing convection thus reducing precipitation, which could explain the lower climatological annual precipitation in the cities that are near the upwelling (Figure 1.17b) such as Phan Thiet (1072 mm.year^{-1}) and Nha Trang (1280 mm.year^{-1}), compared to surrounding coastal cities such as Tuy Hoa (north of Nha Trang, 1826 mm.year^{-1}) and Vung Tau (south of Phan Thiet, 1437 mm.year^{-1} ; data from Climatological Standards used for Construction, released in 2008 by the Ministry of Construction, Vietnam - QCXDVN 02 : 2008/BXD). A second climatic effect concerns the heat and salt transported by the SCS Throughflow (SCSTF, see Metzger and Hurlburt 1996;

Qu et al., 2009; Fang et al., 2009) from the SCS into the Pacific Ocean, Soulou Sea, Java Sea and Indian Ocean (via Malacca strait, Figure 1.16). By cooling the temperature and bringing salt to the surface water layer of the central SCS, the SVU may change this SCSTF heat and salt transport into the surrounding seas and oceans, which could impact the climate of the whole Indo-Pacific region.

1.2.2 Mechanisms

Although its fishing resources have been exploited by local people over a long time, the underlying dynamics of the high productivity SVU area have only been explored in the last few decades. Previous studies found a key role of summer southwest (SW) wind in driving the SVU via three different mechanisms (Figure 1.18).

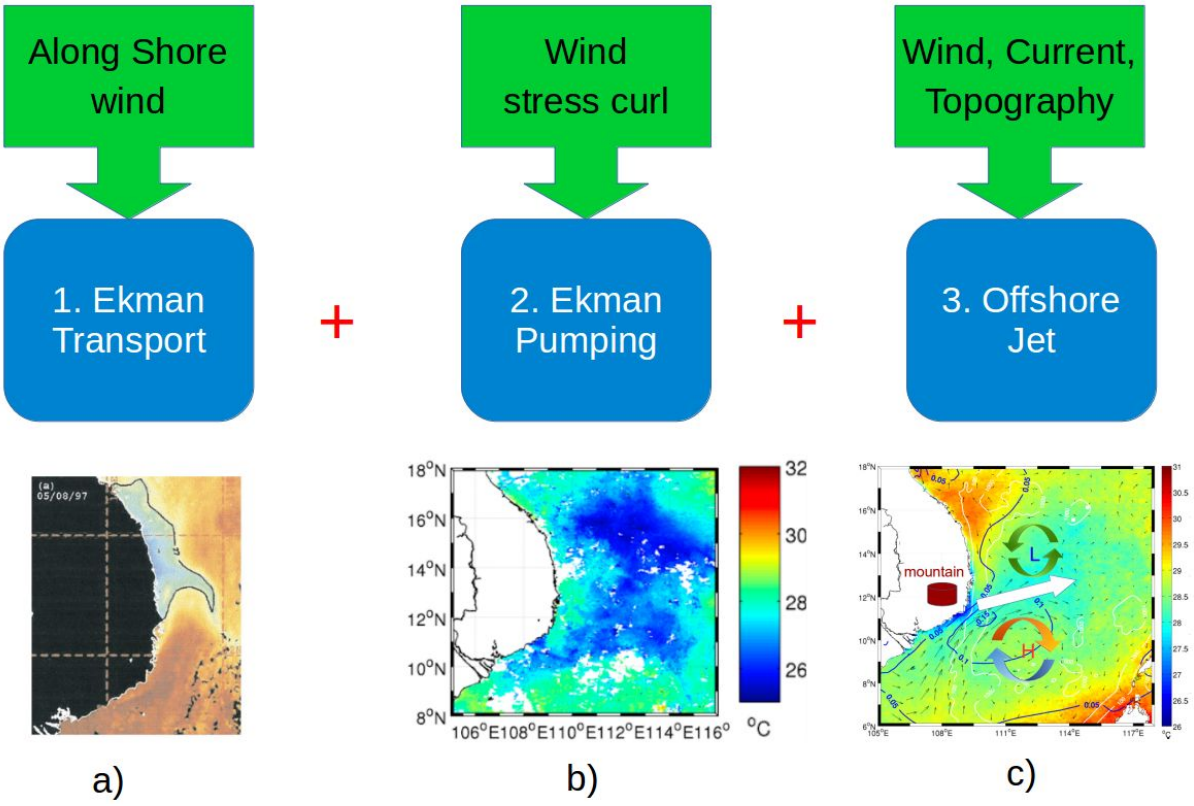

Figure 1.18 Three different upwelling mechanisms in the SVU with illustrations from observations. (a) SST on 05/08/1997 showing a coastal band cooler SST in blue compared to surrounding area (Kuo et al., 2000). (b) AVHRR SST on 23/08/2002 showing a strong offshore cooling area due to offshore upwelling associated with Ekman pumping. (c) a schematic zoom-in of Figure 1.15 showing coastal upwelling that occur upstream of an offshore jet which is in the middle of an eddy dipole.

The first mechanism is via Ekman offshore transport (Figure 1.18a; Wyrtki 1961; Kuo et al., 2000; Wang et al., 2006b; Dippner et al., 2007; Hein 2008). This mechanism often occurs after wind starts blowing along-shore for several days and the basin scale western boundary current is too weak to compensate completely the offshore Ekman transport component of surface water resulting in upwelling of subsurface water. As an illustration, Figure 1.18a shows the existence of a long coastal band of cold water (SST < 27^{o}C) in August 1997 discovered by Kuo et al., 2000.

The second mechanism is via Ekman pumping due to wind stress curl (Xie et al., 2003, 2007; Wang et al., 2006b). Figure 1.18b shows an evidence of a very strong offshore upwelling in August 2002 via AVHRR SST. Figure 1.19a further shows the existence of maximum wind center off Ho Chi Minh city due to the nearby mountain range in southern Vietnam. This maximum wind stress center induces positive and negative win stress curl north and south of it respectively resulting in positive Ekman pumping in Figure 11.9b.

The third mechanism is associated with the formation of an eastward jet and an eddy dipole in the region induced by nonlinear interactions between different factors: the western boundary current driven by large scale wind, a sudden change of local coastline shape and bathymetry, and the orographic induced local maximum wind in the SVU (Wyrtki 1961; Xu et al., 1982; Fang et al., 2002; Kuo et al., 2000; Xie et al., 2003, 2007; Dippner et al., 2007; Hein 2008; Chen et al., 2012). Figure 1.16 illustrates this mechanism by showing climatological August surface circulation, SST and wind forcing. There is a strong boundary current of about 0.5 m/s flows northeastward off the Mekong river and then turns offshore at about 11.5^{o}N due to a sudden change in coastline shape and bathymetry. It is then accelerated by the orographic induced maximum wind stress (blue contours) resulting in a cold SST area of less than 27^{o}C near the coast. This eastward jet then splits and forms an anti-cyclonic eddy in the south and a cyclonic eddy in the north (as summarized in Figure 1.18c). The jet advects coastal upwelled water offshore and forms a tongue like SST pattern as shown in Figure 1.20 (see also Kuo et al., 2000). The location of the eddy dipole and eastward jet and associated coastal upwelling can vary from 10 - 14^{o}N with a mean position around 12^{o}N (Li et al., 2014).

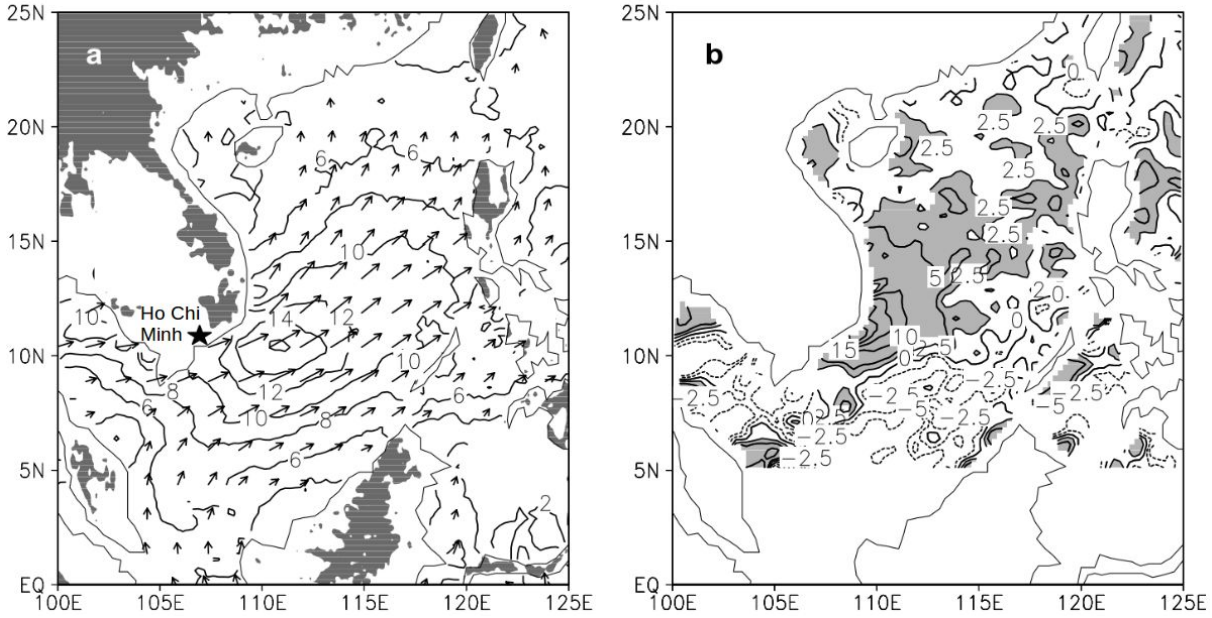

Figure 1.19 (a) QuikSCAT surface wind stress vectors and their magnitude (contours in 10^{-2} Nm^{-2}) averaged for June–August 2000–2002. (b) Ekman pumping velocity (upward positive in 10^{-6} m/s; contour intervals are 2.5 for values between -5 and 5, and are otherwise 5, with values greater than 2.5 shaded). In (a), land topography with elevations greater than 500 m is shaded and the star marks the location of Ho Chi Minh city (after Xie et al., 2003 with modifications)

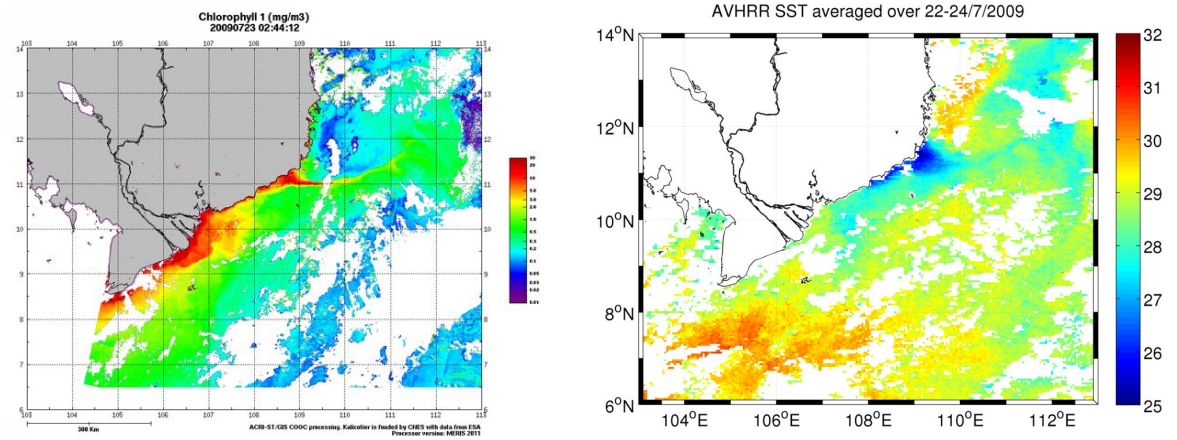

(a) **(b)**

Figure 1.20 Tongue-like pattern of the SVU (low SST and high Chlorophyll) due to advection of coastal upwelled water offshore by an eastward jet. (a) Meris Chlorophyll map on 23/7/2009 (mg.m^{-3}, color shading in LOG10 scale, blue-cyan range = 0.01 - 0.3; green-yellow range = 0.1 - 3, and red range = 3 - 30). (b) AVHRR SST averaged over 22-24/7/2009.

Chen et al., (2012, 2013) confirmed the important role wind and the eddy dipole system. They also proposed another mechanism contributing to the upwelling (from a sensitivity simulation without wind forcing), due to the interaction between a buoyancy-driven, low-salinity current from the north originating from the Red river and a stratified, tidal-rectified current from the southwest (Figure 1.21). However, during normal monsoon conditions, the influence of these phenomena is an order of magnitude smaller than the influence of wind.

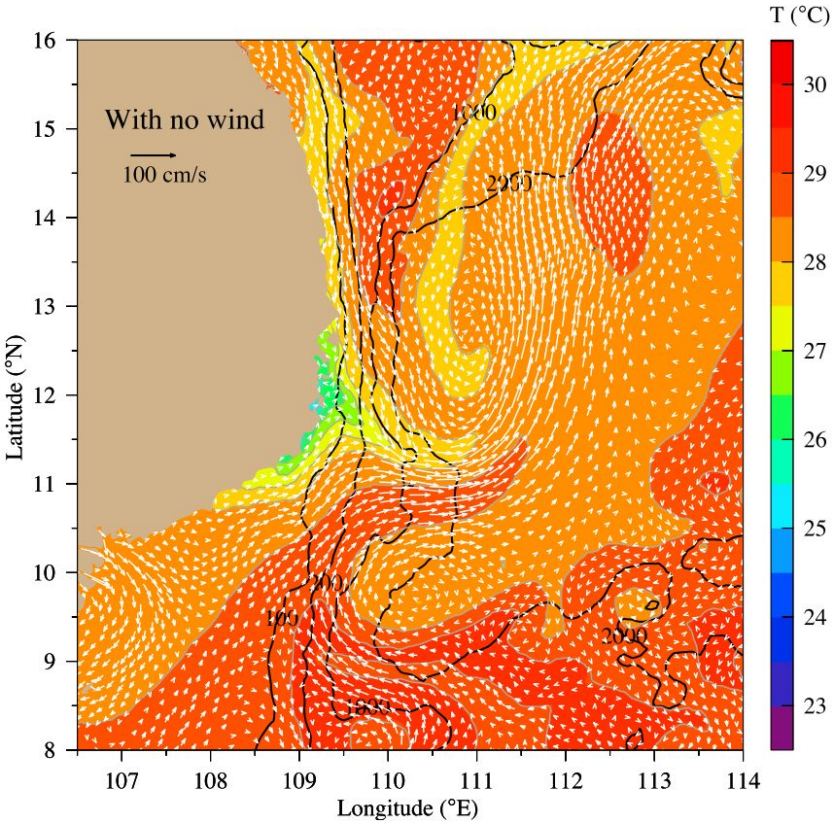

Figure 1.21 Model-computed near-surface subtidal current vectors (cm/s) plotted on the surface temperature field at the 40th day of the spin-up run, starting with August climatology temperature and salinity fields for the case with no wind. Black lines are the contours of 100, 200, 1000, and 2000 m isobaths (after Chen et al., 2012).

Figure 1.18 summarizes the three main mechanisms that drive different upwelling patterns of the SVU. The first two mechanisms drive both eastern and western boundary upwelling systems whereas the last one is quite unique in the western boundary systems with the presence of intensified western boundary currents (Hein 2008). Summer wind play important role in all of the mechanisms.

1.2.3 Seasonal variations

There have been fewer studies on the intra-seasonal variation of the SVU. The SST-based upwelling index developed by Kuo et al., (2000) for summer 1997 showed that the SVU started in May then gradually increased with some small peaks in phase with alongshore wind stress peaks, and reached its maximum in August. They also showed that the position of the upwelling center moved southward from about 14°N in May to 11°N in August over the summer of 1997. Xie et al., (2003) used a 15-year-climatology of satellite-derived SST to show that, on average, the upwelling starts in June, grows stronger in July and reaches a maximum in August. This was confirmed by the study of Li et al., (2014) using NOAA optimum interpolated SST for the 1992-2012 period. Xie et al., (2007), using weekly satellite SST data, showed that the SVU does not develop and decay smoothly over the summer season, but instead that several individual upwelling events occur within a season in response to intraseasonal variations in wind stress (Figure 1.22), which were later attributed to the Madden-Julian Oscillation (MJO) effect by Liu et al., (2012).

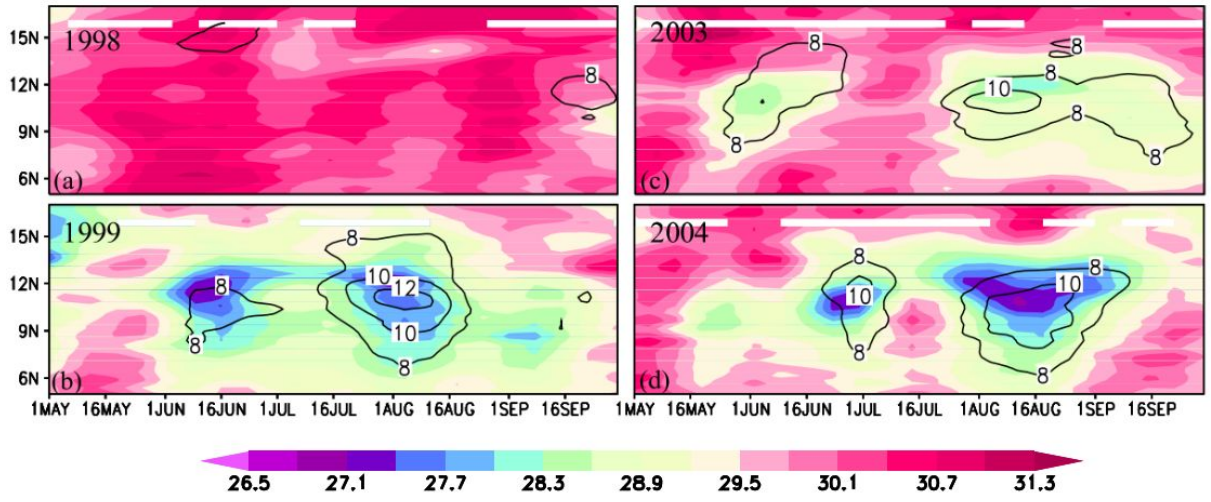

Figure 1.22 Summer intraseasonal pulses seen in time-latitude sections of SST (°C, color shading) and wind speed (ms^{-1}, contour) at 111°E for the summer (May to September) of (a) 1998, (b) 1999, (c) 2003, and (d) 2004 (after Xie et al., 2007).

1.2.4 Interannual Variability

Previous studies have examined the interannual variability of the SCS dynamics, including the SVU, based on satellite observations of SST, altimetric sea surface height (SSH), wind and chlorophyll (Morimoto et al., 2000; Hwang and Chen 2000; Xie et al., 2003; Hein 2008; Hai et al., 2010; Li et al., 2014), in-situ data (Wang et al., 2006a; Dippner et al., 2007; Rong et al., 2007; Bombar et al., 2010; Hein et al., 2013), and numerical modeling (Qu et al., 2004; Wu and Chang 2005; C. Wang et al., 2006b; Wang et al., 2006c; Chang et al., 2008; Li et al., 2014). They suggested a close relation between the SVU intensity and ENSO (El-Niño Southern Oscillation), in that a strong El-Niño weakens the SVU of the following summer. Figure 1.22 shows that upwelling in two post El Niño summer in 1998 and 2003 are weaker than post La Niña summer (1999) and normal year (2004). Xie et al., (2003) built a cold filament index in summer based on satellite-derived SST over the period 1982-2002 and found a 6-month-lagged correlation of 0.67 with the Nino3 index. Hein (2008) constructed a similar index for the period 1998 - 2006 by calculating the averaged chlorophyll concentration in the upwelling area and found a higher correlation of 0.8 with the Multivariate ENSO Index (MEI) in both summer and winter. Dippner et al. (2007), Bombar et al. (2010) and Loick-Wilde et al. (2017) analysed in-situ data from two summer cruises in the SVU area in 2003 and 2004, and found that upwelling was much weaker in 2003 which was a post El-Niño year, than in 2004 which was not particular in terms of ENSO conditions.

The mechanisms for this link between the SVU and the ENSO forcing have also been explored with moderate resolution models. Wu and Chang (2005) analyzed SSH from a 0.4° resolution assimilation system and Wang et al., (2006c) performed a 1/6° resolution ocean circulation simulation over the period 1982-2004 to examine seasonal and interannual variations of the SCS circulation. Both studies showed that ENSO oscillation strongly affects the general winter and summer surface SCS circulation. Post El-Niño years were associated with a weakening of the winter cyclonic circulation (resulting in a warmer surface layer) and a weakening of the summer double gyre (cyclonic to the North and anticyclonic to the South) in the SVU circulation, eventually inducing the disappearance of the SVU. Wang et al., (2006a) analyzed available surface observations over the period 1954-2002, and showed that El-Niño years were followed by a double SST peak in February and August of the following year. The February peak was explained by a winter positive heat flux anomaly and the August peak by a geostrophic advection of temperature anomalies from the coast, that would then affect the SVU. Li et al., (2014) used a 1/4° resolution ocean model and satellite data to study how the SVU intensity but

also its position changed over the period from 1992 to 2012. Their results showed that during this period the upwelling center positions moved around between 10.7°N and 14.3°N and that strong upwelling events were located south of the mean position, whereas weak upwelling events were located further north.

Two different mechanisms have been proposed to explain how ENSO impacts the upwelling. The first one implies a direct effect through local summer wind modulation, suggesting that ENSO modulates the summer SW monsoon and thus impacts the wind-induced SVU (Lau and Yang 1997; Xie et al., 2003; Dippner et al., 2013). The second hypothesis is an indirect effect via changes in the large scale circulation and thermohaline structure (Hein et al., 2013; Li et al., 2014). Qu et al., (2004) suggested that transport at Luzon strait could be a key process conveying the impact of the Pacific ENSO into the SCS, which raises the question of the potential influence of this transport on the SVU.

Recent studies performed for the global ocean or other regional seas (Penduff et al., 2011; Gregoria et al., 2015; Serazin et al., 2016; Waldman et al., 2018) showed that the interannual variability of oceanic circulation can also be significantly influenced by ocean intrinsic variability (OIV), and that mesoscale to submesoscale structures and eddies are a major source of this OIV. A few studies have examined the impact of OIV on the variability of the SCS circulation and the SVU region. Gan et al., (2008) concluded from a 10 to 30 km resolution model that the summer circulation in the Southern SCS is dominated by cyclonic and anticyclonic eddies with strong flow variability that are generated by the eastward wind-driven coastal jet separation from the coast of central Vietnam. They suggested that this strong flow variability could partly arise from the intrinsic dynamic processes associated with the jet separation and eddies formation. Li et al., (2014), using a ¼° resolution model, provided a first assessment of this OIV impact : in their simulations OIV, induced in particular by eddy-current interactions, led to 20% of the interannual variability of the eastward jet. However, the coarse resolution of their model does not reproduce correctly the multiscale dynamics and eddy activity in the SCS, one of the major sources of OIV. Given the scarcity of studies dedicated to the role of OIV in this region, they called for more realistic and higher resolution numerical studies to better assess the role of OIV on SCS circulation and summer jet.

1.3 Objectives

In summary, these previous modeling and observation studies showed that the atmospheric forcing associated with the SW summer monsoon is a key factor in

the SVU interannual variability, and that ENSO could contribute to this interannual variability, either by modulating the SW monsoon directly or through indirect forcing, although the precise mechanisms of this ENSO impact still need to be investigated. Results from previous studies also suggest that large scale oceanic circulation, including exchanges with the Pacific Ocean, freshwater river discharge and OIV could contribute to this variability. To better understand the interannual variability of the SVU and the role of those factors, their respective contributions now need to be quantitatively assessed and compared. Moreover, existing results were mostly based on satellite observations that can have spatial and/or temporal resolution limitations, in particular due to the strong cloud cover in the region. Numerical simulations were mainly performed over short periods or with moderate resolution models that are not able to completely reproduce the multiscale range of the ocean dynamics that govern the circulation of the SCS and SVU regions. The main objectives of our study are therefore to implement over the SCS a high resolution hydrodynamical numerical model able to reproduce the large range of spatial and temporal scales involved in the SCS ocean dynamics, from the submesoscale to the basin scale circulation, and to use it in order to:

- characterize and quantify the interannual variability of the SVU in terms of spatial and temporal scales, intensity and location,

- assess quantitatively and explain physically the contributions of the different factors affecting it: atmospheric variability, large scale oceanic forcing, OIV, river freshwater runoff and tidal forcings,

- understand better how could ENSO affect the SVU,

- evaluate the robustness of our conclusions to the choice of configuration of the numerical model used.

Chapter 2. Methods and tools

In section 1.2, we've shown that the SVU is visible via SST satellite observations. This suggests that we could study its interannual variability via SST observations. The availability of SST observations, lower than 15% in the SVU region in summer (see Figure 2.1) is however not enough for a comprehensive analysis of interannual variability of the SVU. Moreover we aim to quantify the contributions of different forcings on the SVU and study the underlying mechanisms. SST is controlled by vertical mixing, stratification, horizontal circulation, heat and water fluxes with the atmosphere, etc. These complicated relations among forcings and SST are highly nonlinear and tridimensional. Numerical models were developed to study those kind of interactions and thus complement observational data. Moreover, models allow us to perform sensitivity simulations by modifying the prescribed forcing to study their impacts. Thus numerical modelling will be the main tool of this PhD thesis, and observational in-situ and satellite data will be used to estimate and improve the realism of our simulations.

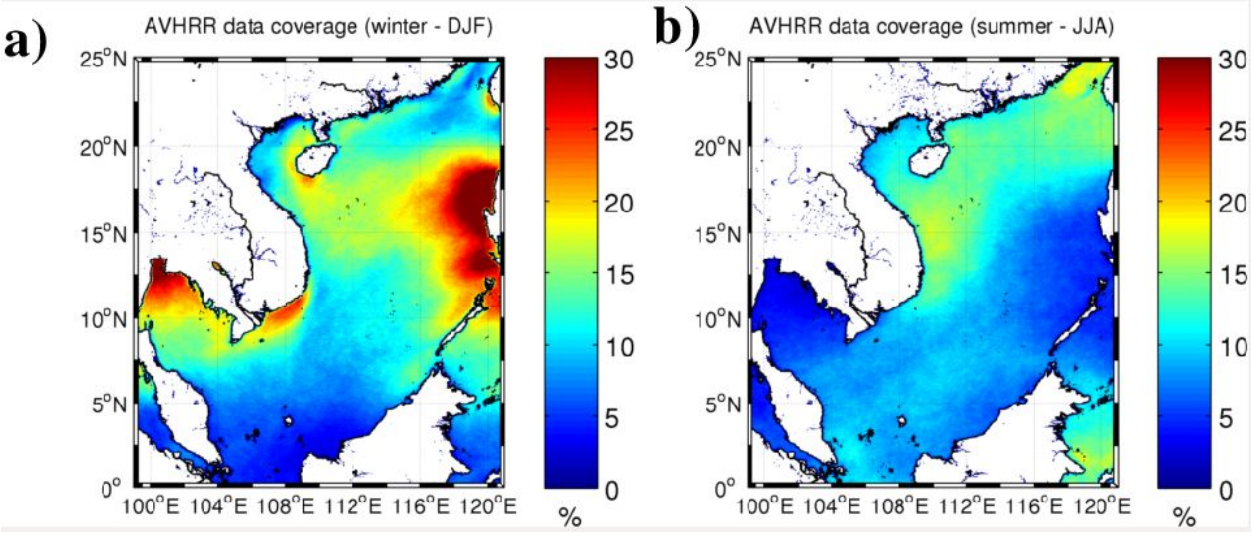

Figure 2.1: Data coverage of the AVHRR SST dataset. Winter (a) and summer (b) data coverage (in %) of AVHRR (daily and nightly) SST from 1991 to 2014.

2.1 The numerical hydrodynamical model ROMS (Regional Ocean Modeling System)

2.1.1 Governing equations

The Regional Ocean Modeling System (ROMS, Schepetkin & McWilliams 2003, 2005) is a three-dimensional, free surface, terrain-following vertical coordinates numerical model. It solves the Reynolds-averaged Navier-Stokes equations which have the following form in Cartesian coordinates (see Stewart, 2008 for detail derivations):

$$\frac{\partial u}{\partial t}+u\frac{\partial u}{\partial x}+v\frac{\partial u}{\partial y}+w\frac{\partial u}{\partial z}=-\frac{1}{\rho_0}\frac{\partial p}{\partial x}+2\Omega\, v\, sin\varphi+\frac{\partial}{\partial x}\left(A_h\frac{\partial u}{\partial x}\right)+\frac{\partial}{\partial y}\left(A_h\frac{\partial u}{\partial y}\right)+\frac{\partial}{\partial z}\left(A_z\frac{\partial u}{\partial z}\right) \quad (2.1)$$

$$\frac{\partial v}{\partial t}+u\frac{\partial v}{\partial x}+v\frac{\partial v}{\partial y}+w\frac{\partial v}{\partial z}=-\frac{1}{\rho_0}\frac{\partial p}{\partial y}-2\Omega\, u\, sin\varphi+\frac{\partial}{\partial x}\left(A_h\frac{\partial v}{\partial x}\right)+\frac{\partial}{\partial y}\left(A_h\frac{\partial v}{\partial y}\right)+\frac{\partial}{\partial z}\left(A_z\frac{\partial v}{\partial z}\right) \quad (2.2)$$

$$\frac{1}{\rho}\frac{\partial p}{\partial z}=-g \quad (2.3)$$

$$\frac{\partial u}{\partial x}+\frac{\partial v}{\partial y}+\frac{\partial w}{\partial z}=0 \quad (2.4)$$

$$\frac{\partial T}{\partial t}+u\frac{\partial T}{\partial x}+v\frac{\partial T}{\partial y}+w\frac{\partial T}{\partial z}=\frac{\partial}{\partial x}\left(K_{Th}\frac{\partial T}{\partial x}\right)+\frac{\partial}{\partial y}\left(K_{Th}\frac{\partial T}{\partial y}\right)+\frac{\partial}{\partial z}\left(K_{Tz}\frac{\partial T}{\partial z}\right)+\Theta_T \quad (2.5)$$

$$\frac{\partial S}{\partial t}+u\frac{\partial S}{\partial x}+v\frac{\partial S}{\partial y}+w\frac{\partial S}{\partial z}=\frac{\partial}{\partial x}\left(K_{Sh}\frac{\partial S}{\partial x}\right)+\frac{\partial}{\partial y}\left(K_{Sh}\frac{\partial S}{\partial y}\right)+\frac{\partial}{\partial z}\left(K_{Sz}\frac{\partial S}{\partial z}\right)+\Theta_S \quad (2.6)$$

$$\rho=\rho(T,S,P) \quad (2.7)$$

Eq. 2.1 and 2.2 represent horizontal momentum equations, where terms on the left side are the rate of change of momentum in time and space, and terms on the right side are forcings per unit mass; *u, v, w* are velocity components in *x, y, z* directions respectively. The first, second and last three terms on the right side represent respectively pressure (*p*) gradient force, Coriolis force and turbulent friction; Ω is the rate of rotation of the Earth; φ is the latitude; A_h, A_z are kinematic eddy viscosities in horizontal and vertical direction respectively.

ROMS uses the hydrostatic assumption and neglects vertical acceleration as well as the Coriolis term associated with vertical velocities. Thus the momentum equation in the vertical direction reduces to the balance between the vertical pressure gradient and the buoyancy force in Eq. 2.3 where *g* is the standard

acceleration due to gravity. ROMS also uses the Boussinesq assumption : whereby the variation of density in the horizontal pressure gradient in Eq. 2.1 and 2.2 is negligible and can be considered as a constant ($\rho_0 = 1025\ kg.m^{-3}$ in our simulations), but not in the vertical pressure gradient in Eq. 2.3. ROMS assumes that sea water is incompressible which lead to the continuity equation 2.4.

Eq. 2.5 and 2.6 express the conservation of tracers which are temperature *T* and salinity *S*. K_{Th}, K_{Tz}, K_{Sh}, K_{Sz} are the kinematic eddy diffusivity for temperature and salinity in the horizontal and vertical directions respectively. Θ_T and Θ_S represent the source terms of temperature and salinity. The equation of state Eq. 2.7 allows us to close the system of 7 unknown variables (*u, v, w, S, T, p,* ρ) with 7 equations.

The coefficients A_h, A_z, K_{Th}, K_{Tz}, K_{Sh}, K_{Sz} are not constant but depend on the advection/mixing scheme used. In this study, we use a K-profile vertical parameterization and a split and rotated 3rd-order upstream-biased advection scheme to resolve the vertical mixing and the lateral tracer advection respectively (see Hedstrom 2009 for details).

The solutions of the above system of differential equations are deterministic only if the boundary and initial conditions are provided. A body of water such as a marginal sea can have three boundaries including:

- **Surface**, where the exchange of momentum, heat and water fluxes with the atmosphere happens. The conditions at the surface $z = \zeta(x, y, t)$ are:

$$\left(A_z \frac{\partial u}{\partial z}\right)_{z=\zeta} = \frac{\tau_s^x}{\rho_0} \tag{2.8}$$

$$\left(A_z \frac{\partial v}{\partial z}\right)_{z=\zeta} = \frac{\tau_s^y}{\rho_0} \tag{2.9}$$

$$\frac{\partial \zeta}{\partial t} - u_s \frac{\partial \zeta}{\partial x} + v_s \frac{\partial \zeta}{\partial y} = w_s \tag{2.10}$$

$$\left(\rho_s C_p K_{Tz} \frac{\partial T}{\partial z}\right)_{z=\zeta} = \Theta_T = Q_{short} - Q_{long} - Q_{latent} - Q_{sens} \tag{2.11}$$

$$\left(K_{Sz} \frac{\partial S}{\partial z}\right)_{z=\zeta} = (E - P)S \tag{2.12}$$

Where Eq. 2.8 and 2.9 describe the momentum flux exchange with the surface wind stress vector $\tau_s = \rho_{air} C_d U_{10} |U_{10}|$, ρ_{air} is air density, C_d is the drag coefficient and U_{10} is surface wind velocity. Eq. 2.10 is the free-surface

equation where the surface elevation depends on the surface velocity. Eq. 2.11 shows the vertical gradient temperature at the surface as a function of the net heat flux/source (Θ_T) at the surface, which depends on shortwave radiation (Q_{short}) coming from the sun, longwave radiation (Q_{long}) going out from the sea surface, latent heat flux (Q_{latent}) exchange with the atmosphere due to evaporation/condensation, and sensible heat flux (Q_{sens}) exchange due to the difference in temperature between the air and the sea surface. ρ_s is the surface density of seawater, C_p is the specific heat of sea water at the surface pressure. Eq. 2.12 represents the salt flux exchange at the surface which depends on the evaporation rate (*E*) and precipitation rate (*P*)

- **Bottom** (*z = -H(x,y)*), where the vertical distribution of velocity depends on bottom stress and the tracer flux exchange across the bottom is set to zero:

$$\left(A_z \frac{\partial u}{\partial z}\right)_{z=-H} = \frac{\tau_b^x}{\rho_0} \tag{2.13}$$

$$\left(A_z \frac{\partial v}{\partial z}\right)_{z=-H} = \frac{\tau_b^y}{\rho_0} \tag{2.14}$$

$$u_b \frac{\partial H}{\partial x} + v_b \frac{\partial H}{\partial y} = w_b \tag{2.15}$$

$$\left(K_{Tz} \frac{\partial T}{\partial z}\right)_{z=-H} = 0 \tag{2.16}$$

$$\left(K_{Sz} \frac{\partial S}{\partial z}\right)_{z=-H} = 0 \tag{2.17}$$

Where $\tau_b = C_d U_b |U_b|$ is the bottom stress/friction; C_d is the bottom drag coefficient and U_b is the bottom velocity. In all our simulations, we use a linear bottom drag coefficient of 0.0003 with a free slip condition at the bottom.

- Lateral boundaries can be open when connected with other bodies of water including oceans or rivers. With open boundaries, the values for *u, v, T, S*, and the surface elevation ζ should be provided at every time step (other variables including *w* and ρ are computed using Eq. 2.4 and 2.7). There can also be closed boundaries along the continent or islands. Closed boundary conditions for momentum can be no slip (*u = v = 0*) or free slip (used in our simulations) where *u,v* at the boundary depends on a friction coefficient. For tracers, it's the same as Eq. 2.16 and 2.17, meaning that no horizontal flux of the tracer can come in and out of the boundary.

Initial conditions specify values for all variables at all grid points at time *t=0*.

2.1.2 Terrain-following coordinate system

ROMS is equipped with sigma vertical coordinates $\sigma(x,y)$ which normalize the water column from $\zeta(x,y)+H(x,y)$ to [-1 0] (Shchepetkin and McWilliams, 2005; Hedstrom 2009). The transformation is as followed:

$$z = (\zeta + H)(1+\sigma) - H \tag{2.18}$$

If $\sigma = -1, z = -H$ *and if* $\sigma = 0, z = \zeta$. Sigma levels of -0.01, -0.5 and -0.99 are respectively equivalent to 1% near the surface, in the middle, and 99% of total depth near the bottom. Z-coordinates are more computationally efficient than sigma coordinates of the same resolution. Yet sigma coordinates provide a strong advantage over z-coordinates in regions with complicated bathymetry where a high resolution of the vertical grid is required not only near the surface but also near the bottom. Adding more vertical grid resolution over sloping areas will result in adding more grid resolution over the whole domain (Figure 2.2a), whereas sigma coordinate can allow high resolution regardless of water depth (Figure 2.2b). Sigma grids can also be arranged to have higher resolution in strong dynamical layers such as the surface mixed layer or bottom boundary layer (Song and Haidvogel, 1994; Shchepetkin and McWilliams, 2005) by adding two parameters θ and b that control the density of sigma grid near the surface and the bottom respectively:

$$z = \zeta(1+\sigma) + h_c.\sigma + (H - h_c)C(\sigma), \qquad -1 \le \sigma \le 0 \tag{2.19}$$

$$with\ C(\sigma) = (1-b)\frac{sinh(\theta\sigma)}{sinh\theta} + b\frac{tanh[\theta(\sigma+0.5)] - tanh(0.5\theta)}{2tanh(0.5\theta)} \tag{2.20}$$

Where $h_c \le h_{min}$ is the depth above which we want to have more resolution, h_{min} is the shallowest depth of the domain, $0 < \theta \le 20$ and $0 \le b \le 1$. Larger theta values will keep more vertical resolution above h_c. *b* represents the fraction of vertical resolution near the bottom compared to the surface. When it equals 1, both bottom and surface have the same vertical resolution. Figure 2.2 c,d shows an example of how those parameters can change the vertical grid density. All related parameters used in the present study are summarized in Table 2.1.

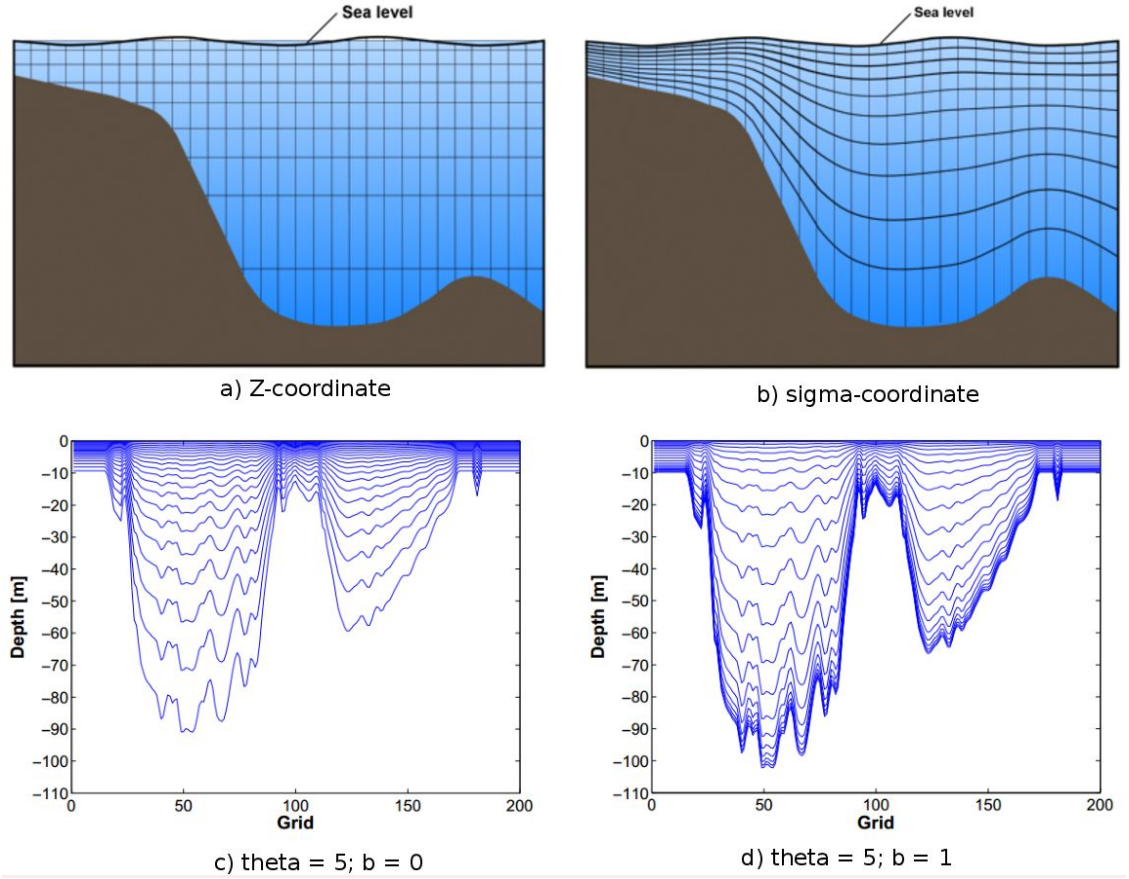

Figure 2.2 Characteristics of Z and sigma vertical coordinates. (a,b) Sigma vs. Z-coordinates (source: The COMET Program). (c,d) sigma grid with different stretching coefficient (source: Minh, 2013).

2.1.3 Reasons for the choice of tool

ROMS_AGRIF is a realistic tool with good cost efficiency. The SVU is a mesoscale dynamical structure where the pressure gradient induced by wind forcing, heat and water flux, and tidal forcing could be significant. Thus only a free surface model (not a rigid lid model) fits our requirements. However, to include the effects of fast moving waves such as tides, the time step must be decreased enough to ensure stable conditions for numerical schemes. This will greatly increase the computational cost. ROMS however is equipped with separated barotropic and baroclinic modes for time stepping. It solves the fast moving waves in 2D barotropic mode with a small time step then averages the results as an input for the 3D baroclinic mode which is solved with a much larger time step (60 times larger by default). This mode splitting scheme ensures realistic solutions with good cost-efficiency.

Table 2.1 Simulation parameters

Group	Parameter	Value	Parameter	Value
Grid	Min longitude	**99ºE**	Max longitude	**125ºE**
	Min latitude	**-4ºN**	Max latitude	**27ºN**
	Horizontal resolution	**1/12º**	Vertical sigma layers	**40**
	S-coordinate surface control parameter (θ)	**8**	S-coordinate bottom control parameter (b)	**0**
	Min depth	**10 m**	Max depth	**5000 m**
Time	Start date	**1/1/1990**	End date	**31/12/2004**
	Time step in barotropic mode (dt)	**600s/300s (with/without tides)**	Baroclinic step (ndtfast)	**60*dt**
	Output frequency for averaged output file (navg)	**2 day**	Output frequency for restart file	**1 month**
Mixing	Vertical mixing scheme	**LMD (K-profile)**	Lateral tracer advection scheme	**TS_HADV_ RSUP3**
	Linear bottom drag (rdrg)	**3.000E-04**	Quadratic bottom drag (rdrg2)	**0.000E+00**
	Bottom roughness for logarithmic law (Zob)	**0.000E+00**	Solid boundary condition (gamma2)	**1.00 (free-slip)**
	Minimum bottom drag coefficient (Cdb_min)	**1.000E-04**	Maximum bottom drag coefficient (Cdb_max)	**1.000E-01**
SST, SSS Relaxation coefficient: **40** and **120** $W.m^{-2}.K^{-1}$ for weak and strong case respectively				

There are other advantages of sigma vertical coordinates implemented in ROMS_AGRIF. The SCS has very complicated topography and a large depth range from 10 to 5000 m. Fast changing and complicated dynamics happen mainly in the mixed layer, with a depth ranging up to 100m in the SCS, and in a thin layer near the bottom. To have consistent bottom resolution in the shallow shelves, continental slope and deep basin regions, Z-coordinates would lead to high vertical resolution everywhere. A sigma coordinate system can follow closely the free surface and bottom topography which would save computing resources. Moreover, users can manipulate the vertical grid density to have higher vertical resolution near surface or bottom or both. However, these advantages have a trade off for the pressure gradient accuracy over steep slopes which requires bathymetry smoothing or further processing of the pressure calculation algorithm (Shchepetkin and McWilliams 2005).

The SCS is a large domain and the requirement of a mesoscale resolution to study the upwelling region will end up with a high horizontal resolution grid with a high demand of computing resources. ROMS_AGRIF is equipped with parallel computing capabilities including OpenMP and MPI. These methods allow us to divide the large domain into multiple smaller subdomains. Each subdomain will be processed with a central processing unit (CPU) in a system. Large computing systems can have thousands of CPUs and can significantly reduce the total computing time. At the moment, parallel computation is the only realistic solution to our problem.

There are three distributed branches of ROMS associated with three different institutions: the University of California Los Angeles (UCLA), Rutgers University and the Institute of Research for the Development (IRD). In this study, we use the ROMS_AGRIF version 3.3.1 (Debreu et al., 2012) and associated ROMS_TOOLS (Penven et al., 2008), distributed by the IRD. ROMS_AGRIF has the same kernel as the UCLA ROMS branch, and is developed by a group of researchers from French laboratories and institutes including LEGOS and the IRD. The main differences are the nesting capability of ROMS_AGRIF and a toolbox for pre- and post-processing that is written in Matlab.

2.2 Grid and forcings

Our computational domain covers the whole SCS and extra areas outside of the open boundaries from 99°E to 125°E and from -4°N to 27°N so that the lateral forcings can reach stable states before entering our region of interest (the red rectangle in Figure 1.16). We divide the domain by an orthogonal horizontal regular grid of 1/12° resolution and a vertical sigma grid with 40 layers. The simulation period starts on 1/1/1990 and ends on 31/12/2004 with a barotropic time step of 600 seconds for the simulation without tides and 300 seconds for the simulation with tides (presented only in the Appendix-A2). The baroclinic time step equals 60 barotropic time steps by default. Using the OpenMP method with 20 CPUs on a Linux cluster, it takes about 1 week and 2 weeks to complete one simulation, without and with tides, respectively.

Surface and lateral boundary conditions and initial conditions are provided by reanalysis products. For the surface forcing we use daily heat, water and momentum fluxes and SST from the NCEP-CFSR dataset, an improved version of the NCEP-NCAR reanalysis (Kalnay et al., 1996) with higher horizontal resolution (0.5°) and more realistic water and heat fluxes (Saha et al., 2010; Wang et al., 2010; Xue et al., 2011). The global dataset covers the period 1979-2009 with hourly outputs. In our study, we use daily averaged CFSR heat, water and momentum fluxes from 1990 to 2004. The upper pane of Figure 2.3 shows the mean wind speed from QuikScat, CFSR and NCAR datasets for the period 2000-2008 when QuikScat wind is available. CFSR wind has much higher resolution and shows better agreement to QuikScat wind than NCAR wind during this period. Furthermore, CFSR and NCAR averaged wind in the period 1990-1999 is similar to the period 2000-2008. These facts suggest a better performance of CFSR wind to NCAR wind for the period 1990-2004.

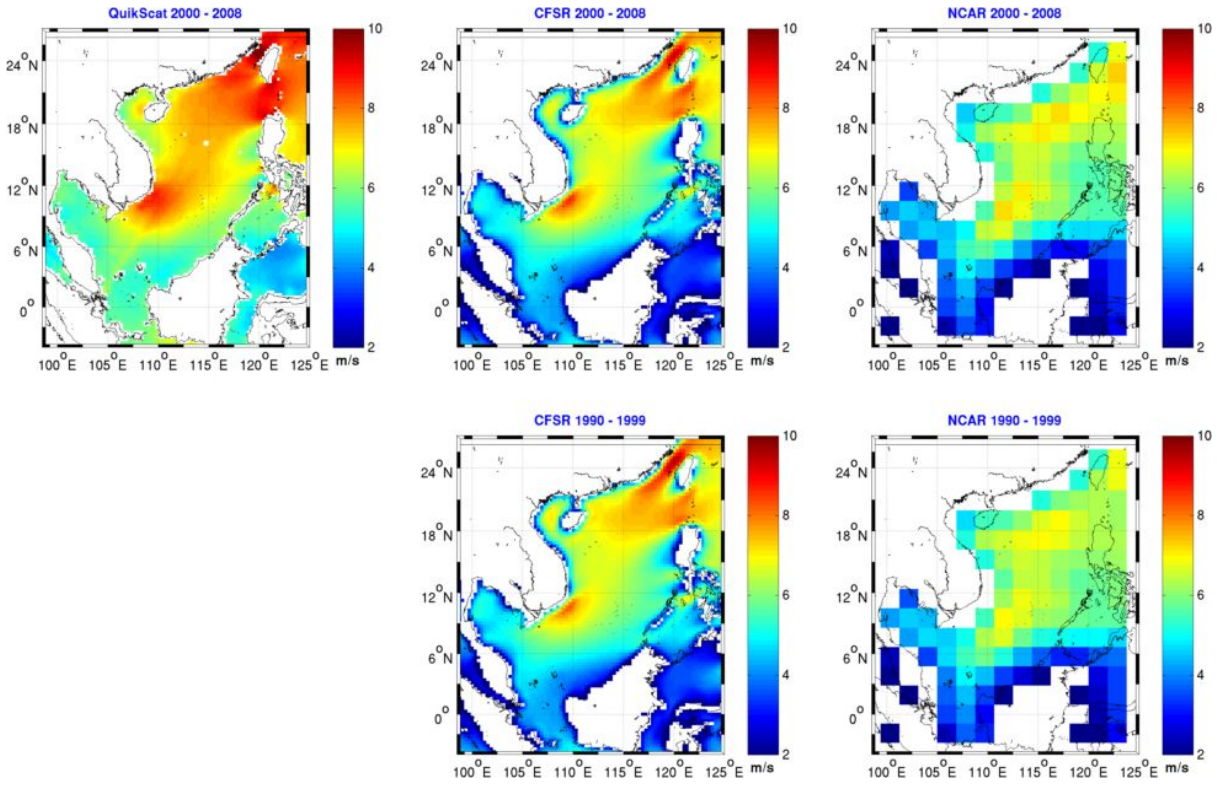

Figure 2.3 Comparison of wind speed at 10 m above the sea surface between QuikScat, CFSR and NCAR dataset for the period 2000 - 2008 (upper pane) and between CFSR and NCAR for the period 1990 - 1999 (lower pane)

We compared SST from AVHRR and CFSR (figure not shown) and found that CFSR SST follows closely AVHRR SST both spatially and temporally. CFSR SST can therefore be used as a reference observed SST dataset for the SST relaxation. Using the heat flux prescribed by NCEP CFSR with a small relaxation coefficient of -40 $W.m^{-2}.K^{-1}$ towards the CFSR SST and SSS, our initial model output showed a systematic positive bias of 1°C in winter to 1.6°C in summer within the mixed layer. We have corrected this bias by adjusting the heat flux following the method used by Somot et al., (2008). We first ran a simulation with a strong SST relaxation (dQdSST) of -120 $W.m^{-2}.K^{-1}$. We then calculated a heat flux correction term equivalent to this SST relaxation: $Q_{correction} = dQdSST\ (SST_{model} - SST_{obs})$, where SST_{model} is the SST computed from this strong SST relaxation simulation and SST_{obs} are the SST fields from the CFSR reanalysis. We computed the climatological monthly average of $Q_{correction}$ over the period 1990-2004 and then smoothed the results with a 1000-km spatial moving average filter. The purpose of the filter is to let the model be free in creating its own small scale structures of SST, but still correct the large scale heat flux bias. Finally, we added the daily interpolated value of this corrective term to the original CFSR heat flux and used a small relaxation coefficient of 40 $W.m^{-2}.K^{-1}$ towards CFSR SST and SSS. This method

helps to reduce the SST bias (compared to AVHRR SST) from 1.31°C in a simulation with no heat flux correction but a 40 $W.m^{-2}.K^{-1}$ relaxation coefficient, to only 0.2°C in a simulation with heat correction and the same relaxation coefficient. Figure 2.4 evaluates the impacts of the heat correction method applied to the original CFSR net heat flux by comparing its annual and interannual domain averaged variations with corrected CFSR net heat flux, OAFlux (Yu et al., 2008) and TropFlux (Kumar et al., 2012). The CFSR original and corrected heat fluxes follow closely OAFlux and TropFlux yet with positive and negative biases respectively. The positive bias of original CFSR net heat flux explains partly the SST bias mentioned. The corrected CFSR net heat flux has negative bias due to the fact that we also have to correct a warming bias coming from the lateral boundary forcings via surface net heat flux (see Section 3.1.2 and 3.3)

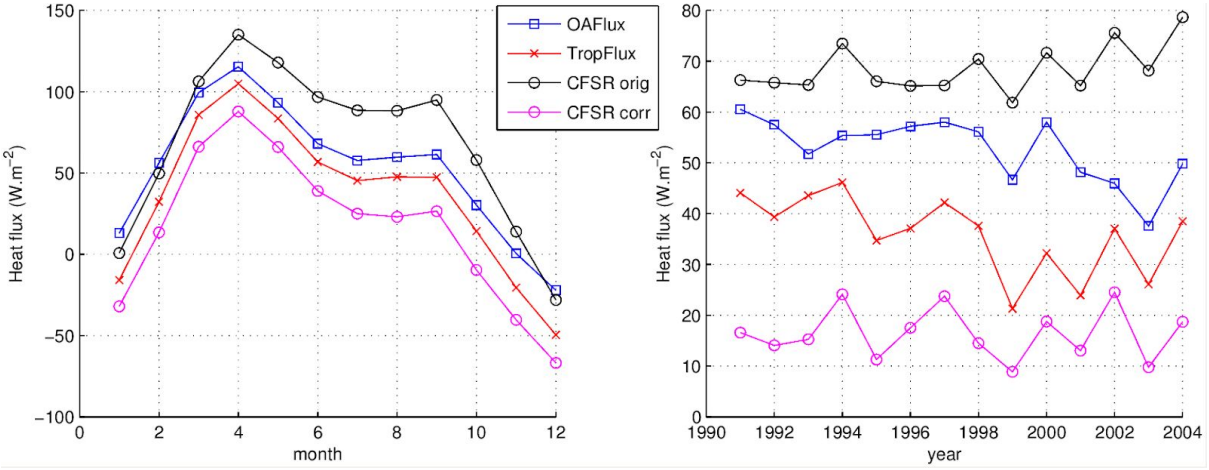

Figure 2.4 Comparison of SCS average of original and corrected CFSR net heat flux with Tropflux and OAflux

At the open lateral boundaries, monthly temperature, salinity, velocity and sea surface elevation fields are prescribed using the 1/4° horizontal resolution and 46 levels ORCA025-G70 reanalysis from the DRAKKAR project (Molines et al., 2007). The reanalysis dataset was conducted using NEMO modeling system and atmospheric forcings from ERA40 and ECMWF for the period 1958-2001 and 2002-2004 respectively.

The main rivers of our domain are the Mekong, the Red river and the Pearl river whose positions are shown in Figure 1.16. Due to the scarcity of data it was not possible to prescribe inter-annually varying monthly river discharge. We therefore prescribed monthly climatological freshwater discharges to the model (see Figure 1.10), computed by compiling available data from Pardé (1938) for the Red river, from the Mekong River Commission (2010) for the Mekong river and from Fekete et al., (2002) for the Pearl river. On the first try, the volume fluxes of the rivers were prescribed at their river mouths. However, we encountered reproducibility problems with this method i.e. two identical run (same compiled file, same forcings, same

settings, same computing system) created different outputs. We identified part of the code problem, but were not able to completely solve the problem (we communicated this problem to the ROMS_AGRIF developers). We then changed our method and adopted a widely used method to account for equivalent fresh water of the rivers by applying an additional flux to the atmospheric water flux E-P (E-P-R, evaporation minus precipitation minus runoff). These equivalent water fluxes are applied over 27, 8 and 15 water cells in the computing domain around the river mouths of the Mekong, Red and Pearl rivers respectively. The varying number of cells is chosen empirically to ensure a yearly average rate R in all river mouths that is equivalent to a heavy rain day over these areas (~56 $cm.day^{-1}$).

2.3 Reference and Sensitivity Simulations

To characterize the interannual variability of the SVU, we performed a reference simulation over the period 01/01/1990 - 31/12/2004, named CTRL. In this simulation, the daily atmospheric forcing and monthly lateral oceanic forcing vary interannually. In order to examine the respective contributions of the different factors of interest, we also performed a group of sensitivity simulations to modify the presence of river runoff, the interannual variability of the atmospheric forcing, and the interannual variability of the lateral oceanic boundary fluxes. We also remove all interannual variability in both the ocean and atmospheric forcing to estimate the effect of the OIV on the SVU. These different simulations are as follows :

- SimR : same forcing as in CTRL but with no river forcing.
- SimA : same forcing as in CTRL but with the removal of the interannual variability of atmospheric forcing. Instead we compute the average climatological year of daily atmospheric forcing over the period 1990-2004, which is then applied to each year of the 1990-2004 simulation.
- SimO : same forcing as in CTRL but with the removal of the interannual variability of lateral oceanic forcing. Instead, we compute an average climatological year of monthly oceanic forcing over the period 1990-2004.
- SimI (=SimA+SimO): All forcings including daily atmospheric forcing, monthly lateral oceanic forcing and monthly river forcing are climatological. SimI produces 15 years with the same external (atmospheric, oceanic and river) forcing but different initial conditions on each January 1st due to the OIV of the ocean.

Impacts of tidal forcing will be described separately in chapter 5. Our simulations quickly reach an equilibrium in terms of kinetic energy in less than 1 year, we therefore perform our analyses over the period 1991-2004.

In Chapters 3 and 4 of this document, we will present evaluations of the model and study the SVU interannual variability using the simulations presented here. In Chapter 5, we will introduce the tidal forcing, and an additional set of sensitivity simulations to test the robustness of the model configuration used in the results and conclusions presented in Chapters 3 and 4, in particular to the use of surface relaxation.

2.4 In-situ and satellite observation datasets

We use various in-situ and satellite datasets to evaluate the performance of the ROMS hydrodynamical model.

For the SST evaluation, we use 4 km resolution daily data from the AVHRR Pathfinder Version 5.2 (Casey et al., 2010) available for the period 1981 - 2012 from http://www.nodc.noaa.gov. The spatial and temporal coverages of AVHRR are hindered by the frequency of measurements and cloud cover. Its quality is indicated by a flag in the data recorder whose values range from 1 to 7 (larger means higher quality). We discarded all of the data which have quality flag less than 4, resulting in 10-15% data coverage over the SVU region in summer and winter (see Figure 2.1).

For validation of the model's vertical structure of temperature and salinity as well as sea surface salinity (SSS), we use the recently published SCSPOD14 gridded dataset (Zeng et al., 2016) available at ¼° resolution with 12 climatological months. It combines the World Ocean Database (WOD13), Argo floats data and in-situ measurements from Chinese research institutes from 1919 to 2014. It covers the whole SCS (Figure 2.5), however the data are unevenly distributed : in the northeast SCS, near Luzon strait, Taiwan and Southern China coast, data are about 10-times denser than in the southwestern and southeastern SCS.

Due to their limited temporal and spatial coverages, in the following we use the satellite AVHRR SST and gridded in-situ SCSPOD14 data only for comparisons of spatial distributions of monthly climatological SST and SSS or of spatial monthly and yearly averages over the whole SCS.

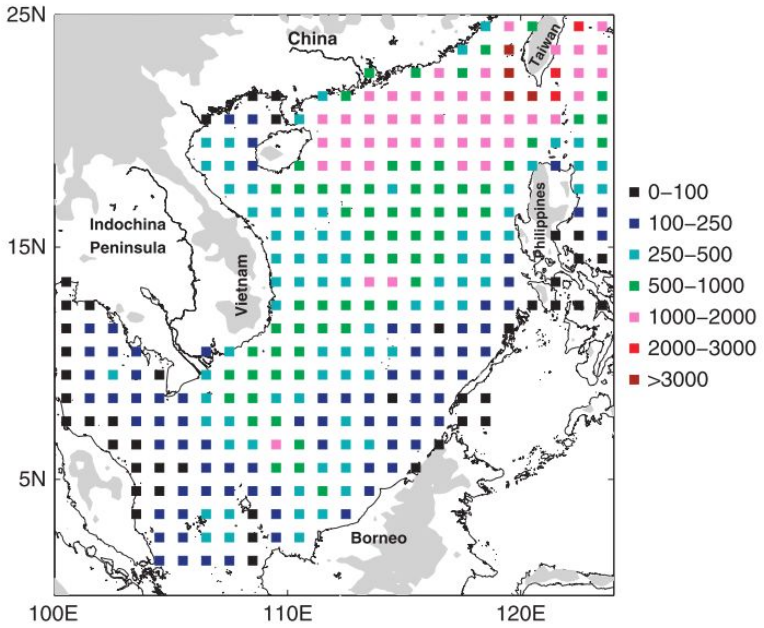

Figure 2.5 Geographical distribution of number of stations within 1x1 degree bin used for gridded SCSPOD14 dataset (after Zeng et al., 2016).

To evaluate the modeled sea level anomaly (SLA) and associated surface geostrophic currents, we use gridded altimetric absolute dynamic topography data over the period 1993-2004 (from SEALEVEL GLO PHY L4 REP OBSERVATIONS 008 047 Global Ocean Gridded L4 Sea-Surface Heights and Derived Variables Reprocessed Product of the CMEMS, available on http://marine.copernicus.eu/). This is a global product with ¼° resolution at weekly time scales. The mean dynamic topography is computed by taking the average of the absolute dynamic topography for the period 1993-2004. SLA is then derived by subtracting the mean dynamic topography from the absolute dynamic topography, over the same time period as our model.

Along the Vietnamese coast, there are 4 tide gauges providing good temporal coverage of sea level over the period 1991 to 2004: HonDau, ConCo, ConDao, ThoChu whose positions are indicated in Figure 1.16. The data are provided by the Vietnam National Centre for Hydro-Meteorological Forecasting at hourly time scales, and are available since 1991 for HonDau and ConCo, 1993 for ConDao and 1995 for ThoChu. Since tides are not included in these first simulations, the tidal and high-frequency signals in the tide gauges are removed by performing a monthly average of the data. The model's sea level variations are analysed on monthly averages.

Results presented in Chapters 3 to 5 of this manuscript constitute the core of the paper submitted to JGR-Oceans in December 2017 (ND. Da, M. Herrmann, R. Morrow, F. Niño, NM. Huan, and NQ. Trinh. *Contributions of Wind, Eddies, Chaotic Variability and ENSO to the Interannual Variability of the South Vietnam Upwelling*).

Chapter 3. Evaluation of model results

In this section we evaluate the realism of our reference simulation CTRL in its representation of the oceanic circulation and water masses in the SCS and SVU regions and of their interannual variability by comparing it with the available satellite SST and SLA data and in-situ salinity, temperature and tide gauge data presented in 2.3. If the modeled and observational data have different spatial/temporal resolution, the finer one will be resampled to the same resolution as the coarser one before making comparisons.

3.1 Seasonal spatial patterns of surface circulation and water masses properties

3.1.1 Sea Level Anomaly (SLA), surface geostrophic circulation and eddy kinetic energy (EKE).

Model outputs and altimetry data are compared over their common period, i.e. 1993-2004. In this section, SLA is therefore calculated both from the model and the data from the SSH fields by removing at each point the mean SSH over the period 1993 - 2004:

$$SLA\,(i,j,t) \;=\; SSH\;(i,j,t) - \overline{SSH}(i,j,\overline{1993-2004}) \qquad (3.1)$$

We start by analysing the realism of the CTRL seasonal SLA fields. Figure 3.1 shows maps of the CTRL and altimetric (ALTI) seasonal mean SLA, together with the seasonal surface geostrophic currents deduced from the SLA fields, in summer (June to August, JJA) and winter (December to February, DJF), averaged over the period 1993 – 2004. CTRL reproduces realistically the spatial and temporal variability of SLA. In winter, under the NE (northeast) monsoon, the general circulation in the SCS is cyclonic (Figure 3.1a,b), corresponding to previous results that showed that this cyclonic circulation was associated with cold and salty surface water brought into the SCS from East China Sea via Taiwan strait and from the Pacific Ocean via Luzon strait (Hu et al., 2000). Both CTRL and ALTI show high SLA in the western shallow area and low SLA in the deeper eastern part of SCS due to this cyclonic general circulation and dense water inflow. There are two noticeable cyclonic eddies in winter: one is northwest of Luzon and the other southeast of

Vietnam. CTRL reproduces realistically these circulation patterns observed in altimetry data. The quantile QQ-plot and the scatter plot of CTRL vs. ALTI (Figure 3.1c) confirm that the SLA spatial distribution in winter is realistically represented in CTRL. The spatial correlation between CTRL and altimetric SLA is 0.95 (p-value p<0.01) over the SCS (defined as the region between 99 - 121°E and 0 - 25°N, the red rectangle in Figure 1.16) and 0.86 (p<0.01) over the SVU domain (defined above as the region between 9°N - 15°N and 108°E - 116°E, the black rectangle in Figure 1.16), with absolute values in very good agreement.

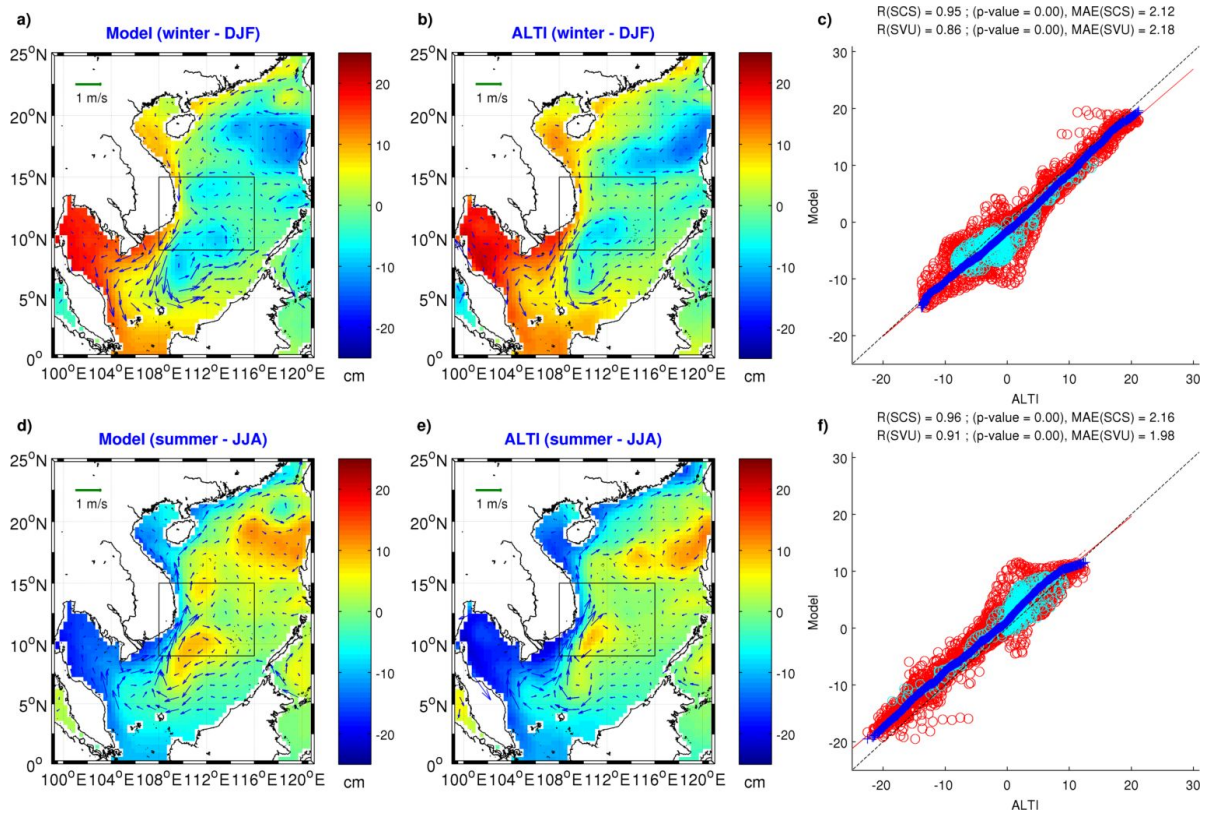

Figure 3.1. Evaluation of CTRL seasonal maps of SLA. Climatological comparisons of sea level anomaly (SLA, cm) between CTRL and CMEMS altimetry data (ALTI) in winter and summer. The arrows represent surface geostrophic currents derived from the SLA fields. Corresponding scatter plots for winter (c) and summer (f) over the whole SCS and over SVU (black rectangle on the maps) are shown in red and cyan circles respectively, and the blue cross points shows the QQplot over the whole SCS.

During the summer upwelling season, the spatial distribution of SLA is also realistically represented in CTRL (Figure 3.1d,e,f), and the spatial correlation between CTRL and ALTI is also high, 0.96 (p<0.01) over the SCS and 0.91 (p<0.01) over the SVU. Compared to winter, SLA changes completely from east to west, and the data show a reversal of the general circulation from cyclonic in winter to anticyclonic in summer, which is well reproduced by the model. These circulation patterns are associated with the summer SW monsoon (Hu et al., 2000; Fang et al., 2012). The two eddies mentioned in winter also exist at the same places in summer with a reversed direction from cyclonic to anti-cyclonic, both in CTRL and in ALTI. At

a smaller scale, in the SVU region, CTRL shows the presence of two anticyclonic eddies (centered at 9°N and 15°N) sandwiching a cyclonic one in the middle (centered at 12.5°N). The geostrophic currents (arrows) highlight the western boundary current that flows northward from the Gulf of Thailand and turns offshore at about 11.5^{O}N, forming the eastward jet that was reported in the literature from former observations and modeling studies (see section 1.2.2). It then splits into two parts: the first part follows the anticyclonic eddy turning southward; the second part turns back onshore at about 12.5^{O}N and continue to flow northward towards the southern China coast and up to Taiwan strait. Although these smaller scale spatial patterns appear in ALTI, they are weaker than in CTRL, and the ALTI summer mean fields show a weaker meandering of the boundary current in the SVU. This could be due to the lower resolution of the altimetry data due to the wide intertrack distance, which does not reproduce completely these small scale structures in the coastal zone.

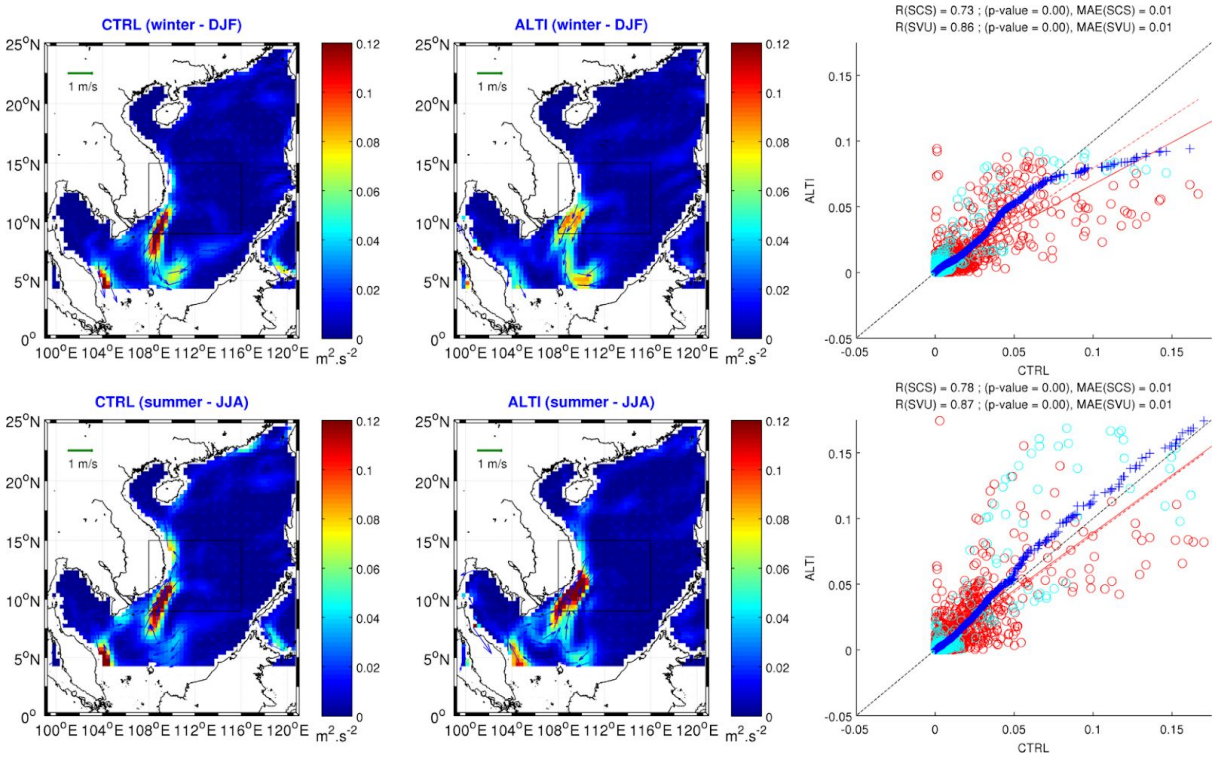

Figure 3.2. Eddy kinetic energy derived from geostrophic currents in Figure 3.1

Figure 3.2 shows the comparison of eddy kinetic energy (EKE) between CTRL and ALTI derived from the geostrophic currents in Figure 3.1 using the following formula:

$$EKE = \frac{1}{2}(U_g^2 + V_g^2) \quad (3.2)$$

where U_g and V_g are zonal and meridional component of geostrophic current respectively. EKE maps represent the energy level and location of permanent mesoscale structures because they are computed from sea level anomaly (see Eq. 3.1) which excludes the temporal mean circulations. The mesoscale structures

southeast of Vietnam stand out from the EKE maps in both summer and winter and of CTRL and ALTI in Figure 3.2. The magnitude of these features in ALTI is slightly weaker than in CTRL in winter, yet similar with CTRL in summer. The distribution of EKE over the SCS in CTRL is highly correlated with ALTI EKE with correlations of 0.73 and 0.78 in winter and summer respectively.

3.1.2 Sea Surface Temperature (SST)

SST is a key parameter for detecting the SVU, it is therefore important that our modelled SST fields are realistic. Figure 3.3 shows the seasonally averaged maps of SST in winter (DJF) and summer (JJA) over the SCS and over 1991-2004, obtained from CTRL and from satellite SST AVHRR observations. Compared to AVHRR, the spatial distribution of SST in summer and winter is well reproduced in CTRL. In winter, as discussed in 3.1.1, the NE cold monsoon sets up the cyclonic SCS circulation, bringing cold surface waters into the SCS from the East China Sea. This strongly affects the SCS SST causing a clear NE-SW gradient (Figure 3.3a,b) : SST varies from 20°C along the southern Chinese coast to about 28°C in the Thailand Gulf and Borneo shelf. These spatial patterns are well reproduced in CTRL, the distribution of spatial SST in CTRL is in good agreement with data (Figure 3.3c), and the overall spatial correlation in winter is very high, respectively 0.98 and 0.97 ($p<0.01$) over the SCS and SVU regions respectively. Absolute SST values are also in very good agreement, and the mean absolute error (MAE) between CTRL and the AVHRR data in the SVU domain is about one third of that over the SCS (0.14°C vs. 0.37°C, Figure 3.3c).

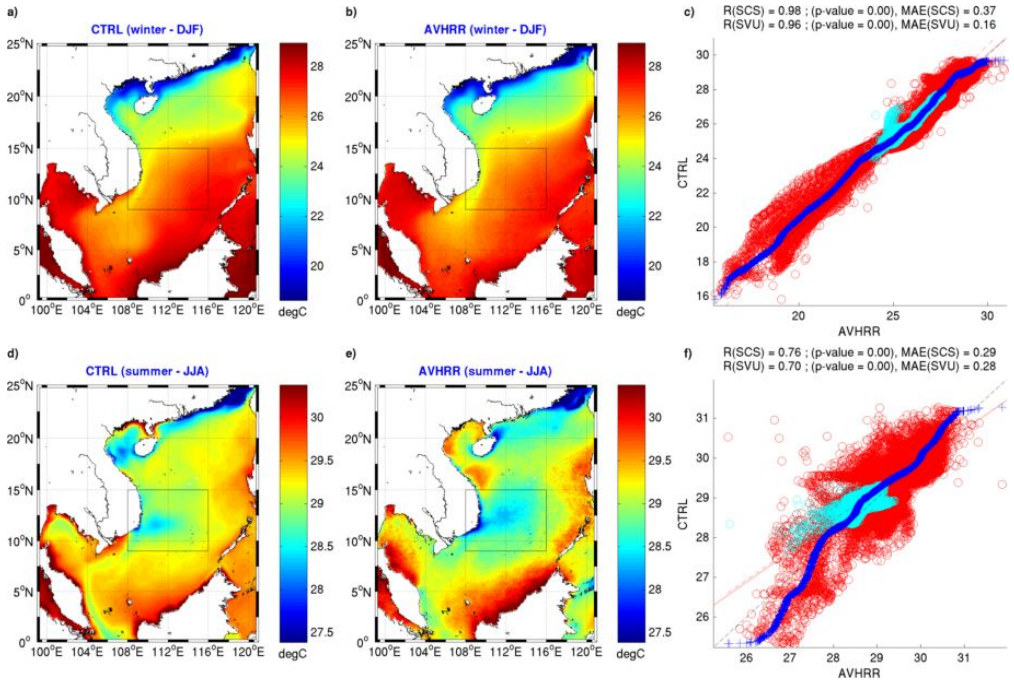

Figure 3.3. Similar to Figure 3.1 but for climatological SST (°C) comparison between CTRL and AVHRR.

In summer, the SST is much more homogeneous and a warm SST of about 27–30°C covers most of the SCS (Figure 3.3d,e). One of the major features of SCS SST in summer is the minimum SST zone (SST < 28.5°C) near Southern Central Vietnamese coast which is associated with the SVU. Observations also show a small cold water area near Taiwan strait, and a warm water band along the Phillipines, Borneo and Thailand coast. Those observed spatial patterns in summer are well reproduced in CTRL. The spatial correlations over the SCS and SVU in summer (0.76 and 0.70 respectively, Figure 3.3f) are lower than those in winter, but remain highly significant ($p<0.01$), and the MAE in summer is still quite small: 0.29°C over the SCS and 0.28°C over the SVU. Those weaker correlations in summer than in winter can be explained by the much smaller range of SST spatial variability, and also by the lower temporal coverage of AVHRR SST data in summer due to cloud (Figure 2.1b).

3.1.3 Sea Surface Salinity (SSS)

Figure 3.4 shows the mean seasonally averaged SSS comparison between CTRL and SCSPOD14 in-situ data. As explained in section 2.2, the coverage of SCSPOD14 data in the southwest (Thailand Gulf) and southeast parts of the SCS is sparser than in the Northern part of the SCS. The comparison between model results and those data should therefore be considered with caution in those regions. In winter, CTRL reproduces correctly the observed spatial variability of SSS over the whole SCS and the SVU (Figure 3.4a,b,c), with respective highly significant correlation values of 0.89 and 0.71 ($p<0.01$), and the MAE of SSS is about 0.2 psu in both SCS and SVU region. CTRL reproduces well the negative north-south gradient of SSS which is linked to the distribution of SST and associated with the cold and high salinity currents entering through Taiwan and Luzon straits. The western boundary current conveys this cold and salty water southward reaching Kalimantan strait. The low salinity area over the Thailand Gulf and along the coast in the Tonkin Gulf are also well-reproduced in CTRL.

In summer, the SW monsoon is associated with heavy rain and the reversal of the surface circulation weakens the intrusion of high salinity water from the East China Sea and the Pacific Ocean (Figure 3.4 d,e). SSS decreases by ~0.5 psu over the whole SCS in the SCSPOD14 data and by about 0.2 psu in CTRL. CTRL reproduces well the SSS over the whole SCS except in the Pearl river mouth and in the Gulf of Thailand. For the Pearl river, where the observation coverage is good, the E-P-R parameterization and the fact that we do not include tides in our model may

lead to an underestimation of the horizontal advection and mixing of the river plumes. This, together with the semi-enclosed shape of Pearl river mouth (Figure 3.5), explains that the propagation of freshwater outside this mouth is underestimated in the model. Note however that the Pearl river mouth is located far from our SVU area of study and may have a very limited impact on the SVU. Over the Gulf of Thailand the SSS underestimation in CTRL may result jointly from the atmospheric forcing (underestimation of the E-P water flux term), lack of tidal mixing or lack of observation (see Figure 2.5). The spatial distribution of summer SSS is very good with correlation values of 0.73 and 0.87 ($p<0.01$) over respectively the SCS and SVU domain, and MAE of respectively 0.25 and 0.12 psu (Figure 3.4f).

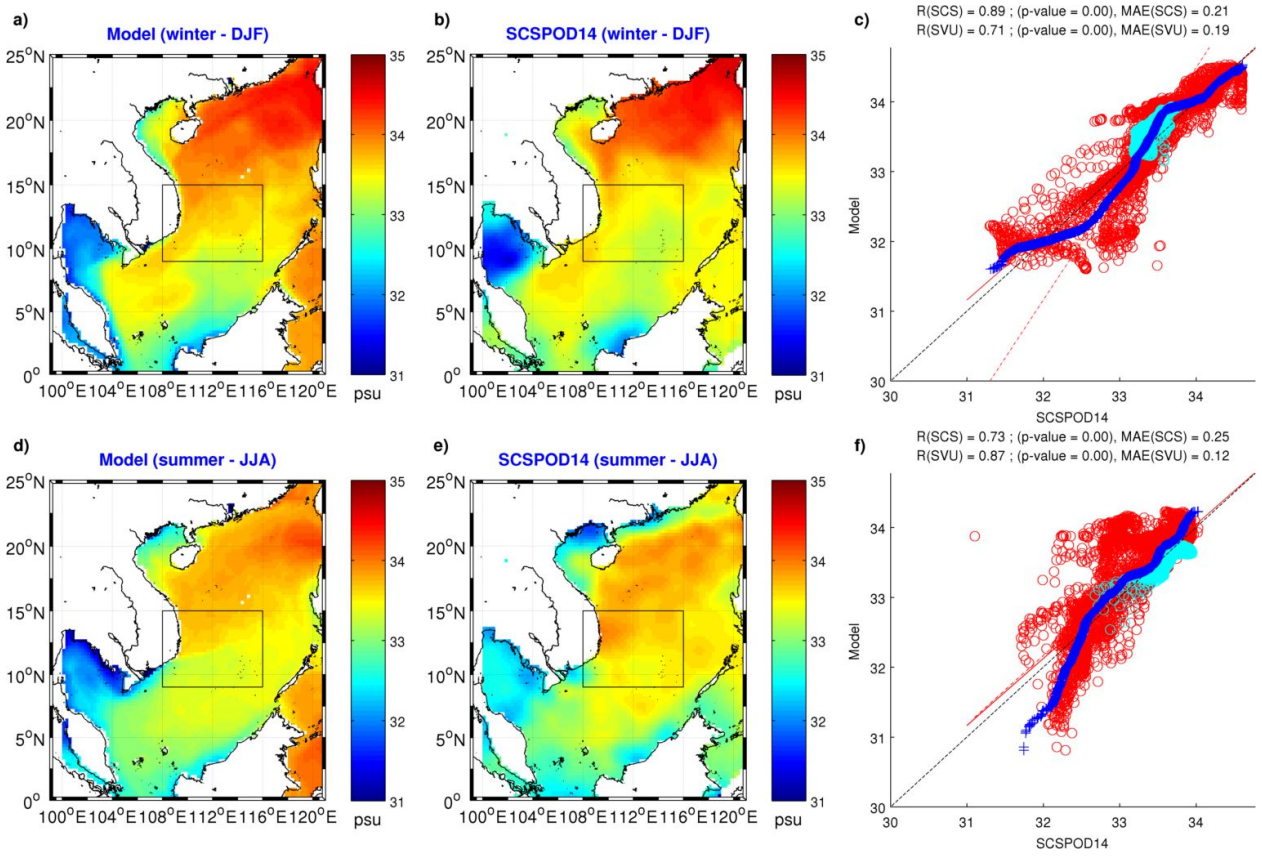

Figure 3.4. Similar to Figure 3.1 but for climatological SSS between comparison CTRL and SCSPOD14.

These results, assessing the ability of our model to reproduce the mean seasonally-averaged climatological fields for SLA, SST and SSS, show that the CTRL simulation is able to reproduce realistically the spatial structures of the surface circulation and hydrological characteristics of the SCS and SVU domain. We will now evaluate how well it can reproduce the seasonal and interannual variations of these parameters.

Figure 3.5 A zoom in of Pearl river mouth (Source: Google Map)

3.2 Seasonal and interannual variations of surface circulation and water masses properties

Figure 3.6 presents the climatological monthly and interannual variation of summer (JJA) mean time series of SST, SSS and SLA averaged over the SCS, obtained from the reference simulation CTRL and from the observations detailed above (AVHRR for SST, SCSPOD14 for SSS and CMEMS for the altimetric SLA). We take summer mean for the interannual signal because we want to focus on evaluating the performance of CTRL in upwelling season. For reference, the climatological and interannual time series of the larger-scale ORCA fields, used to prescribe the open ocean lateral boundary conditions to our model, are also presented over our domain.

The annual cycle of SST is very well reproduced, with a high correlation of 0.98 ($p<0.01$) between CTRL and AVHRR (Figure 3.6a). The model SST follows closely the observed AVHRR values from March to June, and the model has a small warm bias from July to February of about 0.2°C. Figure 3.6a shows a large positive bias of about 1°C of ORCA compared to AVHRR, and a smaller bias of 0.8°C from February to May. This suggests that the bias correction we performed on the CFSR heat flux (see section 2.2) participates in reducing the SST bias that exists in the initial and lateral boundary conditions.

At interannual time scales, CTRL and AVHRR spatial averaged SST are also very well correlated, with a Spearman correlation of 0.62 ($p<0.05$), slightly weaker better than the 0.66 ($p=0.01$) value obtained for ORCA (Figure 3.6b). CTRL follows closely AVHRR from 1992 to 1998, then start to differ from it by ~ 0.5°C from 1999 to 2004. This results in a positive trend in the CTRL SST (0.02°C.year^{-1}) compared to the AVHRR SST (0.00°C.year^{-1}) over the period 1991 – 2004. ORCA on the other hand has a negative trend of 0.01°C.year^{-1}, suggesting that the positive trend in CTRL may be due to atmospheric forcing rather than to lateral boundary conditions. Wang et al., (2006a) showed for the 1945-2002 period that summer SCS SST peaks occurred after El-Niño years, in particular for the strong 1997-1998 El-Niño event. The impact of this event on the following 1998 summer is very clear in the data, CTRL and ORCA, with a strong 0.8°C positive anomaly in 1998.

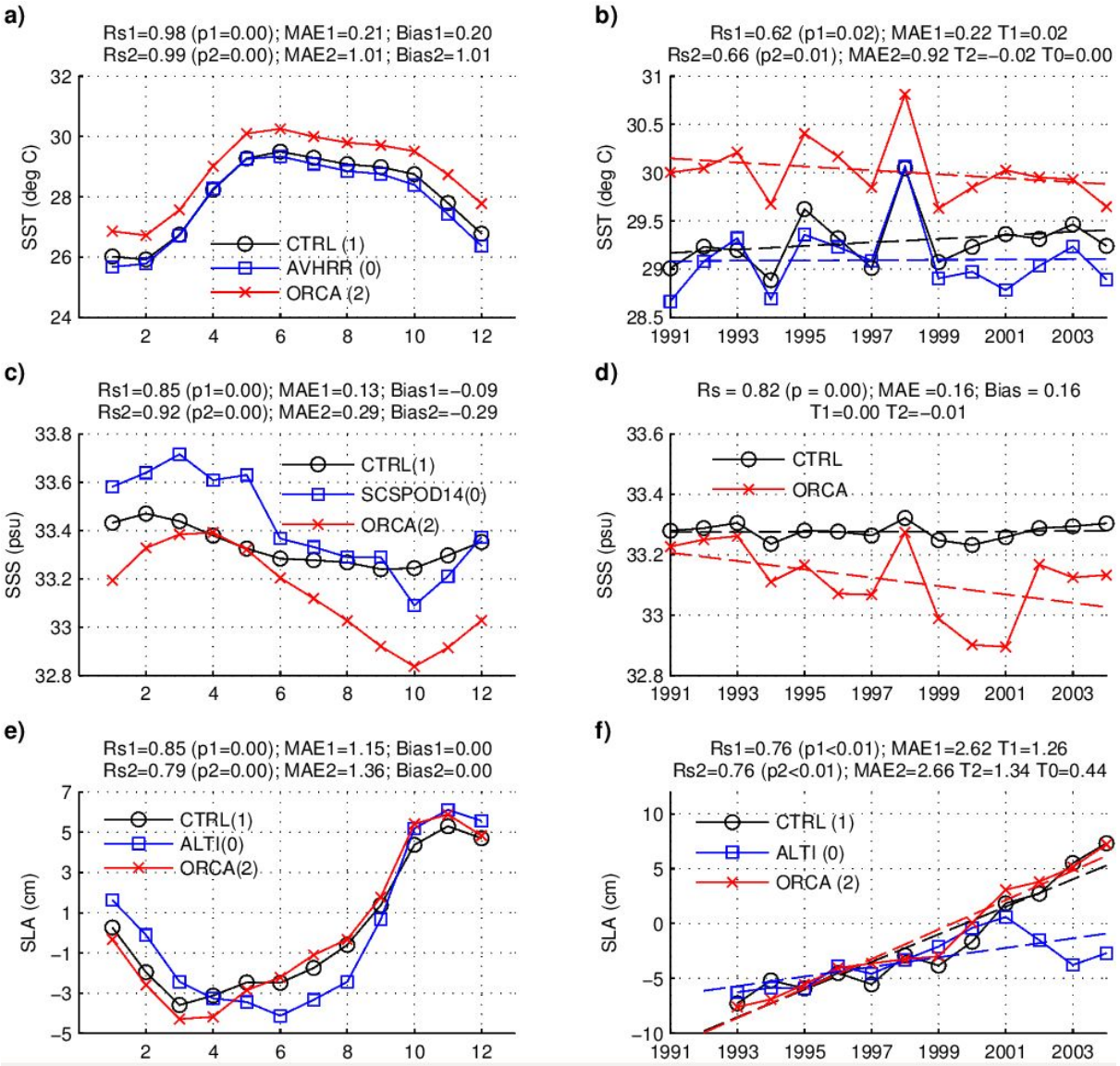

Figure 3.6: Evaluations of annual and interannual signals of CTRL SST, SSS and SLA. Climatological monthly (left) and interannual summer mean (JJA, right) time series of SST, SSS and SLA for CTRL (black), ORCA (red), and observations (blue), averaged over the whole SCS. Rs stands for Spearman correlation coefficient, M stand for mean value and T stands for trend. 0 stands for observations, which are taken as reference when calculating MAE, bias, or correlation (except in d where we don't use SCSPOD14 data for interannual variability because of the insufficient temporal coverage, as explained in 2.3). 1 stands for CTRL and 2 for ORCA.

For SSS, the climatological monthly variation of SSS in CTRL is in phase with the SCSPOD14 SSS data, with a correlation of 0.85 ($p<0.01$) but with smaller amplitude (about 0.25 psu in CTRL vs. 0.50 psu in SCSPOD14, Figure 3.6c). The overall MAE is 0.13 psu and CTRL has a negative bias of -0.09 psu. SSS is maximum in spring and minimum in fall. SSS is very similar in CTRL and SCSPOD14 from June to September. ORCA reproduces slightly better the phase of the SSS data with a higher correlation of 0.92 ($p<0.01$), yet it has a stronger negative -0.29 psu bias. At interannual time scales, the comparison with SCSPOD14 data is

not possible due to the low temporal coverage of those data. Instead, a comparison between the CTRL and ORCA simulations is shown in Figure 3.6d. They are quite in phase with a correlation of 0.82 ($p<0.01$), but ORCA varies with a much stronger amplitude (~ 0.4 psu vs. 0.1 psu in CTRL). This difference could be due to several reasons, including the different model configurations (resolution, domain, mixing and advection scheme, …) and different atmospheric forcing (ORCA used ERA-40 and CTRL used NCEP CFSR).

CTRL reproduces well the climatological annual variation of SLA with a correlation of 0.85 ($p<0.01$) (Figure 3.6e). The model and data winter SLA fit very well from October to March, although the model shows a positive bias of about 3 cm from May to August. This positive model bias was also clear in the summer spatial structure (Figure 3.1 d,e,f). ORCA shows a similar behavior as CTRL yet its correlation with ALTI is slightly smaller (0.79, $p<0.01$). This suggests that the lateral boundary conditions partly explain the difference between CTRL and ALTI behaviors. At interannual time scales, CTRL and ORCA spatially averaged SLA both show significant correlations with ALTI of 0.76 ($p<0.01$), and agree particularly well over the period 1993 – 2001 (Figure 3.6f). However, both models diverge very similarly from 2002 to 2004, leading to a strong trend of sea level of 1.26 and 1.34 $cm.year^{-1}$ in CTRL and ORCA respectively, compared to 0.44 $cm.year^{-1}$ in ALTI : this suggests that the drift observed in ORCA lateral boundary conditions over the 2002-2004 period induces a similar drift in our CTRL simulation, and confirms our hypothesis above that biases in the the lateral boundary conditions SLA are transmitted to our simulations.

Evaluation of the temporal climatological monthly and interannual yearly evolution of SST highlight the very good behaviour of CTRL in terms of the SST representation, which will be our main criteria for developing the upwelling index in section 4.1 (see below). The good comparison with the monthly mean climatological in-situ SSS data shows that CTRL reproduces realistically the seasonal and spatial variability of SSS over the SCS and SVU region, at least at the climatological scale since the data coverage does not allow evaluating the interannual variability. The SLA evaluation shows a very good winter cycle and a positive bias in the summer upwelling season, and the interannual fields indicate a drift in the years from 2002 to 2004. Both biases seem to be associated with the lateral boundary conditions.

3.3 Temperature and salinity vertical structure

We evaluate in this section the ability of CTRL to reproduce the vertical structure of different water masses in the SCS by comparing the modeled temperature and salinity vertical structures with SCSPOD14 in-situ data and where possible with other observations.

Figure 3.7 shows the temperature and salinity profiles for the CTRL and ORCA simulations and the SCSPOD14 data averaged over boxes over three deep water stations P1, P2 and P3 shown in Figure 1.16. 1500m corresponds to the depth limit of SCSPOD14 data. We chose these points because they are representative of the different regions of the SCS (North, Center, South) and their temporal coverage was sufficient (Figure 2.5). Station P1 is in the northern SCS in the region of seasonally varying cyclonic and anticyclonic flows, with a strong input from the Luzon strait. P2 is in the offshore SVU region, and P3 is in the southern SCS, also in a region with the seasonally varying cyclonic and anticyclonic flow (see Figure 3.1).

CTRL temperature is very close to SCSPOD14 in the surface and intermediate layers (~0-700m) at the 3 sites, and over the winter and summer seasons, although a positive ~1°C bias appears from ~700m to ~1500 meter depth (Figure 3.7a-f). The seasonal difference (summer vs. winter) in the surface layer varies between 2.3°C at P2, 2.5°C at P3 and 5.0°C at P1, and is well reproduced in CTRL. ORCA, on the other hand, is warmer than SCSPOD14 in the surface and intermediate layers (with a 1.0 to 2.0°C positive bias) and shows a smaller (negative) bias of 0.5 to 1.0°C in the deeper layer in both summer and winter.

The station P1 and P2 are not so far from three buoy stations SCS1,2,3 which acquired data from 1997 to 2000 in the central SCS (Figure 1 & 4 of Chang et al., 2010). Data from this study infer that the climatological mean temperature at 200m and 500m depth at the three stations are between 14 - 15 ^{o}C and 8-8.5 ^{o}C respectively. Both CTRL and SCSPOD14 shows similar climatological mean temperature at 200 and 500m depth. ORCA also shows good agreement with buoy data at 200m yet a negative bias of 0.5 ^{o}C at 500m.

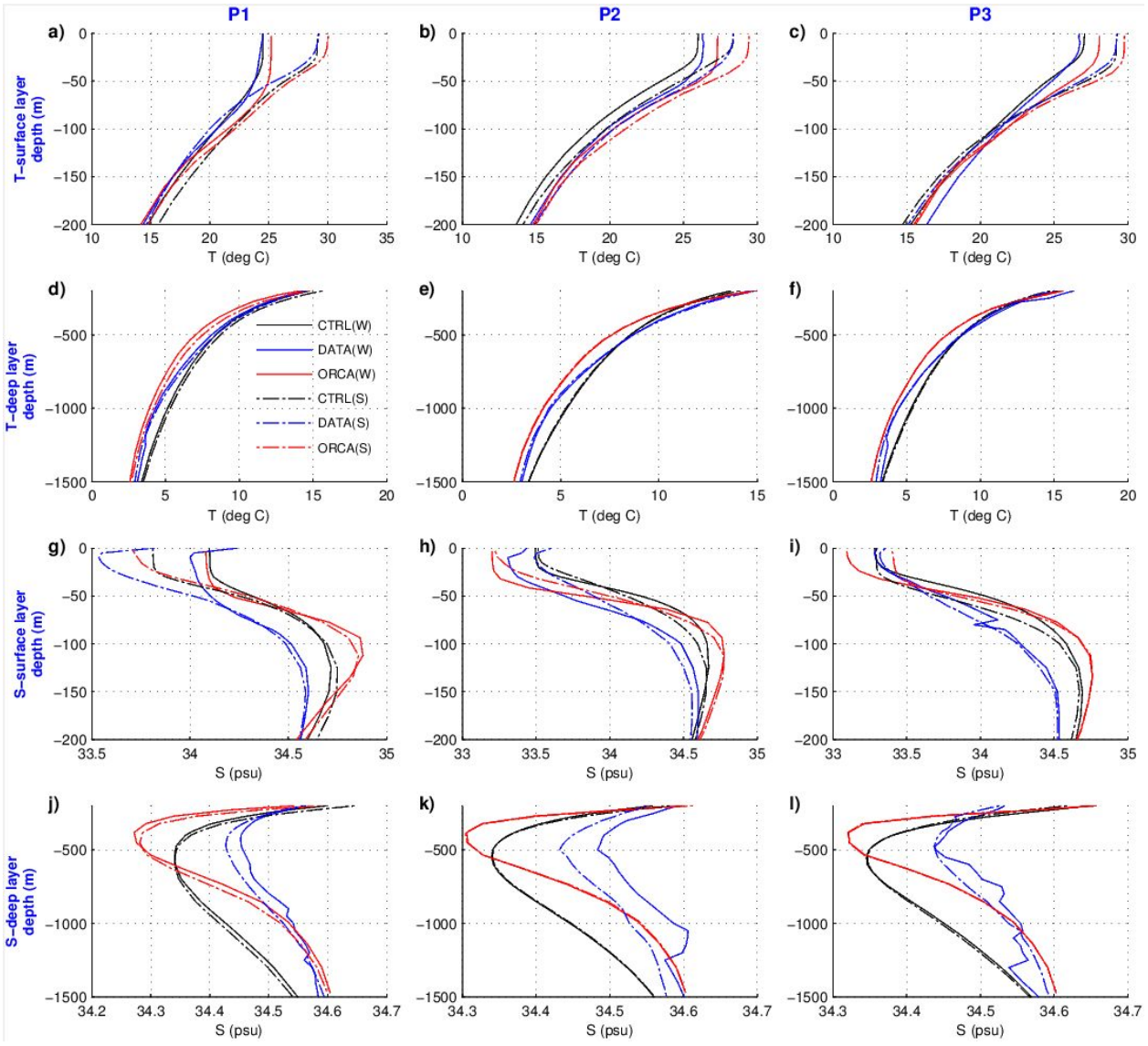

Figure 3.7: Evaluation of CTRL TS vertical structures. Comparisons of temperature (°C, a-f) and salinity (g-l) profiles over the surface (0-200m) and deep (200m - 1500m, corresponding to the depth limit of SCSPOD14 data) layers at 3 stations P1, P2 and P3 shown in Figure 1.16 between CTRL simulation (black lines), SCSPOD14 datasets (blue lines) and ORCA (red lines) in winter (W, December-February, solid lines) and in summer (S, June-August, dot-dashed lines).

The general salinity profile is correctly reproduced by CTRL with a sub-surface maximum and a deeper minimum (Figure 3.7,g-l), but salinity profiles show differences between CTRL and ORCA and SCSPOD14 in terms of values. In the surface layer, SCSPOD14 shows a maximum salinity at ~ 150m in both summer and winter in the three stations and a weak seasonal variation in salinity from the surface to ~ 60m at P1 and P2 (Figure 3.7 g,h,i). At P3, the seasonal variation of salinity is small from the surface to the bottom. The rapid changes of salinity within the upper 20 m at stations P1 and P2 are associated with unrealistic unstable density profiles. This is probably due to the lack of data or error introduced by interpolation in the gridded dataset. Compared to SCSPOD14, CTRL shows similar

maximum salinity at 150 m depth at stations P1 and P3 but a shallower maximum salinity in the SVU at P2 (100-120m). Seasonal variations in salinity in CTRL compared well to SCSPOD14 at P1 and have a similar variability but at shallower depth at P2 (0 - 70m). However, CTRL shows a positive ~0.2 psu salty bias at the three stations at the surface layer. In the deeper layers, CTRL shows at all stations a minimum salinity at ~ 500m depth similar to SCSPOD14 (Figure 3.7 j,k,l). In the deeper layer CTRL is fresher with a negative bias of ~-0.1 psu, which is half the magnitude of the salty bias in the surface layer. These salinity biases in CTRL may result from the ORCA fields are used to prescribe the initial and boundary conditions to our model. ORCA shows a similar depth of the maximum salinity at the three stations around 100-120m and has a slightly shallower minimum salinity at about 400m depth. However, ORCA has a much stronger (~0.4 psu) positive bias of salinity than CTRL at the depths 80-150m, and a stronger (~-1.8 psu) negative bias around its minimum salinity layer at 400 m depth, but is closer from SCSPOD14 for depths larger than ~700m. The difference of configuration between CTRL and ORCA, including the higher resolution in CTRL and difference of surface forcing, apparently contributes to partly correct the ORCA bias in the surface and intermediate layers, but the difference in terms of salinity in the deep layer could be due to the different configuration of ORCA and CTRL numerical models, including the vertical mixing schemes and parameterization.

Comparison of vertical profiles of water hydrological properties with in-situ observations available from the SCSPOD14 dataset therefore shows that CTRL provides a realistic representation of the upper and intermediate ocean spatial and temporal patterns of salinity and temperature.

3.4 Model SLA versus tide gauges SLA

The validation data set used in this section are the 4 tide gauges along the Vietnamese coast (see Figure 1.16), described in Section 2.4. SLA from CTRL and ORCA are interpolated onto the tide gauge positions. We first consider monthly averaged climatological values over the period 1991-2004 to examine the climatological yearly cycle (Figure 3.8, left panel). CTRL reproduces very well the yearly cycle of SLA and is very close to ORCA for the three stations that are in an open coast regime: Con Co, Con Dao and Tho Chu, with respective correlations of 0.97, 1.00 and 0.99 ($p<0.01$) and a MAE of about 2 cm (0.99, 1.00 and 0.97 ($p<0.01$) and MAE of about 2.5cm for ORCA). Hon Dau station is located near the coast in the Tonkin Gulf, a complicated area where the tidal signal is strong (and not included in our simulation), and CTRL shows a small non-significant correlation there (0.52, $p=0.08$). A comparison with ORCA at this station is not possible because it is located outside of the ORCA domain (due to ORCA's coarser resolution).

SLA is averaged over summer for the period 1991 - 2004 to obtain an interannual time series (Figure 3.8, right panel). The inter-annual signals are fairly well reproduced at the stations, and once again CTRL and ORCA are very similar. Positive trends of sea level anomaly exist in both CTRL, ORCA and data, as observed in Section 3.2. At the end of the period, a model drift similar to the one obtained when comparing CTRL and altimetry data is visible from 2002 – 2004. This leads to much stronger average trends at all stations in the CTRL (~1.22 cm.year^{-1}), and in ORCA (~1.27 cm.year^{-1}) simulations than in the data (~0.44 cm.year^{-1} for tide gauges and 0.44 cm.year^{-1} for ALTI). The similar trend of ALTI and tide gauges is an indicator of the good quality of these in-situ data. The stations also show good correlations between CTRL and the in-situ tide data : ConCo (0.81, $p<0.01$), ConDao (0.55, $p=0.05$), HonDau (0.81, $p<0.01$), except Tho Chu (0.55, $p=0.1$) with shorter period.

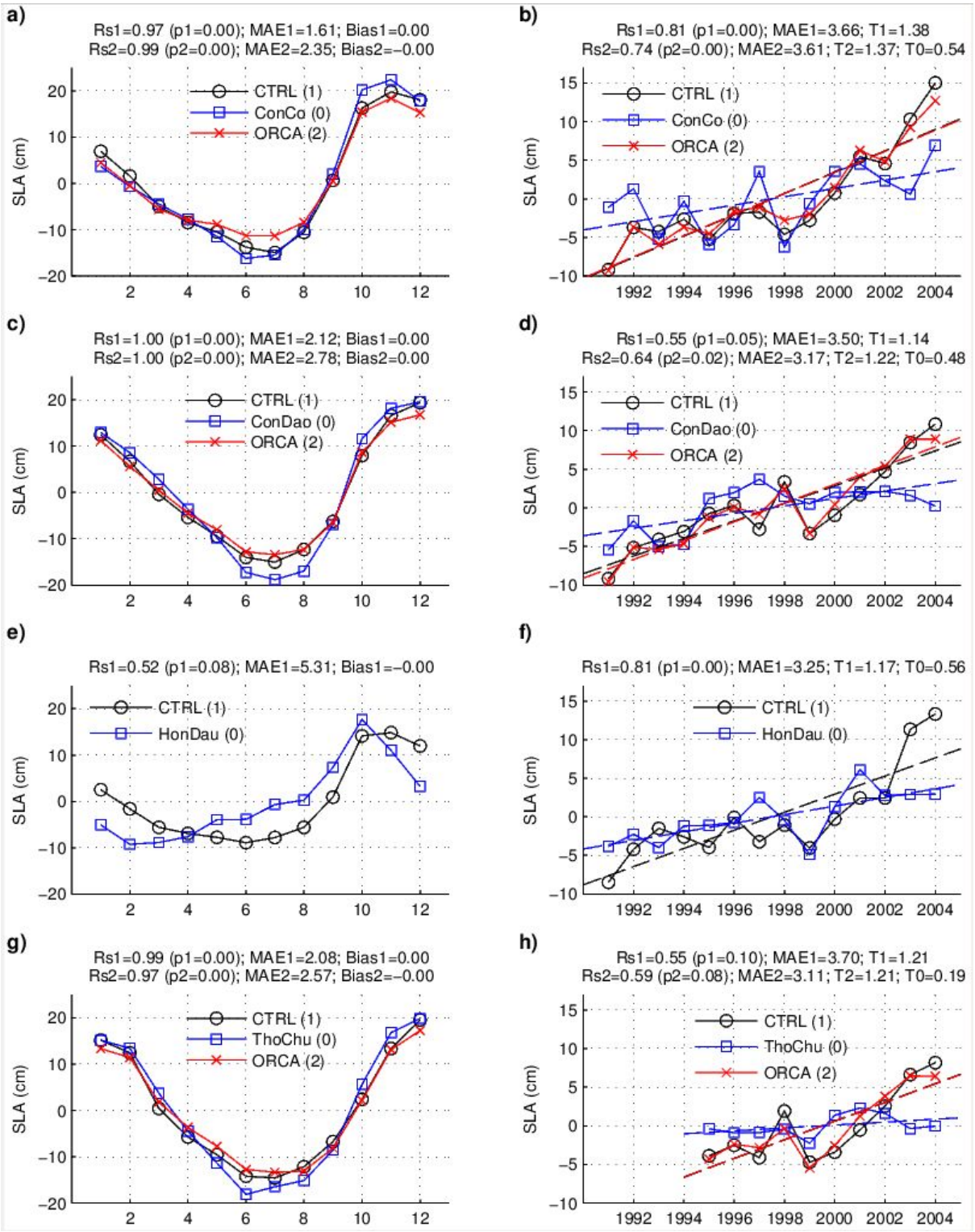

Figure 3.8. Similar to Figure 3.5e,f but for SLA (cm) computed from CTRL, ORCA and tide gauges. Comparison of ORCA at Hon Dau is not possible because this station is located outside of ORCA domain (due to coarser resolution in ORCA).

These comparisons with available temperature, salinity and sea surface level in-situ and satellite data show that our reference simulation CTRL is able to reproduces realistically the water masses characteristics (in particular in the ocean surface and intermediate layers) and surface oceanic circulation and their spatial patterns, yearly cycle and interannual variability in the SCS and in the SVU region.

The major weaknesses of the CTRL simulation are the deep layer salinity underestimation and the SLA drift for the period 2002 – 2004 which is induced by the ORCA lateral oceanic forcing. Vidal-Vijande et al. (2012) discovered that this SLA drift in ORCA025-G70 exists globally. CTRL performs overall better than ORCA, which can be partly explained by its higher spatial resolution in both the ocean model grid and the atmospheric forcing (0.5° in CFSR vs. 125 km~1.25° in ERA40). In the following, we therefore use the CTRL simulation to examine and characterize the interannual variability of the SVU. We then compare it with additional sensitivity simulations to understand in more detail which factors are responsible for the upwelling variability.

Chapter 4. Interannual variability of SVU and contribution of different factors

4.1. Upwelling index definition

Several methods have been developed to build upwelling indices (UI), using mainly surface wind (based on Ekman transport theory) or SST (see Benazzouz et al., 2014 for a review). The advantages of an SST-based UI are first that it provides information on the upwelling intensity, but also on the spatial scale, duration and location of upwelled water that reaches the surface and triggers primary production, and second that it can be applied on real SST data derived from satellite observations to monitor the SVU from observational data. Since our modelled SST was validated by comparison with satellite SST observations in Chapter 3, it is therefore relevant to build a SST-based UI to study the evolution of the upwelling events in this study.

For that, we first identify the SST threshold T_0 that is the most appropriate to detect the upwelling occurrences. Figure 4.1a-c shows maps of the frequency of daily occurrence of SST lower than a threshold of temperature T_0 from June to September (defined as the JJAS period) over the period from 1991 to 2004 for different values of T_0 (26°C, 27.5°C and 28.5°C). For waters cooler than T_0 = 28.5°C (Figure 4.1a), there are three centers of high frequency of occurrence located in the Northern SCS along the Chinese coast, off the Central Vietnamese coast and in the Gulf of Thailand. The second site corresponds to the SVU in which we are interested in this study. These three centers are linked together by coastal bands having a low frequency of occurrence (<20% vs. more than 50% in the centers), and that are certainly associated with horizontal advection of cold water between these 3 centers: waters advected from the Northern SCS may be included with local upwelled water in SVU region, depending on our choice of T_0. As T_0 decreases, the frequency of occurrence in the upwelling centers and in the transition areas is reduced (Figure 4.1b,c). A lower value criteria reveals the cooler upwelling cores, reduces the zones of advected waters between the centers, and excludes weak upwelling activities. Choosing our threshold criteria T_0, requires a tradeoff between a small frequency of occurrence in the transition zones and a high frequency in the upwelling centers. Using a threshold of T_0 = 27.5°C appears as the best trade-off, with a frequency of

occurrence higher than 25% in the upwelling centers and less than 3% in the surrounding areas (Figure 4.1b). The SVU domain defined above covers the whole domain of SVU activity based on this threshold of T_0 = 27.5°C (red rectangle on Figure 4.1b). A background reference temperature (T_{ref}) is calculated in JJAS over the whole period from 1991-2004, by taking the climatological mean of SST in the area outside the SVU domain, defined as the area with the same range of latitudes but with longitudes from 117°E to 118°E (the blue rectangle in Figure 4.1b).

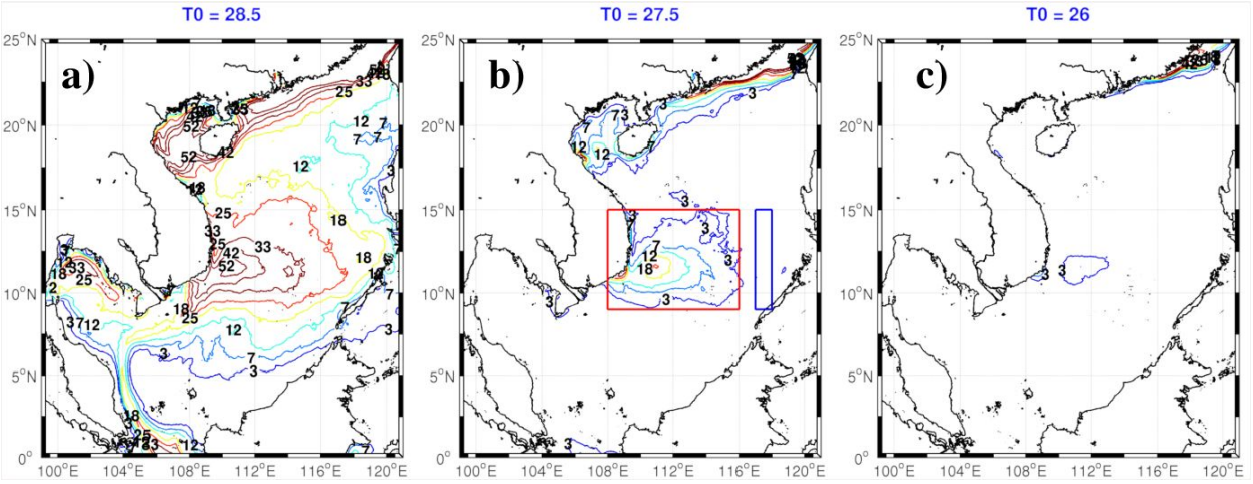

Figure 4.1. Maps of the SVU upwelling frequency with respect to different temperature thresholds T0. Frequency (%) of daily occurrence of SST < T_0 from June to September (JJAS) over the period 1991 – 2004 derived from CTRL simulation for different values of T_0. The red rectangle shows the SVU domain and covers most of upwelling activities. The blue rectangle is used to calculate reference temperature T_{ref} of the surrounding waters for the calculation of upwelling intensity.

Next, we characterize an upwelling event by two groups of indices. The first is the magnitude index group which includes the upwelling period, spatial scale, intensity and total strength. A second spatial index group consists of the upwelling centre's position (longitude and latitude of center) and spatial extent (meridional and zonal extent). Each of these yearly indices are defined as follows:

Upwelling Period index UIt: It is the annual cumulative period of upwelling based on the number of days that upwelling exists within our upwelling domain SVUD during JJAS each year. For a given day, upwelling exists if the criteria of SST < T_0 results in a non-zero area within the SVU domain.

Spatial scale index UIs: On a daily time scale, this is the total area within the SVU domain where SST < T_0. The annual spatial scale index is computed by taking the average of each daily spatial scale over the upwelling period only, i.e. over the days when upwelling exists inside the JJAS period.

Intensity index Uli: For a given point and day, intensity is defined as the temperature difference between the background temperature T_{ref} defined above and the SST at this point for values where T < To. On a daily time scale, the intensity is then defined as the maximum intensity in the SVU domain. The annual upwelling intensity is the mean of this maximum daily intensity over the upwelling period only.

Upwelling strength index Uly: it is computed from the cumulative daily intensity, i.e. the integration of the daily upwelling intensity in time and space over the upwelling period. It regroups the three previous indices:

$$UIy = \int_{June}^{September} \int_{SST(x,y,t) < T_o}^{x,y \in SVU\ domain} (Tref - SST(x,y,t))dt.dx.dy \qquad (4.1)$$

It can be computed similarly for a given point : Figure 4.2 shows the annual maps of the cumulative upwelling strength over JJAS for CTRL for the 1991-2004 period.

Upwelling location: On a daily time scale, it is the location (longitude and latitude) with the maximum intensity. On the annual scale, it is the position (longitude and latitude) of the strongest cumulative upwelling intensity (the position of the red cross in Figure 4.2).

Upwelling spatial extension: This index is a measure of how the upwelling activity is distributed spatially. The same upwelling strength may indeed be highly concentrated in a small area or spread out equally in the upwelling domain. The meridional and zonal extensions are therefore defined as the shortest distance around the upwelling annual center that covers 50% of the upwelling activities. It is shown on Figure 4.2 by the length of the red cross in the zonal/meridional directions.

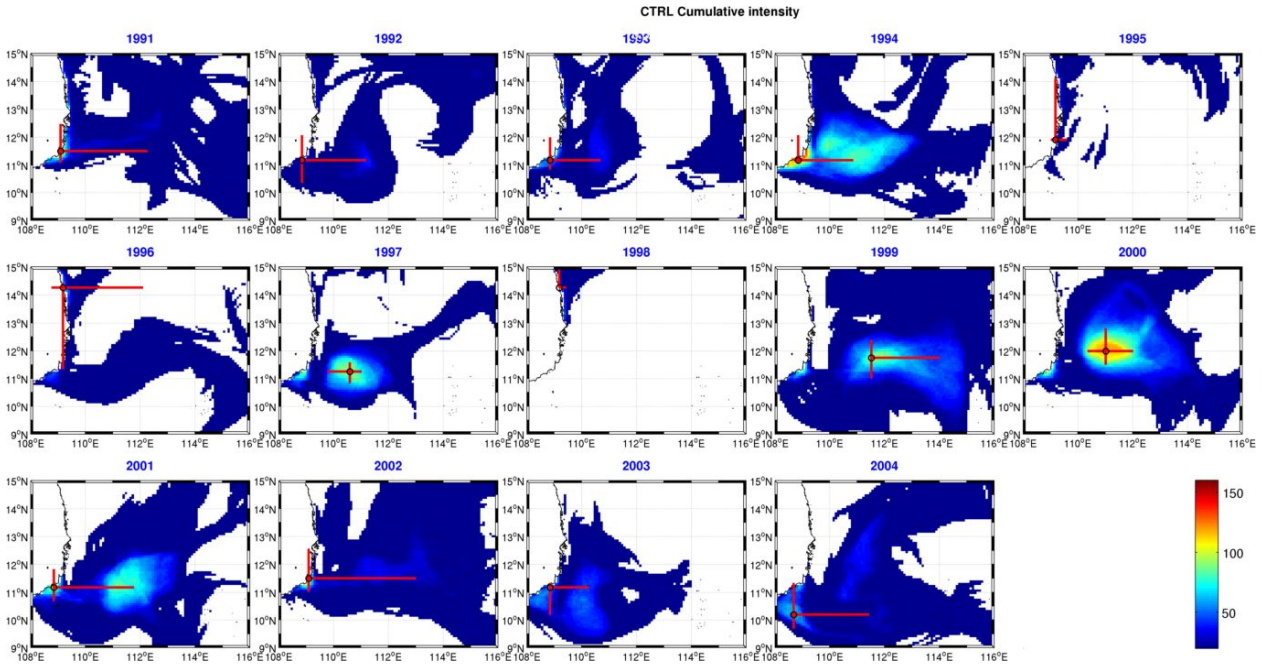

Figure 4.2. Summer (JJAS) cumulative upwelling intensity (ºC.day) in CTRL simulation. The cross positions represent upwelling centers, which corresponds to the point which shows the highest JJAS cumulative intensity. The length of the cross in meridional/zonal direction represents the range of latitude/longitude around the center that covers 50% of upwelling activity.

Figure 4.3 shows for all our simulations the interannual time series of the upwelling indices presented here : UIt, UIs, UIi, UIy, location (latitude and longitude) and spatial extension (meridional and zonal).

4.2 Interannual variability of the SVU

To study and characterize the interannual variability of the SVU, we first consider the year to year variations in the cumulative upwelling strength from CTRL (Figures 4.2, 4.3a). There is a large interannual variability in the geographical distribution of the cumulative upwelling intensity within the SVU domain (Figure 4.2). The red crosses show the central position of the maximum upwelling and its spatial extent in each year. The upwelling position varies strongly from year to year. In most years, there are two centers of upwelling corresponding to coastal upwelling centers located around 109°E and to offshore upwelling centers located around 111°E. These two upwelling centres are often connected by the advection of coastal upwelled waters offshore via the eastward jet, as shown in Figures 3.1d,e. This will be further discussed in the upwelling mechanisms in section 4.5. The coastal upwelling is generally stronger than the offshore upwelling, except for 1997, 1999 and 2000. Strongest upwelling occurs in 1994, 1997, 1999, 2000 and 2001 and are associated with strong offshore upwelling activity. Upwelling mainly occurs within the band 10.5°N to 12.5°N and 109°E to 113°E. The latitude band of the centers of strong upwelling occurs within 11-12°N, whereas the latitude band of the weaker years has a wider range, varying from about 10°N in 2004 to 14°N in 1996 or 1998 (Figure 4.3g,h). These findings are quite similar to the findings of Li et al., (2014) who showed that during the 1992-2012 period, a strong summer eastward jet and upwelling occur intensively at 12ºN whereas weaker events extended further north. On average, the mean zonal extent (2.3°) is larger than the mean meridional extent (1.5°) which is limited by the advection of cold water by the eastward jet.

Strong upwelling years have a high upwelling strength (or cumulative intensity) and are associated with strong intensity, spatial scale and long period (for example, in 1994, 1999, 2000, Figure 4.3). 1998 and 2000 are respectively the year of weakest and strongest SVU. Mean upwelling intensity varies from 2.5°C in 1998 to about 3.7°C in 2000 with a mean value of 3.1°C and a standard deviation of 0.4°C equal to 12% of the average. The upwelling spatial scale varies from ~2800 km^2 in 1998 to about 69000 km^2 (25 times larger) in 2000 with a mean of 38 302 km^2 and a standard deviation of 20 719 km^2. The shortest upwelling period is also in 1998 with only 60 days out of the 4 months of the June-September period. The upwelling period is longest in 1994 when upwelling existed throughout the 120-day June-September period. The mean upwelling period is 98 days, meaning that upwelling occurs over more than 3 months during the June-September period, with a

standard deviation of 16 days. Out of the three indices, the upwelling spatial scale has the strongest relative variability, as seen in Figure 4.2.

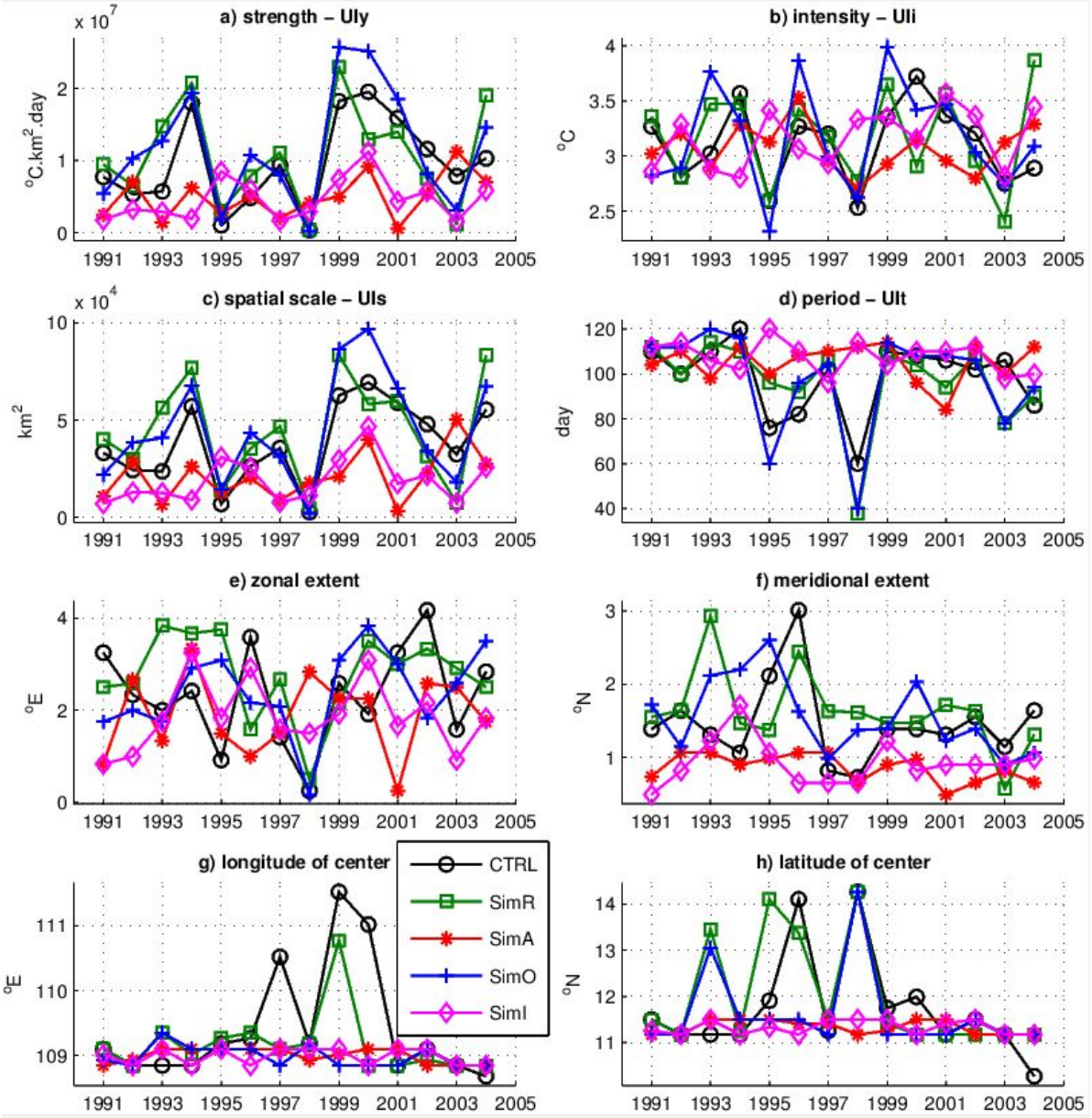

Figure 4.3: Time series of yearly SVU upwelling indices (units indicated on the y-axis) in the CTRL and sensitivity simulations.

Due to the strong cloud cover in this region, it is difficult to systematically compare SVU events produced in the model with real SVU events observed from satellite SST data. Figure 4.4 however shows modeled and observed SST for 4 cases that could be observed with AVHRR data, for the summers of 1994, 1998, 2002 and 2004. Comparison between CTRL and AVHRR data shows that the strong interannual variability of the SVU shown in Figure 4.2 is realistic and correctly reproduced by CTRL : the average to strong coastal and offshore SVU obtained for

1994, 2002 and 2004 in CTRL are observed in the data, as well as the extreme weak SVU obtained for 1998, with SST values in good agreement. In summer 1998, after the strong Niño event in winter 1997/1998, Xie et al (2003) based on TMI-SST averaged from July to August reported that upwelling didn't appear in this year. The year 1998 is indeed the weakest year in our CTRL run (Figure 4.3), however the CTRL coastal upwelling did occur this year but much further north than usual. AVHRR SST data confirms the cold water band along the coast from 12.°5N to 15°N and the absence of offshore upwelling in this year.

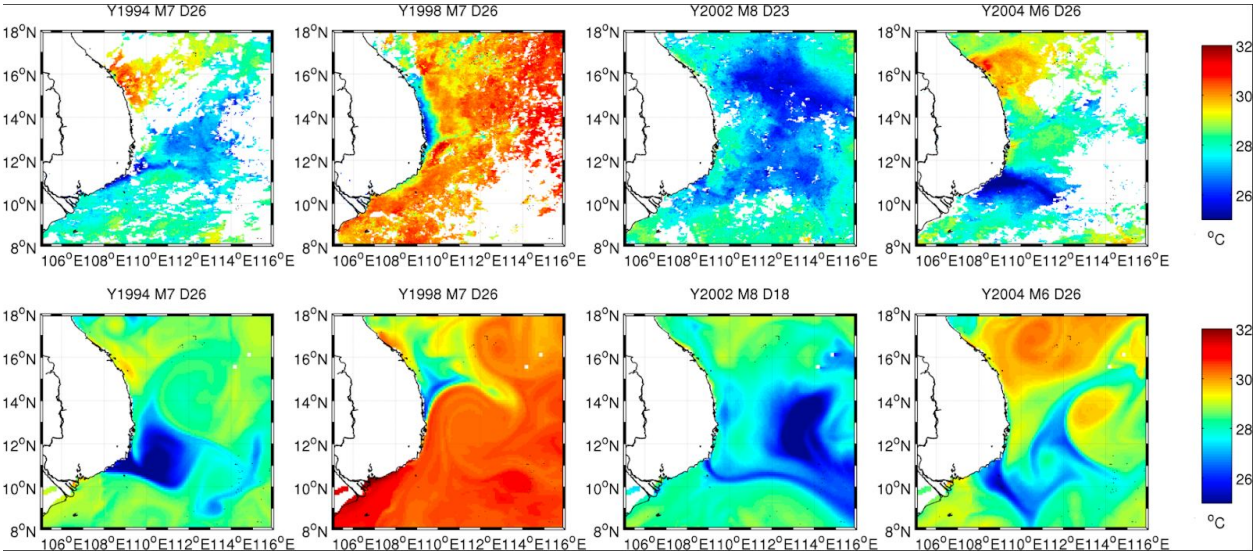

Figure 4.4: Comparisons of CTRL and AVHRR 2-day mean SST for several individual events (AVHRR - upper panel and CTRL - lower panel).

In summary, for the CTRL run, SVU detected with our temperature criteria index shows a strong interannual variability, both in terms of strength and position. The strong upwelling years are associated with strong offshore upwelling, concentrated in the latitude band 10.5°N to 12.5°N with large zonal extensions. The weakest upwelling years (1995, 1996, 1998) have centers located further north and are characterized by a larger meridional extension.

4.3 Contribution of different forcings to the interannual variability of SVU

The sensitivity simulations described in section 2.3 are used to quantify the contributions of the different forcing mechanisms to the interannual variability of the SVU. For this we compare the upwelling indices obtained for the CTRL simulation with the upwelling indices calculated from simulations where we removed the interannual variability of atmospheric forcing (SimA), the interannual variability of oceanic forcing (SimO), the climatological river forcing (SimR) and examined the effect of intrinsic variability by removing both the interannual ocean and atmospheric forcing (SimI). The results for the different simulations are shown in Figure 4.3, for the statistical average indices defined above. Their geographical dispersion is also highlighted in Figure 4.5, which shows for each simulation the annual position, spatial extension and strength of the upwelling. In order to quantify the differences associated to a given factor, we define for each sensitivity simulation the mean and standard deviation (STD) of each index (intensity, spatial scale, period and strength) relative to the CTRL reference simulation as follows:

$$RevMean\ (\%) = \frac{Mean_i - Mean_{CTRL}}{Mean_{CTRL}} \times 100 \quad (4.2)$$

$$RevSTD\ (\%) = \left(\frac{STD_i - STD_{CTRL}}{STD_{CTRL}}\right) \times 100 \quad (4.3)$$

Where subscript i represents the sensitivity simulations. The absolute and relative means and standard deviations of each index and for each simulations are given in Table 4.1.

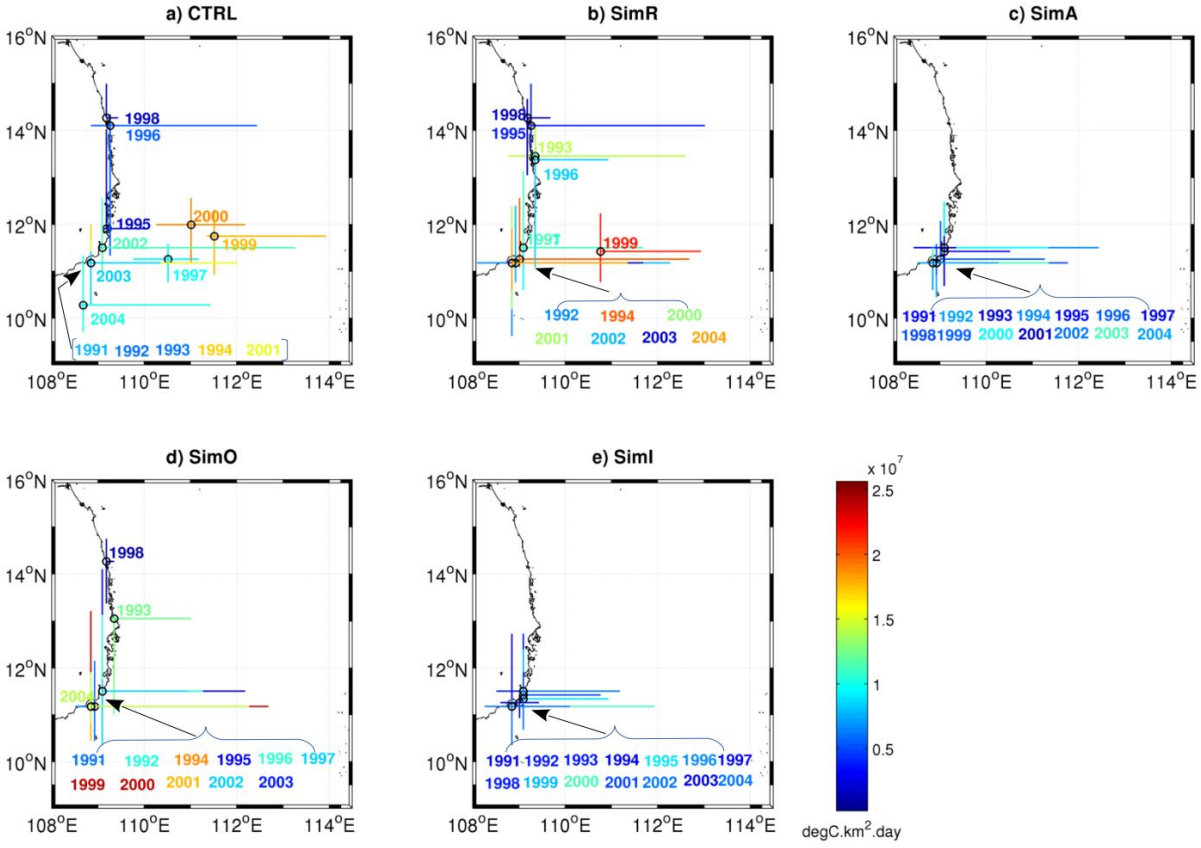

Figure 4.5: Geographical distribution of annual upwelling centers, spatial extent and upwelling strength in different simulations: upwelling centers (black circles) and meridional and zonal spatial extension (bars) represented as in Figure 4.2 and shown together with SVU strength Uly (°C.km^2.day, color) on one map for each simulation.

4.3.1 Atmospheric forcing

In comparison with other external forcings (lateral oceanic and river discharge), the presence of interannual variability in the atmospheric forcing is the one with the most profound impact on upwelling activities in the SVU : when the daily atmospheric forcing is based on a seasonal climatology (SimA), the upwelling intensity is greatly reduced compared to CTRL, and the upwelling centers are concentrated near the coast and within the 11.2°N-11.6°N latitude band (Figure 4.5). Figures 4.3a,g,h indeed shows almost constant values of the upwelling centers' longitude and latitude and small variations of the meridional extent and upwelling strength in SimA, whereas CTRL has much stronger variability in the spatial position of the upwelling centers and in the cumulative upwelling strength. Although the average SVU zonal extent is similar in SimA and CTRL, the meridional extent is also smaller for SimA that for CTRL in 13 over 14 years (Figures 4.3). Years with strong offshore SVU with large meridional extent in 1997, 1999 and 2000 in CTRL are not produced in SimA in the absence of interannual atmospheric forcing (Figure 4.5). Instead, the seasonal atmospheric forcing in SimA regularly generates coastal

upwelling centres each year in the coastal band. Overall, the comparison of SimA and CTRL shows that the interannual variability of the atmospheric forcing is largely responsible for the spreading of upwelling centres both meridionally along the coast and zonally from the coast to offshore.

The mean intensity of the upwelling events UIi does not change significantly with no interannual atmospheric forcing (3.07°C in SimA vs. 3.11°C in CTRL, i.e. -1%, Table 4.1), whereas the upwelling strength UIy (cumulative intensity) decreases strongly (-49% compared to CTRL), due to the much smaller spatial scale UIs (-45%) of the coastal upwelling produced in SimA (Figure 4.3, 4.5). The upwelling period increases by 7%, due to the fact that extreme years with very short and weak SVU (in terms of UIs and UIi) such as 1995 and 1998 in CTRL are not produced in SimA. This decrease of mean upwelling period and intensity in CTRL compared to SimA is actually associated with the larger variability obtained in CTRL. SimA indeed produces a much weaker variability of the SVU indices than CTRL: -37% of UIs, -38% of UIi, -48% of UIt and -51% of UIy (Table 4.1).

Comparing the two pairs of simulations CTRL vs. SimA and SimO vs. SimI shows for both pairs the effect of removing the interannual variability of the atmospheric forcing : both pairs are consistent, showing the strong contribution that interannual atmospheric forcing has on the mean state and variability of the SVU, but acting on different dynamical backgrounds (i.e interannually variable monthly lateral oceanic forcing for CTRL and SimA, and climatological monthly lateral oceanic forcing for SimO and SimI). In both cases the absence of interannual variability of atmospheric forcing strongly reduces the mean spatial extent and the interannual variability of the SVU, in terms of intensity, location and duration (Figure 4.3, 4.5, Table 4.1).

Our results therefore shows the strong contribution of interannual atmospheric forcing to the SVU variability in terms of spatial distribution and upwelling strength : with a climatological average atmospheric forcing, the simulated SVU occurs regularly every year, throughout most of the JJAS period, although over limited coastal areas and positions. Whereas the interannual atmospheric forcing variability introduces a strong variability in the period, spatial coverage and intensity of the simulated SVU (almost twice the variability obtained compared to the seasonal atmospheric forcing).

Table 4.1: Absolute and relative mean and standard deviation of yearly SVU indices in the simulations. Relative mean and standard deviations over 1991-2004 are calculated taking CTRL as the reference (see Eq. 4.2 and 4.3) : blue/red values correspond to a decrease/increase of the mean or standard deviation of the SVU index in the considered sensitivity simulation compared to CTRL.

		Uli		**Uls**		**Ult**		**Uly**	
		(°C)	(%)	(10^4 km^2)	(%)	(day)	(%)	(10^7 °C.km^2.day)	(%)
CTRL	mean	3.11		3.83		98.4		0.97	
	std	0.36		2.07		16.4		0.62	
SimR	mean	3.17	2	4.49	17	96.4	-2	1.08	12
	std	0.44	23	2.63	27	19.6	19	0.70	13
SimA	mean	3.07	-1	2.12	-45	105.1	7	0.50	-49
	std	0.22	-38	1.30	-37	8.6	-48	0.30	-51
SimO	mean	3.17	2	4.50	17	97.7	-1	1.17	21
	std	0.49	39	2.81	36	23.2	41	0.81	30
SimI	mean	3.17	2	1.90	-50	107.7	9	0.47	-52
	std	0.49	-25	1.16	-44	6.9	-58	0.29	-53

4.3.2 Oceanic forcing

In SimO, only climatological monthly remote ocean variability is introduced through the model domain's lateral open boundaries. This excludes the remote interannual ocean forcing coming from the Western Pacific which was shown to impact the large-scale SCS circulation (Gan et al., 2006). The difference in SVU activity between CTRL and SimO is therefore due to the changes of large-scale circulation in the entire SCS that result from the interannual variability of lateral oceanic boundary conditions. This remote interannual ocean forcing induces significant changes in the SVU upwelling activity compared to the CTRL run. The most evident change is the absence of offshore upwelling centres (Figure 4.5d). Three years 1997, 1999 and 2000 which have a large offshore extent in CTRL become centred at the coast in SimO. The upwelling centres that develop further north along the coast are similarly reproduced in CTRL and SimO in some years (e.g. weak upwelling in 1998) but differ in terms of space or intensity in others (1993, 1996). Figure 4.3 and Table 4.1 further detail the difference between CTRL and

SimO. The SVU intensity and temporal scale are not changed significantly in SimO compared to CTRL (respectively +2 and -1%, Table 4.1), but the SVU spatial scale and resulting total strength increase by respectively 17% and 21%. The variability of all indices increases strongly between +30% and +41% : including the atmospheric forcing interannual variability therefore seems to have a stabilizing effect on the SVU interannual variability. The impact of remote ocean forcing can be more significant at the scale of the individual year than in average : removing the variability of the oceanic forcing in SimO vs. CTRL for example respectively increases UIy by a factor ~2 and increases it by ~3 for years 1993 and 2003.

4.3.3 River forcing

Unlike SimA and SimO whose interannual variability of atmospheric and oceanic forcing respectively were replaced by climatological ones, SimR was constructed by turning off the climatological river forcing due to the lack of data discussed in Section 2.4. At first glance, the differences between the SimR and CTRL upwelling indices are small on average, but not negligible (Figures 4.3, 4.5, Table 4.1). Removing the climatological river forcing in SimR negligibly affects the mean intensity (UIi) and temporal (UIt) indices compared to CTRL (respectively +2 and -2 %, Table 4.1), but increases the upwelling spatial (UIs) and resulting strength (UIy) indices (respectively +17% and +12%). Moreover it increases the variability of all the SVU indices by +13% to +27% : including the freshwater river forcing therefore seems to have a stabilizing effect on the SVU interannual variability. This stabilizing impact of river forcing is particularly visible during the period 1999-2004 : while UIy, UIi, UIs exhibit sharp changes during this period for SimR, they show smaller variations in CTRL (Figure 4.3). Moreover, as observed for lateral oceanic forcing, river forcing can have a strong impact at the scale of individual years in terms of total strength and location of upwelling centre. For example removing river forcing increases UIy by factors of respectively ~3 and ~2 in 1993 and 2004, while it decreases it by ~4 in 2003 (Figure 4.3a). Upwelling centre in the year 1999 remains offshore whereas upwelling centres in the year 1997 and 2000 move near the coast when going from CTRL to SimR.

Of the three rivers, Mekong river provides 52% of freshwater into the SCS, and about 67% of its annual discharge is distributed from June to September - the upwelling season (Figure 1.10). The mean summer circulation in the southern SCS (Figure 3.1 d,e) draws the Mekong outflow northward then offshore within the SVU during the summer months, as observed from the lower surface salinity in summer in the coastal and southern part of the SVU region (Figure 3.4d). Our results suggest that the presence of fresher water in the SVU region may have an impact on the

oceanic circulation in this area, that could explain the impact of river forcing on SVU obtained here.

The behaviors of the mean and standard deviation of the magnitude indices in response to the presence of interannual variability of oceanic forcing or to the presence of river forcing are very similar, though the effect of lateral oceanic interannual variability can be about twice the effect of including river freshwater discharge (Table 4.1). Both river forcing and lateral oceanic forcing therefore have a non negligible effect on the interannual variability of the SVU position, intensity and strength, and particularly at the scale of the individual year. The remote ocean forcing and river forcing can influence this background ocean circulation in the SCS and SVU regions and impact on the development and strength of the coastal and offshore SVU. This will be investigated in Section 4.5.

4.3.4 Ocean intrinsic variability (OIV)

SimI has no interannual variability in either the atmospheric forcing or the ocean lateral boundary forcing, but only climatological daily atmospheric and monthly oceanic and river forcing, and was conducted to study the influence of OIV of the SCS on the SVU. The SVU variability produced by SimI is very similar to the one produced by SimA, both qualitatively and quantitatively (Figures 4.3 and 4.5, Table 4.1). Figure 4.3 shows that with only climatological forcing there is a weaker but still significant interannual variability of most indices in SimI, except for the longitude and latitude of the upwelling centers, whose variability is drastically reduced compared to CTRL. As observed for SimA, the climatological forcing tends to produce regular coastal SVU centred near 109°E and 11-11.5°N in SimI, and suppresses the strong offshore SVU variability produced in CTRL.

The mean intensity of the upwelling events UIi does not change significantly with no interannual atmospheric and oceanic forcing (3.16°C in SimI vs. 3.11°C in CTRL, i.e. +2%, Table 4.1), and the spatial index UIt weakly increases (+9%), but the upwelling strength UIy (cumulative intensity) decreases strongly (-52% compared to CTRL), due to the much smaller spatial scale UIs (-50%) of the coastal upwelling produced in SimI (Figure 4.3, 4.5). SVU indices of intensity UIi, spatial scale UIs, period UIt and upwelling strength UIy in SimI have interannual variability weaker that in CTRL but still significant, reaching values equal to 42 to 75% of the values obtained in CTRL. Therefore the interannual variability induced by the OIV represents between about half and 3/4 of the total inter-annual variability of the SVU magnitude indices. Li et al., (2014) found that OIV influence represents about 20% of the interannual variability of the summer eastward jet that was shown to play a major

role in the SVU development. This smaller number (20% compared to 50%) can be attributed to the difference in model resolution : Li et al., (2014) used a 1/4^{o} (~ 28 km) eddy permitting resolution model, which can not resolve the smaller mesoscale eddies in contrast to our eddy-resolving 1/12^{o} model (~ 9 km resolution). Previous studies (e.g. Penduff et al., 2011; Waldman et al., 2018) indeed showed that mesoscale to submesoscale structures and eddies are strong OIV sources, and Xiu et al., (2010), based on 12.5 km resolution model, estimated that 70% of the eddies in the SCS were smaller than 100 km. Our results and those previous studies therefore suggest that OIV can significantly contribute to the SVU interannual variability, and that this impact could be related to the high number of small and energetic eddies in the SCS. This will be further investigated in Section 4.5.

4.4 Interactions between atmospheric and oceanic forcing

Comparing both SimO and SimA vs. CTRL shows that the interannual variability of atmospheric and oceanic forcing can induce comparable changes in the standard deviations of the indices in terms of magnitude, but with opposite sign (Table 4.1). Yet when interannual variability of both forcings is removed in SimI, the induced changes compared with CTRL are very close to the changes induced in SimA, both for the mean and standard deviation. This suggests that the impacts of interannual variability of atmospheric forcing dominates the impacts of interannual variability of oceanic forcing, and that both effects can not be simply added, showing that those forcing impact the SVU variability and interact through highly non-linear processes. Moreover, comparing the difference between CTRL vs. SimO and SimA vs. SimI reveals for both pairs the impacts of interannual variability of oceanic forcing to the SVU, but in different dynamical backgrounds (interannually varying vs. climatological oceanic lateral forcing). If the role of oceanic forcing was consistent, there should be increases in the mean (except UIt) and variability of the magnitude indices from SimA to SimI, similar to that observed between CTRL to SimO (Table 4.1). This is not the case with most indices (except UIi) where the opposite occurs with larger variability of (UIs, UIt, UIy) in SimA than in SimI. This highlights that the forcing factors examined here do not act independently, but in interaction with each others, and suggests that this non-linear behavior of the system can have a stronger impact than the interannual variability of lateral oceanic forcing.

In summary, our results highlight that the key forcing component introducing strong interannual variability in the SVU is the interannual atmospheric forcing. Including the interannual variability of the atmospheric forcing produces SVU with a larger mean spatial extent and stronger variability (about twice that of the climatological forcing) , and also more extreme events (very strong offshore years or extremely weak coastal SVU) that are not produced with climatological forcing. These results agree with the previous studies based on lower resolution models, or short case studies, which suggested that atmospheric forcing, in particular associated with wind, is the main driver of SVU variability (e.g. Dippner et al., 2013). The variability associated with OIV as observed in SimI represents up to 50 to 75 % of the variability observed in CTRL : climatological oceanic and atmospheric forcing can produce regular coastal upwelling centres with significant interannual variability, although the interannual atmospheric forcing leads to a wider range of upwelling events. Freshwater river flux and the interannual variability of remote ocean forcing

have a weaker effect than the atmospheric forcing, but can modulate the interannual variability of the SVU from 13 to 41 % and have strong impact at the scale of individual years. Impacts of OIV, river discharge and remote oceanic forcing contribute to modifying the background oceanic circulation and thus the SVU development, as will be investigated in Section 4.5. Finally comparison of different sets of simulations shows that there is a strong effect of non-linear interactions between those different sources of variability, suggesting that a simple Ekman mechanism in which wind stress curl determines how much upwelled water reaches the surface is not sufficient for the SVU case.

4.5 Discussion : Mechanisms contributing to the SVU variability

In this section we explore the physical mechanisms behind the statistical results obtained in previous sections.

4.5.1 Impact of atmospheric variability: the confirmed key role of wind

As discussed in Section 1.2, many previous studies highlighted the key role of wind forcing on the SVU (e.g. Xie et al., 2003; Dippner et al., 2013). Although we find a major role for interannual atmospheric variability in setting the SVU variability in Section 4.4, this atmospheric variability includes the effects of wind forcing but also of air-sea heat and freshwater fluxes. To check their role in the SVU variability, we compute the correlations over the 1991-2004 period between yearly time series of SVU strength Uly in CTRL and yearly time series of the different components of atmospheric forcing in our model, i.e. wind stress, heat flux and freshwater flux obtained from the NCEP-CFSR reanalysis, averaged over the SVU domain and the JJAS period. Local SVU wind stress and wind stress curl have a high and significant correlation with Uly with respective correlations of 0.73 and 0.81, both at significance level $p < 0.01$ (Figure 4.6). The heat flux and freshwater fluxes have low and not significant correlations with Uly, both with a correlation of -0.16 and significant level $p = 0.59$. This confirms that wind is the major component of the atmospheric forcing inducing the variability of the SVU. The high correlation of July wind stress curl with upwelling strength suggests that the wind acts on SVU through local Ekman pumping, as already suggested by Xie et al., (2003, 2007). Moreover Xie et al., (2003, 2007) and Dippner et al., (2007) showed that summer wind also participates to strengthen the eastward jet which helps to extend the wind-forced coastal upwelling further offshore. Wind can also indirectly affect the SVU by modifying the ocean vorticity field in the SVU area. This will be explored in the following Section 4.5.2.

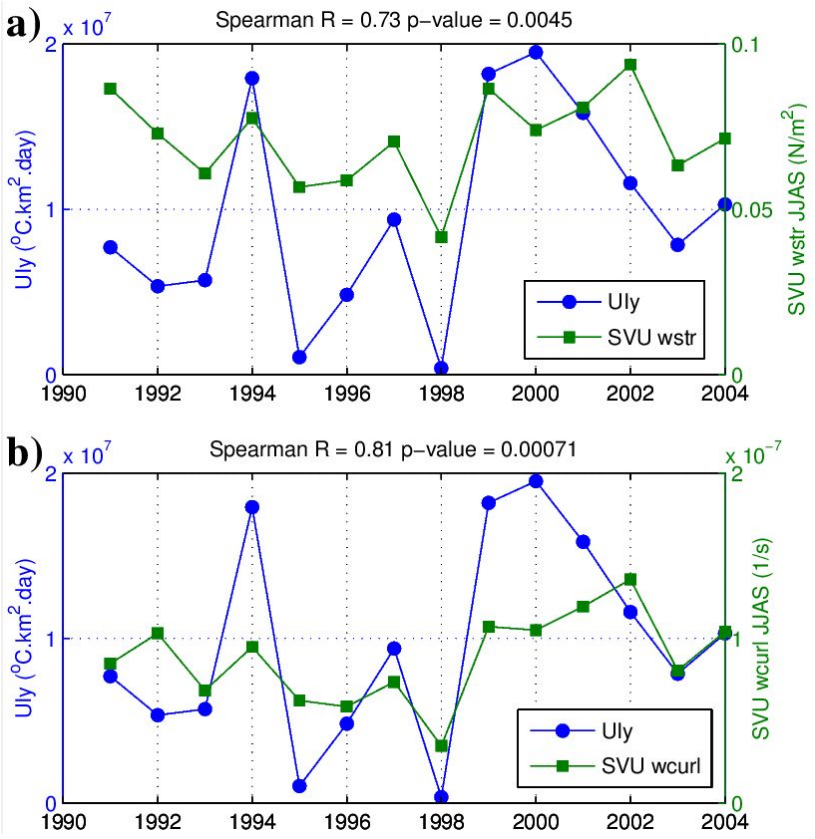

Figure 4.6. Upwelling and wind relation. Yearly time series of upwelling strength Uly (°C.km^2.day, blue) in CTRL and mean JJAS SVU wind stress (a, N.m^{-2}, green) and mean JJAS SVU wind stress curl (b, s^{-1}, green) from CFSR. The correlation coefficient and p-value between those time series is also indicated.

4.5.2 Impact of background ocean circulation

The background ocean circulation is highly non-linear, being impacted by different external forcings and their interactions as well as by OIV. Statistical analysis of our sensitivity simulations showed that wind forcing is a dominant factor in the SVU. However changes in the background ocean circulation in the SVU and SCS regions due to changes in remote oceanic forcing or river inputs and to OIV can strongly modulate the impact of the wind forcing on SVU activities. To understand the role of this background ocean circulation we examined several different case studies obtained from our simulations.

Figure 4.7 show the different ocean and wind-forcing conditions for the upwelling events in summer, during the years 1998, 2000, 2002 based on the CTRL run. The summer mean JJAS wind stress curl spatial patterns prescribed by NCEP-CFSR reanalysis (Figure 4.7 b) are quite similar among these years with maximum positive and minimum negative wind stress curl centered at 11.5° N and

10.5°N respectively, due to orographic effect (Xie et al., 2003, 2007). However their amplitude differs : their wind stress curl values averaged over the SVU domain vary by a factor of ~ 4 between the weakest year (0.35 x 10-7 s^{-1}) in 1998 and the strongest year (1.36 x 10-7 s^{-1}) in 2002 (Figure 4.6). They also differ in terms of upwelling intensity. CTRL-1998 shows no offshore SVU but only weak coastal SVU that occurs much further north (14.2°N, Figure 4.7a) at the location of a second positive wind stress curl site (Figure 4.7b). This northward shift of the SVU compared to the average and the absence of offshore SVU are in agreement with AVHRR satellite SST observations presented in Figure 4.4. The CTRL-2000 and CTRL-2002 cases also show a very different upwelling response to the wind forcing. Although the JJAS wind stress curl in CTRL-2002 is ~ 30% stronger than in CTRL-2000, the SVU cumulative intensity is ~ 40% weaker (Figure 4.6), with a coastal centered SVU in CTRL-2002 vs. a strong offshore SVU center in CTRL-2000 (Figure 4.7a).

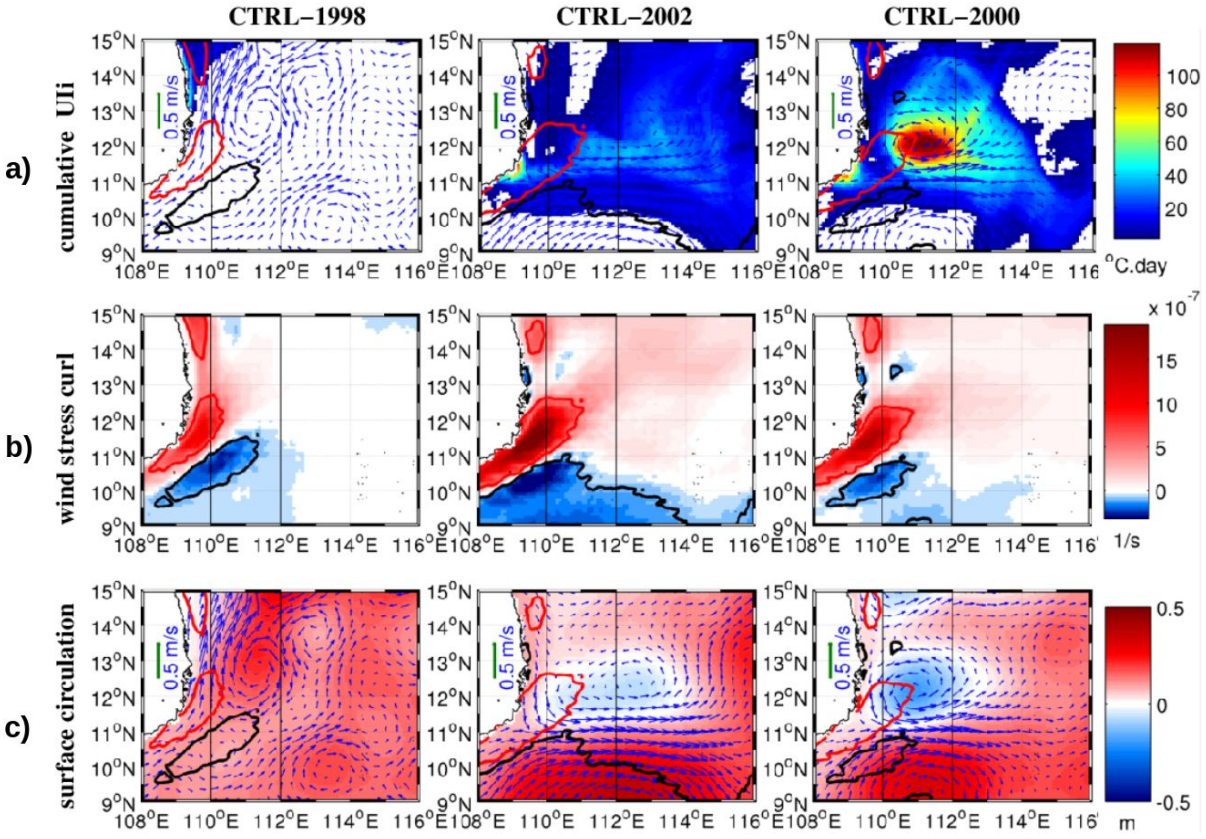

Figure 4.7: From top to bottom are summer (JJAS) mean of: cumulative upwelling intensity (°C.day), surface wind stress curl (s^{-1}), and background sea level anomaly (m) and respective surface circulation (m/s) for different years (1998, 2000, 2002) in CTRL. The contours of wind stress curl of -1x10^{-7} s^{-1} and 5x10^{-7} s^{-1} (solid blue and red lines from middle pane) and mean circulation (from bottom pane) are also superimposed on the top graphs.

Figure 4.8b,c show the ocean and wind conditions for the SimR-2000 and SimO-2000 simulations which by construction have identical wind fields to CTRL-2000. However, their coastal and offshore SVU distributions, as well as their overall SVU strengths, are strongly different, having a factor of ~ 2 between the weakest and strongest UIy. SimR-2000 has a coastal-centred and weak UIy (only 66% of the UIy obtained in CTRL-2000), whereas SimO-2000 is offshore-centred with a greatly extended region of UIy (equal to 129% of the CTRL-2000 UIy), as seen in Figures 4.3 and 4.5. Note that although the SVU intensity (UIi) in SimO-2000 is smaller than in CTRL-2000, its strength (UIy) is greater due to its larger spatial scale (UIs, Figure 4.3).

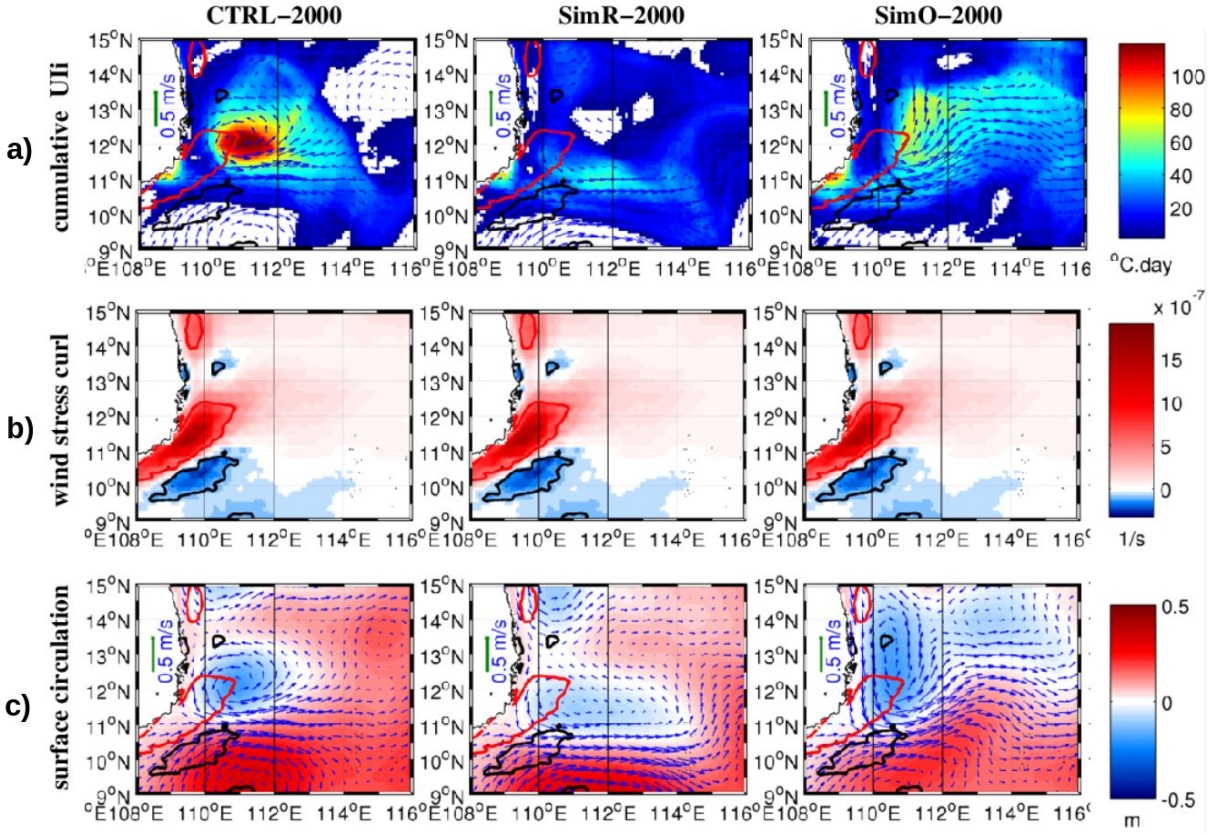

Figure 4.8: Similar to Figure 4.7 but among CTRL and SimR and SimO in the year 2000 whose wind fields are the same.

These case studies raise the following questions: how do years with the same atmospheric forcing show significantly different upwelling ? How can a stronger wind result in a weaker upwelling ? What induces the upwelling to be shifted 2° further north than the average with a similar wind pattern ?

The answer to these questions lies in the background circulation in the SVU. In CTRL-1998, the coastal upwelling occurs much further north due to the presence of a persistent anticyclonic circulation within the SVU centered at about 13°N and

111.5°E, which prevents the coastal upwelling from developing in the 11-12°N region and the development of the eastward jet (Figure 4.7a). In contrast, for the other years CTRL-2000, CTRL-2002, SimO-2000 and SimR-2000, the geographical distribution and higher value of wind stress curl (Figure 4.7b, 4.8b) favors the development of a strong eastward jet associated with an eddy dipole centred around 11°N with a cyclonic eddy in the north and anticyclonic eddy in the south, which helps to extend the wind-forced coastal upwelling further offshore, as already shown in previous studies (Xie et al., 2003, 2007; Dippner et al., 2007). Yet the wind acts over a large, weak cyclonic eddy north of the jet in CTRL-2002, compared to a smaller, intense cyclonic eddy closer to the coast at the same latitude in CTRL-2000. SimR-2000 and SimO-2000 even show a pair of larger cyclonic eddies located north of the jet (Figure 4.7c). The location and strength of these cyclonic eddies in the different simulations correspond well to the distribution of offshore upwelling (Figure 4.7a,c). These case studies agree with the findings of previous studies (Xie et al., 2003, 2007; Dippner et al., 2007; Li et al., 2014) that the development of the coastal upwelling within 11°N and 11.5°N is associated with the existence of an eastward jet and maximum wind stress located around 11°N. They further suggest that the meridional position of this coastal upwelling can be modulated by the background circulation for years of weak wind, for which the eastward jet does not develop and weaker upwelling tends to occur further north than on average (e.g. 1995 but also 1998, Figure 4.2). They finally suggest that ocean eddies contribute to the development and modulation of both the coastal and offshore SVU.

To better clarify how these ocean eddies and wind stress forcing patterns develop over the upwelling season and how they modulate the upwelling position and strength, we investigate the latitude-time evolution of different parameters within a zonal average over 110°E – 112°E, which bounds the center of offshore upwelling (black lines in Figure 4.7, 4.8). Figure 4.9 show (a) the depth of the 1023 $kg.m^{-3}$ isopycnal (1023 $kg.m^{-3}$ that corresponds to the density at the depth of the pycnocline in summer, figure not shown), (b) the relative surface vorticity, (c) the vertical velocity at the base of Ekman layer (at 50 m depth), and (d) the Ekman pumping WE due to wind stress curl using formula from Stewart (2008):

$$WE = - \text{curl} (\tau / \rho f) \qquad (4.4)$$

where $\boldsymbol{\tau}$ is the surface wind stress ($N.m^{-2}$), ρ is the mean sea water density which is 1024 $kg.m^{-3}$ in our calculation, and f is the Coriolis parameter. Contours of Ekman pumping are superimposed on the other parameters in Figure 4.9 to highlight the relative location and strength of wind stress curl with respect to the underlying ocean circulation.

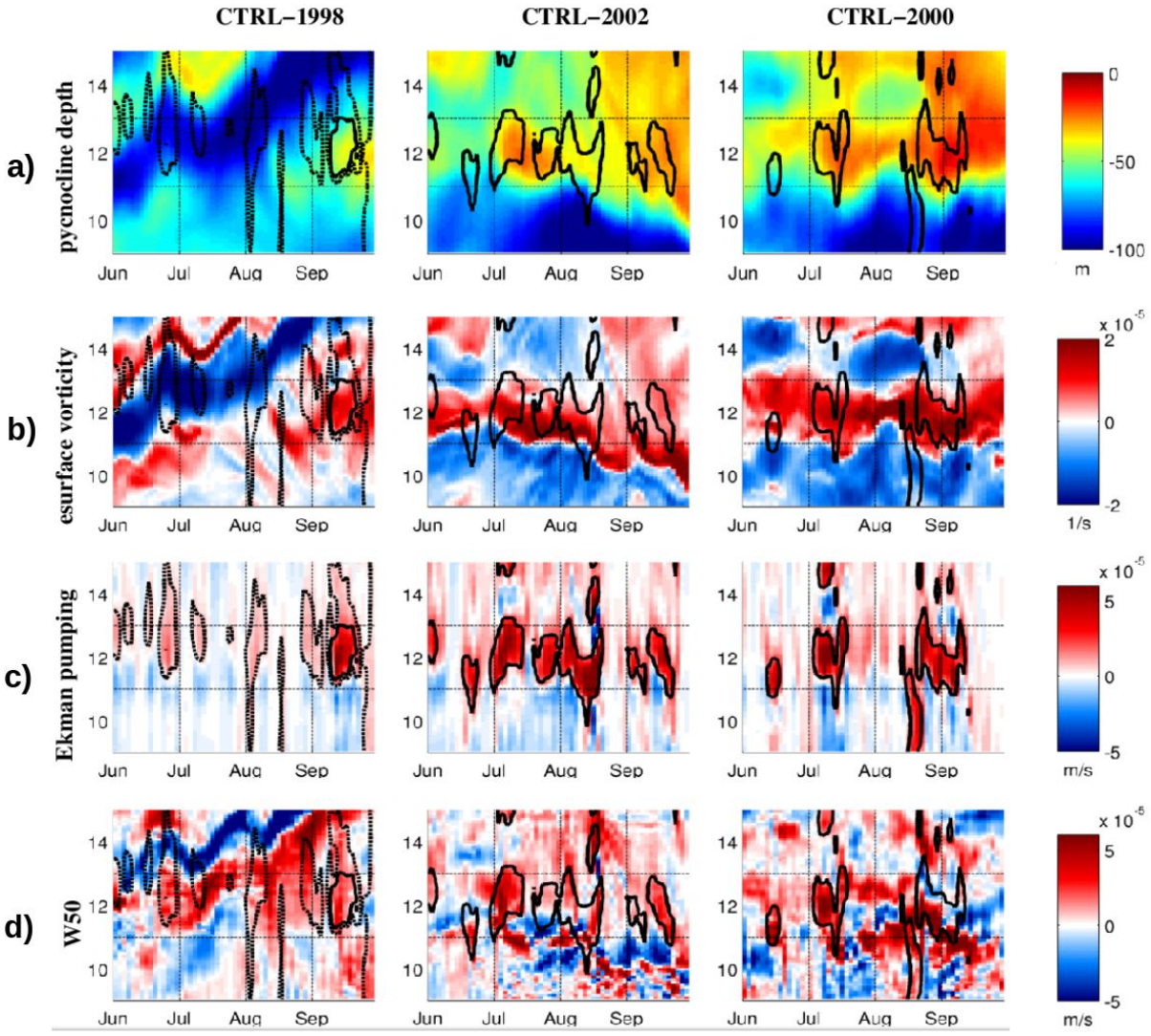

Figure 4.9: Summer evolution of zonal average (110-112E, within solid black lines in Figure 4.7) of depth 1023-isopycnal (pycnocline depth, m), surface vorticity (s^{-1}), Ekman pumping (m/s) and vertical velocity at 50 m depth (m/s). Contours of 0.5 x 10^{-5} $m.s^{-1}$ (dashed line) and 2 x 10^{-5} $m.s^{-1}$ (solid line) of Ekman pumping are superimposed on the other graphs.

Figures 4.9 c,d show that strong positive (upward) vertical velocity values occur around 12°N during the summer period and are collocated with the strong Ekman pumping, confirming the leading role of this mechanism in the SVU development. This can be compared to Figures 4.9 a,b that show the very similar patterns of relative vorticity and pycnocline depth : shallow pycnoclines are associated with positive vorticity, and vice versa. Positive vorticity, i.e cyclonic circulation, raises the pycnocline closer to the surface, and thus can create a preconditioning that favors the wind-driven upwelling of colder, denser water to the surface. This is the opposite for negative vorticity of the anticyclonic circulation, associated with deeper pycnocline displacement. Even though positive Ekman

pumping inducing strong vertical velocities and upwelling conditions can occur over the anti-cyclonic circulation, it brings warmer waters to the surface which do not meet our T<T0 upwelling criteria.

These differences can be observed when examining our case studies in detail. Figure 4.9c shows that for CTRL-1998 the positive Ekman pumping is weaker and shifted slightly to the north during this 1998 summer season compared with other years. Figure 4.9a,b confirms the presence of a strong anticyclonic eddy at 11°N-12°N in June instead of cyclonic eddy at the same place in other years : the strong band of negative vorticity associated with a deep (more than 80 m) 1023 $kg.m^{-3}$ pycnocline illustrates the northward movement of this anticyclonic eddy over the summer. As it moves north, this anti-cyclonic eddy is associated with downwelling (negative vertical velocity) on its northern flank, and upwelling conditions on the southern flank (Figure 4.9d). However the wind-forced positive vertical velocity at 50 m depth on the southern flank occurs within the band of deep 1023 $kg.m^{-3}$ pycnocline within the anti-cyclonic eddy (Figure 4.9a), it thus only brings light and warm waters to the surface, not detected as SVU using our criteria. From mid-June to mid-August, the positive vorticity from the wind-induced upwelling is therefore too weak compared to effect of the negative vorticity of the anti-cyclonic eddy that results in the deep pycnocline in this band. This combined effect of weak wind and background circulation induces the unusually weaker and northern upwelling observed in 1998.

Figure 4.9 also helps to clarify the mechanisms leading to the stronger offshore upwelling in CTRL-2000 than in CTRL-2002 despite the stronger wind stress in CTRL-2002. For both years, the band of favorable positive wind stress curl and Ekman pumping and upward vertical velocity within 11°N – 13°N coincides with strong positive vorticity (and thus a shallow pycnocline) associated with cyclonic circulation. However, their circulation details differ. The strong upwelling winds in July-August in CTRL-2002 blow over a weaker and larger cyclonic eddy (Figure 4.9b, 4.7c) undergoing a southward movement, so by August the wind curl is acting on the northern deeper flank of the eddy. In comparison, the strong wind impulses in CTRL-2000 occur over an intense cyclonic eddy which remains stable at the same latitude range with a consistent positive vorticity. This interaction between the wind and a more stable vorticity with a shallower pycnocline explains why the weaker wind stress curl in CTRL-2000 results in a stronger offshore upwelling than CTRL-2002.

SimR-2000 and SimO-2000 have the same atmospheric forcing as CTRL-2000 but with different ocean circulation patterns (Figure 4.8b,c, 4.10b,c). In SimR-2000, the two strong wind impulses in July and from mid-August to

mid-September act on weaker positive vorticity (July) or even negative vorticity (August-September) associated with a deeper pycnocline than in CTRL-2000 (Figure 4.10 a,b), leading to a much weaker upwelling (Figures 4.3, 4.8a). For SimO-2000, the upwelling favorable wind impulses within 11-13°N in June and July act over weaker positive vorticity than CTRL-2000 (Figure 4.10b), yet the longer wind impulse from mid-August to September act over an intense and large cyclonic eddy associated with a larger area of shallow pycnocline and strong positive vorticity than in CTRL-2000 (Figure 4.10a,b). These conditions lead to offshore upwelling with larger spatial extent in SimO-2000 than CTRL-2000 but weaker mean intensity, resulting in a stronger integrated strength (Figure 4.3, 4.8a). Thus the perfect overlapping of a stable, symmetric, cyclonic eddy within the region of strong positive wind stress curl in CTRL-2000 explains the highly concentrated cumulative offshore SVU in this year.

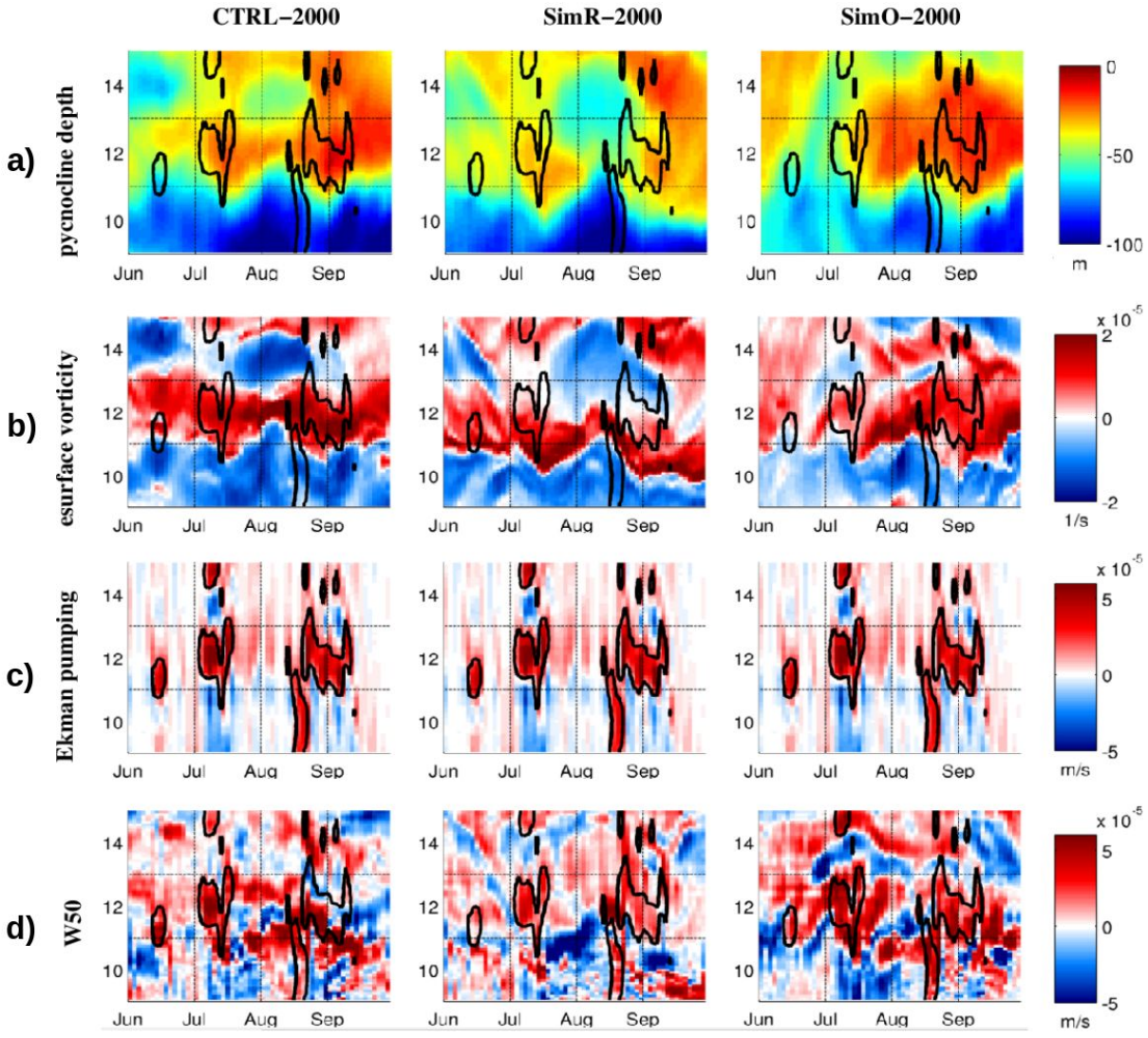

Figure 4.10: Similar to Figure 4.8 but among CTRL and SimR and SimO in the year 2000 whose wind fields are the same.

Those case studies therefore highlight the major influence of the background ocean circulation, in particular of the eddy field and associated vorticity field, on the SVU development. This circulation is influenced by several factors including atmospheric forcing, remote lateral oceanic forcing and river plume. This background ocean circulation is also influenced by the variability associated with the intrinsic chaotic nature of the ocean, i.e. OIV. Figure 4.11 show the ocean conditions for SimI-1994 and SimI-1995; two consecutive years which have identical forcings (atmospheric, lateral oceanic and river forcing). Figure 4.11b and Figure 4.12c show that the dipole wind stress curl forcing is weak within 11-13°N but consistent throughout the summer with some stronger wind impulses in July and August. Both years show a strong eastward jet around 11°N (Figure 4.11c). Yet their upwelling activities are strongly different: much weaker coastal and almost no offshore upwelling in SimI-1994, over a shorter period, compared to stronger coastal and offshore upwelling in SimI-1995 (Figures 4.3, 4.11a). The major difference in ocean circulation between them is the existence of an intense and stable cyclonic eddy in SimI-1995 within 11-13°N which does not occur in SimI-1994 (Figure 4.11c). This is associated with a stable band of positive vorticity in SimI-1995 vs. a highly variable band in SimI-1994 (Figure 4.12b). This leads to a stronger coastal and offshore SVU in SimI-1995, similar to the situation in CTRL-2000. These case studies highlight that the strong contribution of OIV to the SVU interannual variability that was described statistically in section 4.2, 4.3 is associated with eddy activity induced by this OIV.

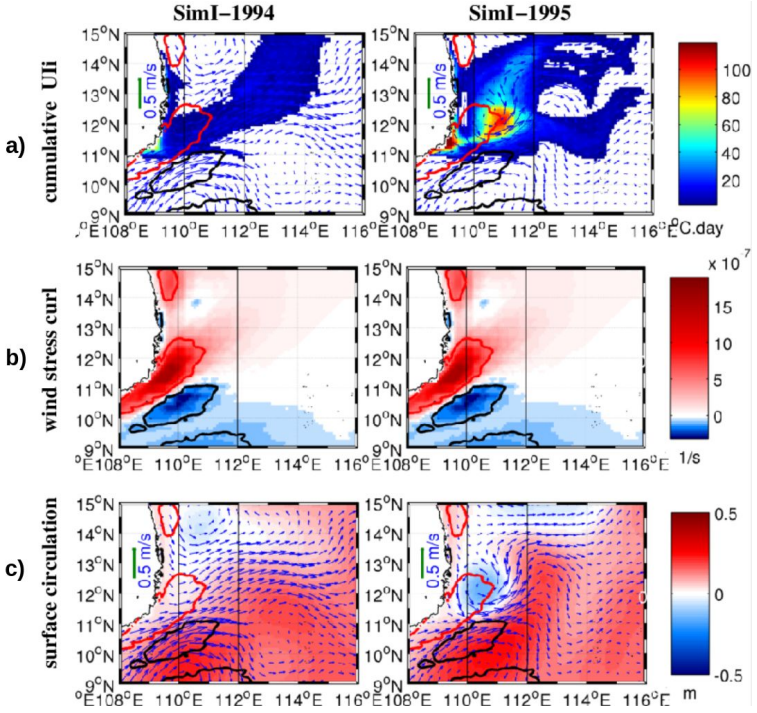

Figure 4.11: Similar to Figure 4.7 but between 2 consecutive summers in SimI whose atmospheric, lateral oceanic and river forcings are identical.

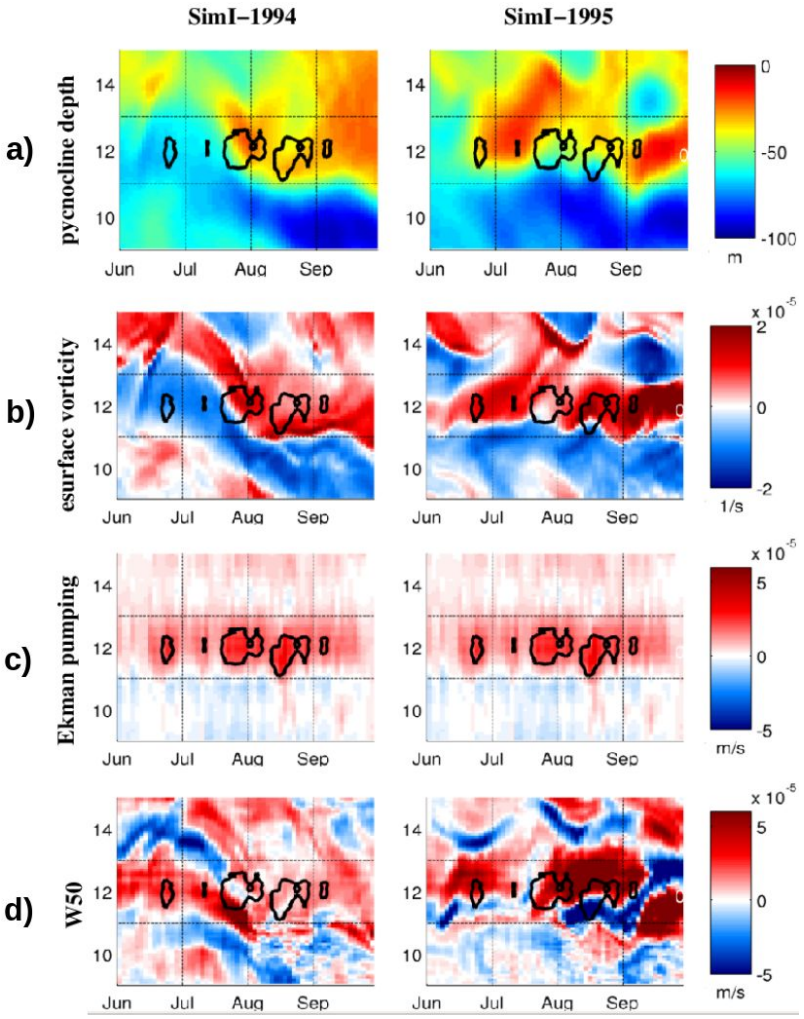

Figure 4.12: Similar to Figure 4.8 but between 2 consecutive summers in SimI whose atmospheric, lateral oceanic and river forcings are identical.

Results from these case studies therefore show that the direct influence of wind on the SVU development through Ekman pumping is strongly modulated by the background ocean circulation. Our results confirm that the development of the coastal SVU around 11°N is associated with the existence of an eastward jet and maximum wind stress at this latitude, but further suggest that the meridional position of this coastal SVU can be modulated by the background circulation, in particular for years of weak wind, for which the eastward jet does not develop and weaker coastal SVU can occur further north. Our study also reveals that offshore SVU not only depends on positive wind stress curl and associated Ekman pumping as suggested by Xie et al., (2003) but is strongly dependant on the interactions between this wind field and the background ocean vorticity field. The presence of strong wind stress and positive wind stress curl is indispensable to induce the offshore SVU, but the location and intensity of this upwelling is strongly influenced by the background circulation, in particular the presence of cyclonic eddies north of the eastward jet.

Strong, stable cyclonic eddies in the zone of positive Ekman pumping tend to generate stronger offshore SVU. For the CTRL simulation, there is a significant correlation (0.68, $p<0.01$) between the yearly time series of SVU strength UIy and surface vorticity averaged over JJAS over the offshore SVU region within the latitude band of positive wind stress curl (110-112°E - 11-13°N, called OFF+ hereafter and where the vorticity is positive-dominant) over 1991-2004, confirming the importance of this ocean contribution to the SVU interannual variability.

Finally, the vorticity field and the wind stress curl patterns are not disassociated. The different case studies show that the interaction of the summer monsoonal wind with the coastal orography induces a dipole wind stress curl (as shown by Xie et al., 2003) and Ekman pumping pattern offshore that are stable over the summer, and the surface vorticity field is mostly in phase. Indeed, years of weak/strong wind stress are associated with weaker/higher than average positive vorticity within the OFF+ region : we obtain a highly significant correlation (0.92, $p<0.01$) between wind stress and surface vorticity in July in the region. So the vorticity field that develops off the coast (positive cyclonic vorticity around 12°N, negative vorticity around 10°N, eastward jet in between) is strongly linked to the summer wind stress curl patterns. However, the simulations having the same atmospheric forcing but different river forcing (SimR vs. CTRL) or remote oceanic forcing (SimO vs. CTRL) or initial conditions (SimI) also show that these three factors modulate the spatial and temporal distribution of the oceanic eddy field and the associated background vorticity. This is related to the chaotic and non-linear nature of the oceanic instabilities generating eddies. In particular, this SVU region is on a western boundary, and whilst it is strongly influenced by the local wind-forced and coastal current instabilities it also has remote instabilities propagating westward into the region.

4.5.3 Variability of the SVU via vertical velocity (w) and limitations of w-based upwelling index

Figure 4.13 shows cumulative upward vertical upwelling velocity at 50m depth for the years (2-day averaged positive velocity is accumulated from June to September, unit in m/s). We can see that indeed years with strong SST-based upwelling which are 1999, 2000, 2001 (Figure 4.2) also have strong offshore vertical velocity. However why is the year 1991 with strong offshore vertical velocity but not very strong SST-based upwelling index?

We are interested in effective upwelling, that is the amount of subsurface water which can reach surface. Thus SST-based upwelling index suits well this

purpose. As shown in previous section, there's strong variation of pycnocline depth due to modulation of ocean eddies, which can vary from 10m in the center of a cyclonic eddy to 100m in the center of an anticyclonic eddy. For vertical velocity at the center of the cyclonic eddy, it takes only hours for subsurface water to spread over the surface, whereas for anticyclonic eddy, it would take days and without certainty that subsurface water could eventually reach the surface. So which depth should we choose for w-based (vertical velocity based) upwelling index?

Another limitation for w-based index is that we don't know where the upwelled water finally reach the surface. Given the order of magnitude of Ekman pumping (Figure 4.9) in the region is 10^{-4} m/s with the summer eastward jet strength of 0.5 m/s. It takes 5 days for a particle at 50 m depth to reach surface and in the same time it would have traveled ~ 200 km horizontally.

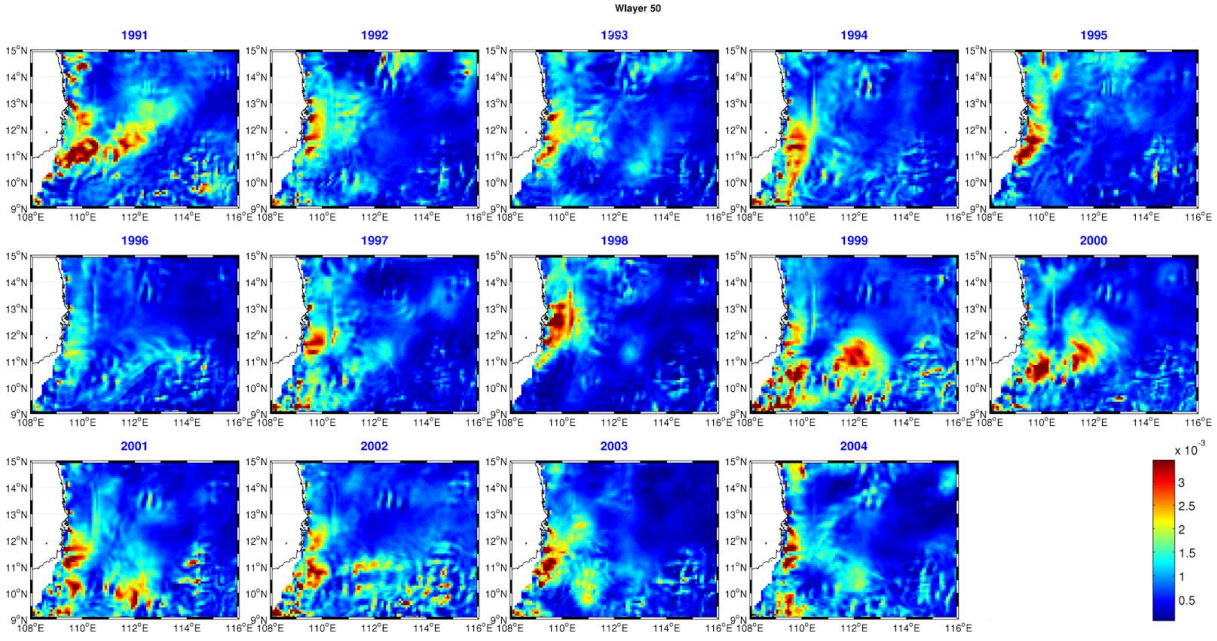

Figure 4.13 Cumulative Vertical positive velocity at 50m over the SVU

Now to answer to the question before: why the year 1991 with strong vertical velocity but doesn't appear as a strong offshore upwelling in terms of SST-based index. Figure 4.14 plots spatial integrated, summer average positive-only vertical flux over the whole SVU domain for the period (unit in Sverdrup). Let's look at the year 1991 and compare it with the year 2000. At 200 m depth positive vertical flux in 1991 is 12 Sv whereas for the year 2000, this flux is only ~ 7 Sv. At 50 m depth vertical fluxes of the year WF(1991) reduces to ~ 9 Sv and WF(2000) remain almost the same. The vertical flux of the two years are almost equal at 10 m. This represent much stronger effectiveness of upwelling in 2000 than in 1991 in terms of volume flux only (besides information on pycnocline depth between the years). In summary,

w-based upwelling index is sensitive to the reference depth and has limitation on the location of upwelled water on the surface.

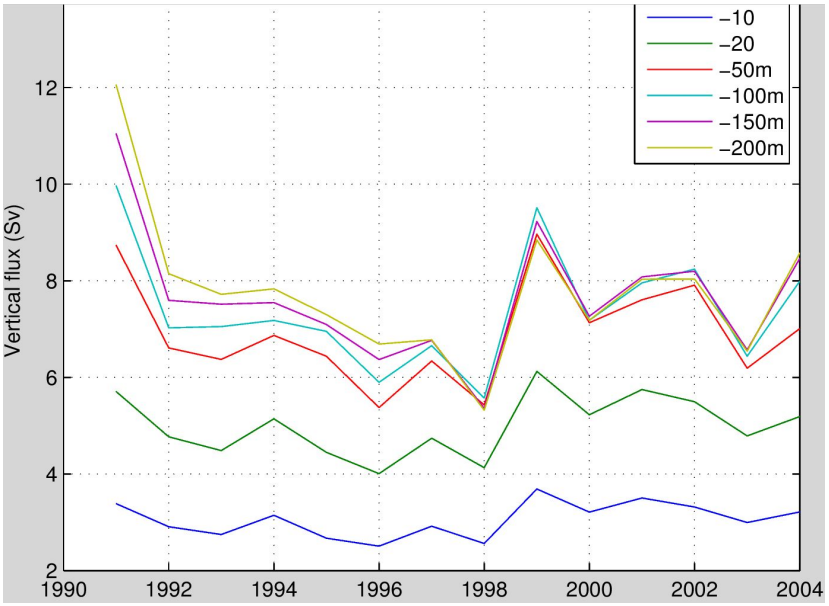

Figure 4.14 Spatial integrated, summer average upward vertical water flux over the whole SVU domain at different depths.

4.5.3 The role of El Niño-Southern Oscillation (ENSO)

In the CTRL simulation, the strongest SVU years are 1999 and 2000 and the weakest SVU years are 1995 and 1998. These extremes are in phase with ENSO : according to the Oceanic Nino Index (ONI, Figure 4.15b) defined by NOAA as the 3 month running mean of SST anomalies in the Niño 3.4 region (5°N-5°S, 120°-170°W, www.cpc.ncep.noaa.gov), 1994-95 and 1997-98 are El-Niño winters and 1998-99 and 1999-2000 are La-Niña winters. Previous studies reviewed in section 1.2 (e.g. Xie et al., 2003, Wang et al., 2006c; Dippner et al., 2007) found that in the summers following a strong El-Niño, the summer SW monsoon wind and its associated SSH dipole and eastward jet in the SVU off central Vietnam are weakened, leading to weaker SVU and warmer than average central SCS. The strongest El-Niño occurred in the winter of 1997-1998, and the summer of 1998 is indeed the weakest year in our CTRL run (Figure 4.2). As shown above, coastal SVU did occur in this year but much further north than usual, due to the weak JJAS winds and the presence of a strong anti-cyclonic eddy in the SVU area. On the other hand, in the summers

following La Niña winters such as the summers of 1999 and 2000, our findings showed a consistent coastal SVU occurring within 11-12º N upstream of the eastward jet and a highly variable but strong offshore SVU whose strength and distribution is determined by the interactions between wind stress curl and stronger than average positive vorticity associated with cyclonic eddies.

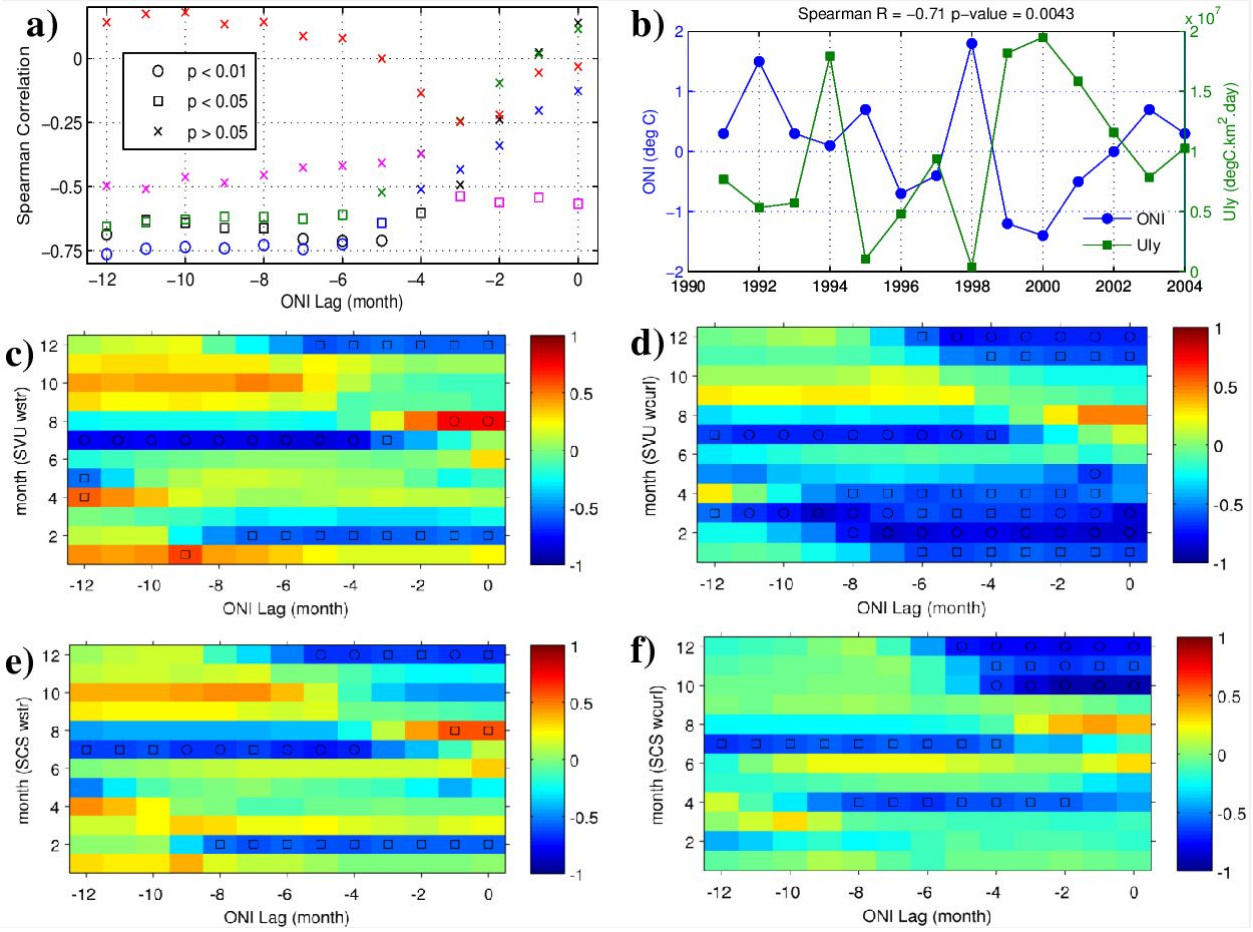

Figure 4.15. Upwelling and ENSO relations. (a) Correlations between ONI and Uly with lag from -12 to 0 months in the 6 simulations, with the same color convention as in Figure 4.3 (CTRL : black; Sim : green; SimA : red; SimO : blue; SimI : Magenta). (b) Yearly time series of Uly in CTRL and ONI index with a -6 month lag (highest correlation obtained in a). (c,d) Correlations between ONI and SVU wind stress and wind stress curl lag from -12 to 0 months. (e,f) Correlations between ONI and SCS wind stress and wind stress curl lag from -12 to 0 months.

To examine the possible contribution of ENSO to the interannual variability of the SVU, we first compute lagged correlations (from -12 to 0 month) between the yearly upwelling strength Uly (which combines the intensity, spatial and temporal indices) and the ONI index : 0 lag corresponds to the August ONI and -6 lag to the previous February ONI (Figure 4.15a). For the CTRL simulation, we obtain significant correlations ($p < 0.05$) for a lag of -12 to -4 months between Uly and ONI, with strongest correlation of -0.71 ($p<0.01$) for a -6 months lag (Figure 4.15a,b). This indicates that the ENSO conditions of the previous winter strongly influence the

strength of the summer SVU. This correlation is similar in terms of magnitude and time lag to the correlation between SST-based cold filament upwelling index and Nino3 index found by Xie et al., (2003; 0.67 and -6 month lag of Nino3 index) over the period from 1982 to 2002. The correlations between UIy and ONI for CTRL and SimO (where the interannual variability of the lateral ocean boundary conditions is removed) are very close, and SimO even shows slightly higher correlation with ONI (Figure 4.15a). This suggests that the interannual variability of the remote oceanic forcing, in particular the SCSTF between the SCS and the Western Pacific including the Luzon strait water exchange, is not involved in the effect of ENSO on the SVU interannual variability. In contrast, the low and nonsignificant correlations between ONI and UIy in SimA implies that the interannual variability of the atmospheric forcing (removed in SimA) plays a major role in the effect of ENSO on the SVU, in agreement with the results of Dippner et al., (2013) and Li et al., (2014). Removing the climatological river forcing slightly decreases the correlation between UIy and ONI in SimR compared to CTRL, with $p < 0.05$ but > 0.01. Finally, though SimI does not include any source of interannual variability (all the forcings are climatological), UIy surprisingly shows a significant correlation ($p<0.05$ but > 0.01) with ONI in SimI, yet with different lag-range from -3 to 0 month compared to CTRL. This is due to the fact that year 2000 is incidentally an extreme (high UIy) year for SimI, as for CTRL : removing 2000 from the UIy time series, the correlation drops to -0.51 ($p > 0.07$) for SimI, while it stays significant with $p<0.05$ for SimR, SimO and CTRL, and nonsignificant for SimA. This confirms that the correlation found in SimI is purely incidental and that the high correlations found in CTRL, SimO and SimR are physically meaningful, as will be confirmed by the physical analysis below.

The strong correlation of UIy with JJAS wind stress and wind stress curl found previously (Section 4.5.1) and the strong correlation of UIy with ONI (ONI leading by 4 to 12 months) agree with previous studies that suggested that ENSO could impact the SVU by modulating the summer monsoon (Lau and Yang 1997; Xie et al., 2003; Dippner et al., 2013). To check this hypothesis, we compute lagged correlations of the yearly time series of the monthly wind stress and wind stress curl averaged over the SVU domain (excluding land area) with yearly time series of monthly ONI, shown in Figure 4.15c-f for each month of the year and with ONI leading by 0 to 12 months. For summer months (JJAS), only the July wind has a significant correlation over the same range of ONI lead times (from 4 to 12 months). The highest correlation between ONI and July wind stress is -0.83 ($p < 0.01$) with ONI leading by 5 months, and the ONI correlation with wind stress curl is -0.73 ($p < 0.01$) with a 6 month lead, similarly to what is found between UIy and ONI. We conclude from this high correlation that ENSO winter conditions impact the SVU through their impact on the

SVU wind of the following July, that triggers the SVU through the mechanisms identified in Section 4.5.1 and 4.5.2 : direct Ekman pumping, strengthening of eastward jet and impact on the ocean vorticity field. However the low and nonsignificant correlations of ONI with wind stress and wind stress curl in June, August, and September and the fact that the SVU does not only occur in July but over the whole JJAS period (Figure 4.9d) also suggests that the strong ENSO impact on SVU (correlation = 0.71, $p < 0.01$) may not be due only to the ENSO modulation of the July monsoon. Since the important role of ocean vorticity in the SVU was shown previously, the second possible mechanism could be that ENSO also impacts the SVU by influencing the background ocean circulation in pre-upwelling seasons and thus pre-conditioning this ocean vorticity.

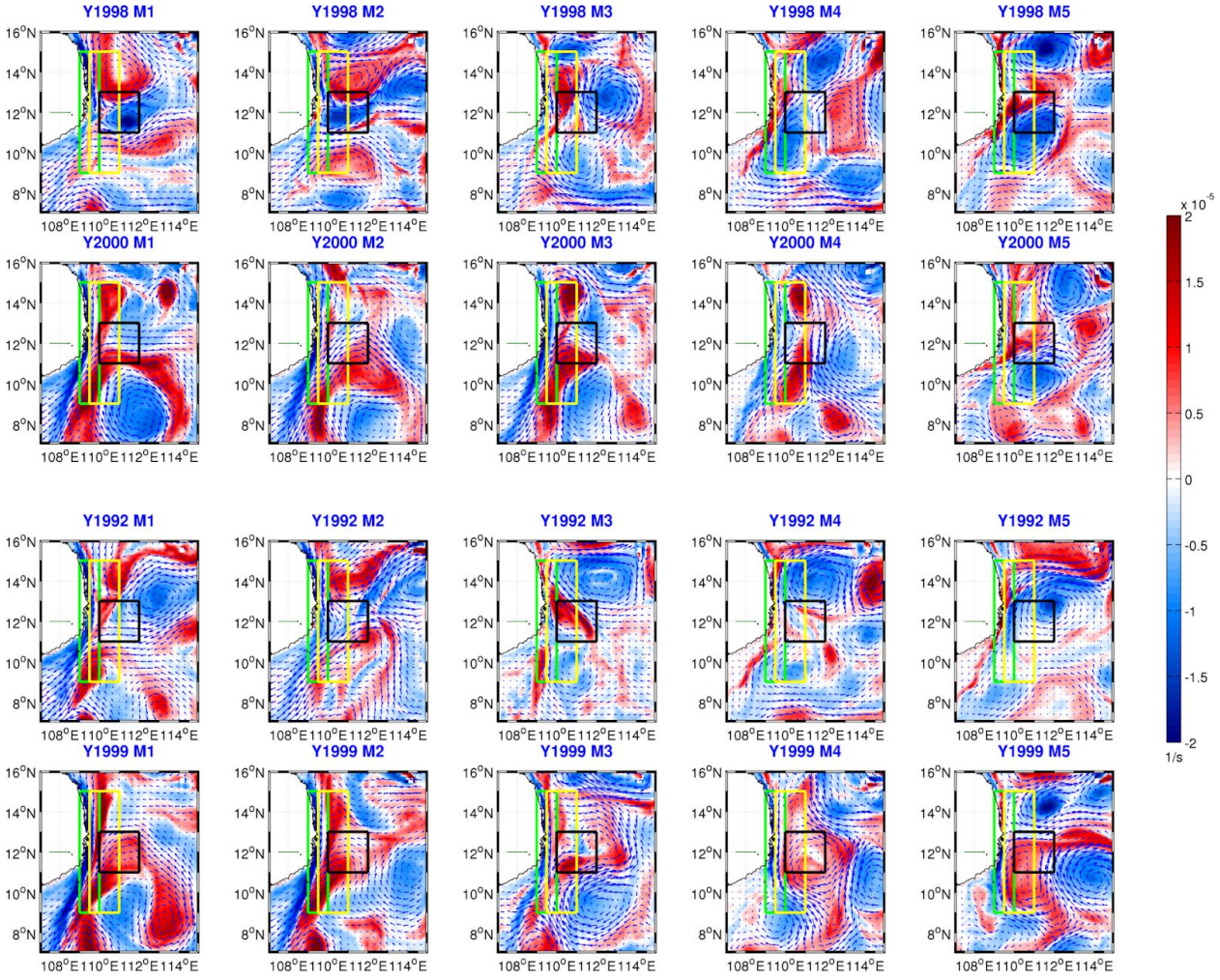

Figure 4.16: ENSO vorticity preconditioning mechanisms. Monthly mean surface vorticity (color, s^{-1}) and circulation (vectors, reference vector is 0.5 $m.s^{-1}$) from January to May of CTRL-1998 (upper panel) and CTRL-2000 (lower panel). Green rectangle show the boundaries for the calculation of western jet. Yellow and black rectangle show the boundaries for the calculation of jet induced vorticity (JET+ zone) and vorticity in OFF+ zone respectively.

The first hint for this mechanism is the opposite vorticity within 110°-112°E in the SVU between CTRL-1998 (a post El-Niño summer) and CTRL-2000 (a post La

Niña summer) observed in Figure 4.9b at the beginning of June, when the summer monsoon is still weak for both years : the 11°-13°N zone is occupied by very strong negative vorticity in CTRL-1998, being positive in CTRL-2000. To understand where this difference in vorticity comes from, we show the evolution of surface monthly mean vorticity in the SVU region in the months leading up to the upwelling season, from January to May for CTRL-1998 and CTRL-2000 in Figure 4.16 (1st and 2nd lines). In January, CTRL-2000 has a strong continuous band of positive vorticity (6°N to 16°N) which is associated with the SCS western boundary winter jet and that persists until April. In May, the usual eddy dipole and eastward jet at 11°N starts developing. For CTRL-1998, in January, the western SCS winter jet and associated positive vorticity is weaker than in CTRL-2000 and is strongly modified by an anticyclonic eddy at about 12°N, 111.5°E. A series of anti-cyclonic eddies develop during the following months west of 111°E in both cases and tend to move westward, as noted by Xiu et al., (2010), but these anticyclonic eddies are much stronger in CTRL-1998 and reach the western boundary, contrary to CTRL-2000. The positive vorticity band produced by the strong winter western jet in CTRL-2000 acts as a barrier that prevents anti-cyclonic eddies from moving inward to the maximum summer wind stress zone west of 111.5°E (Figure 4.7b), whereas the much weaker band of vorticity in CTRL-1998 due to the weaker winter jet cannot stop anti-cyclonic eddies from moving nearshore, explaining the difference in the vorticity background at the beginning of June. This vorticity contrast observed for the post El-Niño year 1998 and the post La-Niña year 2000 also exists for the post El-Niño year 1992 and the post La-Niña year 1999 (Figure 4.16, 3rd and 4th lines), which are the two other years in the 1991-2004 period whose February ONI index magnitude are larger than 1 °C (Figure 4.15b). The comparison of the weak SVU / strong post El-Niño years 1992, and 1998 and the strong SVU / strong post La-Niña years 1999, and 2000 in CTRL therefore suggests first, that the winter and spring ocean circulation and associated vorticity field can precondition the summer vorticity field that was shown to influence the SVU development in Section 4.5.2, and second, that ENSO could influence the SVU by modifying this winter and spring circulation.

To confirm this hypothesis elaborated from case studies and to understand how ENSO could affect this background circulation, we performed statistical analysis of indicators of ENSO, wind, circulation and SVU. Firstly, Figure 4.15c,d,e,f shows the correlation for each month of the year of monthly wind stress and wind stress curl over the SVU and whole SCS with lagged ONI. The winter wind field over both the SCS and the SVU is highly anti-correlated with ONI, with $p < 0.05$, including the wind stress in December and February over both the SVU domain and SCS, and the wind stress curl from October to December and in April for the SCS and from November

to May for the SVU domain. ENSO conditions therefore impact on winter and spring wind conditions preceding the SVU summer period, both in the SVU region and whole SCS. Strong La-Niña/El-Niño events induce a wind increase/decrease, as was suggested by previous studies (Lau and Yang, 1997; Chou et al., 2003; Liu et al., 2012; Dippner 2013). Secondly, many studies (Wyrtki, 1961; Shaw and Chao, 1994; Hu et al., 2000; Liu et al., 2008) considered that the SCS circulation is mainly driven by monsoon winds, in particular the southward western boundary winter jet. Our study indeed confirms that the winter western jet strength (quantified here as the surface meridional southward velocity averaged over 109°E - 110°E and 9°N - 15°N, see green box in Figure 4.16) is highly correlated with wind stress over the SCS and the SVU regions in winter : we obtain correlations of respectively 0.84 ($p < 0.01$) and 0.82 ($p < 0.01$) for the February yearly time series. By its effect on the winter wind, ENSO conditions therefore influence the winter boundary jet, strong La-Niña/El-Niño events inducing an increase/decrease of the wind hence of winter jet strength. Thirdly, as suggested by the 1992, 1998, 1999 and 2000 case studies, the positive vorticity band in the vicinity of the winter jet is related to the strength of this winter jet : there is a correlation of 0.85 ($p < 0.01$) between the average vorticity in the 109.5°E-111°E and 9°N - 15°N area (called JET+ zone hereafter due to dominant positive vorticity induced by the winter jet, see yellow box in Figure 4.16) in February and the winter jet strength in February. These correlation results therefore confirm that ENSO impacts the winter jet and thus winter vorticity through the modulation of winter wind stress and curl : the impact of strong La-Niña/El-Niño events on the winter wind results in a positive/negative anomaly of winter vorticity in the JET+ zone.

Could this ENSO signature on the winter vorticity field persist until summer, contributing to the ENSO influence on the summer vorticity field, and hence on the SVU ? We actually found no significant correlation between the winter vorticity and pre-upwelling or summer vorticity for our 14 years of the CTRL simulation in the SVU region, suggesting that on average, there is no memory in summer of the winter vorticity conditions. We then examined only intense ENSO years, determined using a -1/+1°C ONI threshold : we construct intense La-Niña composites based on the 1999, 2000 years, and El-Niño composites based on the 1992, 1998 years and the average composite with the other 10 years. We then compute the average monthly vorticity in the JET+ and OFF+ (the black box in Figure 4.16) zones for those 3 composite years from January to September (Figure 4.17). There is a significant negative vorticity anomaly in JET+ for the El-Niño composite compared to the average composite in winter, from January to May, due to the reasons explained above (ENSO weakens the winter wind thus the winter jet and vorticity). This

anomaly begins to decrease in May. In the OFF+ zone, where the offshore SVU usually develops, the negative vorticity anomaly for the El-Niño composite begins to develop in April and is strong and significant from May to July. This negative vorticity anomaly in the JET+ and OFF+ regions is associated to the movement of anticyclonic eddies from the south/north into the OFF+ area due to the weakening of the western boundary jet and associate barrier effect shown above for respectively the intense El-Niño years 1998/1992. Chang et al. (2010) showed that the generation and north-south movement of anticyclonic eddies in the SCS is related to the relaxation of weakened (due to El-Niño) winter NE monsoon-induced water set up in the southern SCS in spring and to the weaker than normal state of the western jet. The above case studies and this evolution of the vorticity field in the western winter jet region (JET+) and in the region of offshore SVU (OFF+) thus support our hypothesis that for intense El-Niño years, the negative ocean vorticity anomaly induced by the weaker winter wind in the coastal current region persists during the spring from the JET+ to the OFF+, hence participates to the negative vorticity anomaly in summer in the offshore SVU region thus to the SVU annihilation. For the intense La-Niña year composite the vorticity stays within the standard deviation range both for JET+ and OFF+ during the pre-upwelling period (Figure 4.17), suggesting that the situation for those years is not significantly different than the average situation.

In summary, ENSO conditions of the preceding winter impact on the interannual variability of the SVU through two mechanisms. Firstly, and at the first order, ENSO conditions have a direct impact on the summer monsoon, in particular on the July wind stress and wind stress curl, with stronger/weaker wind driving a stronger/weaker SVU in post La Niña/post El-Niño years. This ENSO-induced variability of summer wind triggers the variability of the SVU through its effect on direct Ekman pumping, eastward jet strength and ocean vorticity field examined in section 4.5.2. Secondly, for intense El-Niño years only, ENSO conditions modify the interannual variability of the SVU by preconditioning the ocean vorticity through their effect of winter wind. During other years (average and La Niña), the winter boundary current provides a barrier to the westward propagating eddies impinging into the coastal region, and when the winds reverse in summer, the coast is clear for the development of summer coastal upwelling, the eastward jet, and an intense dipole which favors the offshore SVU through wind-ocean vorticity interactions explored in section 4.5.2. In contrast, for intense El-Niño years, the weak winter monsoon induces a weak western boundary winter jet which produces a negative vorticity anomaly on its western side and is not able to act as a barrier to negative vorticity associated to anticyclonic eddies. Finally, this analysis is based on a 14-year

simulation having only 2 strong El Niño and 2 strong La Niña events, which is relatively short to be statistically robust for analysing ENSO events. High-resolution simulations performed over longer periods would be necessary to confirm if this preconditioning effect induced by intense El-Niño conditions is statistically significant.

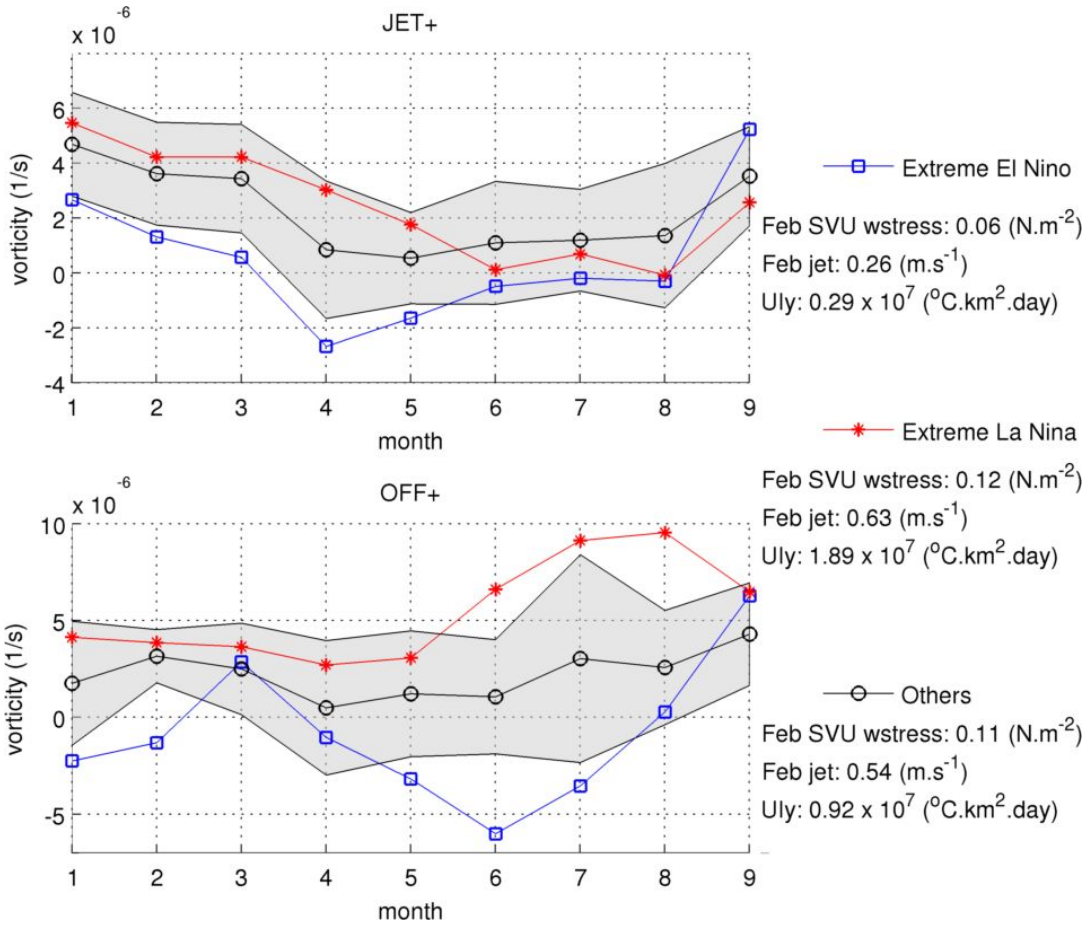

Figure 4.17: Significance of ENSO vorticity preconditioning in JET+ and OFF+ regions. Monthly-spatial mean surface vorticity (s^{-1}) in JET+ zone (109.5°E-111°E and 9°N - 15°N) and OFF+ zone (110°E-112°E and 11°N - 13°N) for composites of extreme El-Niño years (1992, 1998 with February ONI > 1 °C), of extreme La Niña years (1999, 2000, with February ONI < -1 °C) and of the other years of the period 1991-2004. The shaded area represents the +/- 1 standard deviation range. The values of average SVU February wind stress, February western jet strength, and yearly Uly SVU index for each composite are shown on the right.

4.6 Summary of main results

In summary, strong SVU years are offshore-dominant with upwelling centers located within 11-12^{o}N and 110-112^{o}E whereas weak SVU years are coastal-dominant with upwelling centers located near the coast and over a larger latitude range (10-14^{o}N). Coastal upwelling variability is strongly related to the variability of the eastward jet that develops from the coast, whereas offshore upwelling variability is related to the spatio-temporal interactions of cyclonic eddies with wind stress curl. The strong SVU variability is mainly impacted by the summer monsoon, and by OIV whose contribution reaches 50% of the total variability. Ocean and river forcing also modulate the SVU variability due to their contribution to eddy field variability. All of these factors interact in a strongly non-linear way. Most of the years with strong SST-based upwelling index also have strong vertical upward velocity. These two types of upwelling index disagreed in some years such as 1991. This is due to the inference of pycnocline depth background modulated by ocean eddies as well as the limitations of w-based upwelling index on the sensitiveness to reference depth chosen and on locating the upwelled water on the surface. ENSO has a strong influence on SVU, mainly due to its direct influence on summer wind. For intense El Niño years only, weaken winter monsoon conditions could further weaken the SVU through their impact on the background vorticity field in the pre-upwelling season.

Chapter 5. Sensitivity of results to the model configuration choices : surface bias correction and river freshwater fluxes

CTRL was used as the reference simulation for the model evaluation in Chapter 3 and for the assessment and explanation of the SVU interannual variability in Chapter 4. In this chapter, we explore the sensitivity of our results and our conclusions to the choices of configuration of this reference simulation.

5.1 Configuration of the reference simulation : impact of the surface bias correction method and the river mouth locations.

Relaxation and surface forcing corrections are two commonly used methods for reducing SST bias and model drifts. Previous results presented in Chapters 3 and 4 were obtained based on the CTRL and sensitivity simulations that used a combination of the two methods (Section 2.2 and 2.3):

- The additive heat flux correction of the initial atmospheric CFSR heat flux was computed from an initial simulation with a strong relaxation coefficient (120 $W.m^{-2}.K^{-1}$), and using a temporal filter (climatological monthly mean) and a spatial filter of ~1000 km (see Section 2.2).
- Additionally to this heat flux correction, a weak relaxation (coefficient of 40 $W.m^{-2}.K^{-1}$) towards the CFSR SST and SSS fields was applied, in order to further reduce the SST bias and drift.

The resulting CTRL simulations showed weak biases of SST (0.2°C) and SSS (-0.09 psu) and slightly stronger interannual SST trends compared to the observed fields (CTRL : 0.05°C.$year^{-1}$ vs. 0.04°C.$year^{-1}$ for the observations), as shown in Table 5.1. Table 5.1 provides a summary of the evaluations of the testing simulations performed here for three groups of quality indices: temperature, salinity and sea level anomaly. Data used in the evaluation of these indices are the same as those used to evaluate the CTRL simulation in Chapter 3 (AVHRR, SCSPOD14 and SSALTO-DUACS). Performances of the forcing model ORCA are indicated as a

reference. For a given index, values in blue/red correspond to a significant improvement/worsening compared to ORCA, and values in black correspond to values similar to ORCA.

Despite a weak relaxation coefficient, the SST relaxation constrains the surface dynamics in the CTRL and sensitivity simulations. Therefore, the variability of the SVU indices as well as the contributions of different forcings may have been under/overestimated in those simulations. In order to estimate the impacts of the relaxation on the SVU variability and assess the robustness of the results presented above, we present here several tests performed to find the best simulation without relaxation. Comparisons are also made between the relaxed and non-relaxed simulations, focusing on the results of the SVU variability. Before that, we also present a test done to improve the river freshwater plume representation for the Pearl River Bay.

5.1.1 Test on the Pearl River plume representation.

The Pearl River waters flow into a huge semi-enclosed bay located in the North of the domain before reaching the open ocean (see Figure. 3.5). CTRL realistically reproduced the SSS spatial and temporal variability overall (as shown in Chapter 3), but failed to reproduce correctly the Pearl River plume because of two reasons: we applied E-P-R at points located inside the Pearl River bay which, when combined with the lack of volume and momentum fluxes associated with the E-P-R method, resulted in a very localised effect of the river discharge only, that did not propagate into the open ocean outside of the bay. We thus changed the Pearl River mouth configuration to improve the SSS field in the Pearl River offshore plume : for that we “removed” the Pearl River Bay additional river correction and applied the E-P-R fluxes at points located at the exit of the river and bay mouth so that the open ocean dynamics can interact with, mix and advect offshore the freshwater coming from the Pearl river.

The resulting CTRL2 simulation has the same settings as the CTRL presented above, but with the new Pearl river freshwater distribution. Both CTRL and CTRL2 are significantly improved compared to ORCA. The representation of the SSS in CTRL2 is similar to the one in CTRL over the large scale (Table 5.1) and is slightly improved compared to CTRL near the Pearl river mouth in summer (rainy season, Figure A1 in Appendix-A1). CTRL2 is also similar to SCSPOD, both showing a band of low SSS from the Pearl river mouth to the Taiwan Strait in summer due to an anti-cyclonic surface circulation of the SCS which does not exist in CTRL.

However the meridional extent of this low SSS band is much smaller than in SCSPOD14 data and will still need further improvements.

Table 5.1 Evaluations of different simulations and impacts of Relaxation (R) and Heat and Water flux correction (HF, WF). Forcing model output (ORCA) is taken as reference for comparisons. Values in blue means being significantly improved compared to ORCA; values in red means being significantly worse than ORCA and values in black means not significantly different from ORCA. Significance are defined as: (∓ 0.05) for all correlation, (∓ 0.1 °C) for MAE, Bias of SST, (∓0.05 psu) for MAE, Bias of SSS, (∓0.5 cm) for MAE of SLA, (∓0.01 °C) for SST trend, (∓0.1 cm) for SLA trend

					New River locations					
				CTRL	CTRL2	Test 1	Test 2	Test 3	Test 4	Test 5	Test 6
		index	ORCA	HF corr (spatial + clim filter), relax40	HF corr (spatial + clim filter), relax40	no corr, no relax (Analysis based on 1991-1995)	no corr relax 40	no corr relax 120	HF, WF corr (spatial + clim filter)	HF, WF corr (clim filter)	HF, WF corr (no spatial filter, monthly time filter)
SST Bias (deg C)		1	1.01	0.20	0.15	3.27	1.31	0.54	0.51	0.47	0.56
SST annual corr		2	0.98	0.98	0.98	0.87	0.94	0.98	0.98	0.98	0.98
SST annual MAE		3	1.01	0.21	0.18	3.27	1.31	0.54	0.51	0.47	0.56
SST interann MAE		4	1.01	0.21	0.18	NaN	1.31	0.54	0.66	0.65	0.56
SST interann Trend (data = 0.04)		5	0.01	0.05	0.05	NaN	0.05	0.04	0.10	0.12	0.06
SST Interann (corr)		6	0.63	0.76	0.72	NaN	0.75	0.80	0.31	0.36	0.82
SST Spatial corr	summer	7	0.74	0.76	0.76	0.46	0.70	0.86	0.59	0.76	0.81
	winter	8	0.98	0.98	0.98	0.83	0.97	0.99	0.96	0.98	0.98
SST Spatial MAE	summer	9	0.91	0.29	0.30	10.40	1.44	0.60	0.58	0.45	0.53
	winter	10	1.15	0.37	0.36	7.66	1.19	0.56	0.68	0.66	0.72
T-profile MAE clim, 3 stations	0-200m	11	1.13	0.73	0.67	2.89	0.96	0.77	0.71	0.66	0.68
	200-1500 m	12	0.56	0.56	0.55	0.49	0.58	0.56	0.58	0.53	0.55

a) Temperature indices

			ORCA	CTRL	CTRL2	Test 1	Test 2	Test 3	Test 4	Test5	Test 6
SSS bias (psu)		13	-0.28	-0.09	-0.17	-21.54	-0.17	-0.20	-0.06	-0.03	-0.02
SSS annual MAE		14	0.28	0.13	0.18	21.54	0.18	0.22	0.12	0.12	0.12
SSS annual cycle correlation		15	0.92	0.85	0.85	0.77	0.82	0.71	0.92	0.95	0.92
SSS interannual Trend (CFSR = 0.00)		16	-0.01	0.00	0.00	Nan	0.00	0.00	-0.02	-0.02	-0.01
SSS Spatial corr	summer	17	0.62	0.73	0.70	0.59	0.71	0.76	0.62	0.65	0.64
	winter	18	0.77	0.89	0.88	0.81	0.88	0.89	0.76	0.77	0.82
SSS Spatial MAE	summer	19	0.34	0.25	0.25	0.52	0.24	0.24	0.43	0.40	0.38
	winter	20	0.29	0.21	0.21	0.39	0.20	0.20	0.31	0.30	0.27
S-profile MAE clim, 3 stations	0-200m	21	0.26	0.23	0.22	0.58	0.26	0.22	0.27	0.27	0.28
	200-1500m	22	0.07	0.09	0.09	0.09	0.09	0.09	0.09	0.09	0.09

b) Salinity indices

			ORCA	CTRL	CTRL2	Test 1	Test 2	Test 3	Test 4	Test 5	Test 6
SLA spatial corr	summer	23	0.96	0.96	0.96	0.91	0.97	0.95	0.96	0.96	0.95
	winter	24	0.97	0.95	0.95	0.89	0.96	0.96	0.94	0.95	0.96
SLA spatial MAE (cm)	summer	25	2.91	2.16	2.09	3.38	1.97	2.22	2.08	2.01	2.20
	winter	26	2.49	2.12	1.79	3.49	1.92	1.94	2.01	2.00	1.84
SLA annual cycle	corr	27	0.79	0.85	0.85	0.90	0.85	0.81	0.84	0.87	0.84
	MAE	28	1.36	1.15	1.05	0.37	1.05	1.29	1.03	1.06	1.02
SLA interann	corr	29	0.74	0.77	0.78	NaN	0.73	0.77	0.78	0.74	0.77
	MAE	30	3.28	2.98	2.93	NaN	2.94	3.03	3.17	3.18	2.81
	Trend (data = 0.44)	31	1.41	1.25	1.22	NaN	1.21	1.23	1.34	1.36	1.20

c) SLA indices

5.1.2. Tests on the surface biases correction method.

After having improved the Pearl River plume representation in the open ocean, in this section we present sensitivity simulation tests constructed to evaluate the impacts of the relaxation (Tests 1, 2, 3) and heat and water flux corrections (Tests 4, 5, 6) on the model performance. All of the tests presented in the following (from 1 to 6) use the same river mouth settings as in CTRL2 (i.e. no Pearl River bay). The first group includes:

- Test 1 used the original CFSR heat and water fluxes but without the heat and water flux correction terms, nor the SST and SSS relaxation terms, which leads to a blow up of the model in December 1995. Test 1 shows a very strong SST bias and a MAE of 3.3 °C over the entire period and a bias of 10.4 °C compared to the AVHRR SST over the period 1991-1995. Almost all of the indices in Test 1 are significantly worse than ORCA's. This highlights the importance of correcting the surface bias and drifts, either using flux corrections or surface relaxation.
- In Test 2 we then introduced a SST and SSS relaxation only with a coefficient of 40 $W.m^{-2}.K^{-1}$. With this weak relaxation, Test 2 didn't blow up and shows some improvements compared to ORCA, however the SST bias remains very large at 1.31 °C (Table 5.1a).
- Using a stronger relaxation coefficient of 120 $W.m^{-2}.K^{-1}$, Test 3 shows a much better performance than Test 2 in terms of the temperature indicators (eg. SST bias is only 0.54°C, Table 5.1a). It gives a similar good performance to Test 2 in terms of the salinity and SLA indicators in Table 5.1b,c compared to ORCA. However the strong relaxation coefficient used here prevents the model from producing its own surface small scale dynamics. We therefore mainly use this simulation to compute heat and water flux corrective terms for the following tests, as explained below.

In the second group which includes Tests 4-6, we remove the surface relaxation term and only use an additive atmospheric flux correction method, following the method presented in section 2.3, both for temperature and salinity. The heat and water flux correction equivalent to the strong SST and SSS relaxation are computed using the following formula:

$$HFcorr = -120 \times (SST_{Test3} - SST_{CFSR}) \quad (5.1)$$

$$WFcorr = -\frac{120}{SSS_{Test3}} \times (SSS_{Test3} - SSS_{CFSR}) \quad (5.2)$$

The water flux correction is applied over the whole SCS domain, except for the grid points used to specify the river discharge in Tests 4,5,6. Further adjustments to this *HFcorr* and *WFcorr* are applied differently in Tests 4,5,6:

- In Test 4, we use a climatological-monthly mean version of the *HFcorr* and *WFcorr* fields smoothed with a 1000 km moving window spatial filter. These correction terms are then added to the net heat and water fluxes in the forcing files. Therefore the heat and salt correction in Test 4 does not include high frequency or inter-annual variable signals, nor the small spatial scale structures. This is similar to the CTRL and CTRL2 processing, but without the relaxation term. Table 5.1a shows that most of the SST indicators in Test 4 are significantly improved compared to ORCA's, except for 3 indicators: the SST interannual trend (0.1 ^{o}C.year^{-1} vs. 0.01^{o}C year^{-1} for ORCA, with an AVHRR data trend of 0.04^{o}C.year^{-1}); the SST interannual correlation (0.31 vs. 0.63 for ORCA) and the SST summer spatial correlation (0.59 vs. 0.74 for ORCA). These indicators are very important for the SST-based upwelling index that we build and thus need to be improved. In addition, the summer SSS spatial MAE in Test 4 is also significantly worse than ORCA.
- In Test 5, we apply only the climatological mean monthly filter used in Test 4 but with no spatial filtering on *HFcorr* and *WFcorr*. This leads to similar performances for Test 5 compared to Test 4 for most of the indicators, and further improves the summer spatial correlation of SST (0.76 vs. 0.59 for Test 4).
- In Test 6, we only apply the temporal monthly filter (without taking the climatological mean nor applying the spatial filter) so that the *HFcorr* and *WFcorr* can vary interannually and at smaller scale. This choice of filter lead to further improvements in the interannual temperature indices: the SST interannual trend is reduced from 0.12 ^{o}C.year^{-1} in Test 5 to 0.06 ^{o}C.year^{-1} in Test 6, which is much closer to the trend from AVHRR data of 0.04 ^{o}C.year^{-1}. The SST interannual correlation increases from < 0.4 in Test 4 and 5 to 0.82 in Test 6.

This brief analysis has mainly detailed how the SST indices respond to the different surface bias correct tests, but the results are consistent for the other SSS and SLA indices in Tables 5.1b and c.

The Test 6 simulation appears to be our best “no relaxation” simulation for the indicators presented in Table 5.1. In the following, the SVU indices in Test 6 will thus be compared to those in CTRL and CTRL2 to evaluate the impacts of the SST and SSS bias correction methods on the representation of SVU variability and resulting conclusions. Test 6 will be named as NoRel (no relaxation) in the following.

5.2 Adjustment of T0, and Tref

The annual mean SST bias over the SCS modeled domain slightly differs in CTRL, CTRL2 and NoRel (see Table 5.1). The summer mean SST biases are also different, with a mean summer SST bias relative to the CTRL simulation equal to 0.01ºC for CTRL2 and 0.39ºC for NoRel. These offsets will impact on the detection of summer upwelling events in the SCS and SVU since we use an absolute temperature threshold T0 to define this, as explained in Section 4.1. T0 take into account the difference in the mean SST biases between those simulations, the threshold temperature T0 used in CTRL, CTRL2 and NoRel are computed by adding the corresponding bias difference to the reference temperature T0 used in CTRL (27.5°C, see section 4.1) and is therefore 27.5ºC, 27.51ºC and 27.89ºC respectively.

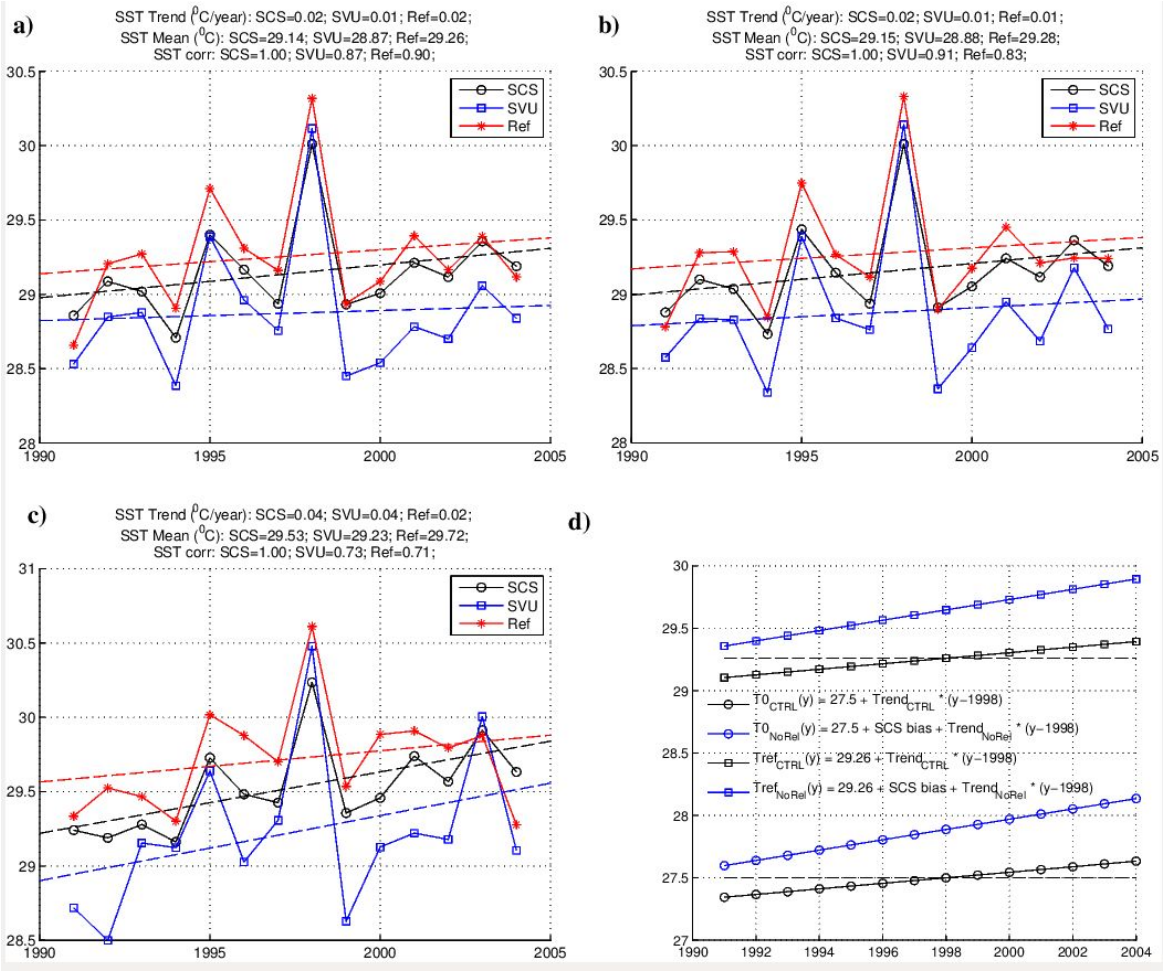

Figure 5.1 : The calculation of T0 and Tref in CTRL, CTRL2 and NoRel. Time series of annual SST and associated trend (dashed lines) over the SCS, SVU and reference area (REF: 9-16ºN, 117-120ºE) for CTRL (a), CTRL2 (b) and NoRel (c), with corresponding values indicated in the title. (d) Computation of upwelling criteria (T0) and reference temperature (Tref) for CTRL and NoRel based on SCS SST trends and bias and mean upwelling criteria and reference temperatures of CTRL . With the same trend and bias of 0.01°C, T0 and Tref used in CTRL2 would be similar to CTRL and are not shown for clarity.

Figure 5.1 a,b,c shows the summer mean SST over the SCS, SVU and reference area of CTRL, CTRL2 and NoRel (data in the Sulu Sea and Malacca Strait were masked out from the computation). Besides the SST biases, all of the simulations show positive SST trends of 0.02, 0.02 and 0.04 ^{o}C/year in CTRL, CTRL2 and NoRel respectively. Previous upwelling criteria (T0 and Tref) were fixed for the whole period for simplicity and also due to the very small trend of SST in CTRL. For a fair comparison between CTRL, CTRL2 and NoRel, the respective bias and trends of the simulations must be accounted for. For that, the T0 values given above for each simulation (i.e., CTRL: 27.5^{o}C, CTRL2: 27.51^{o}C and NoRel: 27.89^{o}C) are centred in the middle of the period (the year 1998), and the SCS SST CTRL trend is then applied to compute trend-corrected T0 values of CTRL in other years. We apply exactly the same method for the computation of the reference temperature Tref computation. Figure 5.1 d illustrates the computations of T0 and Tref in the simulations.

5.3 Variability of the SVU associated with the relocation of the Pearl river, heat and water flux filters and SST-SSS relaxation.

Figures 5.2 - 5.4 show the cumulative upwelling intensity of CTRL, CTRL2 and NoRel respectively. The impact of the Pearl river relocation in CTRL2 is significant when comparing the cumulative upwelling intensity interannual maps of CTRL2 and CTRL in the SUV region, though at the first look the interannual variability of the spatial extent and intensity of the SVU is comparable in both simulations (Figure 5.3 vs. 5.2). The upwelling in the years 1995, 1998 and 2003 remains coastal and weak and the offshore upwelling in 1994 and 2001 remains strong. However the upwelling centers in the years following the strong La Nina of 1999 and 2000 are weaker in CTRL2, and no longer offshore. Whereas the years from 2001 to 2004 have generally stronger offshore upwelling in CTRL2 than CTRL.

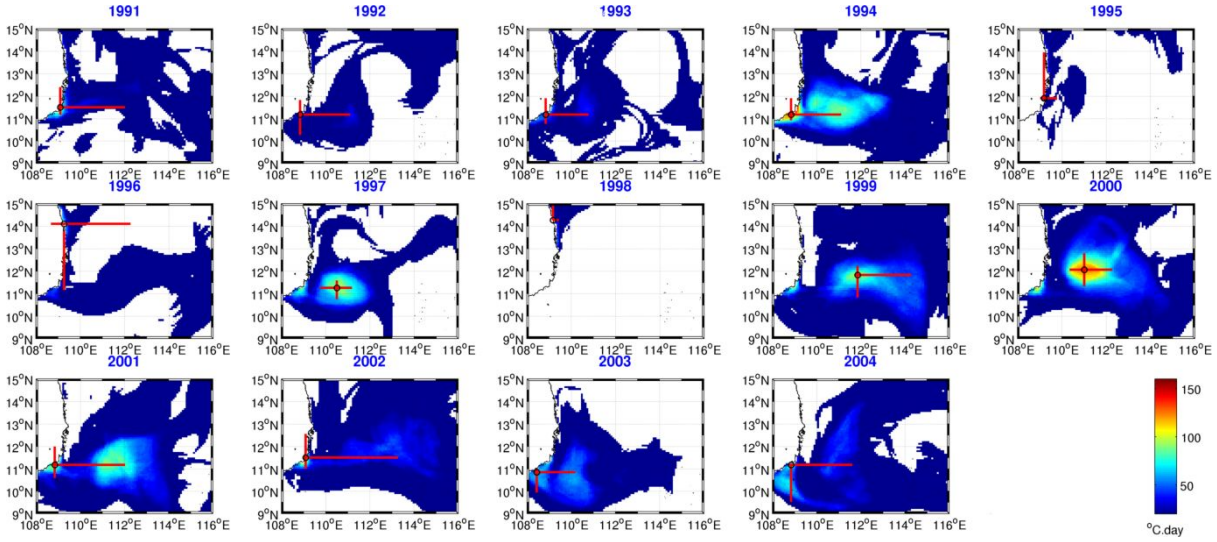

Figure 5.2 CTRL cumulative upwelling intensity (new method of computation)

These results are quite different, even though we are simply changing the climatological monthly mean river component in the spatial distribution of E-P-R, at a remote site near the Pearl River at 22°N, far from the SVU region. This is enough to modify the T/S distribution in the SVU region. Although we have not had time to explore the stability and barrier layer changes adjacent to the Pearl river that lead to this substantial modification in the Uly, it is one of the perspectives that we wish to develop (see Chapter 6).

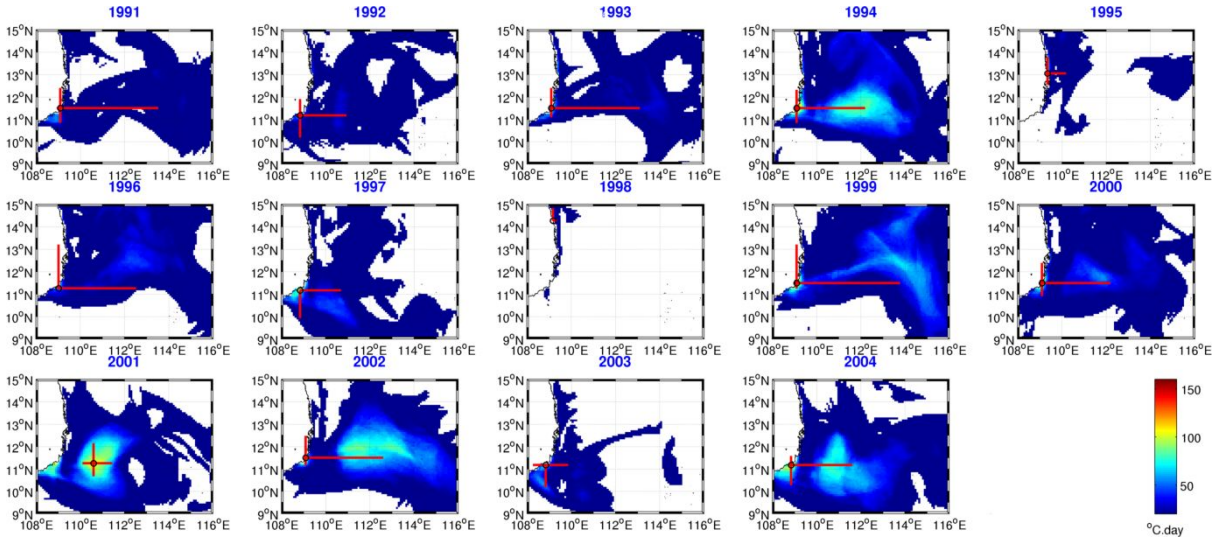

Figure 5.3 Cumulative upwelling intensity of CTRL2 (similar to Figure 5.2)

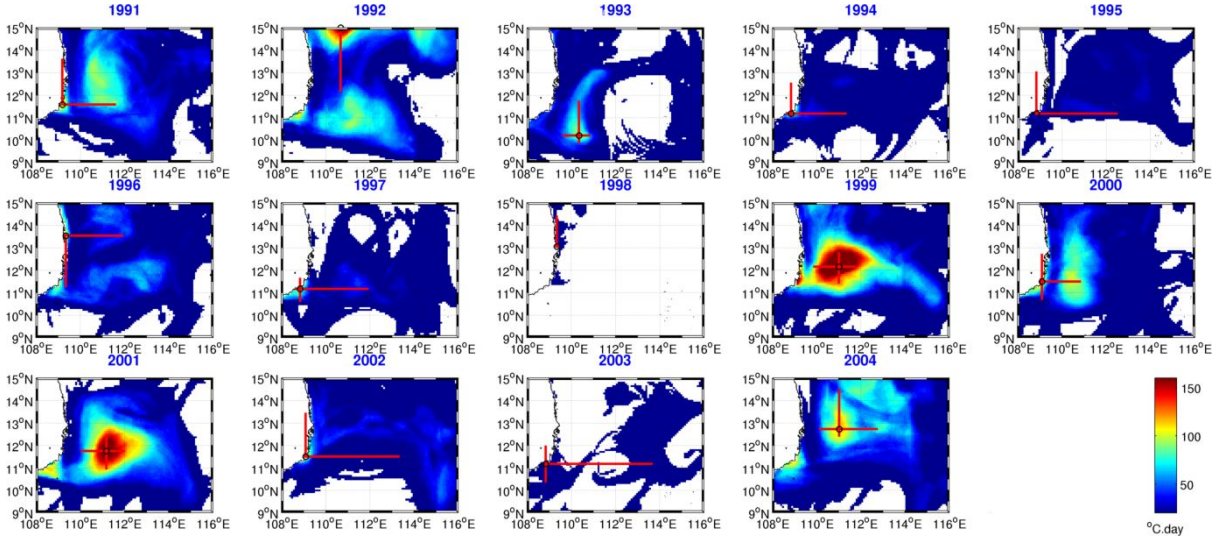

Figure 5.4 Cumulative Upwelling intensity of NoRel (similar to Figure 5.4)

Comparing Figure 5.4 and 5.3 reveals that the SST and SSS relaxation weakens the upwelling variability in time and space in CTRL2 compared to NoRel. The most striking difference is the stronger offshore upwelling in half of the period of NoRel: 1991-1993, 1999-2001, 2004 (Figure 5.3 vs. 5.4). The offshore upwelling center in CTRL, CTRL2 always occurs within 11-13ºN which coincides with the band of strongest wind stress curl (Figure 4.7). For NoRel, the offshore upwelling centres often extend up to 14°N, in 1991 1999, 2000, 2001 and 2004.

There is an unusually strong offshore upwelling in NoRel 1992 that is not associated with the SVU, but results from the southward propagation of a strong cyclonic eddy originating from the Luzon Strait in winter (Figure 5.5). We tracked this eddy by plotting SST contours of the whole region; and the existence of the eddy is revealed by closed circles of SST contours. The values of these contours were chosen empirically to show how its SST in the center evolves with time and that in

summer, its SST in its center still fits the upwelling criteria SST <27.5°C which is the reason why it should be excluded from analysis. Using SLA or vorticity to track the eddy wouldn't give this advantage. In March, this cyclonic eddy is located at [118°E , 19°N] with a very cold SST of 20°C in its core. It moves southwestward along the continental shelf and is almost broken at the end of June due to interaction with the shallow plateau near 112°E and 16.5°N. The local summer positive wind stress curl helps to maintain the eddies until the end of the season (not shown). From July to August, part of the eddy centre is within the SVU domain and its temperature at center is only from 24 - 25°C which fits the upwelling criteria. To avoid including this non-SVU event in the computation of SVU indices used to analyse SVU interannual variability, we have reduced the northern boundary of the previous SVU domain used in Chapters 3 and 4 from 15°N to 14°N : this domain covers most of the SVU activities in CTRL2 and NoRel, but excludes the anomalous 1992 event. The reference area is, however, enlarged at its northern boundary (from 15°N to 16°N) and eastern (from 118°E to 120°E) boundaries for a more stable climatological value.

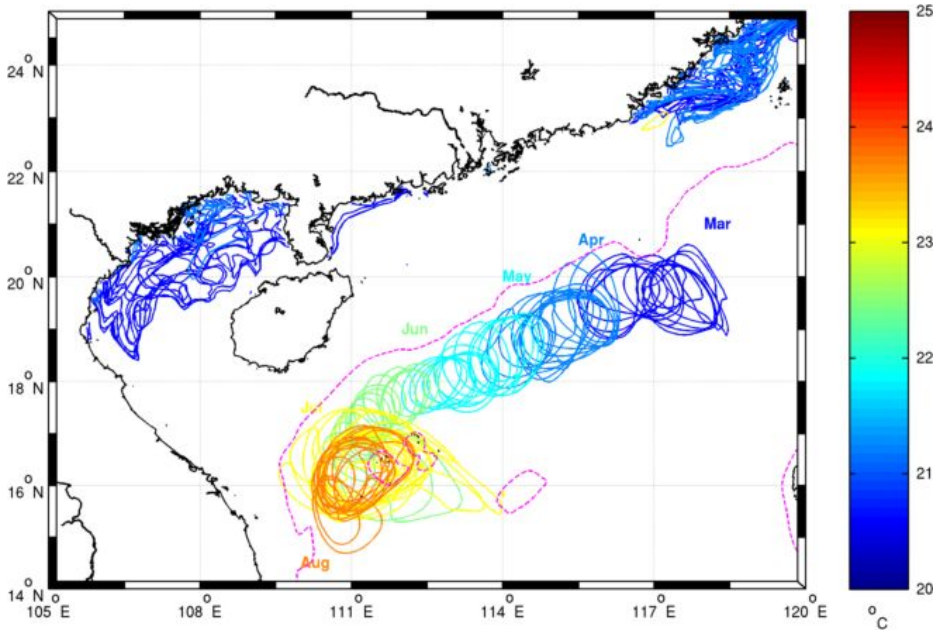

Figure 5.5: The movement of a strong eddy in 1992. Contours represent SST from 20°C in March to 25 °C in August with 1°C increment after each month. Magenta dashed contour show bathymetry of 500m.

Based on the new domain, the annual upwelling strength index UIy in CTRL, CTRL2, NoRel are computed and shown in Figure 5.6a. Comparing the UIy in CTRL and CTRL2 quantifies the significant impacts of the Pearl river relocation to the SVU. The correlation of the UIy between CTRL and CTRL2 is 0.72 ($p<0.01$). The mean value and standard deviation of the UIy in CTRL2 are both larger than CTRL by 0.05 x 10^7 °C.km^2.day, i.e. by about 5% and 8 % (Figure 5.6a) respectively. These changes in the mean and variability of the UIy due to the relocation of river are of the same order as the modulation by turning off river discharge in SIMR computed in Section 4. This modulation of UIy is mainly due to changes in offshore upwelling

activities which we showed above to be strongly impacted by mesoscale eddy activity or, in other words, the SCS OIV. So we conclude that the difference between CTRL and CTRL2 due to the remote E-P-R specification near 22°N is mainly associated to the impact of OIV.

CTRL2 and NoRel are our two best simulations with and without the surface relaxation respectively (Table 5.1). We have quantified that the mean value and variability of the UIy in NoRel strongly increased by 0.63 x 10^7 $^oC.km^2$.day and 0.38 x 10^7 $^oC.km^2$.day respectively (ie. by 64% and 56%) compared to CTRL2, due to the stronger offshore upwelling activity observed in NoRel on Figure 5.6. So the mean strength and interannual variability of SVU in NoRel is stronger than in CTRL2 and CTRL, suggesting that the surface relaxation, by constraining the surface dynamics in our model, actually weakened the variability of the SVU.

5.4 Impacts of relaxation on the relation between SVU, wind, vorticity and ENSO

5.4.1 SVU Uly vs wind

Figure 5.6a shows the interannual variations of wind stress curl and Uly in CTRL, CTRL2 and NoRel for SVUD with the northern boundary at 14ºN. CTRL shows high (0.72) and significant ($p < 0.01$) correlation between Uly and wind stress curl in SVUD. This is similar but lower than the values found in Chapter 4, due to the slightly different SVU domain and the varying definition of To and Tref. Both CTRL2 and NoRel show a slightly weaker yet significant ($p < 0.01$) correlation of 0.67 between the wind stress curl and the Uly. Therefore the strong correlation between the summer wind stress curl in the SVU region and the SVU annual strength obtained in Section 4.5.1 is still obtained in the simulation with no relaxation, though slightly weaker. This shows that our conclusion regarding the important role of wind with respect to upwelling in the region is robust to the choice of the SVUD domain used, a varying river mouth location, and more importantly to the choice of surface correction method.

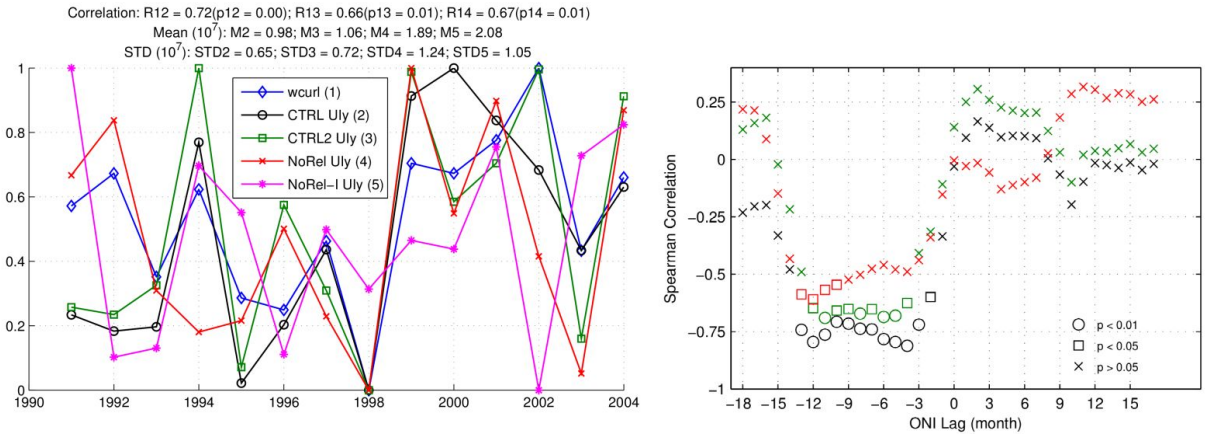

a) Uly vs wind **b) Uly vs ENSO**

Figure 5.6 Relation between Uly in CTRL, CTRL2 and NoRel with wind stress curl (a) and with ONI index (b).

5.4.2 Uly vs surface vorticity

In Chapter 4, we found a significant correlation (0.68, $p < 0.01$) between Uly of CTRL and the surface vorticity in the offshore SVU area OFF+ in summer (JJAS).

This confirmed the important contribution of the surface ocean vorticity and ocean eddy field in this band to the interannual variability of the upwelling strength. With the varying T0 and Tref, correlations between Uly and vorticity in OFF+ zone in CTRL, CTRL2 and NoRel remain high and significant, respectively equal to 0.75 ($p < 0.01$), 0.76 ($p < 0.01$) and 0.64 ($p < 0.02$). Therefore, the strong correlation between the ocean vorticity in OFF+ and the SVU Uly is still valid in NoRel, though slightly weaker. Our conclusion regarding the contribution of the ocean vorticity in the offshore SVU zone to the SVU strength is valid and robust, regardless of the choice of the location of the river input or the SST-SSS bias correction method.

5.4.3 Uly vs ENSO

Figure 5.6b shows the lagged correlation between the ONI and the Uly for the 3 simulations CTRL, CTRL2 and NoRel. The Uly in CTRL shows a highly significant correlation ($p <0.01$) for a 3 - 13 month lead of ONI. The CTRL2 Uly also have significant correlations ($p < 0.05$) for a 4 - 14 month lead of ONI. The Uly in NoRel still shows significant correlation ($p < 0.05$), but only for a reduced 10 - 13 month lead of ONI. Thus the relation between the ONI and the Uly becomes weaker with the river relocation in CTRL2 and when removing the surface relaxation in NoRel, but is still significant, suggesting that our conclusion regarding the impact of ENSO on the SVU is robust but that this impact may be slightly weaker than suggested by our original CTRL simulation.

In conclusion, the correlations between the Uly and the summer wind stress curl, ocean vorticity and ENSO remain significant in the CTRL2 and NoRel simulation, showing that our results concerning the impact of those factors on the SVU interannual variability are robust to the choice of configuration of the model concerning river mouth location and more importantly the surface biases correction. However, in NoRel, all those correlations slightly decrease, and the variability of the SVU increases, also suggesting that these impacts may be slightly weaker than suggested by CTRL, and that the impact of OIV may be stronger. We conducted another simulation the same as Sim-I but using climatological atmospheric forcing computed from atmospheric forcing used in NoRel and excluding SST-relaxation called NoRel-I. We found that the ratio of STD(Uly) between NoRel-I and NoRel is 84% compared to 47% between SimI and CTRL indicating a much stronger impact of the SCS OIV to the SVU interannual variability (Figure 5.6).

Chapter 6. Conclusion and future work

6.1. Objectives and methodology

The SVU is one of the major hydrodynamical processes of the South China Sea circulation and also impacts biological productivity hence fishing resources. Previous studies revealed a strong interannual variability of the SVU. The studies were based on in-situ/satellite observations or on numerical simulations of individual years, or from interannual time series obtained from models with resolution coarser than 1/4°. Those studies revealed the leading role of summer wind in triggering the SVU as well as the influence of ENSO, that was attributed to its direct effect on summer wind, but the precise mechanisms associated with those influences still needed to be clarified. They also raised the questions of the effects of the background circulation, OIV and river freshwater flux, and called for higher resolution numerical studies to better represent and understand the influence of those factors. In the present study, our objectives were first to quantify the interannual variability of the SVU in terms of strength and geographical distribution, and second to investigate the respective contributions to this variability of the atmospheric and remote ocean forcing interannual variability, of OIV and of river discharge, and to identify the underlying mechanisms.

For that, we used a group of 14-year numerical simulations performed for the 1991-2004 period over the whole SCS with a 1/12° resolution model able to represent the eddies, which are a major source of OIV, and their effect on the SVU. We performed a reference simulation where the model is forced at its open boundaries by interannually varying daily atmospheric and monthly oceanic fields, and by climatological monthly river freshwater discharges. We then performed a first set of sensitivity simulations where we vary those forcings to investigate the respective contributions of the different forcings. After that we performed another set of tests to examine the robustness of our results to the model settings (river mouth location, surface biases correction method, representation of tides).

We first compared our reference simulation CTRL with available in-situ and satellite observations of water masses hydrological characteristics and surface circulation. These comparisons show that CTRL reproduces correctly the annual and interannual cycles and spatial patterns of the surface and upper layer ocean characteristics and circulation. Its major weaknesses are a deep layer salinity underestimation and a SLA drift for the period 2002 – 2004 which is induced by a

similar drift in the large-scale ocean model used to derive the lateral oceanic forcing. The upper ocean thermal structure closely matches the observations. Our model can therefore be legitimately used to study the SVU that mainly occurs in the surface and upper layers.

6.2 Interannual variability of the SVU : estimation, driving factors and mechanisms

We developed upwelling indices in the SVU region, based on a surface temperature threshold criteria. We then used the reference simulation CTRL to quantify the SVU interannual variability. For the period 1991 - 2004, the upwelling indices built based on the CTRL simulation reveal a strong inter-annual variability of the SVU, especially in terms of spatial extent : the standard deviation of the yearly indicators represent 12% of the average value for the upwelling intensity (UIi), 17% for its temporal scale (UIt), 54% for the spatial scale (UIs) and 64% for the total strength (UIy) indicators (Table 4.1). CTRL produces very contrasted years, in agreement with conclusions from previous studies and with satellite SST observations. Years with only coastal SVU are mainly centered between 11°N and 12°N but can also extend over a wide meridional range from 10°N to 14°N (e.g. 1998, occurred at 14°N, the weakest and most northern SVU in our 1991-2004 period). Other years have both strong coastal SVU and strong offshore SVU covering a large part of the central SCS (e.g. 2000, the most intense and extended SVU in our period). Coastal SVU occurs for all the years, while offshore SVU develops during the years of strong SVU for which it often dominates the coastal SVU. The SVU develops during the June to September (JJAS) period.

Comparisons between the sensitivity simulations and the reference simulation have allowed us to quantify the respective contributions of the sources of variability. Our results show that the first factor introducing strong SVU interannual variability is the interannual variability of atmospheric forcing. Including the interannual variability of the daily atmospheric forcing indeed increases the mean and variability of the SVU spatial extent by a factor of ~2 compared to climatological daily atmospheric forcing, and produces extreme SVU years which are not produced with climatological atmospheric forcing. Following the results of Li et al., (2014) who studied the variability of the eastward summer jet with a 1/4° resolution model, the variability associated with OIV is weaker but significant and of the same order of magnitude as the variability associated with atmospheric forcing : the variability in terms of intensity, spatial scale and temporal scales, and integrated strength obtained when

using climatological oceanic and atmospheric forcing represents between 25 and 58 % of the variability obtained when using both interannually varying oceanic and atmospheric forcing (Table 4.1). However, although climatological forcing produces coastal SVU every year with a significant interannual variability, those coastal SVU centers are always centered within 11-12°N : OIV therefore weakly impacts on the SVU coastal location and can not produce strong offshore SVU. Remote forcing including climatological river discharge from the Mekong, Red and Pearl rivers and lateral oceanic forcing have a weaker effect than the atmospheric forcing, but still modulate the SVU interannual variability of the SVU from 13 to 41 % and can have a strong impact at the scale of individual years both in terms of intensity and location. Our simulations also highlight the strongly non-linear nature of the SVU functioning and variability : the effects on the SVU of the different variability factors examined here do not add together but rather interact in a highly non-linear way.

The detailed study of our simulations and of particular years helps to understand the physical mechanisms behind these statistical results.

It first shows that the leading effect of atmospheric interannual variability on the SVU interannual variability is related to the role of summer wind in the SVU region, in agreement with previous studies which suggested that atmospheric forcing, in particular wind, is the main driver of SVU variability (e.g. Dippner et al., 2013). We indeed obtain a 0.81 ($p<0.01$) correlation between summer wind stress curl and SVU strength UIy. Wind stress and wind stress curl induce SVU first via Ekman pumping, but also by strengthening the eastward jet which helps to extend the wind-forced coastal SVU further offshore (see Xie et al., 2003, 2007; Dippner et al., 2007).

Second, the case studies show that the interactions between the wind and the ocean vorticity field associated with the background oceanic eddy circulation strongly impact the SVU development and position. For years of normal to strong summer wind, a wind stress curl dipole develops around 11°N due to orographic effect (Xie et al., 2003, 2007), favoring the existence of an ocean eddy dipole with a cyclonic eddy in the north and anticyclonic eddy in the south separated by an eastward jet. Coastal SVU most often occurs upstream of this eastward jet, and its meridional variability is associated with the meridional variability of the eastward jet. The strength and distribution of offshore SVU depends on the strength, location, timing of the wind stress curl and above all on its interactions with the ocean cyclonic circulation that develops north of the eastward jet and preconditions the shallowness of the thermocline : strongest offshore SVU develop during years for which strong wind locally and temporally coincides and positively interacts with stable cyclonic eddies

and associated positive vorticity. The summer average of this positive vorticity field north of the eastward jet shows a weaker but still significant (0.68, $p<0.01$) correlation with SVU strength than the summer wind curl, confirming that this positive vorticity field is the second factor that modulates the direct Ekman pumping wind effect. This vorticity field is actually partly driven by the summer wind : we obtain a 0.92 ($p<0.01$) correlation between July SVU wind stress and July vorticity in the offshore SVU area. For years of very weak wind, the eastward jet and dipole circulation does not develop, the offshore SVU does not develop, and coastal SVU can be shifted to the North due to the interaction between unusually low ocean vorticity and wind.

Our results therefore show that wind is the major driver of the SVU through direct Ekman pumping effect but also through the indirect effects associated with its contribution to the eastward jet intensification and its interaction with the ocean vorticity field. However our case studies moreover show that OIV resulting from the winter ocean initial state as well as remote forcing of the large scale circulation and river discharge also influences the spatial and temporal distribution of eddies and their associated vorticity, during and within the region of SVU. Hence the strength and location of the SVU is also impacted by the turbulent nature of the ocean in a highly unpredictable way. Wind-eddy interactions therefore explain how the OIV, but also river discharge and remote oceanic forcing, can modulate the SVU interannual variability, explaining the statistical results obtained when analysing our sensitivity simulations. Figure 6.1 gives a schematic summary of the SVU mechanisms.

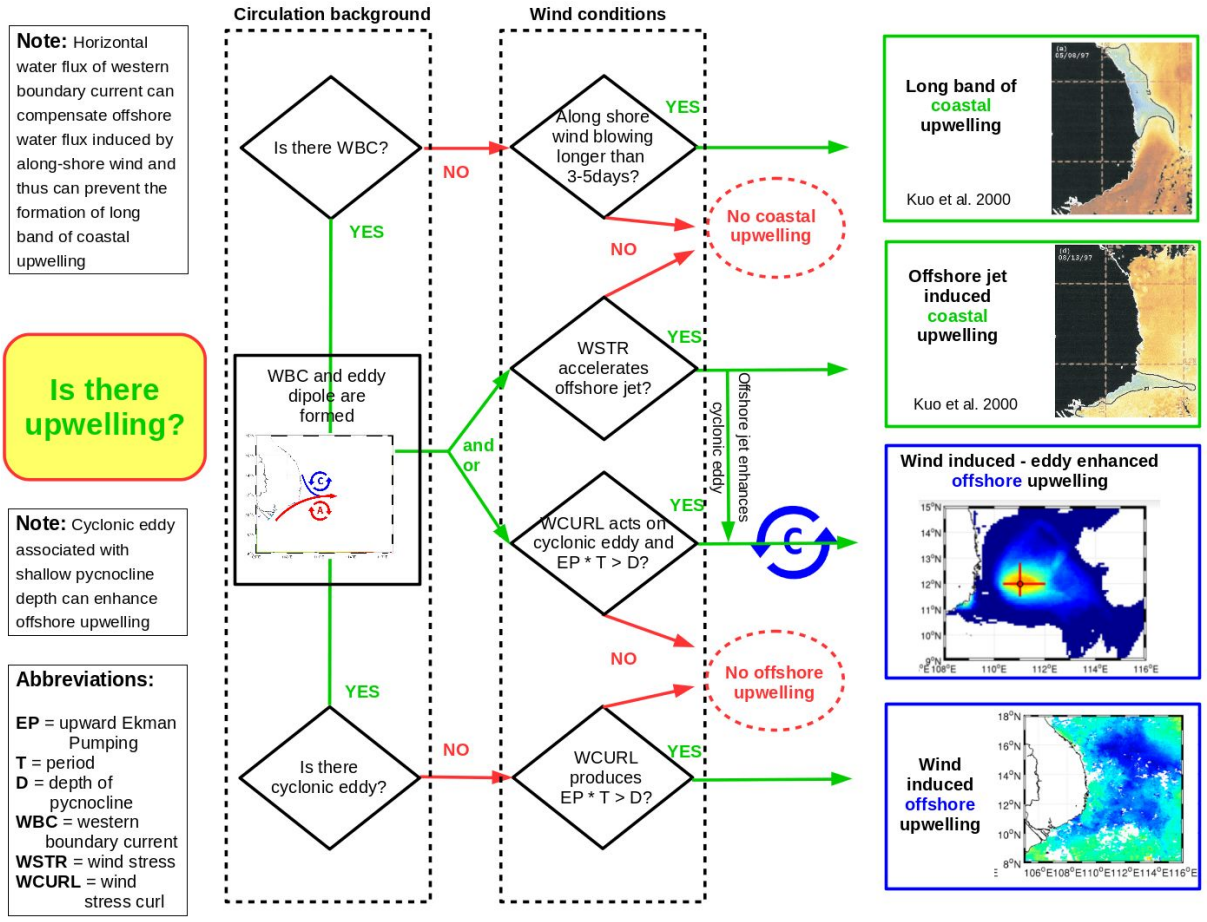

Figure 6.1 A schematic summary of the SVU mechanisms.

In agreement with previous studies cited above, results from our 14 year eddy-resolving reference simulation show that ENSO conditions of a given winter significantly impact SVU of the following summer : SVU strength is strongly correlated with the previous winter's ONI index (0.71, $p < 0.01$ with February ONI). Analysis of our reference simulation confirms that on average the modulation of South East Asia summer monsoon by ENSO predominantly contributes to this impact : El-Niño/La-Niña winters induce negative/positive anomalies of summer wind stress and wind stress curl that result in SVU weakening/strengthening through the physical mechanisms described above. Our results moreover reveal that a second preconditioning mechanism explains the ENSO impact on SVU, although its contribution is significant only for intense El-Niño winters : intense El-Niño winters result in a decrease of the winter monsoon and the associated winter wind and of the induced southward western boundary current, which creates a negative vorticity anomaly during the pre-upwelling season along the western boundary current region. This negative anomaly persists until spring due to the fact that the weaker boundary current allows the penetration of the predominant anticyclonic eddies into the SVU zone. In summer, the weaker wind-induced upwelling (due to weakened summer wind in post-El-Niño summer) therefore develops over the deep upper ocean thermal content associated with the anti-cyclonic eddy circulation, which further inhibits the

SVU. For average and intense La-Niña years, there is no statistically significant effect of such a preconditioning mechanism : the impact of ENSO on wind, western current and ocean vorticity is statistically significant in winter for the whole 1991-2004 period, however this ENSO signature on winter ocean vorticity does not persist into summer for the average and La-Niña years.

6.3 Robustness of previous results to the configuration of the model: impacts surface bias correction method

With the aim of producing realistic simulations, relaxation toward the observed SST and SSS fields were used in the CTRL simulation, as well as in the first set of sensitivity simulations for consistency to reduced the surface biases and drifts. Though we used a weak relaxation coefficient, our SST-based upwelling indices are thus constrained by relaxation and may over-/under-estimate the variability of the SVU, or the contributions of different forcings as well as the relation of the SVU with ENSO. We further investigated the impacts of different SST-SSS relaxation techniques on our model performance and on our conclusions concerning the SVU interannual variability. This was done by running two groups of simulation tests: one group with different relaxation coefficients (0, 40 and 120 $W.m^{-2}.K^{-1}$) and the other group where we only used corrections of surface heat and salt fluxes, but without relaxation. Results from the first group showed that without relaxation nor flux correction, the ocean is overheated leading to the model blowing up after a few years, which confirms the need to correct this drift by using surface relaxation and/or surface fluxes correction. The simulation performed with stronger relaxation leads to better performance not only in temperature and salinity indicators but also in SLA indicators; this is then used to compute the surface fluxes correction terms used in the second group. The best simulation in the second group realistically reproduces the SCS water masses and surface characteristics despite a slightly larger SST bias than the CTRL simulation. The comparison of the reference simulations performed respectively with and without surface relaxation shows that the results presented in Chapters 3 and 4 are still valid and robust to the choice of surface bias correction : we still obtain significant correlations with summer wind curl, surface ocean vorticity in the OFF+ zone as well as with ENSO in the “no relaxation” simulation. However our sensitivity tests also suggest that the surface relaxation may lead to an underestimation of the SVU variability associated with a weakening of OIV.

6.4 Limitations and perspectives

The present study aimed to quantify the respective contributions of factors that can influence the SVU variability, and to explain physically the statistical results obtained. Our work shows some limitation associated with the methodological choices that we made and the tools that were available. Further work and studies are still necessary to better understand the functioning, variability and influence of the SVU:

Firstly, improvements in terms of representation of the river plume and fresh water flux advection associated with large scale circulation is crucial for an accurate estimation of the impacts of river discharge to the SVU variability. Chen et al. (2012) revealed impacts of river to the SVU via buoyancy current from the Red River. In this study, using E-P-R method and a climatological river discharge, we showed that the absence of river forcing in SimR or the relocation of the Pearl River lead to an increase of about 10% in the variability of the SVU mainly due to OIV. Hence the relative importance of direct impacts of freshwater via buoyancy and indirect impacts of rivers via OIV still needs further investigations. To fundamentally improve the situation, we need a more stable implementation of river discharge as volume and momentum fluxes along the lateral boundaries in a model, with interannual variable discharge of the river systems, and realistic tidal mixing in the shallow shelves and river mouths.

Secondly, tides is particularly important not only for the representation of the river plumes but also to the mixing in shallow shelves and in the SCS deep basin via internal waves generated at the Luzon Strait (see section 1.1.2d). Chen et al. (2012) found that tidal rectification due to nonlinear interaction between tides and bathymetry can impact the SVU. Furthermore, instabilities created by tidal current at the Luzon Strait may also produce mesoscale eddies and thus possibly impact the SVU via ocean vorticity. We are currently working to first correctly reproduce tidal distribution in the SCS, and then to investigate the impacts of tides to the SVU variability. Some preliminary results are shown in the Appendix-A2

Concerning the impact of lateral ocean boundary conditions, the comparison of CTRL-SimO and SimA-SimI pairs of simulations suggests that we can not conclude on a significant statistical impact of this remote circulation on the SVU variability, although it clearly affects the SCS circulation variability. For individual years, this remote circulation can impact on the SVU by influencing the stability of the large-scale circulation and the mesoscale eddy distribution in the SVU region.

Our study revealed the strong impact of OIV on the SVU, associated with the role of the ocean eddies and of their interactions with wind curl. This result is in agreement with results obtained for other regions/processes that showed that submesoscale structures are important sources of OIV (Penduff et al., 2011; Gregoria et al., 2015; Serazin et al., 2016; Waldman et al., 2018). Higher resolution models able to represent more realistically those structures are therefore necessary to represent and understand fully their effect on SVU. Furthermore this result highlights that a purely deterministic approach based on single simulations of a given period of interest does not allow us to take into account this OIV effect, and that ensemblist approaches are required to study the SVU, as concluded for other processes (e.g. ocean convection, Waldman et al., 2018).

The SCS circulation involves strongly coupled air-sea processes, in particular wind-eddy interactions, which were shown to play a leading role in the SVU development. There are two interesting perspectives of this wind-eddy coupling. The first is that, being on a western boundary, there is a component of the larger-scale eddy field that is not generated locally, but propagates slowly in from the east. This means that in any given upwelling season, part of the background mesoscale eddy field may have a few months predictability. We have not explored this relation over the SVU domain, but it would be an interesting future study. The second eddy air-sea coupling subject concerns the presence of oceanic anticyclones/cyclones and the modification of SST induced by SVU that can moreover modify the intensities and pathways of typhoons crossing the region. Typhoons are incompletely reproduced in our atmospheric products used to force our ocean simulations, and their coupled interactions with the underlying eddy field even more so (Chelton and Xie, 2010; Morrow et al., 2017). Coupled air-sea modeling studies are required to better represent and understand the impact of those air-sea interactions on the SVU in particular, but also more generally on SCS circulation.

The strong SVU interannual variability impacts on the local marine ecosystems and fishing resources. Scientists involved in the LOTUS international joint laboratory (which gather laboratories from Institute of Research for the Development - IRD, University of Toulouse, Université du Littoral de la Côte d'Opale - ULCO, University of Science and Technology of Hanoi - USTH, and partners institutes from the Vietnam Academy of Science and Technology - VAST) are presently developing high-resolution coupled physical-biogeochemical numerical simulations to study this impact.

Ocean modeling has limitations due to approximations and parameterizations, computing resources and uncertainties in forcing used. There is always a strong needs of real observations both in time and space to help evaluating the model, to constrain it from drifting too far away from reality and to be a complementary reliable source of information. Satellite observations are a precious source of observations of the ocean dynamics, hydrology and biogeochemical contents, however they only provide surface information and show limitations linked to the uncertainties of the algorithms used. A strong effort should be done to fill the lack in terms of in-situ observations of the tridimensional circulation and water masses in the SVU area in particular and in the SCS in general. In this effort, in the framework of the joint IRD-CNRS-VNU HUS project VIRGIL, we are planning to deploy a sea glider in the SVU region in summer 2018 for a better insight of the SVU water masses, mechanisms and variability.

The simulations conducted in this study can also be used to study other processes in the SCS, for instance, the variability of the SCS large scale circulation, the role of different forcings to the mesoscale activities, LST and to heat, water and salt fluxes transported by the South China Sea Through Flow from the Pacific to Sulu sea, Java Sea and the Indian Ocean via the SCS. Finally, the methodology developed in this study may be useful to study other upwelling regions.

Conclusion finale (français)

Objectifs et méthodologie

L'upwelling du Sud Vietnam, SVU, joue un rôle majeur dans la dynamique océanique et la productivité biologique de Mer de Chine du Sud (SCS). Les études précédentes ont mis en évidence sa forte variabilité interannuelle, mais se sont appuyées sur l'observation in-situ/satellite ou la modélisation numérique de quelques cas d'études et/ou sur des simulations numériques pluri-annuelles mais effectuées avec des modèles de basse résolution. Ces modèles ne permettent pas, en particulier, de représenter les tourbillons et méandres de (sub)méso-échelles, qui sont une source importante de variabilité intrinsèque océanique (OIV). Ces études ont mis en évidence la contribution majeure du vent et de l'oscillation ENSO à la variabilité interannuelle du SVU, et ont également suggéré que la circulation de grande échelle, les flux d'eaux douce en provenance des fleuves, l'OIV et la marée pouvaient influencer cette variabilité. Dans ce contexte, les objectifs de cette thèse étaient de quantifier la variabilité interannuelle du SVU et les contributions des différents facteurs de variabilités cités ci-dessus, et d'identifier les mécanismes physiques associées.

Pour cela plusieurs jeux de simulations numériques pluri-annuelles de la dynamique océanique en SCS ont été effectuées avec le modèle ROMS_AGRIF à 1/12° de résolution, permettant de représenter la méso-échelle. La simulation de référence prend en compte des forçages atmosphérique quotidien et océanique mensuel interannuels, et des débits de rivières mensuels climatologiques. Des simulations de sensibilité ont ensuite été effectuées et comparées avec la simulation de référence pour examiner l'impact de la variabilité de ces forçages sur le SVU.

La simulation de référence a d'abord été comparée aux observations in-situ et satellites de température, salinité et d'élévation de surface disponibles afin d'évaluer et optimiser sa capacité à reproduire la dynamique océanique en SCS et dans la région du SVU. Ces comparaisons montrent que la simulation de référence reproduit correctement les caractéristiques des masses d'eau et la circulation de surface et leur variabilité, et peut donc être légitimement utilisée pour étudier le SVU.

Variabilité interannuelle du SVU

Nous avons construit à partir de la température de surface un groupe d'indicateurs de la variabilité interannuelle du SVU en terme d'intensité, d'extension spatiale et de durée. Les résultats de la simulation de référence CTRL montrent que le SVU présente une forte variabilité interannuelle, avec un écart type de l'indicateur total UIy égal à 64% de sa moyenne. Nous obtenons des années très contrastées, certaines avec seulement un faible upwelling côtier, et d'autres avec un upwelling côtier et un fort upwelling se développant au large. L'analyse statistique des simulations de sensibilité suggère que la variabilité interannuelle du SVU est en grande partie liée au forçage atmosphérique, mais qu'elle est fortement modulée par la variabilité intrinsèque océanique (OIV), qui peut représenter ~50% de la variabilité totale, ainsi que par, dans une moindre mesure, le débit des rivières et la circulation océanique de grande échelle.

L'étude détaillées de cas d'études issus de nos simulations permet de comprendre les mécanismes associées à ces conclusions statistiques.

Elle montre d'abord que la variabilité interannuelle du SVU est en grande partie pilotée par le vent, avec une corrélation de 0.81 ($p<0.01$) entre le rotationnel du vent en été et l'intensité totale du SVU UIy, confirmant les résultats obtenus dans les précédentes études (Xie et al., 2003, 2007; Dippner et al., 2007). De plus, on observe que la circulation océanique dans la région influence fortement le développement du SVU : l'intensité du SVU est augmentée les années où des tourbillons cycloniques associés à une vorticité positive coïncident spatialement et temporellement avec le rotationnel positive du vent. De ce fait on obtient une corrélation de 0.68 ($p<0.01$) entre la vorticité de surface moyenne dans la région du SVU en été et UIy. Cette influence de la vorticité de surface, largement liée au champ de tourbillons dont le comportement est fortement chaotique, est à l'origine de la contribution de l'OIV à la variabilité interannuelle du SVU. La quantification et l'explication de la contribution de l'OIV est un résultat novateur.

Nos résultats confirment en outre que le SVU est soumis à l'influence d'ENSO, avec une corrélation de 0.71 ($p<0.01$) entre UIy et l'index ONI en février. Cette influence est en fait liée à l'impact d'ENSO sur la circulation atmosphérique et

en particulier sur le champ de vent dans la région. Ainsi, les hivers El Niño/La Niña induisent respectivement une anomalie négative/positive du rotationnel du vent en SCS l'été suivant, et donc de l'intensité du SVU. Pour les hivers fortement El Niño, on observe de plus une diminution du vent hivernal qui induit une anomalie négative de la vorticité de surface qui persiste jusqu'à l'été et s'ajoute à l'anomalie négative du rotationnel du vent, atténuant d'autant plus le SVU.

Afin d'optimiser le réalisme du jeu de simulations utilisées pour obtenir ces résultats, et en particulier de corriger les biais et dérives de température et salinité de surface, un rappel vers les température et salinité de surface observées a été utilisé. Afin de tester l'impact de ce rappel, qui impose une contrainte sur la représentation des caractéristiques hydrologiques et dynamiques de surface, nous avons effectué un second jeu de simulations. Nous avons successivement testé l'impact du coefficient de rappel utilisé, puis mis en place des simulations sans rappel mais utilisant une correction des flux atmosphériques de chaleur et d'eau afin de corriger les biais de surface. Les résultats de ces simulations montrent que nos conclusions sur l'ordre de grandeur de la contribution des différents facteurs à la variabilité interannuelle du SVU restent valables et sont robustes à ces choix de méthode de correction de biais, mais suggèrent aussi que l'impact de l'OIV pourrait être plus important que celui estimé à partir de la simulation avec rappel de surface.

Perspectives

Outre la méthode ad-hoc utilisée pour corriger les biais de surface, la méthodologie utilisée et les outils disponibles pour réaliser cette étude induisent automatiquement certaines limitations dans notre approche. D'autres études seront nécessaires pour s'affranchir de ces limitations mais également mieux comprendre le fonctionnement, la variabilité et l'influence de la SVU :

- Notre étude ainsi que les travaux précédents (Chen et al., 2012) montrent que les débits des rivières pourraient influencer la dynamique dans la région et donc le SVU. L'explication exacte de l'influence de l'eau douce des rivières liée à leur flottabilité et/ou leur participation à l'OIV nécessite des études plus approfondies, et en particulier une amélioration de la prise en compte des rivières et de la variabilité de leur débit dans le modèle mais aussi de l'impact de la marée qui joue un rôle important dans la dispersion des panaches d'eau douce.

- Nos simulations ne prenaient pas en compte l'influence de la marée, qui conditionne non seulement la dispersion des panaches de rivières mais également le mélange des masses d'eau, en particulier dans les zones de

faible profondeur. Ce travail sur la prise en compte de la marée dans notre modèle est en cours et les premiers résultats ont été présentés en annexe A2.

- Notre étude a mis en évidence la forte contribution de l'OIV à la variabilité du SVU, confirmant les conclusions émises pour d'autres régions et processus (Penduff et al., 2011; Gregoria et al., 2015; Serazin et al., 2016; Waldman et al., 2018). Ce résultat souligne d'une part la nécessité de mettre en place des simulations à haute résolution permettant de représenter encore mieux les structures de (sub)méso-échelle qui contribuent significativement à l'OIV. Il remet également en question les approches purement déterministes basées sur l'utilisation d'une simulation unique d'une période d'intérêt, et soulignent la pertinence de mettre en place des approches numériques ensemblistes.

- La dynamique océanique en SCS fait intervenir un grand nombre de processus couplés entre l'océan et l'atmosphère (en particulier les typhons), et notre étude a mis en évidence l'importance des interactions vent-tourbillons. La mise en place d'un modèle couplé océan-atmosphère permettrait de mieux prendre en compte et étudier l'impact de ces processus couplés.

- Le SVU participe non seulement à la dynamique océanique de la SCS, mais également au fonctionnement des écosystèmes marins et des ressources halieutiques. Le LMI (Laboratoire Mixte International) LOTUS (Study center of the Land-Ocean-aTmosphere coUpled System) réunit des scientifiques de l'IRD, de l'ULCO (Université du Littoral de la Côte d'Opale), de l'Université de Toulouse, de l'USTH (University of Science and Technology of Hanoi) et de la VAST (Vietnam Academy of Science and Technology), dont une partie développe des simulations couplées physique-biogéochimie à partir des outils numériques du groupe SIROCCO afin d'étudier cette influence du SVU sur les écosystèmes marins.

- La modélisation numérique n'a de sens que si elle est utilisée en complémentarité avec les observations réelles, satellites et in-situ. En particulier, contrairement aux données satellites qui présentent une bonne couverture spatio-temporelle mais restent limitées à la surface, les observations in-situ permettent d'accéder aux caractéristiques hydrologiques et dynamiques de toute la colonne d'eau. La région de la SCS et du SVU sont pour le moment sous-échantillonnées. Pour participer à combler ce manque,

le projet franco-vietnamien VIRGIL mené par l'IRD, le CNRS et la VNU-HUS (Vietnam National University - Hanoi University of Science) prévoit de déployer un glider de la DT-INSU (Division Technique de l'Institut National des Sciences de l'Univers) au printemps-été 2018 dans la région.

- Un travail important a été réalisé afin de mettre en place notre modèle. Nos simulations pluri-annuelles à haute résolution devraient être utilisées afin d'étudier d'autres processus d'intérêt en SCS, en particulier le fonctionnement et la variabilité de la circulation de surface, de l'activité de méso-échelle, du transport au détroit de Luzon (LSTTF). Une meilleure compréhension de la dynamique de la région permettra en effet de progresser dans notre connaissance du SCSTF, qui joue un rôle important dans le transport d'eau, de chaleur et de sel entre l'océan Pacifique et l'océan Indien et participe ainsi à la circulation thermohaline globale.

APPENDIX

A1. Impacts of the relocation of the Pearl River on the SSS distribution

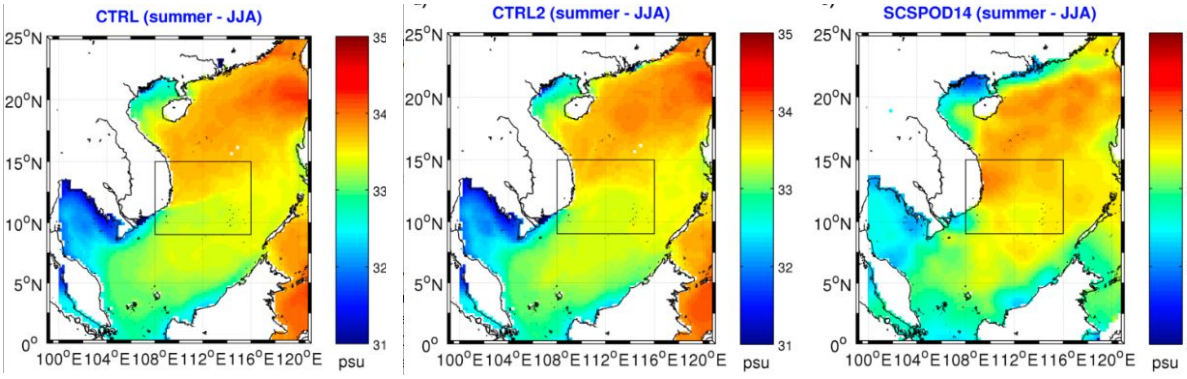

Figure A1 - Summer SSS in CTRL, CTRL2 (with Pearl river bay closed) and SCSPOD14.

In the waters surrounding the Pearl River near 21°N, the summer SSS data of SCSPOD14 shows significant freshening right along the coast? Whereas the CTRL simulation has higher SSS along the coast. The revised CTRL2 simulation has improved coastal freshening along the coast, but with a limited offshore extent. SSS within the SUV domain (black box) also shows a minor modification due to changes at this remote site.

A2. Influence of Tides

The motivation of this part is to estimate the impacts of tidal forcing on the SVU variability. These impacts were not included originally with the other forcings due to the complication of including tides in our simulations, due to the complicated bathymetry of the SCS as well as high computation costs. In this section, we present our initial efforts and preliminary results in studying the impacts of the tidal forcings on the SCS dynamics and the SVU variability.

A2.1. Representation of tides

Firstly we want to produce the most realistic simulation with the inclusion of tidal forcing. Thus we started by adding tidal forcing from the TPXO7 dataset (Egbert and Erofeeva, 2002) along the lateral boundaries of the CTRL2 simulation (the most realistic one without tidal forcing). Due to tidal mixing, the heat correction used in CTRL2 is no longer suitable and needs to be adjusted. For that we apply the same method described in Chapter 2 by running a simulation called TRel120 with:

- the same forcing and river locations used in CTRL2,

- Both SSH fluctuations and tidal currents of 8 components (M2, S2, N2, K2, K1, O1, P1, Q1) from the tidal atlas TPXO7 are imposed along the lateral boundaries,

- a strong relaxation coefficient is imposed of 120 $W.m^{-2}.K^{-1}$.

The heat flux correction is then computed based on the SST from TRel120 and CFSR SST. This heat flux correction is then filtered using both spatial filter (moving window of 1000km) and climatological monthly filter. Finally, we run two different simulation tests with:

- the same setting in CTRL2 in terms of forcings and river locations,
- using the heat flux correction as well as a small relaxation coefficient of 40 $W.m^{-2}.K^{-1}$,
- with both tidal SSH and currents at lateral boundaries (called Test-0t-a) and with only tidal SSH variation at lateral boundaries (called Test-0t-b).

The representation of the tidal distribution in the different tests is then evaluated by comparison with the TPXO7 tidal amplitudes and phases inside the SCS. Table A2.1 shows that Test-0t-a has significantly better agreement with TPXO7 for the diurnal components and Test-0t-b shows better agreement for the M2 component. Both tests show high and significant correlations for the major components: M2, S2, K1 and O1. Figure A2.1 and A2.2 show the comparisons of tidal amplitudes and phases of Test-0t-a and TPXO7 for the 4 major components. Strong differences in terms of amplitude occur in shallow areas probably due to unrealistic bathymetry (Figure A2.1). The Test-0t-a shows relatively good agreement in terms of the phase for the S2 and K1 components with phases of 29° and 14° respectively (Figure A.2.2, Table A2.1) yet strong differences for the rest. We are currently working to improve this situation.

Table A2.1: correlation and MAE over the SCS of tidal amplitudes and phases of different tests compared to TPXO7

	Test-0t-a (SSH + UV, 1991)			Test-0t-b (SSH only, 1991)		
	Amplitude (m)		Phase (deg)	Amplitude (m)		Phase (deg)
	R	MAE	MAE	R	MAE	MAE
M2	0.78	0.20	65	0.78	0.13	64
S2	0.70	0.08	33	0.68	0.06	29
N2	0.78	0.04	134	0.77	0.03	130
K2	0.57	0.03	144	0.59	0.02	150
K1	0.84	0.11	13	0.77	0.15	14
O1	0.88	0.05	94	0.83	0.14	84
P1	0.52	0.04	34	0.43	0.04	36
Q1	0.49	0.01	131	0.45	0.03	119

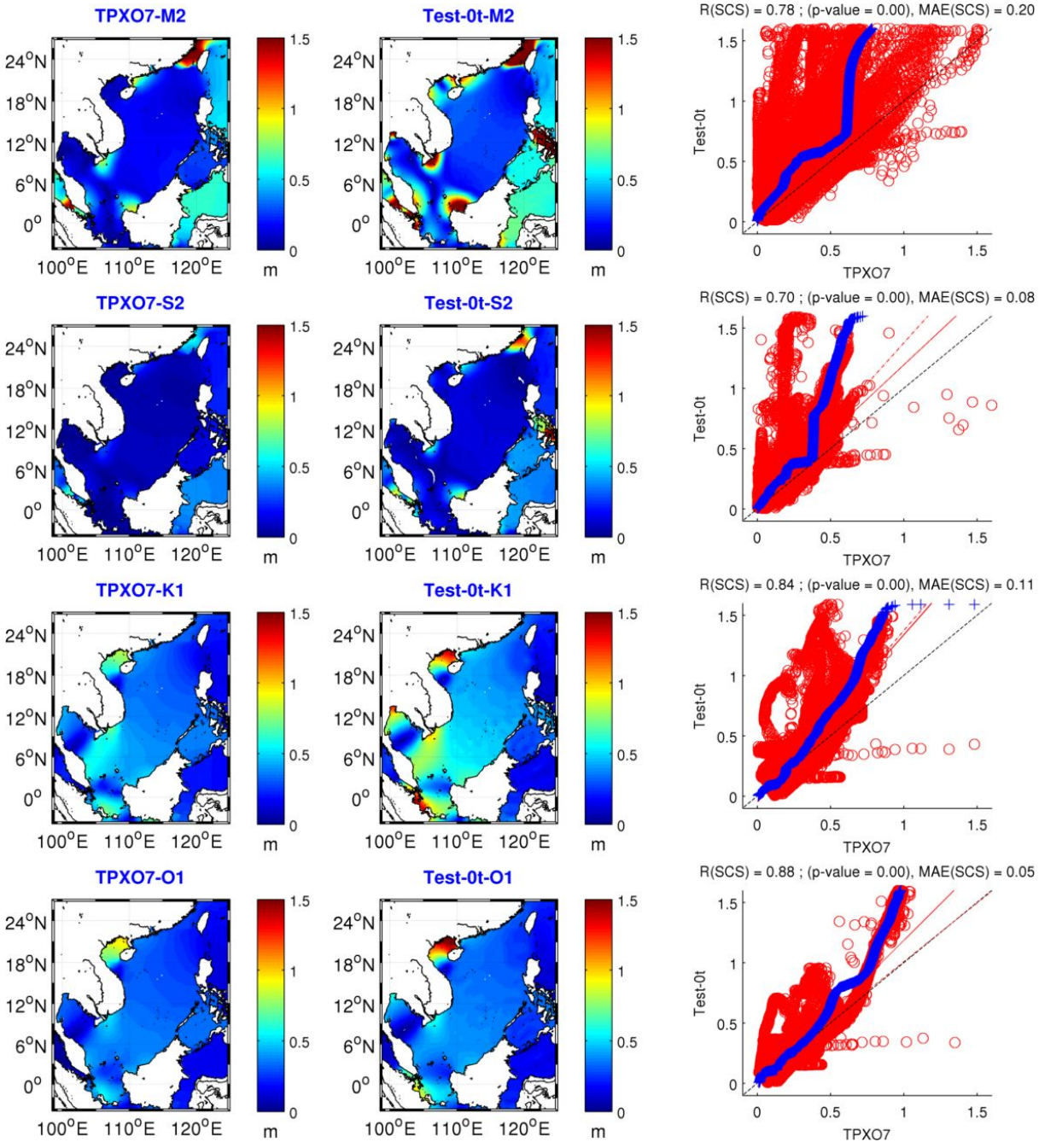

Figure A2.1 Comparison of amplitudes (m) of major components (M2, S2, K1, O1) between Test-0t-a and TPXO7 : maps (left) and scatter plots and Q-Qplots over the SCS.

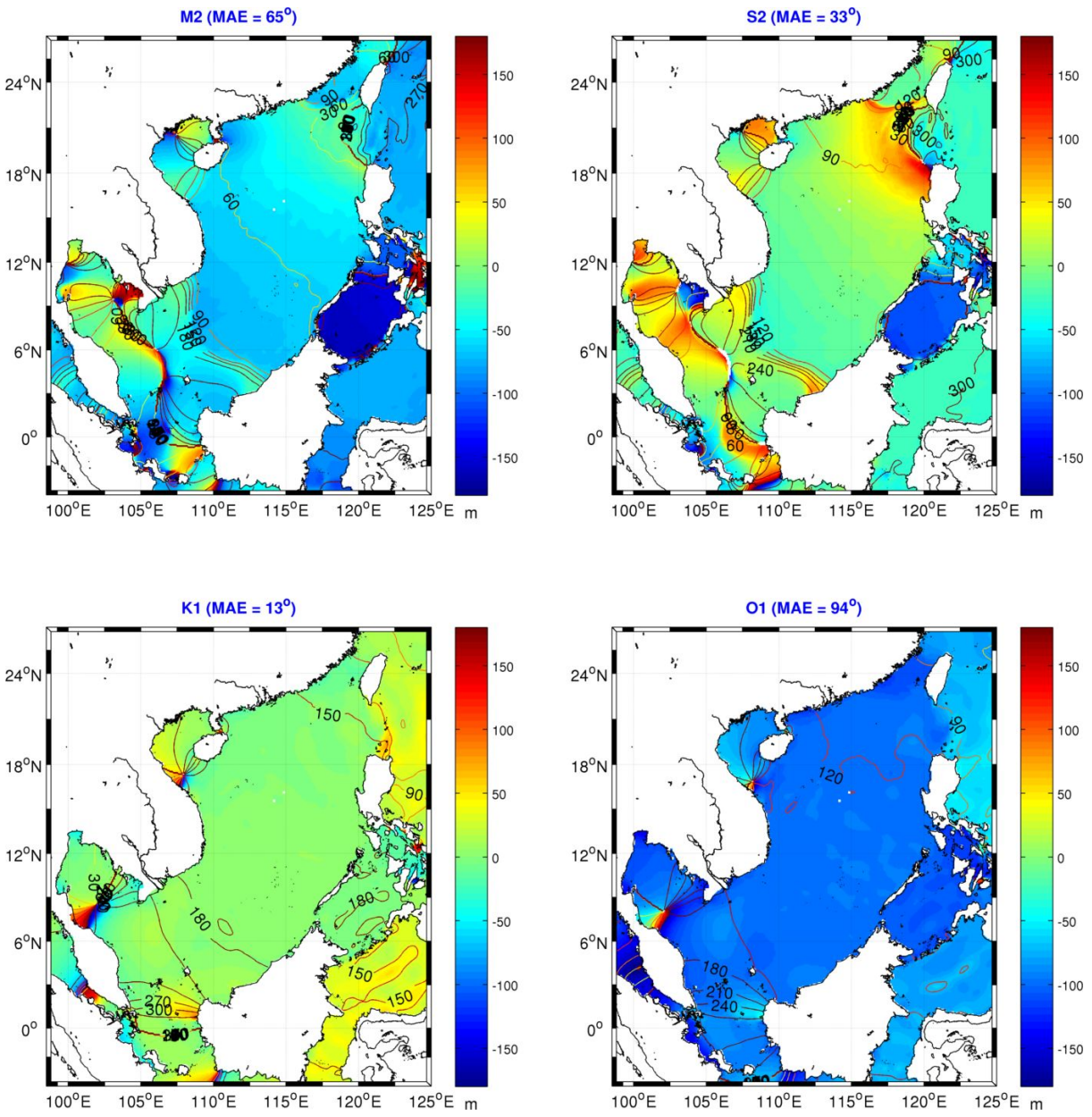

Figure A2.3 Comparisons of phase of major components (K1, O1, M2, S2) components between Test-0t-a and TPXO7. Contours show phase in TPXO7 and color shade represent phase lag of Test-0t compared to TPXO7.

A2.2 Impacts of tidal forcings on the SCS dynamics

Although these versions of the model have the limitations shown above, it's interesting to see the impacts of the tidal mixing on the representation of the SCS dynamics. We did the same range of tests as in Chapter 5 but with the inclusion of tides. We imposed both SSH and tidal currents in the tests. We evaluated these tests by the same indicators used in Chapter 5, but this time taking CTRL2 as the reference simulation. The descriptions and evaluations of these tests are given in Table A2.2. The inclusion of tidal mixing leads to better agreement of thermohaline

structure in the deep layer (200-1500m) in all of the tests (see variable index 12,18 in Table A2.2). Since the SCS is diurnal dominant (section 1.1.2d) and Test-0t-a shows a better performance for the diurnal components, it is consistent that Test-0t-a shows a slightly better performance than CTRL2. Both Test-1t (without surface correction nor relaxation) and Test-4t (with spatial-climatological filtered HF and WF correction and without relaxation) have significantly worse performances than CTRL2 and they blew up in the middle of the runs. The stronger relaxation in Test-3t leads to a better performance than for Test-2t. This means that surface corrections and/or relaxation are still crucial in simulations that include tidal forcing. Test-5t shows a more realistic SST interannual trend (0.04^{o}C.year^{-1}, same as in data) compared to Test-6t (0.08 ^{o}C.year^{-1}), however Test-6t shows a much higher SST interannual correlation with data than Test-5t (0.68 vs. 0.13). These are only preliminary results and we are still working to improve the representation of tides in the SCS as well as finding the most realistic simulation for the study of tidal impacts on the SVU interannual variability.

Table A2.2 Similar to Table 5.1 but for different tests with tide inclusion.

			CTRL2	Test-0t-a	Test-1t	Test-2t	Test-3t	Test-4t	Test-5t	Test-6t
		Variable index	(without tides)	HF corr (spatial + clim filter), relax 40	no corr, no relax (Analysis based on 1991-1993)	no corr relax 40	no corr relax 120	HF, WF corr (spatial + clim filter), analysis based on 1991-1999	HF, WF corr (clim filter)	HF, WF corr (no spatial filter, monthly time filter)
SST Bias (deg C)		1	0.19	0.11	0.79	0.72	0.32	0.04	0.14	0.15
SST annual corr		2	0.97	0.97	0.97	0.98	0.99	0.87	0.99	0.99
SST annual MAE		3	0.20	0.14	0.79	0.72	0.32	0.14	0.17	0.17
SST interann MAE		4	0.19	0.13	0.79	0.72	0.32	0.22	0.37	0.35
SST interann Trend (data = 0.04)		5	0.05	0.05	-2.05	0.04	0.04	-2.88	0.04	0.08
SST Interann (corr)		6	0.86	0.84	Nan	0.76	0.81	0.75	0.13	0.68
SST Spatial corr	summer	7	0.76	0.81	0.52	0.78	0.87	0.61	0.77	0.79
	winter	8	0.98	0.98	0.83	0.97	0.99	0.95	0.97	0.97
SST Spatial MAE	summer	9	0.34	0.30	5.00	0.88	0.39	0.57	0.32	0.31
	winter	10	0.44	0.38	3.49	0.57	0.34	0.53	0.44	0.44

T-profile MAE clim, 3 stations	0-200m	11	0.67	0.99	1.35	1.05	0.98	1.14	1.16	1.06
	200-1500m	12	0.55	0.47	0.39	0.48	0.47	0.49	0.50	0.44

a) Temperature indices

			CTRL2	Test-0t-a	Test-1t	Test-2t	Test-3t	Test-4t	Test-5t	Test-6t
SSS bias (psu)		13	-0.16	-0.10	-27.15	-0.11	-0.18	-13.47	0.09	0.13
SSS annual MAE		14	0.18	0.14	27.15	0.14	0.21	13.47	0.14	0.15
SSS annual cycle correlation		15	0.85	0.82	0.87	0.75	0.64	0.90	0.92	0.92
SSS interannual Trend (CFSR = 0.00)		16			Nan	0.00	0.00	-3.47	-0.01	-0.01
S-profile MAE clim, 3 stations	0-200m	17	0.22	0.23	0.59	0.27	0.23	0.35	0.32	0.35
	200-1500m	18	0.09	0.07	0.07	0.07	0.06	0.07	0.07	0.06
SSS Spatial corr	summer	19	0.70	0.72	0.56	0.71	0.76	0.65	0.64	0.62
	winter	20	0.88	0.90	0.79	0.89	0.89	0.76	0.78	0.81
SSS Spatial MAE	summer	21	0.28	0.31	0.84	0.26	0.24	0.52	0.51	0.52
	winter	22	0.23	0.23	0.63	0.23	0.20	0.37	0.37	0.37

b) Salinity indices

			CTRL2	Test-0t-a	Test-1t	Test-2t	Test-3t	Test-4t	Test-5t	Test-6t
SLA spatial corr	summer	23	0.96	0.96	0.81	0.95	0.97	0.93	0.94	0.96
	winter	24	0.95	0.95	0.81	0.95	0.95	0.93	0.95	0.95
SLA spatial MAE (cm)	summer	25	2.31	2.37	4.53	2.62	2.22	2.06	1.99	1.86
	winter	26	1.84	2.25	3.74	2.37	2.61	2.21	1.93	2.06
SLA annual cycle	corr	27	0.85	0.82	0.52	0.71	0.85	0.96	0.86	0.90
	MAE	28	1.05	1.72	0.08	1.71	1.78	0.62	1.15	1.06
SLA interann	corr	29	0.78	0.76	Nan	0.67	0.39	0.68	0.79	0.64
	MAE	30	2.93	2.54	0.00	2.51	2.47	0.45	2.66	2.41
	Trend (data = 0.44)	31	1.22	1.08	0.00	0.96	0.72	0.07	1.20	1.01

c) SLA indices

BIBLIOGRAPHY

Ashok, K., Z. Guan, and T. Yamagata (2001), Impact of the Indian Ocean Dipole on the Relationship between the Indian Monsoon Rainfall and ENSO Karumuri Ashok •, Zhaoyong Toshio Yamagata technique, *Geophys. Res. Lett.*, *28*(23), 4499–4502, doi:10.1029/2001GL013294.

Benazzouz, A., S. Mordane, A. Orbi, M. Chagdali, K. Hilmi, A. Atillah, J. Lluís Pelegrí, and D. Hervé (2014), An improved coastal upwelling index from sea surface temperature using satellite-based approach - The case of the Canary Current upwelling system, *Cont. Shelf Res.*, *81*, 38–54, doi:10.1016/j.csr.2014.03.012.

Bombar, D., J. W. Dippner, H. N. Doan, L. N. Ngoc, I. Liskow, N. Loick-Wilde, and M. Voss (2010), Sources of new nitrogen in the Vietnamese upwelling region of the South China Sea, *J. Geophys. Res.*, *115*(C6), C06018, doi:10.1029/2008JC005154.

Cai, S., X. Long, H. Liu, and S. Wang (2006), Tide model evaluation under different conditions, *Cont. Shelf Res.*, *26*(1), 104–112, doi:10.1016/j.csr.2005.09.004.

Carton, J. A., and B. S. Giese (2008), A Reanalysis of Ocean Climate Using Simple Ocean Data Assimilation (SODA), *Mon. Weather Rev.*, *136*(8), 2999–3017, doi:10.1175/2007MWR1978.1.

Casey, K. S., T. B. Brandon, P. Cornillon, and R. Evans (2010), The past, present, and future of the AVHRR pathfinder SST program, in *Oceanography from Space: Revisited*, pp. 273–287, Springer Netherlands, Dordrecht.

Chang, Y.-T., T. Yung Tang, S.-Y. Chao, M.-H. Chang, D. S. Ko, Y. Jang Yang, W.-D. Liang, and M. J. McPhaden (2010), Mooring observations and numerical modeling of thermal structures in the South China Sea, *J. Geophys. Res.*, *115*(C10), C10022, doi:10.1029/2010JC006293.

Chao, S.-Y., P.-T. Shaw, and S. Y. Wu (1996), Deep water ventilation in the South China Sea, *Deep Sea Res. Part I*, *43*(4), 445–466, doi:10.1016/0967-0637(96)00025-8.

Chelton, D., and S.-P. Xie (2010), Coupled Ocean-Atmosphere Interaction at Oceanic Mesoscales, *Oceanography*, *23*(4), 52–69, doi:10.5670/oceanog.2010.05.

Chelton, D. B., M. G. Schlax, R. M. Samelson, and R. A. de Szoeke (2007), Global observations of large oceanic eddies, *Geophys. Res. Lett.*, *34*(15), 1–5, doi:10.1029/2007GL030812.

Chen, C., Z. Lai, R. C. Beardsley, Q. Xu, H. Lin, and N. T. Viet (2012), Current separation and upwelling over the southeast shelf of Vietnam in the South China Sea, *J. Geophys. Res.*, *117*(3), C03033, doi:10.1029/2011JC007150.

Chen, G., Y. Hou, and X. Chu (2011), Mesoscale eddies in the South China Sea: Mean properties, spatiotemporal variability, and impact on thermohaline structure, *J. Geophys. Res. Ocean.*, *116*(6), 1–19, doi:10.1029/2010JC006716.

China Power Team (2017), How much trade transits the South China Sea?, Available from: https://chinapower.csis.org/much-trade-transits-south-china-sea/ (Accessed 26 January 2018)

Chou, C., J. Y. Tu, and J. Y. Yu (2003), Interannual variability of the Western North Pacific summer monsoon: Differences between ENSO and non-ENSO years, *J. Clim.*, *16*(13), 2275–2287, doi:10.1175/2761.1.

Chu, P., Y. Chen, and S. Lu (1998), Wind-driven South China Sea deep basin warm-core/cool-core eddies, *J. Oceanogr.*, *54*(1997), 347–360, doi:10.1007/BF02742619.

Chu, P. C., and R. Li (2000), South China Sea isopycnal-surface circulation, *J. Phys. Oceanogr.*, *30*(9), 2419–2438, doi:10.1175/1520-0485(2000)030<2419:SCSISC>2.0.CO;2.

Chu, P. C., N. L. Edmons, and C. Fan (1999), Dynamical Mechanisms for the South China Sea Seasonal Circulation and Thermohaline Variabilities, *J. Phys. Oceanogr.*, *29*(11), 2971–2989, doi:10.1175/1520-0485(1999)029<2971:DMFTSC>2.0.CO;2.

David Neelin, J., and M. Latif (1998), El Niño Dynamics, *Phys. Today*, *51*(12), 32–36, doi:10.1063/1.882496.

Debreu, L., P. Marchesiello, P. Penven, and G. Cambon (2012), Two-way nesting in split-explicit ocean models: Algorithms, implementation and validation, *Ocean Model.*, *49–50*, 1–21, doi:10.1016/j.ocemod.2012.03.003.

Dippner, J. J. W., K. K. V. Nguyen, H. Hein, T. Ohde, and N. Loick (2007), Monsoon-induced upwelling off the Vietnamese coast, *Ocean Dyn.*, *57*(1), 46–62, doi:10.1007/s10236-006-0091-0.

Dippner, J. W., L. Nguyen-Ngoc, H. Doan-Nhu, and A. Subramaniam (2011), A model for the prediction of harmful algae blooms in the Vietnamese upwelling area, *Harmful Algae*, *10*(6), 606–611, doi:10.1016/j.hal.2011.04.012.

Dippner, J. W., D. Bombar, N. Loick-Wilde, M. Voss, and A. Subramaniam (2013a), Comment on “current separation and upwelling over the southeast shelf of Vietnam in the South China Sea” by Chen et al., *J. Geophys. Res. Ocean.*, *118*(3), 1618–1623, doi:10.1002/jgrc.20118.

Dippner, J. W., D. Bombar, N. Loick-Wilde, M. Voss, and A. Subramaniam (2013b), Comment on “current separation and upwelling over the southeast shelf of Vietnam in the South China Sea” by Chen et al., *J. Geophys. Res. Ocean.*, *118*(3), 1618–1623, doi:10.1002/jgrc.20118.

Duc, N. H., and M. Umeyama (2011), Saline Intrusion Due to the Accelerative Sea Level in the Red River System in Vietnam, *World Environ. Water Resour. Congr. 2011 Bear. Knowl. Sustain.*, *41173*(May), 4413–4422, doi:10.1061/41173(414)459.

Egbert, G. D., & Erofeeva, S. Y. (2002). Efficient inverse modeling of barotropic ocean tides. Journal of Atmospheric and Oceanic Technology, 19(2), 183-204.

Emanuel, K. A. (1999), Thermodynamic control of hurricane intensity, *Nature*, *401*(6754), 665–669, doi:10.1038/44326.

Fang, G., Y. K. Kwok, K. Yu, and Y. Zhu (1999), Numerical simulation of principal tidal constituents in the South China Sea, Gulf of Tonkin and Gulf of Thailand, *Cont. Shelf Res.*, *19*(7), 845–869, doi:10.1016/S0278-4343(99)00002-3.

Fang, G., Y. Wang, Z. Wei, Y. Fang, F. Qiao, and X. Hu (2009), Interocean circulation and heat and freshwater budgets of the South China Sea based on a numerical model, *Dyn. Atmos. Ocean.*, *47*(1–3), 55–72, doi:10.1016/j.dynatmoce.2008.09.003.

Fang, G., G. Wang, Y. Fang, and W. Fang (2012), A review on the South China Sea western boundary current, *Acta Oceanol. Sin.*, *31*(5), 1–10, doi:10.1007/s13131-012-0231-y.

Fang, W. (2002), Seasonal structures of upper layer circulation in the southern South China Sea from in situ observations, *J. Geophys. Res.*, *107*(C11), 3202, doi:10.1029/2002JC001343.

Fang, W., G. Fang, and P. Shi (2002), Seasonal structures of upper layer circulation in the southern South China Sea from in situ observations, *J. Geophys. Res.*, *107*(C11), 3202, doi:10.1029/2002JC001343.

Fekete, B. M. B. M., C. J. Vörösmarty, and W. Grabs (2002), High-resolution fields of global runoff combining observed river discharge and simulated water balances, *Global Biogeochem. Cycles*, *16*(3), 10–15, doi:10.1029/1999GB001254.

Gan, J., and T. Qu (2008), Coastal jet separation and associated flow variability in the southwest South China Sea, *Deep. Res. Part I Oceanogr. Res. Pap.*, *55*(1), 1–19, doi:10.1016/j.dsr.2007.09.008.

Gan, J., H. Li, E. N. Curchitser, and D. B. Haidvogel (2006), Modeling South China Sea circulation: Response to seasonal forcing regimes, *J. Geophys. Res. Ocean.*, *111*(6), C06034, doi:10.1029/2005JC003298.

Gan, J., L. Li, D. Wang, and X. Guo (2009), Interaction of a river plume with coastal upwelling in the northeastern South China Sea, *Cont. Shelf Res.*, *29*(4), 728–740, doi:10.1016/j.csr.2008.12.002.

Gao, J., Z. Dai, X. Mei, Z. Ge, W. Wei, H. Xie, and S. Li (2015), Interference of natural and anthropogenic forcings on variations in continental freshwater discharge from the Red River (Vietnam) to sea, *Quat. Int.*, *380–381*, 133–142, doi:10.1016/j.quaint.2015.01.007.

Goh, A. Z. C., and J. C. L. Chan (2010), Interannual and interdecadal variations of tropical cyclone activity in the South China Sea, *Int. J. Climatol.*, *30*(6), 827–843, doi:10.1002/joc.1943.

Grégorio, S. et al. (2015a), Intrinsic Variability of the Atlantic Meridional Overturning Circulation at Interannual-to-Multidecadal Time Scales, *J. Phys. Oceanogr.*, *45*(7), 1929–1946, doi:10.1175/JPO-D-14-0163.1.

Grégorio, S., T. Penduff, G. Sérazin, J.-M. Molines, B. Barnier, and J. Hirschi (2015b), Intrinsic Variability of the Atlantic Meridional Overturning Circulation at Interannual-to-Multidecadal Time Scales, *J. Phys. Oceanogr.*, *45*(7), 1929–1946, doi:10.1175/JPO-D-14-0163.1.

Hai, D. N., N. N. Lam, and J. W. Dippner (2010), Development of Phaeocystis globosa blooms in the upwelling waters of the South Central coast of Viet Nam, *J. Mar. Syst.*, *83*(3–4), 253–261, doi:10.1016/j.jmarsys.2010.04.015.

Hedström, K. S. (2009), Technical Manual for a Coupled Sea-Ice/Ocean Circulation Model (Version 4), , (Version 3), 1–151.

Hein, H. (2008), Vietnam Upwelling, Hamburg.

Hein, H., B. Hein, T. Pohlmann, and B. H. Long (2013), Inter-annual variability of upwelling off the South-Vietnamese coast and its relation to nutrient dynamics, *Glob. Planet. Change*, *110*, 170–182, doi:10.1016/j.gloplacha.2013.09.009.

Ho, C.-R., Q. Zheng, Y. S. Soong, N.-J. Kuo, and J.-H. Hu (2000), Seasonal variability of sea surface height in the South China Sea observed with TOPEX/Poseidon altimeter data, *J. Geophys. Res.*, *105*(C6), 13981, doi:10.1029/2000JC900001.

Holland, W. R. (1978), The Role of Mesoscale Eddies in the General Circulation of the Ocean—Numerical Experiments Using a Wind-Driven Quasi-Geostrophic Model, *J. Phys. Oceanogr.*, *8*, 363–392, doi:10.1175/1520-0485(1978)008<0363:TROMEI>2.0.CO;2.

Hu, J., H. Kawamura, H. Hong, and Y. Qi (2000), A Review on the currents in the South China Sea: Seasonal circulation, South China Sea warm current and Kuroshio intrusion, *J. Oceanogr.*, *56*(6), 607–624, doi:10.1023/A:1011117531252.

Hwang, C., and S.-A. Chen (2000), Fourier and wavelet analyses of TOPEX/Poseidon-derived sea level anomaly over the South China Sea: A contribution to the South China Sea Monsoon Experiment, *J. Geophys. Res.*, *105*(C12), 28785, doi:10.1029/2000JC900109.

Jan, S., C.-S. S. Chern, J. Wang, and S.-Y. Y. Chao (2007), Generation of diurnal K1 internal tide in the Luzon Strait and its influence on surface tide in the South China Sea, *J. Geophys. Res. Ocean.*, *112*(6), 1–13, doi:10.1029/2006JC004003.

Jilan, S. (2004), Overview of the South China Sea circulation and its influence on the coastal physical oceanography outside the Pearl River Estuary, *Cont. Shelf Res.*, *24*(16), 1745–1760, doi:10.1016/j.csr.2004.06.005.

Jing, Z., Y. Qi, and Y. Du (2011), Upwelling in the continental shelf of northern South China Sea associated with 1997-1998 El Nio, *J. Geophys. Res. Ocean.*, *116*(2), 1–11, doi:10.1029/2010JC006598.

Jing, Z. you, Y. quan Qi, Z. lin Hua, and H. Zhang (2009), Numerical study on the summer upwelling system in the northern continental shelf of the South China Sea, *Cont. Shelf Res.*, *29*(2), 467–478, doi:10.1016/j.csr.2008.11.008.

Kalnay, E. et al. (1996), The NCEP/NCAR 40-Year Reanalysis Project, *Bull. Am. Meteorol. Soc.*, *77*(3), 437–471, doi:10.1175/1520-0477(1996)077<0437:TNYRP>2.0.CO;2.

Kevin E. Trenberth (1997), The definition of El Nino - ProQuest, *Bull. Am. Meteorol. Soc.*, (August), 2771–2777, doi:10.1175/1520-0477(1997)078<2771:TDOENO>2.0.CO;2.

Kumar, B. P., Vialard, J., Lengaigne, M., Murty, V. S. N., & Mcphaden, M. J. (2012). TropFlux: air-sea fluxes for the global tropical oceans—description and evaluation. Climate Dynamics, 38(7-8), 1521-1543.

Kuo, N., Q. Zheng, and C.-R. Ho (2000), Satellite Observation of Upwelling along the Western Coast of the South China Sea, *Remote Sens. Environ.*, *74*(3), 463–470, doi:10.1016/S0034-4257(00)00138-3.

Lan, J., Y. Wang, F. Cui, and N. Zhang (2015), Seasonal variation in the South China Sea deep circulation, *J. Geophys. Res. Ocean.*, 1682–1690, doi:10.1002/2014JC010413.

Lau, K. M., and S. Yang (1997), Climatology and interannual variability of the southeast asian summer monsoon, *Adv. Atmos. Sci.*, *14*(2), 141–162, doi:10.1007/s00376-997-0016-y.

Le, T. P. Q., J. Garnier, B. Gilles, T. Sylvain, and C. Van Minh (2007), The changing flow regime and sediment load of the Red River, Viet Nam, *J. Hydrol.*, *334*(1–2), 199–214, doi:10.1016/j.jhydrol.2006.10.020.

Levadoux, M. ., N. K. Ich, and T. X. Quang (1935), *Địa chí tỉnh Bình Thuận (Geography of Binh Thuan Province/ Monographie de la province de Binh Thuan)*, Binh Thuan: Nha Học chánh Bình Thuận.

Li, L., W. D. Nowlin, and S. Jilan (1998), Anticyclonic rings from the Kuroshio in the South China Sea, *Deep. Res. Part I Oceanogr. Res. Pap.*, *45*(9), 1469–1482, doi:10.1016/S0967-0637(98)00026-0.

Li, Y., W. Han, J. L. Wilkin, W. G. Zhang, H. Arango, J. Zavala-Garay, J. Levin, and F. S. Castruccio (2014), Interannual variability of the surface summertime eastward jet in the South China Sea, *J. Geophys. Res. Ocean.*, *119*(10), 7205–7228, doi:10.1002/2014JC010206.

Li, Z., Y. Saito, E. Matsumoto, Y. Wang, S. Tanabe, and Q. L. Vu (2006), Climate change and human impact on the Song Hong (Red River) Delta, Vietnam, during the Holocene, *Quat. Int.*, *144*(1), 4–28, doi:10.1016/j.quaint.2005.05.008.

Lien, R.-C. C., T. Y. Tang, M. H. Chang, and E. A. D'Asaro (2005), Energy of nonlinear internal waves in the South China Sea, *Geophys. Res. Lett.*, *32*(5), 1–5, doi:10.1029/2004GL022012.

Lin, I.-I., W. Timothy Liu, C.-C. Wu, J. C. H. Chiang, and C.-H. Sui (2003), Satellite observations of modulation of surface winds by typhoon-induced upper ocean cooling, *Geophys. Res. Lett.*, *30*(3), 1131, doi:10.1029/2002GL015674.

Liu, C., D. Wang, Y. Chao, and C. Nan (1998), Internal Waves Generated by the Tidal Current in Luzon Strait, , 1–3.

Liu, Q., A. A. Kaneko, S. Jilan, and J. Su (2008), Recent progress in studies of the South China Sea circulation, *J. Oceanogr.*, *64*(5), 753–762, doi:10.1007/s10872-008-0063-8.

Liu, X., J. Wang, X. Cheng, and Y. Du (2012), Abnormal upwelling and chlorophyll-a concentration off South Vietnam in summer 2007, *J. Geophys. Res. Ocean.*, *117*(7), 2–11, doi:10.1029/2012JC008052.

Liu, Z., and J. Gan (2017), Three-dimensional pathways of water masses in the South China Sea: A modeling study, *J. Geophys. Res. Ocean.*, *122*(7), 6039–6054, doi:10.1002/2016JC012511.

Loick-Wilde, N., D. Bombar, H. N. Doan, L. N. Nguyen, A. M. Nguyen-Thi, M. Voss, and J. W. Dippner (2017), Microplankton biomass and diversity in the Vietnamese upwelling area during SW monsoon under normal conditions and after an ENSO event, *Prog. Oceanogr.*, *153*, 1–15, doi:10.1016/j.pocean.2017.04.007.

Loick, N., J. Dippner, H. N. Doan, I. Liskow, and M. Voss (2007a), Pelagic nitrogen dynamics in the Vietnamese upwelling area according to stable nitrogen and carbon isotope data, *Deep. Res. Part I Oceanogr. Res. Pap.*, *54*(4), 596–607, doi:10.1016/j.dsr.2006.12.009.

Loick, N., J. Dippner, H. N. Doan, I. Liskow, and M. Voss (2007b), Pelagic nitrogen dynamics in the Vietnamese upwelling area according to stable nitrogen and carbon isotope data, *Deep. Res. Part I Oceanogr. Res. Pap.*, *54*(4), 596–607, doi:10.1016/j.dsr.2006.12.009.

Madden, R. a., and P. R. Julian (1972), Description of Global-Scale Circulation Cells in the Tropics with a 40–50 Day Period, *J. Atmos. Sci.*, *29*(6), 1109–1123, doi:10.1175/1520-0469(1972)029<1109:DOGSCC>2.0.CO;2.

Madden, R. A., and P. R. Julian (1971), Detection of a 40–50 Day Oscillation in the Zonal Wind in the Tropical Pacific, *J. Atmos. Sci.*, *28*(5), 702–708, doi:10.1175/1520-0469(1971)028<0702:DOADOI>2.0.CO;2.

Madden, R. A., and P. R. Julian (1994), Observations of the 40–50-Day Tropical Oscillation—A Review, *Mon. Weather Rev.*, *122*(5), 814–837, doi:10.1175/1520-0493(1994)122<0814:OOTDTO>2.0.CO;2.

Mao, Q., P. Shi, K. Yin, J. Gan, and Y. Qi (2004), Tides and tidal currents in the Pearl River Estuary, *Cont. Shelf Res.*, *24*(16), 1797–1808, doi:10.1016/j.csr.2004.06.008.

Metzger, E. J., and H. E. Hurlburt (1996), Coupled dynamics of the South China Sea, the Sulu Sea, and the Pacific Ocean, *J. Geophys. Res.*, *101*(C5), 12,331-12,352, doi:0148-0227/96/95JC-03861.

Minh, N. N. (2013), Characteristics of tides in the Gulf of Tonkin (PhD Thesis - Toulouse University)

Molines, J., B. Barnier, and T. Penduff (2007), Definition of the interannual experiment ORCA025-G70, 1958-2004, *Update*, 1–34, doi:LEGI-DRA-2-11-2006i.

Morimoto, A., K. Yoshimoto, and T. Yanagi (2000), Characteristics of sea surface circulation and eddy field in the South China Sea revealed by satellite altimetric data, *J. Oceanogr.*, *56*(3), 331–344, doi:10.1023/A:1011159818531.

Morrow, R., L.-L. Fu, T. Farrar, H. Seo, and P.-Y. Le Traon (2017), Ocean Eddies and Mesoscale Variability, in *Satellite Altimetry over Oceans and Land Surfaces*, pp. 313–340.

Oberhuber, J. M. (1988), An atlas based on the "COADS" data set: the budgets of heat, buoyance and turbulent kinetic energy at the surface of the global ocean, *Max-Planck-Institute Meteorol. Rep.*, *15*, 1–20.

OSE, T., Y. SONG, and A. KITOH (1997), Sea surface temperature in the South China Sea : An index for the Asian monsoon and ENSO system, *J. Meteorol. Soc. Japan*, *75*(6), 1091–1107.

Pardé, M. (1938), Le régime du Fleuve Rouge, *Ann. Georgr.*, *47*(266), 191–195.

Park, Y., and A. Choi (2016), Long-term changes of South China Sea surface temperatures in winter and summer, *Cont. Shelf Res.*, 0–1, doi:10.1016/j.csr.2016.07.019.

Penduff, T., M. Juza, B. Barnier, J. Zika, W. K. Dewar, A. M. Treguier, J. M. Molines, and N. Audiffren (2011), Sea level expression of intrinsic and forced ocean variabilities at interannual time scales, *J. Clim.*, *24*(21), 5652–5670, doi:10.1175/JCLI-D-11-00077.1.

Penven, P., P. Marchesiello, L. Debreu, and J. Lefèvre (2008), Software tools for pre- and post-processing of oceanic regional simulations, *Environ. Model. Softw.*, *23*(5), 660–662, doi:10.1016/j.envsoft.2007.07.004.

Philander, S. G. (1985), El Niño and La Niña, *J. Atmos. Sci.*, *42*(23), 2652–2662, doi:10.1175/1520-0469(1985)042<2652:ENALN>2.0.CO;2.

Qiu, B., and S. Chen (2004), Seasonal Modulations in the Eddy Field of the South Pacific Ocean, *J. Phys. Oceanogr.*, *34*(7), 1515–1527, doi:10.1175/1520-0485(2004)034<1515:SMITEF>2.0.CO;2.

Qiu, Y., W. Cai, X. Guo, and B. Ng (2014), The asymmetric influence of the positive and negative IOD events on China's rainfall, *Sci. Rep.*, *4*, 1–6, doi:10.1038/srep04943.

Qu, T., H. Mitsudera, and T. Yamagata (2000), Intrusion of the North Pacific waters into the South China Sea, *J. Geophys. …*, *105*, 6415–6424.

Qu, T., Y. Y. Kim, M. Yaremchuk, T. Tuzuka, A. Ishida, and T. Yamagata (2004), Can Luzon Strait transport play a role in conveying the impact of ENSO to the South China Sea?, *J. Clim.*, *17*(18), 3644–3657, doi:10.1175/1520-0442(2004)017<3644:CLSTPA>2.0.CO;2.

Qu, T., Y. T. Song, and T. Yamagata (2009), An introduction to the South China Sea throughflow: Its dynamics, variability, and application for climate, *Dyn. Atmos. Ocean.*, *47*(1–3), 3–14, doi:10.1016/j.dynatmoce.2008.05.001.

Ray, R. D., and E. D. Zaron (2011), Non-stationary internal tides observed with satellite altimetry, *Geophys. Res. Lett.*, *38*(17), 1–5, doi:10.1029/2011GL048617.

Rayner, N. A., D. E. Parker, E. B. Horton, C. K. Folland, L. V. Alexander, D. P. Rowell, E. C. Kent, and A. Kaplan (2003), Global analysis of sea surface temperature, sea ice, and night marine air temperature since the late nineteenth century, *J. Geophys. Res.*, *108*(D14), 1–20, doi:10.1029/2002JD002670.

Richardson, P. L. (1983), Eddy kinetic energy in the North Atlantic from surface drifters, *J. Geophys. Res.*, *88*(C7), 4355, doi:10.1029/JC088iC07p04355.

Rong, Z., Y. Liu, H. Zong, and Y. Cheng (2007), Interannual sea level variability in the South China Sea and its response to ENSO, *Glob. Planet. Change*, *55*(4), 257–272, doi:10.1016/j.gloplacha.2006.08.001.

Saha, S. et al. (2010), The NCEP climate forecast system reanalysis, *Bull. Am. Meteorol. Soc.*, *91*(8), 1015–1057, doi:10.1175/2010BAMS3001.1.

Saji, N. H., P. N. Vinayachandran, and T. Yamagata (1999), A dipole in the tropical Indian Ocean, *Nature*, *401*(September), 360–363.

Sérazin, G., B. Meyssignac, T. Penduff, L. Terray, B. Barnier, and J. M. Molines (2016), Quantifying uncertainties on regional sea level change induced by multidecadal intrinsic oceanic variability, *Geophys. Res. Lett.*, *43*(15), 8151–8159, doi:10.1002/2016GL069273.

Shaw, P., S.-Y. Chao, K.-K. Liu, S.-C. Pai, and C.-T. Liu (1996), Winter upwelling off Luzon in the northeastern South China Sea, *J. Geophys. Res.*, *101*(C7), 16435–16448, doi:10.1029/96JC01064.

Shchepetkin, A. F. (2003), A method for computing horizontal pressure-gradient force in an oceanic model with a nonaligned vertical coordinate, *J. Geophys. Res.*, *108*(C3), 3090, doi:10.1029/2001JC001047.

Shchepetkin, A. F., and J. C. McWilliams (2005), The regional oceanic modeling system (ROMS): A split-explicit, free-surface, topography-following-coordinate oceanic model, *Ocean Model.*, *9*(4), 347–404, doi:10.1016/j.ocemod.2004.08.002.

Somot, S., F. Sevault, M. Déqué, and M. Crépon (2008), 21st century climate change scenario for the Mediterranean using a coupled atmosphere-ocean regional climate model, *Glob. Planet. Change*, *63*(2–3), 112–126, doi:10.1016/j.gloplacha.2007.10.003.

Song, X., Z. Lai, R. Ji, C. Chen, J. Zhang, L. Huang, J. Yin, Y. Wang, S. Lian, and X. Zhu (2012), Summertime primary production in northwest South China Sea: Interaction of coastal eddy, upwelling and biological processes, *Cont. Shelf Res.*, *48*, 110–121, doi:10.1016/j.csr.2012.07.016.

Song, Y., and D. Haidvogel (1994), A semi-implicit ocean circulation model using a generalized topography-following coordinate system, *J. Comput. Phys.*, *115*(1), 228–244, doi:10.1006/jcph.1994.1189.

Stewart, R. H. (2008a), *Introduction to physical oceanography*, Orange Grove.

Stewart, R. H. (Robert H. R. H. (2008b), *Introduction to physical oceanography*, Orange Grove.

Tan, W., X. Wang, W. Wang, C. Wang, and J. Zuo (2016), Different responses of sea surface temperature in the South China Sea to various El Niño events during boreal autumn, *J. Clim.*, *29*(3), 1127–1142, doi:10.1175/JCLI-D-15-0338.1.

Tang, D. L., H. Kawamura, P. Shi, W. Takahashi, L. Guan, T. Shimada, F. Sakaida, and O. Isoguchi (2006), Seasonal phytoplankton blooms associated with monsoonal influences and coastal environments in the sea areas either side of the Indochina Peninsula, *J. Geophys. Res. Biogeosciences*, *111*(1), G01010, doi:10.1029/2005JG000050.

Tong, H. W., J. C. L. Chan, and W. Zhou (2009), The role of MJO and mid-latitude fronts in the South China Sea summer monsoon onset, *Clim. Dyn.*, *33*(6), 827–841, doi:10.1007/s00382-008-0490-7.

Tri, D. Q., N. T. M. Linh, and N. C. Don (2017), Using numerical modelling in the simulation of mass fish death phenomenon along the Central Coast of Vietnam, *Mar. Pollut. Bull.*, (October), 0–1, doi:10.1016/j.marpolbul.2017.10.065.

Tseng, Y. H., S. Jan, D. E. Dietrich, I. I. Lin, Y. T. Chang, and T. Y. Tang (2010), Modeled oceanic response and sea surface cooling to typhoon Kai-Tak, *Terr. Atmos. Ocean. Sci.*, *21*(1), 85–98, doi:10.3319/TAO.2009.06.08.02(IWNOP).

UNESCAP (2016), *Droughts and saltwater intrusions in Vietnam*, Bangkok.

Vidal-Vijande, E., A. Pascual, B. Barnier, J. M. Molines, N. Ferry, and J. Tintore (2012), Multiparametric analysis and validation in the western Mediterranean of three global OGCM hindcasts, Sci. Mar., 76(S1), 147–164, doi:10.3989/scimar.03613.19D.

Waldman, R., S. Somot, M. Herrmann, F. Sevault, and P. E. Isachsen (2018), On the chaotic variability of ocean deep convection in the Mediterranean Sea, *Geophys. Res. Lett.*, doi:10.1002/2017GL076319.

Wang, B., R. Wu, and X. Fu (2000a), Pacific – East Asian Teleconnection : How Does ENSO Affect East Asian Climate ?, , 1517–1536, doi:10.1175/1520-0442(2000)013<1517:PEATHD>2.0.CO;2.

Wang, B., F. Huang, Z. Wu, J. Yang, X. Fu, and K. Kikuchi (2009), Multi-scale climate variability of the South China Sea monsoon: A review, *Dyn. Atmos. Ocean.*, *47*(1–3), 15–37, doi:10.1016/j.dynatmoce.2008.09.004.

Wang, C., W. Wang, D. Wang, and Q. Wang (2006a), Interannual variability of the South China Sea associated with El Niño, *J. Geophys. Res.*, *111*(C3), C03023, doi:10.1029/2005JC003333.

Wang, G. (2003), Mesoscale eddies in the South China Sea observed with altimeter data, *Geophys. Res. Lett.*, *30*(21), 2121, doi:10.1029/2003GL018532.

Wang, G., D. Chen, and J. Su (2006b), Generation and life cycle of the dipole in the South China Sea summer circulation, *J. Geophys. Res. Ocean.*, *111*(6), 1–9, doi:10.1029/2005JC003314.

Wang, G., D. Chen, and J. Su (2008), Winter Eddy Genesis in the Eastern South China Sea due to Orographic Wind Jets, *J. Phys. Oceanogr.*, *38*(3), 726–732, doi:10.1175/2007JPO3868.1.

Wang, H. J., and S. P. He (2012), Weakening relationship between East Asian winter monsoon and ENSO after mid-1970s, *Chinese Sci. Bull.*, *57*(27), 3535–3540, doi:10.1007/s11434-012-5285-x.

Wang, L., C. J. Koblinsky, and S. Howden (2000b), Mesoscale variability in the South China Sea from the TOPEX/Poseidon altimetry data, *Deep Sea Res. Part I Oceanogr. Res. Pap.*, *47*(4), 681–708, doi:10.1016/S0967-0637(99)00068-0.

Wang, W., P. Xie, S.-H. Yoo, Y. Xue, A. Kumar, and X. Wu (2010), An assessment of the surface climate in the NCEP climate forecast system reanalysis, *Clim. Dyn.*, *37*(7–8), 1601–1620, doi:10.1007/s00382-010-0935-7.

Wang, Y., G. Fang, Z. Wei, F. Qiao, and H. Chen (2006c), Interannual variation of the South China Sea circulation and its relation to El Nino, as seen from a variable grid global ocean model, *J. Geophys. Res. Ocean.*, *111*(11), 1–15, doi:10.1029/2005JC003269.

Wolanski, E., N. Huu Nhan, and S. Spagnol (1998), Sediment Dynamics during Low Flow Conditions in the Mekong River Estuary, Vietnam, *J. Coast. Res.*, *14*(2), 472–482.

Wu, C.-R., and T.-L. Chiang (2007), Mesoscale eddies in the northern South China Sea, *Deep Sea Res. Part II Top. Stud. Oceanogr.*, *54*(14–15), 1575–1588, doi:10.1016/j.dsr2.2007.05.008.

Wu, C. R., and C. W. J. Chang (2005), Interannual variability of the South China Sea in a data assimilation model, *Geophys. Res. Lett.*, *32*(17), 1–4, doi:10.1029/2005GL023798.

Wyrtki, K. (1961), *Physical oceanography of the Southeast Asian waters.*

Xie, S., Q. Xie, D. Wang, and W. Liu (2003), Summer upwelling in the South China Sea and its role in regional climate variations, *J. Geophys. ...*, *108*(C8), 3261, doi:10.1029/2003JC001867.

Xie, S.-P. (2003), Summer upwelling in the South China Sea and its role in regional climate variations, *J. Geophys. Res.*, *108*(C8), 3261, doi:10.1029/2003JC001867.

Xie, S. P., C. H. Chang, Q. Xi, and D. Wang (2007), Intraseasonal variability in the summer South China Sea: Wind jet, cold filament, and recirculations, *J. Geophys. Res. Ocean.*, *112*(10), C10008, doi:10.1029/2007JC004238.

Xiu, P., F. Chai, L. Shi, H. Xue, and Y. Chao (2010), A census of eddy activities in the South China Sea during 1993-2007, *J. Geophys. Res. Ocean.*, *115*(3), C03012, doi:10.1029/2009JC005657.

Xu, X. (1982), The general descriptions of the horizontal circulation in the South China Sea, in *Proceedings of the 1980 Symposium on Hydrometeorology, Chinese Society of Oceanology and Limnology*, pp. 137–145, Science Press.

Xue, H., F. Chai, N. Pettigrew, D. Xu, M. Shi, and J. Xu (2004), Kuroshio intrusion and the circulation in the South China Sea, *J. Geophys. Res.*, *109*(C2), 1–14, doi:10.1029/2002JC001724.

Xue, Y., B. Huang, Z. Z. Hu, A. Kumar, C. Wen, D. Behringer, and S. Nadiga (2011), An assessment of oceanic variability in the NCEP climate forecast system reanalysis, *Clim. Dyn.*, *37*(11–12), 2511–2539, doi:10.1007/s00382-010-0954-4.

Yanagi, T., T. Takao, and A. Morimoto (1997), Co-tidal and co-range charts in the South China Sea derived from satellite altimetry data, *Mer*, *35*(3), 85–93.

Yu, L., and R. A. Weller (2007), Objectively analyzed air-sea flux fields for the global ice-free oceans (1981-2005), *Bull. Am. Meteorol. Soc.*, *88*(January), 527–539, doi:10.1175/BAMS-88-4-527.

Yu, L., Jin, X., & Weller, R. A. (2008). Multidecade Global Flux Datasets from the Objectively Analyzed Air-sea Fluxes (OAFlux) Project: Latent and sensible heat fluxes, ocean evaporation, and related surface meteorological variables. OAFlux Project Technical Report. OA-2008-01, 64pp.

Yuan, Y., H. Yang, W. Zhou, and C. Li (2008), Influences of the Indian ocean dipole on the asian summer monsoon in the following year, *Int. J. Climatol.*, *28*(14), 1849–1859, doi:10.1002/joc.1678.

Zeng, L., D. Wang, J. Chen, W. Wang, and R. Chen (2016), SCSPOD14, a South China Sea physical oceanographic dataset derived from in situ measurements during 1919–2014, *Sci. Data*, *3*, 160029, doi:10.1038/sdata.2016.29.

Zhang, C. (2005), Madden-Julian Oscillation, *Rev. Geophys.*, *43*(2), 1–36, doi:10.1029/2004RG000158.

Zhang, C., and M. Dong (2004), Seasonality in the Madden-Julian oscillation, *J. Clim.*, *17*(16), 3169–3180, doi:10.1175/1520-0442(2004)017<3169:SITMO>2.0.CO;2.

Zhang, L., B. Wang, and Q. Zeng (2009), Impact of the Madden-Julian oscillation on summer rainfall in Southeast China, *J. Clim.*, *22*(2), 201–216, doi:10.1175/2008JCLI1959.1.

Zhang, S., X. X. Lu, D. L. Higgitt, C. T. A. Chen, J. Han, and H. Sun (2008), Recent changes of water discharge and sediment load in the Zhujiang (Pearl River) Basin, China, *Glob. Planet. Change*, *60*(3–4), 365–380, doi:10.1016/j.gloplacha.2007.04.003.

Zhao, Z., V. Klemas, Q. Zheng, and X.-H. Yan (2004), Remote sensing evidence for baroclinic tide origin of internal solitary waves in the northeastern South China Sea, *Geophys. Res. Lett.*, *31*(6), n/a-n/a, doi:10.1029/2003GL019077.

Zhuang, W., S.-P. Xie, D. Wang, B. Taguchi, H. Aiki, and H. Sasaki (2010), Intraseasonal variability in sea surface height over the South China Sea, *J. Geophys. Res.*, *115*(C4), C04010, doi:10.1029/2009JC005647.

Zu, T., J. Gan, and S. Y. Erofeeva (2008a), Numerical study of the tide and tidal dynamics in the South China Sea, *Deep. Res. Part I Oceanogr. Res. Pap.*, *55*(2), 137–154, doi:10.1016/j.dsr.2007.10.007.

Zu, T., J. Gan, and S. Y. Erofeeva (2008b), Numerical study of the tide and tidal dynamics in the South China Sea, *Deep Sea Res. Part I Oceanogr. Res. Pap.*, *55*(2), 137–154, doi:10.1016/j.dsr.2007.10.007.